Magnetic Microbubbles: investigation and design of new formulations for targeted therapy

Joshua William Owen



A thesis submitted in partial fulfilment
of the requirements for the degree of
Doctor of Philosophy
(DPhil)
of
St Catherine's College
University of Oxford

IBME
Department of Engineering Science
University of Oxford
Trinity 2014

Abstract

Targeted therapy is a significant area of research in pharmaceutical and biomedical science. Its overall aim is to achieve maximum impact on malignant cells with minimum side effects to healthy tissue. In this thesis the capabilities of magnetic microbubbles as targeted therapeutic delivery vehicles are explored. New characterisation techniques were developed in order to understand and improve the current magnetic microbubble formulation. Electron microscopy was used to analyse the nanoscale structure of microbubble shells and observe nanoparticles attached to the shell surface. A new flow phantom was developed and the targeting of magnetic microbubbles against flow conditions corresponding to those in the human body was found to be feasible in numerous vessel sizes and flow conditions. Magnetic targeting of microbubbles was also observed in a perfused porcine liver model. Magnetic targeting was then attempted against flowing blood and a decrease in targeting efficiency observed. This was also seen for biochemical targeting and collisions with red blood cells identified as the most likely cause. Importantly, the number of magnetically targeted microbubbles significantly exceeded those targeted via biochemical interactions in both blood and water. In the second part of the thesis new types of magnetic microbubble were developed. The first exploits the fusion of nano-scale magnetic droplets with phospholipid microbubbles. In the second magnetic nanoparticles were incorporated directly into the lipid shell. The new magnetic microbubble formulation could be magnetically targeted, observed via contrast ultrasound and was successfully used to deliver siRNA to neuroblastoma cells.

Publications

J. Owen, B. Zhou, P. Rademeyer, M. Tang, Q. Pankhurst, R. Eckersley, E. Stride. Understanding the Structure and Mechanism of Formation of a New Magnetic Microbubble Formulation. Theranostics 2012; 2: 1127-1139 (**invited**)

J. Owen, Q. Pankhurst and E. Stride. Magnetic targeting and ultrasound mediated drug delivery: benefits, limitations and combination. International Journal of Hyperthermia 2012;28:362-373.

Hosny NA, Mohamedi G, Rademeyer P, Owen J, Wu Y, Tang MX, Eckersley RJ, Stride E, Kuimova MK, close, 2013, Mapping microbubble viscosity using fluorescence lifetime imaging of molecular rotors, Proceedings of the National Academy of Sciences of the United States of America, Vol:110, ISSN:0027-8424, Pages:9225-9230

T. P. Millard, M. Endrizzi, L. Rigon,, F. Arfelli, R. H. Menk, J. Owen, E. Stride, and A. Olivo. Quantification of microbubble concentration through x-ray phase contrast Imaging. Applied Physics Letters (in press)

J. Owen, P. Gove, P. Rademeyer, E. Stride. Blood is Thicker than Water: The effect of Blood on Targeted Drug Delivery Efficiency (in press).

J. Owen, A. Siebert, K Grunwald, E. Stride. Understanding the Coating of Phospholipid Microbubbles for Biomedical Applications, (under review)

Conor McEwan, Joshua Owen, Eleanor Stride, Colin Fowley, Heather Nesbitt, David Cochrane, Constantin. C. Coussios, M. Borden, Anthony P. McHale and John F. Callan, Oxygen Carrying Microbubbles for Enhanced Sonodynamic Therapy of Hypoxic Tumours (under review).

J. Owen, P. Rademeyer, E. Stride. Magnetic Targeting of Microbubbles at Physiologically relevant flow rates, (in preparation)

Conference Presentations

Joshua William Owen, Paul Rademeyer, Eleanor Stride, The Influence of Blood on Targeted Microbubbles, 14th International Symposium on Therapeutic Ultrasound, Las Vegas, 2-5th April 2014.

Joshua Owen, The influence of blood on targeted microbubbles, Competition, 19th European Symposium on Ultrasound Imaging, 23-24th January 2014.

Joshua W. Owen, Paul Rademeyer, Eleanor Stride, Magnetic targeting of microbubbles at physiologically relevant flow rates, 166th Meeting of The Acoustical Society of America, San Francisco, 2-6 December 2013.

Crake, C., de Saint Victor, M., Coviello, C., Owen, J., Coussios, C., Stride, E. Passive acoustic mapping of magnetic microbubbles in an *in vitro* flow model. Joint Meeting of the Acoustical Society of America, The Canadian Acoustical Association and International Congress on Acoustics, Montreal, 2-7 June 2013.

Mohamedi, G., Hosny, N., Rademeyer, P., Park, Y., Owen, J., Pham, T.,Joyce Wong, J.,Kuimova, M., Stride, E. Investigating the effect of fabrication method on the stability and acoustic response of microbubble agents. Joint Meeting of the Acoustical Society of America, The Canadian Acoustical Association and International Congress on Acoustics, Montreal, 2-7 June 2013.

Joshua W Owen, Paul Rademeyer, Quentin Pankhurst, Eleanor Stride. Imaging and retention of magnetic microbubbles at physiologically relevant shear rates 245th American Chemical Society Meeting, Colloid and Surface Chemistry Technical Symposium, New Orleans, April 7th-11th 2013.

Graciela Mohamedi, Neveen A Hosney, Paul Rademeyer, Yoonjee Park, Joshua Owen, Tuan Pham, Joyce Y Wong, Marina Kuimova, Eleanor Stride. Influence of fabrication method on functional properties of microbubble agents for theranostic applications. 245th American Chemical Society Meeting, Colloid and Surface Chemistry Technical Symposium, New Orleans, April 7th-11th 2013.

J. Owen, Magnetic microbubbles: controllable agents for ultrasound imaging and therapeutic delivery. St. Catherine's College Biomedical Society Meeting. February 21st 2013.

Owen, J., Rademeyer, P., Pankhurst, Q., Stride, E. Magnetic Targeting of Microbubbles at Physiologically Relevant Flow Rates. 18th European Symposium on Ultrasound Contrast Imaging. Rotterdam Hilton Hotel. 16-18 January 2013.

Owen, J., Zhou, B., Hayotte, N., Tang, M., Pankhurst, Q., Eckersley, R., Stride, E. Retention of magnetic microbubbles in a flow phantom. 12th International Symposium on Therapeutic Ultrasound, Heidelberg, Germany June 10-13 2012.

Stride, E., Owen, J., Mulvana, H., Pankhurst, Q., Tang, M., Eckersley, R. 2012. Magnetic microbubbles for localised imaging and drug delivery: Development, characterisation and preliminary application in vivo. Acoustics 2012 Hong Kong, Hong Kong Convention and Exhibition Center 14th-18th May 2012 (**invited**).

Owen, J., Zhou, B., Hayotte, N., Tang, M., Pankhurst, Q., Eckersley, R., Stride, E. Magnetic Microbubbles Therapeutic Ultrasound Interest Group, University College London, February 13 2012.

Acknowledgements

First and foremost I would like to thank my supervisor Professor Eleanor Stride without whom this research would not be possible. Her hard work, dedication, belief and innovative approach to scientific discovery have been the inspiration and foundation of my entire Doctorate. I would also like to thank Robert Eckersley for his support and use of lab space during the beginning of my thesis.

Secondly I would like to thank my secondary supervisor Professor Quentin Pankhurst for his support and input during this thesis.

I would also like to thank my colleagues in BUBBL. In particular Paul Rademeyer, Caroline Harfield, Graceila Mohamedi, Richard Browning, Marie de Saint Victor, Calum Crake, Matt Adams, Dr. Jeong Li and Dr. Dario Carugo. Their help and support both inside and outside of lab has been essential. Also Dr Cristina Blanco-Andujar and Dr Daniel Ortega for their support.

Last but not least I would like to thank my family for putting up with my absence, my girlfriend Katarina for putting up with me and Oxford Lindy Hoppers for helping with stress relief.

“That’s an amazing invention, but who would ever want to use one of them?”

President Rutherford B. Hayes after being shown a telephone

Table of Contents

1 INTRODUCTION AND BACKGROUND 16

1.1 Therapeutic delivery for targeting disease. 16

1.2 Objectives of the research 19

1.2.1 Characterisation of magnetic microbubbles 19

1.2.2 Assessing the feasibility of magnetic targeting of microbubbles on length scales and flow conditions relevant to human physiology 20

1.2.3 The effect of blood on microbubble targeting 20

1.2.4 New magnetic microbubble formulation 20

1.3 Thesis Outline 21

1.4 References 23

2 LITERATURE REVIEW 26

2.1 Summary 26

2.2 Magnetism and drug delivery 26

2.2.1 Types of magnetic materials 26

2.2.2 Magnetic nanoparticles 29

2.2.3 Drug delivery applications 30

2.2.4 Gene delivery applications 32

2.2.5 Limitations 34

2.3 Ultrasound and drug delivery 34

2.3.1 Basic physical principles 35

2.3.2 Microbubbles 36

2.3.2.1 Coating materials 38

2.3.2.2 Filling gas 40

2.3.2.3 Nanoparticle coatings 41

2.3.2.4 Fabrication techniques 41

2.3.3 Drug delivery applications 42

2.3.4 Microbubble delivery benefits 43

2.3.5 Gene delivery applications 44

2.3.6 siRNA delivery 47

2.3.7 Targeting 49

2.3.8 Conjugation strategies 50

2.3.9 Limitations 52

2.4 Ultrasound and magnetism 53

2.4.1 High intensity focused ultrasound (HIFU) surgery 53

2.4.2 Stimulated release 54

2.5 Magnetic microbubbles 54

2.5.1 Magnetic microbubbles as dual contrast agents 54

2.5.2 Magnetic microbubbles for drug delivery 56

2.6 Analysis techniques 61

2.6.1 Introduction 61

2.6.2 Fluorescence microscopy 61

2.6.3 Fluorescence lifetime viscosity measurements 63

2.6.4 Electron microscopy 64

2.7 References 65

3 MATERIALS AND METHODS 76

3.1 Materials 76

3.2 Methods 77

3.2.1 Microbubble production methods 77

3.2.1.1 Introduction 77

3.2.1.2 Phospholipid/emulsifier microbubbles (PMBs) 77

3.2.1.3 Gold coated microbubbles (GMBs) 78

3.2.1.4 Magnetic microbubble formulation 1 (MMB) 78

3.2.1.5 Magnetic microbubble formulation 2 (CAMMB) 79

3.2.1.6 Magnetic droplets and microbubbles (MDMBs) 79

3.2.1.7 Biotin microbubbles formulation (BMBs) 79

3.2.1.8 Magnetic microbubble formulation 3 (LMMB) 80

3.2.1.9 Charged magnetic microbubble solution 3 (CLMMB) 80

3.2.1.10 siRNA attachment 81

3.2.2 Optical analysis of microbubbles 81

3.2.2.1 Sizing software for bubble analysis 82

3.2.3 Fluorescence microscopy 83

3.2.3.1 Introduction 83

3.2.3.2 Fluorescence microscopy 83

3.2.4 Transmission electron microscopy (TEM) 84

3.2.5 Zeta Potential 85

3.2.5.1 Introduction 85

3.2.5.2 Overview 85
3.2.5.3 Technique 85
3.2.6 Magnetic relaxivity 86
3.2.7 Magnetic targeting study 87
3.2.7.1 Introduction 87
3.2.7.2 Overview 87
3.2.7.3 Magnetic field strength....88
3.2.7.4 Vessel sizes 89
3.2.7.5 Flow conditions 91
3.2.7.6 Ultrasound Image analysis 91
3.2.8 Acoustic response and targeting 92
3.2.9 Targeting against blood flow 93
3.2.9.1 Experimental set up 93
3.2.9.2 Magnetic microbubbles quantification 94
3.2.9.3 Biotin bubbles targeting quantification 95
3.2.9.4 Non linear response 96
3.2.10 Liver perfusion study 97
3.2.10.1 Perfusion set up 97
3.2.11 siRNA delivery 100
3.2.11.1 Cell culture 100
3.2.11.2 Ultrasound set up....100
3.2.11.3 Opticell set up....101
3.2.11.4 Ultrasound field calibration....102
3.2.11.1 Fluorescence measurements....102
3.2.11.2 Large image analysis....103
3.2.11.3 Plate reader experiments 103

3.3 References....103

4 TRANSMISSION ELECTRON MICROSCOPY 105

4.1 Summary....105

4.2 Introduction....105

4.3 Preliminary experiments....106

4.4 Low temperature transmission electron microscopy (LTTEM) 108
4.4.1 Preliminary Results 109

4.5 Uranyl Acetate Coating for Electron Microscopy 110
4.5.1 Microbubble preparations 110

4.6 Initial characterisation 111
4.6.1 Phospholipid microbubbles 114
4.6.2 Gold Coated microbubbles 116
4.6.3 Magnetic microbubble formulation 1 121
4.6.4 Magnetic microbubble formulation 3 126
4.6.5 Magnetic droplets and microbubbles 130

4.7 Discussion 132
4.7.1 Technique 132
4.7.2 Domains 133
4.7.3 Confirming hypothesised structures 134
4.7.4 Limitations 135

4.8 References 136

5 CHARACTERISATION OF MAGNETIC MICROBUBBLES 137

5.1 Introduction 137
5.1.1 Magnetic targeting 137

5.2 Flow regimes to be investigated 140
5.2.1 Acoustic observation of magnetic targeting 142
5.2.2 Targeting analysis 142
5.2.3 Targeting time and intensity analysis. 143
5.2.4 Optical observation of targeting 144
5.2.5 Effect of targeting on microbubbles 145

5.3 Results 145
5.3.1 Retention of magnetic microbubbles against flow 145
5.3.2 Targeting time 148
5.3.3 Quantification of targeting 149
5.3.4 Optical observation of magnetic targeting 152
5.3.5 The effect of targeting on microbubbles 153

5.4 Discussion 154

5.5 Limitations 157

5.6 References 158

6 *IN VIVO* FACTORS 160

6.1 Summary **160**

6.2 Liver study **160**

6.2.1 Materials and methods 161

6.2.2 Results 161

6.2.3 Limitations 164

6.3 The impact of blood upon the targeting of microbubbles **164**

6.3.1 The impact of blood upon targeting 164

6.3.2 The effect of blood on the microbubbles 167

6.3.3 Limitations 169

6.4 Examination of the impact of blood on magnetic targeting in a medium size vessel **170**

6.4.1 Introduction 170

6.4.2 Materials and methods 170

6.4.3 Results 171

6.5 Optical analysis of the impact of blood **174**

6.6 The effect of blood on magnetic targeting **174**

6.6.1 The effect of blood on biochemical targeting 176

6.6.2 Results 177

6.7 Discussion **178**

6.7.1 Reason for reduction in targeting efficiency 179

6.7.2 Limitations to the technique 181

6.8 References **182**

7 NEW MAGNETIC MICROBUBBLE FORMULATIONS **184**

7.1 Summary **184**

7.2 Introduction **184**

7.3 Results of droplets and bubbles. **185**

7.3.1 Targeting Under Flow 187

7.4 Discussion of Magnetic Droplets/Microbubbles **191**

7.4.1 Proposed Mechanism 191

7.5 Design of New Magnetic Microbubbles **194**

7.6 Magnetic microbubbles with lipid coated nanoparticles (LMMB) **197**

7.6.1 Preliminary Studies 199
7.6.2 Improvements to the formulation 199

7.7 Results 200
7.7.1 Magnetic Response 201
7.7.2 Size and Concentration 202
7.7.3 Acoustic response 203
7.7.4 Retention Analysis 204
7.7.5 Contrast ultrasound imaging mode 206
7.7.6 Magnetic relaxivity 208
7.7.7 Improvements to size and Concentration 209

7.8 Discussion 212

7.9 References 213

8 SIRNA DELIVERY USING MAGNETIC MICROBUBBLES 215

8.1 Summary 215

8.2 Introduction 215

8.3 Methods 217
8.3.1 Experimental procedure 217

8.4 Results 218
8.4.1 Zeta potential 220
8.4.2 Fluorescence imaging 222
8.4.3 Ultrasound field calibration 224

8.5 Transfection results 224
8.5.1 Plate reader results 224
8.5.2 Fluorescence microscopy 226
8.5.3 Cell morphology 230

8.6 Discussion 231

8.7 Limitations. 233
8.7.1 Potential Limitations in vivo 234

8.8 References 234

9 CONCLUSIONS AND FUTURE WORK 236

9.1 Conclusions 236
9.1.1 Overview 236
9.1.2 Electron Microscopy 236
9.1.3 Magnetic Targeting 237
9.1.4 In vivo Liver Targeting 238
9.1.5 Targeting against Blood 238
9.1.6 Magnetic Droplets and Microbubbles 239
9.1.7 New Microbubble Formulation 240
9.1.8 Transfection study of newly designed Magnetic microbubbles 240

9.2 Future Work 241
9.2.1 Electron microscopy of microbubbles with liposomes bound to the surface 241
9.2.2 Agglomeration of microbubbles in blood 242
9.2.3 Effect of single red blood cells in an 8 μm channel. 242
9.2.4 Magnetic Droplets and Commercial Contrast Agents 242
9.2.5 Citric acid coated iron oxide nanoparticles 243
9.2.6 Janus Bubbles 243
9.2.7 Biotoxicity, Biocompatability and Pharmacokinetics 244
9.2.8 Examination of knockdown with siRNA and in vivo experiments. 244
9.2.9 Three dimensional magnetic arrays for targeting 245

9.3 References 245

10 APPENDIX 247

1 Introduction and background

1.1 Therapeutic delivery for targeting disease.

The concept of targeted drug delivery was originally put forward in the literature by Paul Ehrlich (1854 – 1915) who theorised that if malignant tissue could be selectively targeted then a toxin could also be selectively delivered in a manner akin to a "magic bullet" [1]. The central principle of drug targeting is that the distribution of drug within an organism is manipulated in such a manner that the majority interacts exclusively with the target tissue [2]. A successful drug delivery system should provide maximum therapeutic efficacy with minimal unwanted side effects [3]. To do so it must: (i) protect the therapeutic material to prevent unwanted degradation during its passage through the body, (ii) concentrate the material at the desired location(s) and (iii) promote uptake in the target tissue.

The rapid advances in the development of new types of pharmaceutical product have greatly increased demand for more effective delivery systems [4]. In addition, new formulations and delivery methods for existing products are increasingly being sought to mitigate the impact of patent expiration, the so called "patent cliff" [5]. In 2008 the US demand for drug delivery systems was predicted to increase by more than 10% per year reaching $132 billion by 2012 [6]. Conventional delivery methods such as injections and oral administration have significant advantages in terms of convenience and cost, but are unsuitable for several classes of therapeutic compound. For example, administration of poorly soluble drugs and large molecules such as proteins and DNA via intravenous or oral routes is largely ineffective [4]. Moreover, systemic administration results in the exposure of all tissues and this can lead to harmful side

effects [7]. The most well-known examples are perhaps those relating to cancer chemotherapy and compounds such as Paclitaxel, which inhibits the proliferation of cancer cells but is often associated with neutropenia and nausea [8].

Numerous strategies from the use of light sensitive polymeric carriers to viruses [6, 9] have been proposed for therapeutic delivery and the development of delivery systems represents a significant research field in its own right [5, 10]. Solid nanoparticles, liposomes and micelles are the three most common types of non-viral delivery vehicle investigated [4, 11].

One therapeutic delivery vehicle which has shown great potential for drug delivery is the microbubble. Below 8 μm in size, the diameter of a red blood cell, with a gas core stabilised by a biocompatible shell, suspensions of microbubbles are currently in use in the clinic as ultrasound contrast agents. The oscillations of microbubbles when exposed to ultrasound have also been shown to promote the uptake of therapeutic compounds by nearby cells. The microbubble shell can further be functionalised in order to attach therapeutic compounds and/or targeting species. Targeted microbubbles with moieties attached to the surface have been designed to image inflammation [12-20], angiogenesis [21-23], thrombi [24-29], tumours [30-32] and to treat thrombi [33] and tumours [34]. However despite successful *in vitro* results, biochemical targeting of microbubbles *in vivo* has proved challenging [35].

Other methods have been used to target microbubbles; for example, exploiting the acoustic radiation force produced when microbubbles are exposed to ultrasound [36]. Attaching magnetic nanoparticles to the microbubble surface such that the

microbubble can be moved by an external magnetic field has also shown great promise for targeted therapy [37]. Magnetic nanoparticles have been used for drug delivery in their own right with varying degrees of success [1]. The material used usually consists of coated iron oxide, and magnetic nanoparticle formulations are already available in the clinic as MRI contrast agents.

To date, however, magnetic nanoparticle formulations have not been used for therapy in a clinical setting despite successful *in vitro* and *in vivo* results. This is because large magnetic field strengths and gradients are required in order to successfully target nanoparticles [38]. Moreover, even when localised at a target site, magnetic nanoparticles alone cannot promote uptake of therapeutic material by the target cells. The use of charged polyelectrolytes such as PEI is required [39] or, the nanoparticles must be modified in some other way to facilitate delivery [40].

Magnetic microbubbles have several distinct advantages over non-magnetic microbubbles or magnetic nanoparticles:

-The location of the microbubbles can be controlled via an externally applied magnetic field for a much wider range of target locations than is possible with biochemical targeting. Unlike acoustic radiation force, the magnetic field will not perturb and potentially destroy the microbubbles; and the magnetic field strengths and gradients are much lower than those required for targeting nanoparticles.

-A very wide range of therapeutic agents can be bound to or incorporated into microbubbles and the oscillations of the microbubbles under ultrasound have been shown to promote uptake of both small and large molecule drugs including DNA and

siRNA. Solid or liquid microparticles and liposomes can transport and passively release therapeutic compounds but cannot promote uptake.

-The microbubbles can be imaged via both ultrasound and MRI. As such, the location of the drug delivery vehicles can be determined at all times and therapeutic release also potentially monitored.

-Microbubble formulations have been FDA approved as ultrasound contrast agents and certain types of iron oxide magnetic nanoparticles have been FDA approved as MRI contrast agents. This will potentially be beneficial in achieving regulatory approval for magnetic microbubbles as a clinical product.

Notwithstanding these advantages, there are a number of key questions that need to be addressed if the potential of magnetic microbubbles as therapeutic delivery vehicles is to be realised. Addressing these questions is the aim of the work described in this thesis and the specific objectives are outlined below.

1.2 Objectives of the research

1.2.1 Characterisation of magnetic microbubbles

The first objective of the research was to undertake a detailed study of the characteristics of existing magnetic microbubble formulations to understand their mechanisms of formation and their structure, with a view to ultimately improving their formulation.

1.2.2 Assessing the feasibility of magnetic targeting of microbubbles on length scales and flow conditions relevant to human physiology

The vast majority of *in vivo* drug delivery experiments utilise small animal models, typically mice. However, a mouse is a very poor model for magnetic targeting on account of the very different length scales and strong dependence of magnetic field strength on distance from the magnet. The second objective was therefore to examine whether or not magnetic microbubbles could target under conditions relevant to clinical applications in humans.

1.2.3 The effect of blood on microbubble targeting

Previously published studies of *in vitro* testing of microbubble targeting have examined the influence of flow in a saline suspension. The third objective was to examine the effect of blood on both magnetic and biochemical microbubble targeting. This objective was extended in a series of preliminary experiments to examine the influence of other features of the *in vivo* environment using a perfused organ model.

1.2.4 New magnetic microbubble formulation

The fourth objective was to develop a new type of magnetic microbubble that would address the shortcomings of the existing formulation and to demonstrate its potential as a therapeutic agent.

1.3 Thesis Outline

The present Chapter 1 provides background information about the research performed and a brief overview of magnetic and ultrasound responsive therapeutic delivery vehicles. The objectives, outline and scope of the thesis are stated.

Chapter 2 presents a detailed literature review. The origins and applications of magnetic nanoparticles are extensively examined as well as the use of ultrasound and microbubbles for therapeutic delivery. Existing techniques used to understand microbubble structure are also reviewed.

Chapter 3 describes the materials, experimental apparatus, procedures and characterisation techniques used in the subsequent chapters.

Chapter 4 describes a new technique developed to examine microbubble surface structure on the nanoscale using electron microscopy. Images of phospholipid microbubbles, including microbubbles with nanoparticles bound to the surface, are presented. The information provided by these images in terms of microbubble coating structure is discussed in relation to that proposed in previous studies from theoretical considerations.

Chapter 5 examines results obtained from the targeting of magnetic microbubbles. Flow systems were designed and constructed to test the limits of magnetic targeting of microbubbles against flow rates and shear rates found *in vivo*. The chapter has three sections: The first presents observation of targeting in varying vessel sizes and flow rates under ultrasound imaging. The time microbubbles successfully target and the

intensity of the ultrasound signal from targeted microbubbles is also examined over a variety of flow conditions and trends analysed. The second section examines the targeting of magnetic microbubbles at high shear rates, whilst the third section examines the effect of targeting on magnetic microbubble characteristics and stability.

Chapter 6 studies the effect of other important factors that may affect microbubble targeting *in vivo*. The first section presents experiments performed in a perfused porcine liver to examine magnetic targeting *in vivo* on a scale relevant to a human being. The second section investigates the impact of blood on the targeting of magnetic microbubbles and compares this to the impact of blood on biochemically targeted microbubbles.

Chapter 7 is divided into two sections presenting new formulations of magnetic microbubbles. A combination of magnetic droplets and microbubbles is explored first, based on the results of a previous study in which this combination was found to be an effective transfection agent. Second, a new magnetic microbubble formulation is presented. This has been designed to eliminate the need for a separate carrier liquid for the nanoparticles, which had previously been shown to impair the microbubbles' acoustic response. The new formulation was successfully manufactured and its characteristics compared to those of the previous formulation.

Chapter 8 examines the potential of the new magnetic microbubble formulation presented in Chapter 7 as a therapeutic delivery vehicle. Microbubbles were used to deliver siRNA to cells *in vitro* under combined exposure to ultrasound and a magnetic field.

Chapter 9 summarises the results and conclusions of the work presented in the previous chapters. Recommendations for future work based upon the techniques developed and results obtained throughout the thesis are then proposed.

1.4 References

1. Arruebo, M., et al., *Magnetic nanoparticles for drug delivery.* Nano Today, 2007. **2**(3): p. 22-32.
2. Lubbe, A.S., C. Alexiou, and C. Bergemann, *Clinical applications of magnetic drug targeting.* Journal of Surgical Research, 2001. **95**(2): p. 200-206.
3. Schlicher, R.K., et al., *Mechanism of intracellular delivery by acoustic cavitation.* Ultrasound in Medicine and Biology, 2006. **32**(6): p. 915-924.
4. Langer, R., *Drug delivery and targeting.* Nature, 1998. **392**(6679 Suppl.): p. 5-10.
5. Harrison, C., *The patent cliff steepens.* Nature Reviews Drug Discovery, 2011. **10**(1): p. 12-13.
6. Arruebo, M., *Drug delivery from structured porous inorganic materials.* Wiley Interdisciplinary Reviews: Nanomedicine and Nanobiotechnology, 2011: p. n/a-n/a.
7. Pankhurst, Q.A., et al., *Applications of magnetic nanoparticles in biomedicine.* Journal of Physics D: Applied Physics, 2003. **36**(13): p. R167-R181.
8. Jackson, J.K., et al., *Increased accumulation of paclitaxel and doxorubicin in proliferating capillary cells and prostate cancer cells following ultrasound exposure.* Ultrasonics, 2011. **51**(8): p. 932-939.
9. Verma, I.M. and N. Somia, *Gene therapy - Promises, problems and prospects.* Nature, 1997. **389**(6648): p. 239-242.
10. Voinea, M., et al., *Immunoliposomes directed toward VCAM-1 interact specifically with activated endothelial cells - A potential tool for specific drug delivery.* Pharmaceutical Research, 2005. **22**(11): p. 1906-1917.
11. Vinogradov, S., et al., *Polyion complex micelles with protein-modified corona for receptor-mediated delivery of oligonucleotides into cells.* Bioconjugate Chemistry, 1999. **10**(5): p. 851-860.
12. Villanueva, F.S., et al., *Microbubbles targeted to intercellular adhesion molecule-1 bind to activated coronary artery endothelial cells.* Circulation, 1998. **98**(1): p. 1-5.
13. Lindner, J.R., et al., *Microbubble persistence in the microcirculation during ischemia/reperfusion and inflammation is caused by integrin- and complement- mediated adherence to activated leukocytes.* Circulation, 2000. **101**(6): p. 668-675.
14. Lindner, J.R., et al., *Ultrasound assessment of inflammation and renal tissue injury with microbubbles targeted to P-selectin.* Circulation, 2001. **104**(17): p. 2107-2112.

15. Takalkar, A.M., et al., *Binding and detachment dynamics of microbubbles targeted to P-selectin under controlled shear flow.* Journal of Controlled Release, 2004. **96**(3): p. 473-482.
16. Rychak, J.J., et al., *Deformable gas-filled microbubbles targeted to P-selectin.* Journal of Controlled Release, 2006. **114**(3): p. 288-299.
17. Rychak, J.J., et al., *Enhanced Targeting of Ultrasound Contrast Agents Using Acoustic Radiation Force.* Ultrasound in Medicine and Biology, 2007. **33**(7): p. 1132-1139.
18. Christiansen, J.P., et al., *Noninvasive imaging of myocardial reperfusion injury using leukocyte-targeted contrast echocardiography.* Circulation, 2002. **105**(15): p. 1764-1767.
19. Fisher, N.G., et al., *Influence of microbubble surface charge on capillary transit and myocardial contrast enhancement.* Journal of the American College of Cardiology, 2002. **40**(4): p. 811-819.
20. Della Martina, A., et al., *Grafting of abciximab to a microbubble-based ultrasound contrast agent for targeting to platelets expressing GP IIb/IIIa - Characterization and in vitro testing.* European Journal of Pharmaceutics and Biopharmaceutics, 2008. **68**(3): p. 555-564.
21. Leong-Poi, H., et al., *Assessment of endogenous and therapeutic arteriogenesis by contrast ultrasound molecular imaging of integrin expression.* Circulation, 2005. **111**(24): p. 3248-3254.
22. Dayton, P.A., et al., *Ultrasonic analysis of peptide- And antibody-targeted microbubble contrast agents for molecular imaging of α vβ 3-expressing cells.* Molecular Imaging, 2004. **3**(2): p. 125-136.
23. Ellegala, D.B., et al., *Imaging tumor angiogenesis with contrast ultrasound and microbubbles targeted to αvβ3.* Circulation, 2003. **108**(3): p. 336-341.
24. Unger, E.C., et al., *In vitro studies of a new thrombus-specific ultrasound contrast agent.* American Journal of Cardiology, 1998. **81**(12 A): p. 58G-61G.
25. Schumann, P.A., et al., *Targeted-microbubble binding selectively to GPIIb IIIa receptors of platelet thrombi.* Investigative Radiology, 2002. **37**(11): p. 587-593.
26. Culp, W.C., et al., *Intracranial clot lysis with intravenous microbubbles and transcranial ultrasound in swine.* Stroke, 2004. **35**(10): p. 2407-2411.
27. Alonso, A., et al., *Molecular imaging of human thrombus with novel abciximab immunobubbles and ultrasound.* Stroke, 2007. **38**(5): p. 1508-1514.
28. Martin, M.J., et al., *Enhanced detection of thromboemboli with the use of targeted microbubbles.* Stroke, 2007. **38**(10): p. 2726-2732.
29. Xie, F., et al., *Diagnostic ultrasound combined with glycoprotein IIb/IIIa-targeted microbubbles improves microvascular recovery after acute coronary thrombotic occlusions.* Circulation, 2009. **119**(10): p. 1378-1385.
30. Willmann, J.K., et al., *Dual-targeted contrast agent for US assessment of tumor angiogenesis in vivo.* Radiology, 2008. **248**(3): p. 936-944.
31. Willmann, J.K., et al., *Targeted contrast-enhanced ultrasound imaging of tumor angiogenesis with contrast microbubbles conjugated to integrin-binding knottin peptides.* Journal of Nuclear Medicine, 2010. **51**(3): p. 433-440.

32. Korpanty, G., et al., *Monitoring response to anticancer therapy by targeting microbubbles to tumor vasculature.* Clinical Cancer Research, 2007. **13**(1): p. 323-330.
33. Alonso, A., et al., *In vivo clot lysis of human thrombus with intravenous abciximab immunobubbles and ultrasound.* Thrombosis Research, 2009. **124**(1): p. 70-74.
34. Weller, G.E.R., et al., *Ultrasonic imaging of tumor angiogenesis using contrast microbubbles targeted via the tumor-binding peptide arginine-arginine-leucine.* Cancer Research, 2005. **65**(2): p. 533-539.
35. Ferrara, K., R. Pollard, and M. Borden, *Ultrasound microbubble contrast agents: Fundamentals and application to gene and drug delivery.* Annual Review of Biomedical Engineering 2007. **9**: p. 415-447.
36. Zhao, S., et al., *Radiation-force assisted targeting facilitates ultrasonic molecular imaging.* Molecular Imaging, 2004. **3**(3): p. 135-148.
37. Stride, E., et al., *Enhancement of Microbubble Mediated Gene Delivery by Simultaneous Exposure to Ultrasonic and Magnetic Fields.* Ultrasound in Medicine & Biology, 2009. **35**(5): p. 861-868.
38. Vlaskou, D., et al., *Magnetic and Acoustically Active Lipospheres for Magnetically Targeted Nucleic Acid Delivery.* Advanced Functional Materials, 2010. **20**(22): p. 3881-3894.
39. Plank, C., et al., *The magnetofection method: Using magnetic force to enhance gene delivery.* Biological Chemistry, 2003. **384**(5): p. 737-747.
40. Cai, D., et al., *Highly efficient molecular delivery into mammalian cells using carbon nanotube spearing.* Nature Methods, 2005. **2**(6): p. 449-454.

2 Literature review

2.1 Summary

This chapter examines the background of magnetic and ultrasonic drug delivery and the combination of the two; in particular the development and principles of magnetic microbubbles, their applications and current techniques which can be used in order to characterise them [1][1].

2.2 Magnetism and drug delivery

The first documented medical application of magnets dates back to the 17th century when magnets were used to remove fragments of iron from the body [2]. In the present day, in addition to their now widespread use in magnetic resonance imaging (MRI), magnetic fields are utilised in several therapeutic applications. This section examines their use in magnetic drug targeting.

2.2.1 Types of magnetic materials

Magnetism is a phenomenon associated with the motion of electric charges. All material is to some extent influenced by a magnetic field and can be classified as diamagnetic or paramagnetic. For diamagnetic materials the electron spins line up in opposition to the direction of the magnetic field and for paramagnetic materials the spins line up in the

[1] A modified version of this chapter was published as a review article in The International Journal of Hyperthermia

same direction as the magnetic field. However, both diamagnetic and paramagnetic materials have a relatively weak magnetic response. Materials where the electron spins line in the same direction as the magnetic field which respond strongly to a magnetic field and remain aligned after the removal of the magnetic field, such as iron, are termed ferromagnetic and have a permanent dipole. The magnetic response varies with temperature, for example ferromagnetic materials behave as paramagnets above the Curie temperature. The same is true for Ferrimagnets (where the majority of electron spins align with the magnetic field) above the Neel temperature [3].

When a magnetic material is placed within a magnetic field, the individual atomic moments of the material contribute to the overall response or magnetic induction. The magnetic characteristics of a given material thus vary with temperature and atomic structure. This can be quantified in terms of the material's magnetic volumetric susceptibility (χ) and magnetisation (M): defined as the magnetic volumetric susceptibility (χ) multiplied by the applied magnetic field strength (H) [4]. As highlighted above paramagnetic materials ($\chi > 0$) magnetise very weakly in the direction of the magnetic field whereas diamagnetic materials ($\chi < 0$) magnetise in the opposite direction [5]. Due to the disordered structure of their magnetic moments (quantity that determines torque experienced in an external magnetic field), neither of these types of material show spontaneous magnetisation in the absence of an external magnetic field. Other materials exhibit internal ordered states which remain ordered after the removal of the magnetic field. On the one hand, when their magnetic moments are coupled parallel, a ferromagnetic structure is observed. On the other hand, antiparallel coupling of

magnetic moments will generate antiferromagnets when the magnetic moments cancel each other delivering a zero average magnetisation, and ferrimagnets when such cancellation does not take place because of the higher magnitude of magnetic moments pointing in one of the two possible orientations (Figure 2.1).

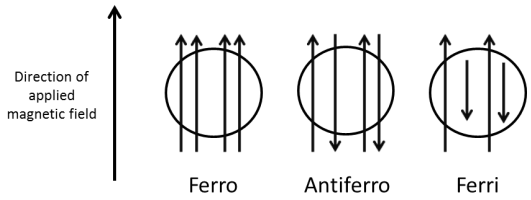


Figure 2.1, ferro, antiferro and ferromagnetic materials indicating how the magnetic moments align upon application of a magnetic field.

Due to remnant magnetisation, ferri and ferromagnetic materials tend to aggregate. This remnant magnetisation occurs because once a ferro or ferrimagnetic material is magnetically saturated in one direction, the moments tend to preserve the so-induced orientation to a certain extent, depending on the internal structure. This can be seen in a hysteresis curve (Figure 2.2). The resulting aggregation is undesirable in most biomedical applications. Consequently materials that are used in these applications are usually superparamagnetic. Superparamagnetism is a phenomenon whereby materials exhibit a strong magnetic response with no remnant magnetisation.

This effect is observed only at the nanoscale. The internal structure of bulk magnetic materials is divided into magnetic domains where all the magnetic moments are aligned parallel to each other. But below a certain size, formation of domains becomes

energetically unfavourable resulting in particles consisting of a single domain state [3]. For single domain particles on the nano scale the magnetic moment of the whole particle is free to fluctuate in response to thermal energy, at room temperature, in the absence of a magnetic field. Therefore when a magnetic field is removed, the magnetic moment returns to zero magnetisation as shown in Figure 2.2. The same effect would be observed in ferromagnetic materials above the Curie temperature, where ferromagnets show paramagnetic behaviour. Superparamagnetic materials thus provide a compromise between strong magnetisation and avoidance of particle aggregation [5]. As such superparamagnetic materials will not agglomerate after the removal of a magnetic field as ferromagnetic particles would.

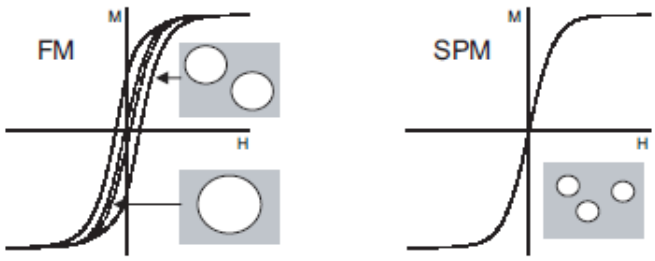


Figure 2.2, Magnetisation (M) plotted against the magnetic field strength (H) of magnetic particles of differing size. For large ferromagnetic materials the hysteresis loop is small owing to many domains, as the material becomes one domain it is harder to reverse the magnetisation, so the loop is larger owing to remnant magnetisation. However, below a certain critical size superparamagnetism occurs where no hysteresis loop is observed and as such no remnant magnetisation. This picture was taken from [4].

2.2.2 Magnetic nanoparticles

Particles with dimensions of a few 10s of nanometres are able to be transported not only through the narrowest blood vessels in the human body but also across blood vessel walls and even through cell membranes [6]. To avoid uptake by the reticuloendothelial system (RES), magnetic carriers typically have two structural configurations; a magnetic core coated by a biocompatible polymer or magnetic nanoparticles inside a porous

biocompatible polymer matrix into which drugs, genes or targeting agents can also be incorporated [4, 5, 7].

As a consequence of the phenomena discussed above, superparamagnetic nanoparticles have become the subject of intensive research in recent years. They have three key additional features making them attractive for biomedical applications: their ability to be visualised under MRI [8], to be localised at a target site by means of a magnetic field gradient [4] and to produce localised heating when exposed to an oscillating magnetic field for hyperthermia and/or to promote drug delivery [9].

Ferrimagnetic iron oxides maghemite and magnetite, which are able to form superparamagnetic iron oxide nanoparticles (SPION) typically below 15 nm, are currently in use as MRI contrast agents [10]. Iron oxides are relatively safe compared to other substances used as MRI contrast agents such as gadolinium in terms of their toxicity [11].

2.2.3 Drug delivery applications

The use of magnetic particles for drug delivery appeared in the literature in 1960 when Freeman *et al*. proposed that magnetic nanoparticles could be transported through the vasculature and concentrated in a specific part of the body with the aid of a magnetic field [2]. In 1963 Meyers described how magnetic iron particles in the lymphatic and

vascular system of a dog could be used as a contrast and isotopic agent[2] [12, 13]. Zimmerman and Pilwat used magnetically tagged erythrocytes (red blood cells) for the delivery of cytotoxic drugs in 1976 [14]. In the 1970s Senyei *et al.* produced albumin microspheres, incorporating superparamagnetic magnetite, and successfully retained these against *in vivo* capillary flow conditions using a magnetic field [15, 16]. Widder *et al.* used magnetic albumin microspheres containing doxorubicin and showed tumour regression in rats when a localised magnetic field was applied and with no occurrences of embolism observed [17].

Novel drug delivery systems have also been developed using polymer matrices containing drugs and magnetic beads. This pulsatile delivery system opens pores to release the drug when an oscillating magnetic field is applied [18, 19]. In 1994, Hafeli *et al.* prepared biodegradable poly(lactic acid) microspheres that incorporated magnetite and a beta emitter for targeted radiotherapy and applied it to subcutaneous tumours [20, 21]. A ferrofluid (fluid containing a magnetic suspension, in this case magnetic nanoparticles) comprising drugs was used *in vivo* by Lubbe *et al.* No toxic effects were seen in trials in mice and an effect upon tumours was noticed [22]. Another successful trial concentrated the ferrofluid Chemicell®, bound to mitoxantrone, in murine tumours with the application of a magnetic field [23]. The first phase I clinical trial was performed by Lubbe *et al.* Each patient tolerated the ferrofluid and the NPs were seen to be concentrated in tumours after the application of a magnetic field [24]. A second phase

[2] Radioactive isotopes of iron were used for detection and potential treatment.

I/II trial was conducted by a start-up company, FeRx Inc, in 1997 where carbon coated iron particles (0.5-5 μm) which had adsorbed doxorubicin were localised and retained in target sites [10, 25].

2.2.4 Gene delivery applications

Magnetic nanoparticles also hold great potential for gene therapy. DNA delivery to cells can induce production of therapeutic proteins to treat malignancies. Use of short interfering RNA can temporarily down regulate the expression of a gene of choice (gene silencing) and potentially any disease causing gene can be silenced [26]. If simply injected or ingested, however, DNA or RNA can degrade and are not able to pass through cellular membranes [27]. There are four primary ways to deliver molecules for gene therapy into cells: through the use of viral vectors which is highly efficient but which can have unwanted side effects; electroporation, in which cells are electrically stimulated which is again very efficient but causes a large number of cell deaths, non-viral transfection agents can assist nucleic acid entry into cells and maintain cell viability but tend to be inefficient [11]; and finally sonoporation of microbubbles under ultrasound which will be discussed in detail later.

The first study of magnetically targeted DNA delivery was performed by Mah *et al.* in 2000 [28]. A recombinant adeno-associated virus (rAAV), encoding for a green fluorescent protein was coated onto the surface of magnetic microspheres. Under the influence of an applied magnetic field, 1% of the vector-microsphere formulation gave the same transfection efficiency as 100% free vector. This was continued by Hughes *et*

al. to produce "infectious, paramagnetic, retroviral vector particles" using paramagnetic streptavidin particles conjugated to antibodies which the retrovirus associated with [29].

Non-viral magnetic vectors are also being developed with an emphasis upon improving nucleic acid transfection efficiency. The association of genes with magnetic nanoparticles for magnetically guided nucleic acid delivery has been termed magnetofection [30]. Magnetofection is thought to operate by a very similar mechanism to other transfection agents, such as lipofectine 2000 [31] from life technologies[3], except that the plasmid DNA forms complexes with magnetic nanoparticles coated with a cationic polymer - usually polyethylenimine (PEI) which is able to bind and condense DNA [32] - a magnetoplex with magnetically controllable behaviour. The magnetic particle is used in order to bring the therapeutic agent into close proximity with the target cells via application of a magnetic field. But the means by which the gene enters the cell with magnetoplexes has so far been found to be no different to that associated with normal transfection reagents via a positively charged magnetoplex fusing with a negatively charged cell membrane [30, 33, 34].

Other novel approaches include that adopted by Cai *et al.* who used nickel embedded carbon nanotubes coated with DNA to act as "spears" to pierce the cells when actuated by a magnetic field, resulting in high transfection efficiency [35]. Oz Biosciences offer

[3] A commercially available cationic liposome which binds negatively charged genetic material and fuses with negatively charged cell membranes to transfect cells in vitro.

four different cationic, magnetic nanoparticle formulations for specific gene delivery applications [36]. The use of pulsating fields is also being investigated further and, for example, Kamau *et al.* have shown an increase in the number of transfected cell relative to static fields [37].

2.2.5 Limitations

Magnetic drug targeting is subject to two main constraints. First, there may be rapid clearance of particulate drug carriers from the circulation. Second, the strength and gradient of the magnetic field that needs to be applied, given the small size of the nanoparticles and hence their reduced magnetic strength, may be very high for successful localisation of a carrier [38] against the hydrodynamic forces produced e.g. by blood flow [4]. Hence there is a demand for magnetic particles with larger diameters but that are capable of travelling through capillaries without causing an embolism and of delivering therapeutic molecules to target cells [34]. According to Neuberger *et al.* magnetic particles smaller than 4 μm are removed by RES cells mainly in the liver and spleen [38, 39] In general, the larger the particle the shorter its plasma half-life [5].

2.3 Ultrasound and drug delivery

One of the first investigations into the therapeutic use of ultrasound for drug delivery was performed in the 1950s by Fellinger and Schmid who used ultrasound to enhance the permeation of ointment into inflamed tissue, thereby successfully treating polyarthritis [40]. The first ultrasound assisted transfection *in vitro* was reported in 1987 when

Fechheimer *et al.* reported low level transfection of murine fibroblasts when exposed to 20 kHz ultrasound [41]. Since then ultrasound has been utilised in a wide range of drug delivery, gene delivery and other therapeutic applications [42].

2.3.1 Basic physical principles

Ultrasound can be defined as "sound waves of such a high frequency (above 20 kHz) as to be inaudible to humans" [43]. In diagnostic imaging, it is the scattering of these waves from regions of differing density and compressibility that is used to produce the images. In addition to being scattered, however, ultrasound undergoes three other types of interaction with tissue and it is these which underlie its effect in therapeutic applications. First, a fraction of the energy in the propagating wave is also absorbed by tissue resulting in local heating. This is due to frictional forces of particles in the medium and as such, increased viscosity of the medium leads to increased ultrasound absorption. If the intensity is sufficient, tissue ablation will occur through protein denaturation and/or boiling [44-47]. At lower intensities effects such as increased perfusion and/or stimulated release from drug delivery vehicles may be realised [44]. Second, ultrasound energy may produce cavitation. Acoustic cavitation is defined as the formation and activity of gas and/or vapour filled bubbles, of natural or artificial origin, in a medium exposed to sound [48]. The motion of the bubbles can temporarily increase individual cell membrane permeability [49], termed "sonoporation", stimulate endocytosis and open tight junction gaps, At higher intensities it can contribute to cell death [50]. Third, transfer of momentum from the ultrasound wave to the liquid produces streaming motions and associated shear stresses on tissue interfaces. In the presence of a bubble oscillating under

ultrasound excitation, microstreaming [51] occurs through a similar mechanism and this may in fact be one of the main contributors to sonoporation [52]. The shear rates experienced by cells results in a temporary increase in cell membrane permeability and streaming of the liquid moves any particles or drugs nearby which may pass through the cell membrane.

2.3.2 Microbubbles

Acoustic impedance is defined as the product of the speed of sound in a medium and its density [53]. Any difference in acoustic impedance between tissues causes ultrasound reflection at the interface, for example at the interface between a solid and a liquid or a gas. Ultrasound contrast agents are gas filled microbubbles with diameters of a few micrometres; approximately the same size as red blood cells. The high compressibility of the microbubbles compared with the surrounding tissue gives rise to a large acoustic impedance difference and, more importantly, causes the bubbles to undergo volumetric oscillations producing nonlinear acoustic radiation at moderate ultrasound intensities [54]. The average microbubble size is between 1 – 7 μm in order to pass through the capillary bed [55]. The ultrasound frequencies used for imaging represent a compromise between penetration depth and image resolution where 2.5 -5 MHz is used for abdominal scanning including heart, liver and uterus, 5-10 MHz for carotid, breast, testes and superficial tissues, 10 -15 MHz for the eye and finally 20-40 MHz for Intravascular ultrasound. [43, 56]. In addition, microbubbles between 1 – 7 μm resonate at frequencies within the medical US frequency band of 2 – 15 MHz owing to their size being in the micrometre range [45, 55]. It is these phenomena which provide the contrast

enhancement between regions with and without bubbles in ultrasound images [57, 58]. For use in the human body they must also be biochemically inert, stable to injection and stable under human body conditions; ideally with a narrow size range and a known ultrasound response at medical frequencies[4] [58]. A narrow size range is critical for drug delivery applications in order to ensure accurate dosage and also the ability to predetermine the acoustic response of a microbubble suspension is becoming more important for more advanced imaging applications which exploit non-linear features [59].

According to the literature the effectiveness of microbubbles as ultrasound contrast agents was first observed accidentally in 1962 by Doctor Claude Joyner. An echocardiogram was being taken of the human heart whilst the output rate was being measured by the injection of indocynanine dye. After each injection into the left ventricle the ultrasound signal increased for a brief period of time [60]. It was not understood what caused the signal improvement until 1968 when Gramiak and Shah reported the backscatter of blood appearing as a "cloud of echoes" after injections of saline during an echocardiogram of the aortic root due to air microbubbles forming at the catheter tip [61]. This was verified when the ambient pressure was increased to suppress bubble formation resulting in no improvement in contrast [62]. During the injection the air microbubbles, formed in the solution by cavitation, gave rise to the strong ultrasound

[4] Arguably commercially available contrast agents do not meet the last of these requirements as they are polydisperse both in size and coating properties (such as individual microbubble viscosity [59]).

scattering and hence the improvement in contrast [63]. Agitation of the fluid just prior to injection formed microbubbles and adding a surfactant to the solution stabilised the microbubbles [64]. In particular it was found that mixing patients' blood with saline increased the number and prolonged the stability of the bubbles formed. Feinstein *et al.* identified that the crucial component in the blood was albumin [65]. Albumin coats the microbubble and reduces the surface tension and surface diffusivity leading to an extended bubble lifetime and hence improved ultrasound contrast. Feinstein *et al.* also found that sonication rather than just shaking produced more stable microbubbles with better size control due to cross linking of the albumin and this led to the first commercial echo contrast agent Albunex® [55].

2.3.2.1 Coating materials

Following the launch of Albunex® a number of other microbubble ultrasound contrast agents were also developed. Echovist® (Schering AG) was a contrast agent commercially available in Germany stabilised by D-Galactose. Levovist® was a derivative of Echovist® consisting of a suspension of galactose and a small quantity of palmitic acid mixed with sterile water. The sugar matrix dissolves in the plasma and microbubbles coated with a thin layer of palmitic acid are released [58]. Palmitic acid is amphiphilic (hydrophilic and lypophilic properties) and it was found that a more effective bubble stabilisation could be obtained with a layer of phospholipid (amphiphilic molecule in cell membranes) adsorbed onto the bubble surface. This led to new contrast agents in particular Sonovue® (Bracco), Sonazoid® (GE Healthcare) and Definity® (Lantheus Medical Imaging) [59] and also avoided the immunogenicity issues associated with

Albumin. A number of microbubbles stabilized by polymers have also been developed, the first via gelation of the naturally occurring polysaccharide alginate by Wheatley *et al.* [66]. Other polymer microbubbles have been produced with a variety of polymers such as arginine by Florinas *et al*. [67] and polyallylamine hydrochloride grafted onto albumen by Lentacker *et al.* [68]. The polymer polymerises around the gas core producing a stiff stable bubble but so far there are no clinically approved polymer agents [66, 69].

The presence of a surface coating, while essential for stabilisation, does however reduce the amplitude of the microbubbles' oscillation[5]. It is possible to classify microbubbles based upon their stiffness: "hard" shelled microbubbles are usually coated with a polymer or cross linked albumin, whereas "soft" shelled microbubbles are coated with a surfactant layer of e.g. a phospholipid. Soft shelled microbubbles produce a stronger acoustic response because of the more fluid nature of surfactant membranes which have no covalent bonds. Phospholipid coated microbubbles for example do not rupture, whereby the coating no longer stabilises the gas microbubble, even after large amplitude oscillations [70]. Hard shelled microbubbles are more stable both before and after injection [53] but show a tendency to rupture beyond a certain critical strain [71]. This is owing to shell structure where cross-linked covalent bonds can be broken during isonation, thus rupturing the shell. A more fluid phospholipid shell, which does not contain any covalent bonds, can effectively reseal [59]. However, for *in vivo* applications, 10 – 15 min after injection the gas core of the microbubble is exhaled and the shell is filtered by the kidney's and eliminated by the liver [72]. As such

[5] The amplitude of microbubble oscillation also depends upon the acoustic pressure and frequency of the applied ultrasound.

improvements to microbubble stability are only important relative to a clearance time of maximum 15 minutes.

2.3.2.2 Filling gas

Air filled microbubbles have a short lifetime in blood as the highly diffusive air rapidly escapes. This limitation was addressed in the second generation of microbubble contrast agents through the use of high molecular weight gases such as perfluorocarbons. Examples of these are the albumin coated Optison® (GE Healthcare) and Phospholipid coated SonoVue® and Definity® (Bristol Myers Squibb). Other contrast agent formulations have been developed that work on different principles, for instance Echogen consisted of perfluoropentane, a liquid at normal room temperature but which becomes a gas at human body temperature thus forming microbubbles *in vivo* [55]. However, Echogen was not successfully translated into clinical use. This is because large bubbles formed too readily in the syringe due to the pressure drop during injection. The permeability and mechanical properties of a microbubble's coating have a strong influence upon the microbubble's acoustic response and destruction threshold [59, 73]. Stride *et al*. demonstrated theoretically the significance of shell properties in determining contrast agent particle behaviour and explaining unexpected variations that can occur [71].

2.3.2.3 Nanoparticle coatings

In addition to imparting extra functionality to microbubbles, depositing nanoparticles on the surface can increase their stability and the non-linear character of their response to ultrasound at low excitation amplitudes. This is thought to be because the nanoparticles "jam" during compression leading to an asymmetric volume oscillation [74] and preventing Ostwald ripening and diffusion [75]. However, the exact structure of the microbubble coating and how the nanoparticle is situated on the microbubble's surface are unknown.

2.3.2.4 Fabrication techniques

Microbubbles formed by shaking or sonicating usually have a wide size range and the origins of this bubble polydispersity were elucidated by Li and Fogler in 1978 [76, 77]. Bubble formation occurs in a two-stage process. An unstable water surface leads to the entrainment of bubbles in the aqueous solution and cavitation within the medium results in the large bubbles breaking up and the formation of smaller microbubbles. The critical bubble size is reached when the surface tension forces balance the inertial forces on the bubble [78]. With multiple mechanisms operating within the system it is more or less inevitable that the bubbles will be polydisperse (1-20 μm) and alternative methods have therefore been investigated to produce monodisperse microbubbles, for example, membrane emulsification [79], ink jet printing [80] and microfluidic devices [81] [59].

There are however disadvantages associated with these techniques also. First the timescale for production: Sonication produces much larger quantities of microbubbles in

higher concentration over a short space of time (< 1 minute compared with several hours for a state of the art microfluidic device). Parallel processing is possible, but reliable multiplexing is challenging and expensive and clogging of membranes or the fine channels in microfluidic/ink jet printing system also presents a significant difficulty. Moreover, the structure of surfactant coatings is significantly altered by sonication possibly due to the high temperatures generated from inertial cavitation and this appears to enhance their stability compared with bubbles prepared by microfluidics and also affect their acoustic response [82].

2.3.3 Drug delivery applications

Microbubbles are also being widely investigated for therapeutic applications. They can be used as nuclei to increase cavitation activity [48] and/or as vehicles for drug delivery/gene therapy by incorporation of therapeutic material into their coatings which can subsequently be released by destroying the microbubbles with a high amplitude ultrasound pulse [83, 84].

Ultrasound has been shown to increase the thrombolytic efficacy of urikonase [85]. This is most likely due to localised cavitation which can weaken the clot surface and/or improve penetration of the drug; and this process has been shown to be enhanced by the presence of microbubbles [86, 87]. Similarly, exposure to ultrasound in the presence of microbubbles has been shown to reversibly produce pores on the surfaces of cells [88, 89]. Unger *et al.* obtained similar results with microbubbles containing a drug filled layer of soy bean oil and the drug paclitaxel [84]. Guzman *et al.* quantified molecular uptake

of calcein in prostate cancer and aortic smooth muscle cells, the heterogeneity of cavitation and factors that influence drug uptake [90, 91]. Microbubbles have also been used with cells to increase uptake of Doxorubicin and colloidal particles [92, 93]. However, research into how the acoustic response of microbubbles affects drug delivery is still taking place [94, 95].

2.3.4 Microbubble delivery benefits

Microbubbles have further applications beyond delivering therapeutic agents into cells such as distributing a therapeutic throughout target vasculature. For example, Sonovue microbubbles and ultrasound distributed polymer coated virus throughout tumour vasculature over 200 μm from the nearest blood vessel, a greater distance than the uncoated virus alone [96]. Coating the adenovirus with polymer chains for longer circulation kinetics reduced tumour uptake whereas human erythrocytes were able to bind to and inactivate the uncoated adenovirus [97].

Standardised administration of anticancer agents is difficult owing to variations in pharmacokinetic variability and the small therapeutic window. Anticancer drugs are dosed per unit of body surface and administered at the maximum tolerated dose. Interpatient pharmacokinetic variability is usually large due to variations in distribution, drug absorbtion and elimination processes. Dose, injection time and the requirement for re-injection vary from drug to drug for maximum therapeutic effect with reduced toxicity [98]. Microbubble based delivery can reduce the dosage of drug required for therapeutic effect. For example, use of nanoparticles incorporating 2.5 mg/kg dose of paclitaxel,

microbubbles and ultrasound resulted in similar tumour growth reduction to 5.0 mg/kg paclitaxel nanoparticles alone [99]. Greater therapeutic effect for lower injected dose could also result in a lower probability for the number of reinjections required.

The inability to deliver nucleic acids to target cells via systemic delivery is the biggest rate-limiting barrier to gene therapy [100]. Polynucleic acids are prone to nuclease mediated degradation and rapid clearance by the reticuloendothelial system when introduced into the blood stream [101]. Microbubbles as carriers have the potential to improve circulation time in the bloodstream, protect the genes from degradation and improve specificity of targeted delivery. Targeted gene delivery by co-injection of plasmid DNA with microbubbles can be effective for producing detectable levels of gene expression for a lower quantity of DNA used. For example Bekeredjian et al. used 400 μg for transfecting a mouse heart with microbubbles whereas Shwartz et al used 500 μg for direct myocardial injection [102, 103].

2.3.5 Gene delivery applications

In 1996 Kim *et al*. used ultrasound to transfect a variety of cells with plasmid DNA. They found that the ultrasound power, duration, ambient pressure and the occurrence of cavitation were critical and all positively correlated with transfection efficiency [104]. The same authors also injected albumin MBs with plasmid DNA into rat knees and under ultrasound observed transfection [104]. Greenleaf *et al.*, continuing the work by Kim *et al.*, demonstrated an increase in the transfection rate of DNA *in vitro* with ultrasound, in

the presence of Albumin coated bubbles [105]. Lawrie *et al.* similarly reported that combined exposure to Optison® microbubbles and ultrasound achieved an approximately 300 fold higher transgene expression *in vitro* than exposure to plasmid DNA alone [106].

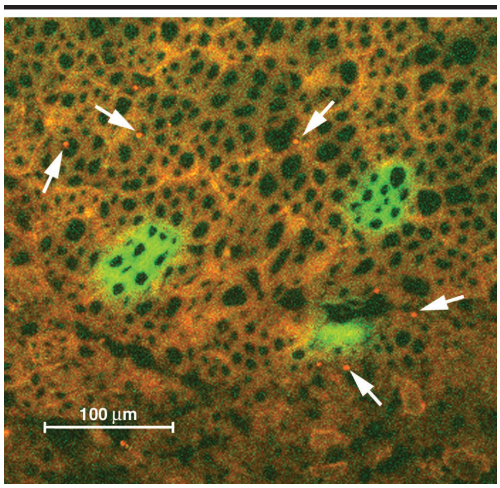


Figure 2.3, Confocal laser microscopic image of GFP in muscle tissue (cross-sectional view) treated with plasmid DNA and ultrasound irradiation in the presence of Optison depicts rhodamine-labeled DNA (arrows) from Li and Tachibana et al [107].

However, low transfection efficiency still remains a major factor (Figure 2.3) and the same mechanisms that cause drug uptake can also lead to cell death [107]. The physical parameters effecting gene delivery with ultrasound and microbubbles were investigated by Rahim *et al*. who identified optimal pulse amplitude, exposure time and bubble concentration for transfecting Chinese Hamster Ovary cells with plasmid DNA containing the β-galactosidase gene [108]. Matsumura's group has administered gelatin coated microspheres binding a gene to rat livers with the application of ultrasound [109]. Transfection with microbubbles and ultrasound has been performed in the lungs and hearts of mice and the hearts of rats [110-112]. Comparisons between different ultrasound contrast agents have been performed *in vivo* to determine which gave the best

cellular uptake of genes, finding that Optison® gave a 10 fold increase in GFP expressing muscle fibers in mice relative to Albunex® or Levovist® [107, 113].

Transfer of gene delivery *in vivo* has proved challenging. The first delivery was in 1996 yet microbubble mediated gene delivery has not progressed to the clinic [104]. However this is also true of non-viral gene therapy in general as even though the first gene therapy clinical trial was in the 1990s gene therapy is still in its infancy with respect to other anticancer treatments. There are four criteria for assessing efficiency of gene therapy in vivo: (i) Target cell specificity of gene transfer, (ii) the number of cells transduced, (iii) the level of expression and (iv) the duration of expression. [114]. Achieving all four of these goals, particularly iii and iv, to an extent for therapeutic efficacy has not been achieved to date. This is owing to the number of factors which have to be overcome for an *in vivo* relative to an *in vitro* environment.

Firstly, protection of the therapeutic agent against the body such that a significant proportion can reach the target location. Blood flow to tumours is generally low in comparison with large organs such as the liver and the kidney so the delivery of any pharmaceutical compound to tumour tissues requires prolonged circulation in the blood. However, microbubbles are cleared from the blood within 10 – 15 minutes [72]. This severely limits the time frame for bubble accumulation at the tumour and ultrasound application. The number of microbubbles which successfully pass through the tumour will only represent a small quantity of the maximum injected dose. Once microbubbles

and the gene of choice are in the tumour blood vessels uptake is difficult owing to intratumoural pressure, lack of convective flow and a dense extracellular matrix [96]. The gene must also be moved out of the blood vessels and into the tumour vasculature over a distance of 100 of μm to enter every tumour cell in sufficient quantity to have a sustained therapeutic effect. Microbubbles have been shown to deliver therapeutics far from blood vessels but a sustained therapeutic effect from the quantity delivered is a major challenge [96]. The blood flow within tumours has been shown to be heterogeneous on a micro and macroscopic scale and there is tremendous variability among tumours from the same line. As such, observing a consistent significant therapeutic effect for cancer therapy is a major challenge [115].

2.3.6 siRNA delivery

In 1998, Fire, Mello and colleagues discovered the ability of double stranded RNA to silence gene expression in the nematode worm Caenorhabditis elegans. Three years later Tuschl *et al.* published a proof of principal experiment demonstrating that synthetic siRNA could achieve sequence specific knockdown in a mammalian cell. Theoretically, appropriately designed siRNA can exploit RNAi machinery to silence nearly any gene in the body [116].

siRNA can be introduced directly into the cell to be incorporated into the RNA induced silencing complex (RISC). The activated RISC-siRNA then seeks out the corresponding mRNA and degrades that which is complimentary to the antisense strand. The activated RISC can then move further on to destroy additional mRNA targets. The capability

exists to inhibit expression of a target gene through specific cleavage of perfectly complimentary mRNA. siRNA can modulate the expression of any gene involved in tumor initiation, growth and metastasis formation [117].

Microbubbles have been used for the delivery of siRNA. Carson *et al*. used microbubbles for inhibition of EGF receptor signalling, an established strategy for treating numerous types of cancer. Charged microbubbles were produced via shaking with siRNA, which attached through an electrostatic interaction. Electrophoresis was used to determine siRNA loading. Western blot analyses were conducted 3 days after sonoporation using anti-mouse antibody. After successful *in vitro* results experiments *in vivo* indicated tumour growth was slowed, arrested or even reversed in EGFR treated mice [118].

bPEI is a cationic polymer which binds siRNA through electrostatic interactions and has been used for gene delivery (12). bPEI is limited by its toxicity as the backbone of the polymer won't degrade. Florinas *et al*. used bPEI with an argenine backbone to bind siRNA, which can be degraded, and combined the ensuing nanoparticle with a microbubble. The microbubble-nanoparticle complex was then used to deliver siRNA via sonoporation. Knockdown of VEGF was successfully observed *in vitro* with ELISA. This microbubble complex also decelerated tumour growth in a mouse model [67]. siRNA delivery via microbubbles will be discussed in further detail in Chapter 8.

2.3.7 Targeting

Albumin and lipid coated microbubbles have been found to persist in areas of inflammation. This is due to leukocytes, from an inflammatory response, attaching to the microbubble. As the leukocytes target the area of inflammation the microbubbles also accumulate at the target area due to this interaction [119]. Attaching specific molecules to the surface of microbubbles should allow them to be retained at other malignant sites within the body and as such microbubbles with targeting moieties attached have been formulated [120].

Microbubbles have been successfully targeted via electrostatic attachment. Villanueva *et al*. performed the first study on albumin labelled microbubbles in a parallel plate perfusion chamber showing microbubbles adhering to cells [121]. Albumin microbubbles were successfully targeted to leukocytes [119] and addition of phosphatidylserine to lipid microbubbles was found to increase targeting to inflamed tissue in dogs, determined by analysis of the ultrasound signal [122]. Fisher *et al.* examined the effect of charge on lipid microbubble targeting in mice. Retention of microbubbles was frequently observed with anionic microbubbles but rarely occurred with neutral microbubbles [123]. Albumin microbubbles targeted to platelets via glycoprotein 2b/3a receptor inhibitor eptifibatide were also used for clot treatment with low frequency ultrasound [124].

Microbubble targeting based on biomimetic techniques, imitating models or materials found in nature, has been widely trialled. Microbubbles have been successfully targeted

via incorporation of adhesion molecules into the microbubble coating. For example, Villenueva *et al*. developed a lipid coated microbubble with anti-ICAM-1 antibody incorporated into its shell which showed a 40 fold increase in targeting to activated endothelial cells relative to non-targeted microbubbles *in vitro* [120]. The shear rate dependence of antibody-targeted microbubbles to activated endothelial cells was determined by Weller *et al*. [125]. Tumour angiogenesis was detected in 14 athymic rats via microbubbles targeted to $\alpha_v\beta_3$ integrin via an increase in relative acoustic intensity [126]. Another microbubble formulation was developed with the tumour binding peptide Arginine-Arginine-Leucine to image tumour angiogenesis via ultrasonic imaging [125]. Unger *et al*. also developed a microbubble with a hexapeptide coupled to a lipid moiety incorporated into the microbubble shell. It was found that targeted microbubbles successfully bound to a blood clot relative to untargeted microbubbles *in vitro* [127, 128]. A phase 0 clinical trial has been launched to assess the potential of ultrasound contrast agents targeted to Vascular endothelial growth factor receptor type 2 for molecular imaging of prostate cancer [129].

2.3.8 Conjugation strategies

Microbubbles can be used to improve cell permeation if the drug is coadministered at the target location but this limits efficacy to malignancies reached by injection [109]. Microbubbles with the drug loaded on the surface can also be directly injected into the tumour as a means of achieving localisation of the therapeutic compound [130]. For the majority of targets some form of conjugation between the drug and the microbubble is

required. [131]. As such strategies for attaching therapeutic compounds to microbubbles have been developed:

i) Electrostatic interactions allow charged drugs to be bound to the surface of cationic lipid coated microbubbles. DNA is a polyanion, due to the negative sugar phosphate groups on the molecule, and as such easily binds to cationic microbubbles [132].

ii) Multilamellar coatings whereby therapeutic compounds can also be incorporated into microbubbles in a layer of oil beneath the lipid outer layer which can further stabilise the outer surface of microbubbles [109].

iii) Molecular conjugation of drug containing vehicles. For example, Lum *et al.* bound polystyrene nanoparticles to the microbubble shell through an avidin biotin bridge which could be replaced by nanoparticles loaded with genes or drugs [133]. Liposomes have also been loaded onto microbubbles via avidin-biotin and maleimide-thiol linkages (Figure 2.4) [134, 135].

iv) Shell incorporation; Cochran *et al.* produced Paclitaxel and Doxorubicin loaded polymer microbubbles which cavitate under ultrasound forming polymer nanoparticles which enter cells and slowly release drugs [136]. The drug rapamycin, which is highly soluble in lipids, has been successfully incorporated into lipid shelled microbubbles and delivered to smooth muscle cells *in vitro* under ultrasound [137].

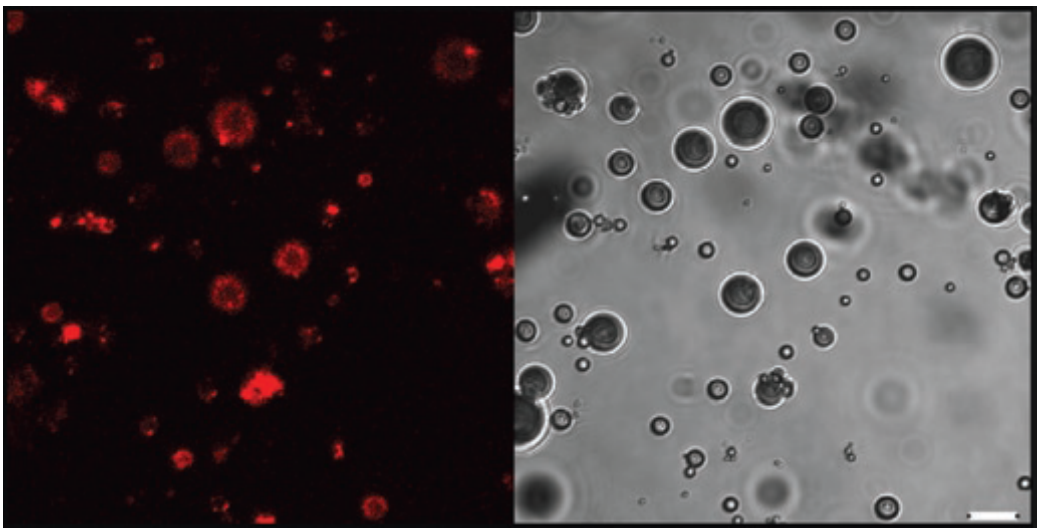


Figure 2.4, Confocal laser scanning microscopy image (left) and corresponding transmission image (right) of DOX liposome-loaded microbubbles. The DOX-liposomes were visualized using the fluorescence of the bound doxorubicin. DOX, doxorubicin. From Lentacker *et al [135]*.

2.3.9 Limitations

Close proximity between microbubbles and target cells is required for therapeutic effects to be realised at moderate ultrasound intensities and without unwanted damage [108]. The number of cells transfected increases with peak negative pressure but so does the number of cells killed [108]. The concentration of microbubbles at target site needs to be optimised as adequate numbers are needed both for sonoporation and to achieve the required dose; but increased microbubble concentration poses a greater risk of embolism and may also produce excessive ultrasound scattering or "shielding," preventing exposure of the target tissue. Currently, repeatable, efficient bio-chemical targeting of microbubbles is still proving to be a challenge *in vivo* [138]. Surface architecture designed to maximise ligand exposure to the target tissue also runs the risk of boosting presentation of an immunogenic compound that leads to early particle clearance or worse

a hypersensitivity response [131]. Methods have also been developed in order improve targeting efficiency. Acoustic radiation force was successfully used to push microbubbles closer to targeting moieties [139, 140]. Dual targeted microbubbles for VEGF receptor 2 and $\alpha_v\beta_3$ integrin improved *in vivo* visualisation of tumour angiogenesis in a human ovarian cancer xenograft tumour model in mice [141]. Another method for improving targeting involved use of deformed microbubbles imitating the deformation of leukocytes. Microbubbles targeted to P-selectin were pressurised in a syringe and showed higher targeting efficiency than non-deformed microbubbles *in vitro* and *in vivo* [142].

2.4 Ultrasound and magnetism

A further method that shows promise for targeted drug delivery is the combination of magnetic nanoparticles and microbubbles to produce magnetic and ultrasound responsive contrast agents. The previous work on the combination of ultrasound and magnetism is reviewed in the next section.

2.4.1 High intensity focused ultrasound (HIFU) surgery

High intensity focused ultrasound and MRI were combined in 1991 with the latter used for the purposes of treatment monitoring. Since then, both animal experiments and human trials have been performed. A commercial device has been created and FDA approved with further clinical systems currently undergoing trials [143]. In 1993, a lipid coated microbubble incorporating paramagnetic particles was patented for use as an ultrasound and MRI contrast agent. It was also proposed as an agent for mediating

therapeutic effects through cavitation nucleation [144]. More recently Smith *et al.* showed that magnetite nanoparticle agglomerates could be used to promote cavitation in HIFU treatments with applications for drug release [145].

2.4.2 Stimulated release

Ultrasound has also been used to improve drug delivery from magnetic particles. Saravan *et al.* found that the application of ultrasound enhanced the release kinetics of gelatin magnetic microspheres [146]. Kaminski *et al.* (2008) showed that ultrasound increased enzyme release from magnetic microcarriers but temperature rises within the carrier could denature the enzyme [147].

2.5 Magnetic microbubbles

Magnetic nanoparticles can be incorporated into microbubbles in order to form magnetic microbubbles. These have been synthesised to take advantage of the benefits of both ultrasound and magnetism in drug delivery and as dual purpose MRI and ultrasound contrast agents.

2.5.1 Magnetic microbubbles as dual contrast agents

Even in the absence of magnetic nanoparticles the gas liquid interface in microbubbles induces large local magnetic susceptibility differences. This was demonstrated experimentally *in vivo* with Optison® microbubbles in rat liver [148]. This then prompted in 2008 the use of emulsion stabilised particles of varying size with inclusions

of superparamagnetic iron oxide nanoparticles as dual modality (MRI and Ultrasound) contrast agents. The SPIO loaded nanobubbles were shown to improve the contrast of Ultrasound and MRI [149]. Yang *et al.* improved upon this by preparing a larger microbubble construct loaded with both gas and SPIOs [150]. When the bubbles were destroyed by ultrasound nanoscale particles, from the bubble shell, were deposited in the cells which slowly released therapeutic agents as the shell fragments degraded. Park *et al.* have similarly produced stable microbubbles which can attach numerous nanoparticles, magnetic and non-magnetic, to their surface for use in image contrast enhancement [151].

Other studies have indicated that the location of the nanoparticles in the coating was also found to influence the acoustic and magnetic response. In one study PVA microbubbles incorporating magnetic nanoparticles in the shell or with nanoparticles attached to the shell had their acoustic and magnetic properties examined. Having the nanoparticles on the outside of the shell was found to increase the acoustic attenuation coefficient, more so than if nanoparticles were embedded in the shell. The elastic modulus, measured by atomic force microscopy, also increased when nanoparticles were embedded in the shell and decreased when attached to the shell. The effect of nanoparticle attachment on magnetic properties was not examined [152].

He *et al.* developed a polymer magnetic microbubble for MRI with iron oxide nanoparticles on the surface of the microbubble. The acoustic non-linear character of the

microbubbles was improved by having the nanoparticles on the surface of the microbubble and the magnetic nanoparticles on the surface had a greater effect on alternating R2 value of surrounding water protons [153].

2.5.2 Magnetic microbubbles for drug delivery

In 2000, Soetanto *et al.* attached magnetic microparticles to microbubbles to enable remote manipulation of the microbubbles for both imaging and therapeutic applications. The microbubbles were formed from charged stearates and the microparticles were also coated in charged stearate and a calcium ion was used to bind them to the microbubble. The magnetic microbubbles responded to a magnet with a 20 N force [154, 155]. It is unknown, however, what effect ions in the blood will have upon the electrostatic interaction between the microbubbles and the microparticles. The large size of the microbubble-microparticle would also be of concern for *in vivo* application and this technique has not undergone any further testing according to the literature.

The use of magnetic microbubbles for ultrasound mediated therapeutic agent delivery was published by Stride *et al.* in 2009. Different magnetic bubble preparations were synthesised and their efficacy as transfection reagents under the influence of a magnetic field and/or ultrasound was tested *in vitro* in chinese hamster ovary cells. The hypothesised structure of the magnetic microbubbles used in this study is shown below in Figure 2.5. Each bubble formulation was co-injected with naked plasmid DNA encoding for luciferase. Exposure of the bubble formulations to either ultrasound or a magnetic

field alone had very little effect but a combination of ultrasound and a magnetic field showed a significant increase in transfection. A mixture of non-magnetic microbubbles and magnetic micelles (containing magnetic nanoparticles but no gas) in fact showed a slightly higher transfection efficiency upon exposure to both ultrasound and a magnetic field. It was hypothesised that this could be due to aggregation of the micelles and microbubbles or a sensitisation of the cell surface by the magnetic particles perhaps related to the mechanisms responsible for magnetofection. These hypotheses are discussed further later [156]. A similar experiment was subsequently conducted in a preliminary *in vivo* study in a mouse model with magnetic microbubbles and plasmid DNA again co-injected. A small magnet was positioned above the right lung and both *in vivo* and *ex vivo* bioluminescence imaging demonstrated that the transfection was confined to this organ and only observed with exposure to both ultrasound and the magnetic field [157].

Mulvana *et al.* subsequently used high speed video microscopy to show that the amplitude of oscillation was very similar for magnetic and non-magnetic microbubbles of the same size for the same ultrasound exposure conditions; and was not noticeably affected by the application of a magnetic field. For a suspension of microbubbles exposed to ultrasound the ratio between the amount of ultrasound signal scattered to the amount of signal attenuated by the microbubble population was calculated. The total scattered and non-linear scattered components of the signal can be calculated in each case. The scattering to attenuation ratio (STAR) and the non-linear scattering to attenuation ratio (nSTAR) provide a means of assessing the efficiency of contrast agents. It was found that

the non-linear scattering to attenuation ratio was reduced by 50% for magnetic microbubbles relative to non magnetic microbubbles and is hypothesised to be due to the damping effect of the oil layer [158].

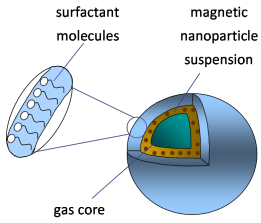


Figure 2.5, Theoretical structure of a magnetic microbubble synthesised by Stride *et al.* A gas core coated by a layer of magnetic nanoparticles in isoparaffin (ferrofluid) and a surface coating of phospholipids. From [138]

In 2010 Vlaskou *et al.* published a study on magnetically and acoustically active lipospheres [27, 159]. Lipospheres differ to microbubbles as they contain a bilayer stabilised by a polar fluid rather than a monolayer at a gas water interface. Lipospheres were synthesised based on a technique by Unger *et al.* who produced lipospheres with soy bean oil incorporating paclitaxel [84]. The lipospheres are synthesised by shaking a mixture of soybean oil, a cationic lipid, magnetic nanoparticles, DNA, aqueous buffer and a perfluoropropane gas in a sealed vial. The lipospheres showed contrast to tissue ratios of 5.6 dB at a centre frequency of 2.5 MHz for tissue harmonic imaging using a CH4-1 transducer [159]. This figure is lower than contrast to tisse ratios of ultrasound contrast agents that have been approved for clinical use, unlike those developed by Stride *et al.*

As therapeutic delivery agents the lipospheres did achieve nucleic acid delivery comparable to commercially available transfection reagents when a magnetic field was applied. However when ultrasound and a magnetic field were applied there was no improvement in transfection efficiency *in vitro*. The reason was thought to be due to the soybean oil reducing the acoustic responsiveness and as such did not increase cell membrane permeability. However, using a skin fold chamber on a mouse and injections of lipospheres with ultrasound and a magnetic field a large deposition of fluorescent material occurred but no direct observation or quantitative data was obtained for the transfection [159] .

The lipospheres were then substituted by Vlaskou *et al.* for lipid shelled microbubbles conjugated with positively charged magnetic nanoparticles through electrostatic interactions. These microbubbles had a much greater response to ultrasound [135] and the ultrasound contrast to tissue ratio of the magnetic microbubbles was found to be higher than SonoVue and a combination of ultrasound and magnetic forces improved transfection efficiency *in vitro* [160]. This work was continued by Mannel *et al*. for gene delivery *in vivo* [161].

Magnetic nanoparticles have also been used in order to augment biomimetic targeting. In 2011 magnetic microbubbles were targeted via VCAM-1 for molecular imaging and a magnetically targeted microbubble system resulted in greater attachment to VCAM-1 in atherosclerotic aortas in mice in conditions of high shear stress. The magnetic field

slowed down the magnetic microbubbles and allowed greater contact with the vascular endothelium and more opportunities for microbubble target interactions. The authors proved that magnetic fields were better at deflecting microbubbles from the centre line of flow to the target wall than acoustic radiation force [162].

Barrefelt *et al.* also looked at the biodistribution of PVA (polyvinyl alcohol) microbubbles incorporating magnetic nanoparticles in rats over a period of 6 weeks [163] using MRI. The results indicated that magnetic microbubbles are taken up in the lungs and then redistributed to the liver and spleen over time, in line with the administration of nanoparticles. There were no signs of necrosis in the liver and the spleen. The authors did however suggest possible adverse effects from high numbers of microbubbles in the lung leading to the formation of granulomas in association with aggregates of microbubbles.

Each of the magnetic microbubble formulations for drug delivery outlined above has benefits and drawbacks as outlined. Soetanto *et al.* has ferromagnetic particles which could cause clogging *in vivo* [155]. Vlaskou *et al.* did not show any increase in transfection efficiency for magnetic targeting and ultrasound application relative to magnetic targeting alone [160]. The formulation created by Stride *et al*. has shown transfection capability *in vitro* and *in vivo* under application of a magnetic field and ultrasound and the only drawback is the reduction in non-linear STAR [156]. As such

this formulation was taken forward for further experiments and used as the basis for new formulations.

2.6 Analysis techniques

2.6.1 Introduction

Understanding the structure of microbubbles is important for understanding what composition and structure are most efficacious for a given application. Which features of microbubbles can affect performance in biomedical applications and how these can be controlled in the fabrication techniques are very important for designing new microbubble formulations. The current methods to characterise microbubbles will be described below along with their current limitations to understand where most evidence for microbubble composition is obtained. In the scope of this research two techniques, fluorescence microscopy and electron microscopy, will be examined.

2.6.2 Fluorescence microscopy

Non-random mixing in the lipid layer can lead to the formation of lipid domains. Phospholipid layers usually exist in an ordered gel phase at low temperatures, above a melting temperature the lipid is liquid-disordered and the acyl chains are more fluid. Mixtures of lipids with different melting temperatures have been examined and when one component is present at low levels the mixture is uniform. However, above a threshold concentration phase separation occurs and ordered gel phases and liquid disordered phases coexist. Results are temperature dependant [164]. Mixtures of lipids with expanded phase and condensed phase in high enough concentration will separate out into

domains with a boundary in-between. The lipid phase can be influenced by the type of lipid used and the materials within the lipid layer capable of influencing lipid properties. This could be cholesterol and proteins in the case of cell membranes and PEG-40-Stearate or other emulsifiers in the case of microbubbles [165].

Borden *et al*. examined surface phase behaviour of lipid coated microbubbles producing a systematic study that linked composition and processing history with phase behaviour and microstructure. Microbubbles were created via sonication and a fluorophore was introduced into the lipid coating stabilized by PEG-40-stearate. Domains were found on the microbubble surface and domain size was generally uniform but did not correlate with microbubble diameter. Films in Langmuir troughs of the same composition as the microbubble were also used and examined. PEG-40-stearate can be irreversibly lost from the monolayer and presumably the microbubble shell at surface pressures below that required for lipid shedding. Two phases were observed on the microbubble surface; an expanded phase containing only PEG-40-stearate (and the fluorophore) and the condensed phase comprised of only lipid. For chain lengths of 16 carbons or more increasing the pressure drives more lipids into the condensed phase eventually squeezing out the PEG-40-stearate and the fluorophore. On larger microbubbles emulsifier is distributed heterogeneously over the bubble surface. Thus it will not provide a uniform steric shield against contact by other microbubbles and blood plasma proteins. Also this will not provide a uniform targeting surface for drug delivery when adhesive molecules are contained on the termini of the PEG chains [166]. However, all research was

performed on microbubbles above 20 μm, and phase structures on smaller microbubbles, within biomedical limits, could not be visualised with the fluorescence technique.

Kim *et al.* measured the mechanical properties of polycrystalline phospholipid shells. A fluorophore was added to the microbubble coating and the effect of microbubble cooling was explored. It was found that a faster microbubble cooling time resulted in larger domains on the surface. The results indicated that the material properties of phospholipid monolayer shells in shear deformation exhibit a composition dependence, which can be explained via intermolecular forces such as van der Waals, electrostatic repulsion and hydration forces [167].

2.6.3 Fluorescence lifetime viscosity measurements

Fluorescence lifetime imaging exploits the viscosity-sensitive photophysical properties of a molecular rotor such as BODIPY-C10. This fluorescent dye can be incorporated into surfactant coatings and the phenyl ring of the BODIPY-C10 is free to rotate as it is not bound to the surfactants. As a result of this rotation nonradiative decay pathways are activated leading to a reduction in fluorescence quantum yield and fluorescence lifetime. A calibration curve of fluorescence lifetime against known viscosities of solutions is produced and as such the viscosity of phospholipid layers can be determined from the fluorescence lifetime. Hosny *et al*. directly measured microbubble shell viscosity via a molecular rotor showing that the viscosity is directly influenced by the shell composition and manufacturing process [168]. The molecular rotor was embedded in the lipid shell

and its fluorescence lifetime was directly proportional to the viscosity of the microbubble coating.

2.6.4 Electron microscopy

Polymer microbubbles have been analysed using transmission electron microscopy by Yang *et al*. The polymer microbubbles were fixed in Osmium tetroxide, dehydrated in acetone and embedded in liquid epoxy resin [150]. A similar technique appears to have been used on polymer microbubbles [149, 153] and Chitosan microbubbles [169] usually with nanoparticles attached to the surface or embedded inside. The technique has also been successfully used to examine lipid coated magnetic and acoustically active liposomes. The liposomes were embedded in 10 % gelatin. Thin sections were selected from epon blocks and stained with uranyl acetate and lead citrate for contrast. This research sectioned the microbubbles to see the distribution of nanoparticles within the liposome coating [159].

Scanning electron microscopy (SEM), with gold palladium, has been performed on microbubbles. Fresh thrombi were exposed to targeted or non targeted microbubbles, the thrombi-microbubble mixture was dehydrated, dried, sputter coated with gold palladium and SEM images were obtained. Smooth spherical bubbles were observed bound to the thrombus but details of microbubble structure did not seem possible [170].

Kim *et al.* also cryo fixed microbubbles for transmission electron microscopy. The samples were cooled rapidly via plunge freezing, fractured, and complimentary fracture

surfaces were replicated with platinum and carbon. A replica bubble surface showed well-defined surface domains that resembled those observed via fluorescence microscopy. However, this technique only analyses a replica and is associated with high cost [167].

2.7 References

1. Owen, J., Q. Pankhurst, and E. Stride, *Magnetic targeting and ultrasound mediated drug delivery: Benefits, limitations and combination.* International Journal of Hyperthermia, 2012. **28**(4): p. 362-373.
2. Freeman, M.W., A. Arrott, and J.H.L. Watson, *Magnetism in medicine.* Journal of Applied Physics, 1960. **31**(5): p. S404-S405.
3. Andrä, W. and H. Nowak, *Magnetism in Medicine : a handbook*. 2nd ed. 2007: Weinheim : Wiley-VCH ;. 629.
4. Pankhurst, Q.A., et al., *Applications of magnetic nanoparticles in biomedicine.* Journal of Physics D: Applied Physics, 2003. **36**(13): p. R167-R181.
5. Polyak, B. and G. Friedman, *Magnetic targeting for site-specific drug delivery: Applications and clinical potential.* Expert Opinion on Drug Delivery, 2009. **6**(1): p. 53-70.
6. Willard, M.A., et al., *Chemically prepared magnetic nanoparticles.* International Materials Reviews, 2004. **49**(3-4): p. 125-170.
7. Hans, M.L. and A.M. Lowman, *Biodegradable nanoparticles for drug delivery and targeting.* Current Opinion in Solid State and Materials Science, 2002. **6**(4): p. 319-327.
8. Sun, C., J.S.H. Lee, and M. Zhang, *Magnetic nanoparticles in MR imaging and drug delivery.* Advanced Drug Delivery Reviews, 2008. **60**(11): p. 1252-1265.
9. Durán, J.D.G., et al., *Magnetic colloids as drug vehicles.* Journal of Pharmaceutical Sciences, 2008. **97**(8): p. 2948-2983.
10. McBain, S.C., H.H.P. Yiu, and J. Dobson, *Magnetic nanoparticles for gene and drug delivery.* International journal of nanomedicine, 2008. **3**(2): p. 169-180.
11. Kami, D., et al., *Application of magnetic nanoparticles to gene delivery.* International Journal of Molecular Sciences, 2011. **12**(6): p. 3705-3722.
12. Meyers, P.H., F. Cronic, and C.M. Nice Jr, *Experimental approach in the use and magnetic control of metallic iron.* The American journal of roentgenology, radium therapy, and nuclear, 1963. **90**: p. 1068-1077.
13. Medeiros, S.F., et al., *Stimuli-responsive magnetic particles for biomedical applications.* International Journal of Pharmaceutics, 2011. **403**(1-2): p. 139-161.

14. Zimmerman, U., et al., *Cells with manipulated functions: New perspectives for cell biology, medicine, and technology.* Angewandte Chemie - International Edition in English, 1981. **20**(4): p. 325-344.
15. Senyei, A., K. Widder, and G. Czerlinski, *Magnetic guidance of drug-carrying microspheres.* Journal of Applied Physics, 1978. **49**(6): p. 3578-3583.
16. Senyei, A.E., et al., *In vivo kinetics of magnetically targeted low-dose doxorubicin.* Journal of Pharmaceutical Sciences, 1981. **70**(4): p. 389-391.
17. Widder, K.J., et al., *Selective targeting of magnetic albumin microspheres containing low-dose doxorubicin - total remission in Yoida Srcoma-bearing rats.* European Journal of Cancer & Clinical Oncology, 1983. **19**(1): p. 135-139.
18. Edelman, E.R., et al., *In vitro and in vivo kinetics of regulated drug release from polymer matrices by oscillating magnetic fields.* Journal of Biomedical Materials Research, 1987. **21**(3): p. 339-353.
19. Langer, R., *Drug delivery and targeting.* Nature, 1998. **392**(6679 Suppl.): p. 5-10.
20. Hafeli, U.O., et al., *Magnetically directed poly(lactic acid) 90Y-microspheres: Novel agents for targeted intracavitary radiotherapy.* Journal of Biomedical Materials Research, 1994. **28**(8): p. 901-908.
21. Hafeli, U.O., et al., *Effective targeting of magnetic radioactive 90Y-microspheres to tumor cells by an externally applied magnetic field. Preliminary in vitro and in vivo results.* Nuclear Medicine and Biology, 1995. **22**(2): p. 147-155.
22. Lübbe, A.S., et al., *Preclinical experiences with magnetic drug targeting: Tolerance and efficacy.* Cancer Research, 1996. **56**(20): p. 4694-4701.
23. Alexiou, C., et al., *Locoregional cancer treatment with magnetic drug targeting.* Cancer Research, 2000. **60**(23): p. 6641-6648.
24. Lubbe, A.S., et al., *Clinical experiences with magnetic drag targeting: A phase I study with 4'-epidoxorubicin in 14 patients with advanced solid tumors.* Cancer Research, 1996. **56**(20): p. 4686-4693.
25. Koda, J., et al., *A multicenter, phase I/II trial of hepatic intra-arterial delivery of doxorubicin hydrochloride adsorbed to Magnetic Targeted Carriers in patients with hepatocellular carcinoma.* European Journal of Cancer, 2002. **38**: p. S18-S18.
26. Dykxhoorn, D.M. and J. Lieberman, *Running interference: Prospects and obstacles to using small interfering RNAs as small molecule drugs*, M.L. Yarmush, Editor 2006. p. 377-402.
27. Mykhaylyk, O., et al., *Magnetic nanoparticle formulations for DNA and siRNA delivery.* Journal of Magnetism and Magnetic Materials, 2007. **311**(1 SPEC. ISS.): p. 275-281.
28. Mah, C., et al., *Improved method of recombinant AAV2 delivery for systemic targeted gene therapy.* Molecular Therapy, 2002. **6**(1): p. 106-112.
29. Hughes, C., et al., *Streptavidin paramagnetic particles provide a choice of three affinity-based capture and magnetic concentration strategies for retroviral vectors.* Molecular Therapy, 2001. **3**(4): p. 623-630.

30. Scherer, F., et al., *Magnetofection: Enhancing and targeting gene delivery by magnetic force in vitro and in vivo.* Gene Therapy, 2002. **9**(2): p. 102-109.
31. Dalby, B., et al., *Advanced transfection with Lipofectamine 2000 reagent: primary neurons, siRNA, and high-throughput applications.* Methods, 2004. **33**(2): p. 95-103.
32. Abdallah, B., et al., *A powerful nonviral vector for in vivo gene transfer into the adult mammalian brain: Polyethylenimine.* Human Gene Therapy, 1996. **7**(16): p. 1947-1954.
33. Plank, C., et al., *The magnetofection method: Using magnetic force to enhance gene delivery.* Biological Chemistry, 2003. **384**(5): p. 737-747.
34. Plank, C., O. Zelphati, and O. Mykhaylyk, *Magnetically enhanced nucleic acid delivery. Ten years of magnetofection-Progress and prospects.* Advanced Drug Delivery Reviews.
35. Cai, D., et al., *Highly efficient molecular delivery into mammalian cells using carbon nanotube spearing.* Nature Methods, 2005. **2**(6): p. 449-454.
36. Bonetta, L., *The inside scoop - Evaluating gene delivery methods.* Nature Methods, 2005. **2**(11): p. 875-882.
37. Kamau, S.W., et al., *Enhancement of the efficiency of non-viral gene delivery by application of pulsed magnetic field.* Nucleic Acids Research, 2006. **34**(5): p. e40.
38. Neuberger, T., et al., *Superparamagnetic nanoparticles for biomedical applications: Possibilities and limitations of a new drug delivery system.* Journal of Magnetism and Magnetic Materials, 2005. **293**(1): p. 483-496.
39. Arruebo, M., et al., *Magnetic nanoparticles for drug delivery.* Nano Today, 2007. **2**(3): p. 22-32.
40. Ng, K.Y. and Y. Liu, *Therapeutic ultrasound: Its application in drug delivery.* Medicinal Research Reviews, 2002. **22**(2): p. 204-223.
41. Newman, C.M., et al., *Ultrasound gene therapy: On the road from concept to reality.* Echocardiography, 2001. **18**(4): p. 339-347.
42. Yuh, E.L., et al., *Delivery of systemic chemotherapeutic agent to tumors by using focused ultrasound: Study in a murine model.* Radiology, 2005. **234**(2): p. 431-437.
43. Farr R., F. and J. Allisy-Roberts P., *Physics for Medical Imaging*. 2005: Saunders.
44. Ferrara, K.W., *Driving delivery vehicles with ultrasound.* Advanced Drug Delivery Reviews, 2008. **60**(10): p. 1097-1102.
45. Deckers, R., C. Rome, and C.T.W. Moonen, *The role of ultrasound and magnetic resonance in local drug delivery.* Journal of Magnetic Resonance Imaging, 2008. **27**(2): p. 400-409.
46. Bailey, M.R., et al., *Physical mechanisms of the therapeutic effect of ultrasound (a review).* Acoustical Physics, 2003. **49**(4): p. 369-388.
47. Azhari, H., *Basics of Biomedical ultrasound for engineers*. 1 ed. 2010, New Jersey: John Wiley and sons, Inc.
48. Apfel, R.E., *Sonic effervescence: A tutorial on acoustic cavitation.* Journal of the Acoustical Society of America, 1997. **101**(3): p. 1227-1237.

49. Iwanaga, K., et al., *Local delivery system of cytotoxic agents to tumors by focused sonoporation.* Cancer Gene Therapy, 2007. **14**(4): p. 354-363.
50. Zhong, W., et al., *Sonoporation induces apoptosis and cell cycle arrest in human promyelocytic leukemia cells.* Ultrasound in Medicine and Biology, 2011. **37**(12): p. 2149-2159.
51. Nyborg, W.L., *Ultrasonic microstreaming and related phenomena.* British Journal of Cancer, 1982. **45**(Suppl. 5): p. 156-160.
52. Marmottant, P. and S. Hilgenfeldt, *Controlled vesicle deformation and lysis by single oscillating bubbles.* Nature, 2003. **423**(6936): p. 153-156.
53. Kiessling, F., J. Huppert, and M. Palmowski, *Functional and Molecular Ultrasound Imaging: Concepts and Contrast Agents.* Current Medicinal Chemistry, 2009. **16**(5): p. 627-642.
54. Harvey, C.J., et al., *Advances in ultrasound.* Clinical Radiology, 2002. **57**(3): p. 157-177.
55. Calliada, F., et al., *Ultrasound contrast agents: Basic principles.* European Journal of Radiology, 1998. **27**(SUPPL. 2): p. S157-S160.
56. Maresca, D., et al., *Mapping intravascular ultrasound controversies in interventional cardiology practice.* PLoS ONE, 2014. **9**(5).
57. Klibanov, A.L., *Ligand-carrying gas-filled microbubbles: Ultrasound contrast agents for targeted molecular imaging.* Bioconjugate Chemistry, 2005. **16**(1): p. 9-17.
58. Quaia, E., *Contrast Media in Ultrasonography*. 2005.
59. Stride, E. and M. Edirisinghe, *Novel microbubble preparation technologies.* Soft Matter, 2008. **4**(12): p. 2350.
60. Feigenbaum, H., et al., *Identification of ultrasound echoes from the left ventricle by use of intracardiac injections of indocyanine green.* Circulation, 1970. **41**(4): p. 615-621.
61. Gramiak, R. and P.M. Shah, *Echocardiography of the aortic root.* Investigative Radiology, 1968. **3**(5): p. 356-366.
62. Kremkau, F.W., et al., *Ultrasonic detection of cavitation at catheter tips.* The American journal of roentgenology, radium therapy, and nuclear medicine, 1970. **110**(1): p. 177-183.
63. Bove, A.A., M.C. Ziskin, and W.L. Mulchin, *Ultrasonic detection of in-vivo cavitation and pressure effects of high-speed injections through catheters.* Investigative Radiology, 1969. **4**(4): p. 236-240.
64. Meltzer, R.S., et al., *The source of ultrasound contrast effect.* Journal of Clinical Ultrasound, 1980. **8**(2): p. 121-127.
65. Feinstein, S.B., F.J. Ten Cate, and W. Zwehl, *Two-dimensional contrast echocardiography. I. In vitro development and quantitative analysis of echo contrast agents.* Journal of the American College of Cardiology, 1984. **3**(1): p. 14-20.
66. Wheatley, M.A., B. Schrope, and P. Shen, *Contrast agents for diagnostic ultrasound: Development and evaluation of polymer-coated microbubbles.* Biomaterials, 1990. **11**(9): p. 713-717.

67. Florinas, S., et al., *Ultrasound-assisted siRNA delivery via arginine-grafted bioreducible polymer and microbubbles targeting VEGF for ovarian cancer treatment.* Journal of Controlled Release, 2014. **183**(1): p. 1-8.
68. Lentacker, I., et al., *Ultrasound-responsive polymer-coated microbubbles that bind and protect DNA.* Langmuir, 2006. **22**(17): p. 7273-7278.
69. Bjerknes, K., et al., *Preparation of polymeric microbubbles: Formulation studies and product characterisation.* International Journal of Pharmaceutics, 1997. **158**(2): p. 129-136.
70. Borden, M.A., et al., *Influence of lipid shell physicochemical properties on ultrasound-induced microbubble destruction.* Ieee Transactions on Ultrasonics Ferroelectrics and Frequency Control, 2005. **52**(11): p. 1992-2002.
71. Stride, E. and N. Saffari, *On the destruction of microbubble ultrasound contrast agents.* Ultrasound in Medicine and Biology, 2003. **29**(4): p. 563-573.
72. Quaia, E., *Microbubble ultrasound contrast agents: An update.* European Radiology, 2007. **17**(8): p. 1995-2008.
73. Stride, E., *The influence of surface adsorption on microbubble dynamics.* Philosophical Transactions of the Royal Society A: Mathematical, Physical and Engineering Sciences, 2008. **366**(1873): p. 2103-2115.
74. Stride, E., et al., *Increasing the nonlinear character of microbubble oscillations at low acoustic pressures.* Journal of the Royal Society Interface, 2008. **5**(24): p. 807-811.
75. Mohamedi, G., et al., *Effects of gold nanoparticles on the stability of microbubbles.* Langmuir, 2012. **28**(39): p. 13808-13815.
76. Li, M.K. and H.S. Fogler, *ACOUSTIC EMULSIFICATION - 1. THE INSTABILITY OF THE OIL-WATER INTERFACE TO FORM THE INITIAL DROPLETS.* Journal of Fluid Mechanics, 1978. **88**(pt 3): p. 499-511.
77. Li, M.K. and H.S. Fogler, *ACOUSTIC EMULSIFICATION - 2. BREAKUP OF THE LARGE PRIMARY OIL DROPLETS IN A WATER MEDIUM.* Journal of Fluid Mechanics, 1978. **88**(pt 3): p. 513-528.
78. Feshitan, J.A., et al., *Microbubble size isolation by differential centrifugation.* Journal of Colloid and Interface Science, 2009. **329**(2): p. 316-324.
79. Joscelyne, S.M. and G. Trägårdh, *Membrane emulsification - A literature review.* Journal of Membrane Science, 2000. **169**(1): p. 107-117.
80. Kukizaki, M. and M. Goto, *Spontaneous formation behavior of uniform-sized microbubbles from Shirasu porous glass (SPG) membranes in the absence of water-phase flow.* Colloids and Surfaces A: Physicochemical and Engineering Aspects, 2007. **296**(1-3): p. 174-181.
81. Pancholi, K., E. Stride, and M. Edirisinghe, *Generation of microbubbles for diagnostic and therapeutic applications using a novel device.* Journal of Drug Targeting, 2008. **16**(6): p. 494-501.
82. Wang, W., C.C. Moser, and M.A. Wheatley, *Langmuir trough study of surfactant mixtures used in the production of a new ultrasound contrast agent consisting of stabilized microbubbles.* Journal of Physical Chemistry, 1996. **100**(32): p. 13815-13821.
83. Unger, E.C., et al., *Gene delivery using ultrasound contrast agents.* Echocardiography, 2001. **18**(4): p. 355-361.

84. Unger, E.C., et al., *Acoustically active lipospheres containing paclitaxel - A new therapeutic ultrasound contrast agent.* Investigative Radiology, 1998. **33**(12): p. 886-892.
85. Tachibana, K. and S. Tachibana, *Albumin microbubble echo-contrast material as an enhancer for ultrasound accelerated thrombolysis.* Circulation, 1995. **92**(5): p. 1148-1150.
86. Lindner, J.R. and S. Kaul, *Delivery of drugs with ultrasound.* Echocardiography, 2001. **18**(4): p. 329-337.
87. Wu, Y., et al., *Binding and lysing of blood clots using MRX-408.* Investigative Radiology, 1998. **33**(12): p. 880-885.
88. Prentice, P., et al., *Membrane disruption by optically controlled microbubble cavitation.* Nature Physics, 2005. **1**(2): p. 107-110.
89. Schlicher, R.K., et al., *Mechanism of intracellular delivery by acoustic cavitation.* Ultrasound in Medicine and Biology, 2006. **32**(6): p. 915-924.
90. Guzmán, H.R., et al., *Ultrasound-mediated disruption of cell membranes. I. Quantification of molecular uptake and cell viability.* Journal of the Acoustical Society of America, 2001. **110**(1): p. 588-596.
91. Guzmán, H.R., et al., *Ultrasound-mediated disruption of cell membranes. II. Heterogeneous effects on cells.* Journal of the Acoustical Society of America, 2001. **110**(1): p. 597-606.
92. Price, R.J., et al., *Delivery of colloidal particles and red blood cells to tissue through microvessel ruptures created by targeted microbubble destruction with ultrasound.* Circulation, 1998. **98**(13): p. 1264-1267.
93. Lentacker, I., et al., *Design and evaluation of doxorubicin-containing microbubbles for ultrasound-triggered doxorubicin delivery: Cytotoxicity and mechanisms involved.* Molecular Therapy, 2010. **18**(1): p. 101-108.
94. Kooiman, K., et al., *Acoustic behavior of microbubbles and implications for drug delivery.* Advanced Drug Delivery Reviews, 2014. **72**: p. 28-48.
95. Lentacker, I., et al., *Understanding ultrasound induced sonoporation: Definitions and underlying mechanisms.* Advanced Drug Delivery Reviews, 2014. **72**: p. 49-64.
96. Carlisle, R., et al., *Enhanced tumor uptake and penetration of virotherapy using polymer stealthing and focused ultrasound.* Journal of the National Cancer Institute, 2013. **105**(22): p. 1701-1710.
97. Carlisle, R.C., et al., *Human erythrocytes bind and inactivate type 5 adenovirus by presenting Coxsackie virus-adenovirus receptor and complement receptor 1.* Blood, 2009. **113**(9): p. 1909-1918.
98. Van Den Bongard, H.J.G.D., et al., *Pharmacokinetically guided administration of chemotherapeutic agents.* Clinical Pharmacokinetics, 2000. **39**(5): p. 345-367.
99. Mullin, L., et al. *Tumor treatment with microbubble enhanced low-intensity ultrasound and paclitaxel nanocapsules reduces drug dose required for therapeutic effect*. in *IEEE International Ultrasonics Symposium, IUS*. 2011.
100. Sirsi, S.R. and M.A. Borden, *Microbubble compositions, properties and biomedical applications.* Bubble Science, Engineering and Technology, 2009. **1**(1-2): p. 3-17.

101. Nishikawa, M. and L. Huang, *Nonviral Vectors in the New Millennium: Delivery Barriers in Gene Transfer.* Human Gene Therapy, 2001. **12**(8): p. 861-870.
102. Bekeredjian, R., et al., *Ultrasound-Targeted Microbubble Destruction Can Repeatedly Direct Highly Specific Plasmid Expression to the Heart.* Circulation, 2003. **108**(8): p. 1022-1026.
103. Schwarz, E.R., et al., *Evaluation of the effects of intramyocardial injection of DNA expressing vascular endothelial growth factor (VEGF) in a myocardial infarction model in the rat-angiogenesis and angioma formation.* Journal of the American College of Cardiology, 2000. **35**(5): p. 1323-1330.
104. Kim, H.J., et al., *Ultrasound-mediated transfection of mammalian cells.* Human Gene Therapy, 1996. **7**(11): p. 1339-1346.
105. Greenleaf, W.J., et al., *Artificial cavitation nuclei significantly enhance acoustically induced cell transfection.* Ultrasound in Medicine and Biology, 1998. **24**(4): p. 587-595.
106. Lawrie, A., et al., *Microbubble-enhanced ultrasound for vascular gene delivery.* Gene Therapy, 2000. **7**(23): p. 2023-2027.
107. Li, T., K. Tachibana, and M. Kuroki, *Gene Transfer with Echo-enhanced Contrast Agents: Comparison between Albunex, Optison, and Levovist in Mice - Initial Results.* Radiology, 2003. **229**(2): p. 423-428.
108. Rahim, A., et al., *Physical parameters affecting ultrasound/microbubble-mediated gene delivery efficiency in vitro.* Ultrasound in Medicine and Biology, 2006. **32**(8): p. 1269-1279.
109. Unger, E.C., et al., *Local drug and gene delivery through microbubbles.* Progress in Cardiovascular Diseases, 2001. **44**(1): p. 45-54.
110. Xenariou, S., et al., *Use of ultrasound to enhance nonviral lung gene transfer in vivo.* Gene Therapy, 2007. **14**(9): p. 768-774.
111. Shohet, R.V., et al., *Echocardiographic destruction of albumin microbubbles directs gene delivery to the myocardium.* Circulation, 2000. **101**(22): p. 2554-2556.
112. Tsunoda, S., et al., *Sonoporation using microbubble BR14 promotes pDNA/siRNA transduction to murine heart.* Biochemical and Biophysical Research Communications, 2005. **336**(1): p. 118-127.
113. Kodama, T., et al., *Evaluation of transfection efficiency in skeletal muscle using nano/microbubbles and ultrasound.* Ultrasound in Medicine and Biology, 2010. **36**(7): p. 1196-1205.
114. Nishikawa, M., Y. Takakura, and M. Hashida, *Pharmacokinetic considerations regarding non-viral cancer gene therapy.* Cancer Science, 2008. **99**(5): p. 856-862.
115. Vaupel, P., F. Kallinowski, and P. Okunieff, *Blood flow, oxygen and nutrient supply, and metabolic microenvironment of human tumors: A review.* Cancer Research, 1989. **49**(23): p. 6449-6465.
116. Whitehead, K.A., R. Langer, and D.G. Anderson, *Knocking down barriers: Advances in siRNA delivery.* Nature Reviews Drug Discovery, 2009. **8**(2): p. 129-138.

117. Gomes-Da-Silva, L.C., et al., *Lipid-based nanoparticles for siRNA delivery in cancer therapy: Paradigms and challenges.* Accounts of Chemical Research, 2012. **45**(7): p. 1163-1171.
118. Carson, A.R., et al., *Ultrasound-targeted microbubble destruction to deliver siRNA cancer therapy.* Cancer Research, 2012. **72**(23): p. 6191-6199.
119. Lindner, J.R., et al., *Microbubble persistence in the microcirculation during ischemia/reperfusion and inflammation is caused by integrin- and complement- mediated adherence to activated leukocytes.* Circulation, 2000. **101**(6): p. 668-675.
120. Villanueva, F.S., et al., *Microbubbles targeted to intercellular adhesion molecule-1 bind to activated coronary artery endothelial cells.* Circulation, 1998. **98**(1): p. 1-5.
121. Villanueva, F.S., et al., *Albumin microbubble adherence to human coronary endothelium: Implications for assessment of endothelial function using myocardial contrast echocardiography.* Journal of the American College of Cardiology, 1997. **30**(3): p. 689-693.
122. Christiansen, J.P., et al., *Noninvasive imaging of myocardial reperfusion injury using leukocyte-targeted contrast echocardiography.* Circulation, 2002. **105**(15): p. 1764-1767.
123. Fisher, N.G., et al., *Influence of microbubble surface charge on capillary transit and myocardial contrast enhancement.* Journal of the American College of Cardiology, 2002. **40**(4): p. 811-819.
124. Culp, W.C., et al., *Intracranial clot lysis with intravenous microbubbles and transcranial ultrasound in swine.* Stroke, 2004. **35**(10): p. 2407-2411.
125. Weller, G.E.R., et al., *Ultrasonic imaging of tumor angiogenesis using contrast microbubbles targeted via the tumor-binding peptide arginine-arginine-leucine.* Cancer Research, 2005. **65**(2): p. 533-539.
126. Ellegala, D.B., et al., *Imaging tumor angiogenesis with contrast ultrasound and microbubbles targeted to αvβ3.* Circulation, 2003. **108**(3): p. 336-341.
127. Unger, E.C., et al., *In vitro studies of a new thrombus-specific ultrasound contrast agent.* American Journal of Cardiology, 1998. **81**(12 A): p. 58G-61G.
128. Schumann, P.A., et al., *Targeted-microbubble binding selectively to GPIIb IIIa receptors of platelet thrombi.* Investigative Radiology, 2002. **37**(11): p. 587-593.
129. Kaneko, O.F. and J.K. Willmann, *Ultrasound for molecular imaging and therapy in cancer.* Quantitative Imaging in Medicine and Surgery, 2012. **2**(2): p. 87-97.
130. Haag, P., et al., *Microbubble-enhanced ultrasound to deliver an antisense oligodeoxynucleotide targeting the human androgen receptor into prostate tumours.* The Journal of Steroid Biochemistry and Molecular Biology, 2006. **102**(1–5): p. 103-113.
131. Ferrara, K., R. Pollard, and M. Borden, *Ultrasound microbubble contrast agents: Fundamentals and application to gene and drug delivery.* Annual Review of Biomedical Engineering 2007. **9**: p. 415-447.

132. Chen, S., et al., *Efficient gene delivery to pancreatic islets with ultrasonic microbubble destruction technology.* Proceedings of the National Academy of Sciences of the United States of America, 2006. **103**(22): p. 8469-8474.
133. Lum, A.F.H., et al., *Ultrasound radiation force enables targeted deposition of model drug carriers loaded on microbubbles.* Journal of Controlled Release, 2006. **111**(1-2): p. 128-134.
134. Geers, B., et al., *Self-assembled liposome-loaded microbubbles: The missing link for safe and efficient ultrasound triggered drug-delivery.* Journal of Controlled Release, 2011. **152**(2): p. 249-256.
135. Lentacker, I., et al., *Lipoplex-loaded microbubbles for gene delivery: A trojan horse controlled by ultrasound.* Advanced Functional Materials, 2007. **17**(12): p. 1910-1916.
136. Cochran, M.C., et al., *Doxorubicin and paclitaxel loaded microbubbles for ultrasound triggered drug delivery.* International Journal of Pharmaceutics, 2011. **414**(1-2): p. 161-170.
137. Phillips, L.C., et al., *Localized ultrasound enhances delivery of rapamycin from microbubbles to prevent smooth muscle proliferation.* Journal of Controlled Release, 2011. **154**(1): p. 42-49.
138. Thanh, N.T.K., *Magnetic Nanoparticles: From Fabrication to Clinical Applications, Chapter 19*. 2011: Taylor and Francis.
139. Zhao, S., et al., *Radiation-force assisted targeting facilitates ultrasonic molecular imaging.* Molecular Imaging, 2004. **3**(3): p. 135-148.
140. Zhao, S., et al. *Increasing binding efficiency of ultrasound targeted agents with radiation force*. in *IEEE Ultrasonics Symposium*. 2004. Montreal, Que.
141. Willmann, J.K., et al., *Dual-targeted contrast agent for US assessment of tumor angiogenesis in vivo.* Radiology, 2008. **248**(3): p. 936-944.
142. Rychak, J.J., et al., *Deformable gas-filled microbubbles targeted to P-selectin.* Journal of Controlled Release, 2006. **114**(3): p. 288-299.
143. Hynynen, K., *MRIgHIFU: A tool for image-guided therapeutics.* Journal of Magnetic Resonance Imaging, 2011. **34**(3): p. 482-493.
144. D'Arrigo, J.S., *Method for the production of medical-grade lipid-coated microbubbles, paramagnetic labeling of such microbubbles and therapeutic uses of microbubbles*, in *United States Patent Office*1993.
145. Smith, M.J., et al., *Effect of Magnetite Nanoparticle Agglomerates on Ultrasound Induced Inertial Cavitation.* Ultrasound in Medicine and Biology, 2009. **35**(6): p. 1010-1014.
146. Saravanan, M., et al., *Ultrasonically controlled release and targeted delivery of diclofenac sodium via gelatin magnetic microspheres.* International Journal of Pharmaceutics, 2004. **283**(1-2): p. 71-82.
147. Kaminski, M.D., et al., *Encapsulation and release of plasminogen activator from biodegradable magnetic microcarriers.* European Journal of Pharmaceutical Sciences, 2008. **35**(1-2): p. 96-103.
148. Wong, K.K., et al., *In vivo study of microbubbles as an MR susceptibility contrast agent.* Magnetic Resonance in Medicine, 2004. **52**(3): p. 445-452.

149. Yang, F., et al., *Superparamagnetic nanoparticle-inclusion microbubbles for ultrasound contrast agents.* Physics in Medicine and Biology, 2008. **53**(21): p. 6129-6141.
150. Yang, F., et al., *Superparamagnetic iron oxide nanoparticle-embedded encapsulated microbubbles as dual contrast agents of magnetic resonance and ultrasound imaging.* Biomaterials, 2009. **30**(23-24): p. 3882-3890.
151. Park, J.I., et al., *Microbubbles loaded with nanoparticles: A route to multiple imaging modalities.* ACS Nano, 2010. **4**(11): p. 6579-6586.
152. Poehlmann, M., et al., *On the interplay of shell structure with low- and high-frequency mechanics of multifunctional magnetic microbubbles.* Soft Matter, 2014. **10**(1): p. 214-226.
153. He, W., et al., *Microbubbles with surface coated by superparamagnetic iron oxide nanoparticles.* Materials Letters, 2012. **68**: p. 64-67.
154. Soetanto, K. and H. Watarai, *Development of magnetic microbubbles for drug delivery system (DDS).* Japanese Journal of Applied Physics, Part 1: Regular Papers and Short Notes and Review Papers, 2000. **39**(5 B): p. 3230-3232.
155. Soetanto, K. and H. Watarai. *Ferromagnetic Ultrasound Microbubbles Contrast Agent*. 2003. Cancun.
156. Stride, E., et al., *Enhancement of Microbubble Mediated Gene Delivery by Simultaneous Exposure to Ultrasonic and Magnetic Fields.* Ultrasound in Medicine & Biology, 2009. **35**(5): p. 861-868.
157. Mulvana, H., et al. *Enhanced gene transfection in vivo using magnetic localisation ofultrasound contrast agents: Preliminary results*. 2010. San Diego, CA.
158. Mulvana, H., et al., *Theoretical and Experimental Characterisation of Magnetic Microbubbles.* Ultrasound in Medicine and Biology, 2012. **38**(5): p. 864-875.
159. Vlaskou, D., et al., *Magnetic and Acoustically Active Lipospheres for Magnetically Targeted Nucleic Acid Delivery.* Advanced Functional Materials, 2010. **20**(22): p. 3881-3894.
160. Vlaskou, D., et al. *Magnetic microbubbles: Magnetically targeted and ultrasound-triggered vectors for gene delivery in vitro*. 2010. Rostock.
161. Mannell, H., et al., *Site directed vascular gene delivery in vivo by ultrasonic destruction of magnetic nanoparticle coated microbubbles.* Nanomedicine: Nanotechnology, Biology, and Medicine, 2012.
162. Wu, J., et al., *Efficacy of contrast-enhanced US and magnetic microbubbles targeted to vascular cell adhesion molecule-1 for molecular imaging of atherosclerosis.* Radiology, 2011. **260**(2): p. 463-471.
163. Barrefelt, Å., et al., *Biodistribution, kinetics, and biological fate of SPION microbubbles in the rat.* International Journal of Nanomedicine, 2013. **8**: p. 3241-3254.
164. Brown, D.A. and E. London, *Structure and origin of ordered lipid domains in biological membranes.* Journal of Membrane Biology, 1998. **164**(2): p. 103-114.
165. Mouritsen, O., *Life - As a Matter of Fat*. 2001: Springer.

166. Borden, M.A., et al., *Surface phase behavior and microstructure of lipid/PEG-emulsifier monolayer-coated microbubbles.* Colloids and Surfaces B: Biointerfaces, 2004. **35**(3-4): p. 209-223.
167. Kim, D.H., et al., *Mechanical properties and microstructure of polycrystalline phospholipid monolayer shells: Novel solid microparticles.* Langmuir, 2003. **19**(20): p. 8455-8466.
168. Hosny, N.A., et al., *Mapping microbubble viscosity using fluorescence lifetime imaging of molecular rotors.* Proceedings of the National Academy of Sciences of the United States of America, 2013. **110**(23): p. 9225-9230.
169. Liu, T.Y., et al., *A novel ultrasound-triggered drug vehicle with multimodal imaging functionality.* Acta Biomaterialia, 2012.
170. Martin, M.J., et al., *Enhanced detection of thromboemboli with the use of targeted microbubbles.* Stroke, 2007. **38**(10): p. 2726-2732.

3 Materials and Methods

3.1 Materials

1,2-distearoyl-sn-glycero-3-phosphocholine (DSPC), 1,2-dipalmitoyl sn-glycero-3-phosphocholine (DPPC), 1,2-distearoyl-sn-glycero-3-ethylphosphocholine (DSEPC), 1,2-distearoyl-sn-glycero-3-phosphoethanolamine-N-(polyethylene glycol)-2000 DSPE-PEG(2000), and 1,2-distearoyl-*sn*-glycero-3-phosphoethanolamine-N-[biotinyl(polyethylene glycol)-2000] DSPE-PEG(2000)-biotin were purchased from Avanti polar lipids Inc. (Alabaster, Alabama, USA). Polyethyleneglycol (PEG) (40) Stearate, ethanol, kerosene, chloroform, Dulbecco's phosphate buffered saline, fetal bovine serum, glycerol, propylene glycol, avidin, FITC avidin, biotin and agarose powder were purchased from Sigma Aldrich Ltd. (Gillingham, Dorset, UK). A suspension of 10 nm spherical magnetite nanoparticles in isoparaffin (10% volume fraction) was purchased from Liquids Research Ltd. (Bangor, UK). Phospholipid (phosphatidylcholine) coated 50 nm magnetite nanoparticles (FluidMAG-lipid), FluidMAG-CT (citric acid) and FluidMAG-OA (oleic acid) were purchased from Chemicell GmbH (Berlin, Germany). Sulphur Hexafluoride (SF_6) was purchased from The BOC Group (Guilford, Surrey, UK). Gold nanoparticles were kindly donated by Prof. Luis Liz-Marzan from the Universidade de Vigo, Vigo Spain. BODIPY-C10 was kindly donated by Dr. Marina Kuimova from Imperial College London, London, UK.

BLOCK-iT FLUORESCENT OLIGO (Lot No:1477937) was purchased from Invitrogen (Life Technologies). This is a generic siRNA with a fluorophore attached that does not cause knockdown of a specific gene. Phenol free Dulbecco's DMEM

media and trypsin –EDTA (0.05%) phenol red were also purchased from Life Technologies, Inchinnan Business Park, Paisley, UK. SY5Y neuroblasto cells (from ATCC from LGC Standards –UK Office, Teddington, United Kingdom) were used as a model neuroblastoma cell line on account of neuroblastoma being the most common extracranial solid tumours in childhood with certain tumours expressing resistance to multimodal treatment [1]. They were also chosen because of their rapid replication rate and ability to be transfected using viral methods.

3.2 Methods

3.2.1 Microbubble production methods

3.2.1.1 Introduction

Different microbubble compositions were used in the research described in subsequent chapters and the fabrication techniques are described below.

3.2.1.2 Phospholipid/emulsifier microbubbles (PMBs)

DSPC and PEG-40-stearate were dissolved in chloroform and mixed in a glass vial at a molar ratio of 9:1 using 15.52 mg and 4.48 mg respectively. This was heated to 50 °C and left for 12 hours to evaporate the chloroform. The resulting lipid film was suspended in filtered deionised water (10 ml) over 1 hour at 75 °C under constant stirring. The solution was then sonicated (power setting 4) for 90 s to disperse the lipids using an ultrasonic cell disruptor (XL 2000, probe diameter 3 mm, 100 Watts, 22.5 kHz, Misonix Inc. Farmingdale, NY, USA). This was followed by sonication at the gas water interface under a positive pressure of SF_6 for 20 s at sonicator power 19.

The microbubble solution was then placed in an ice bath for cooling for approximately 10 minutes.

3.2.1.3 Gold coated microbubbles (GMBs)

An aqueous gold citrate suspension (0.51 mM) was used as the base for the microbubble coating. Small gold colloids with an average diameter of approximately 15 nm ±10% were synthesized according to the sodium citrate reduction method [2], by boiling 95 mL of $5x10^{-4}$ M tetra-chloroauric acid ($HAuCl_4$•4H2O), adding 5 mL of a warm sodium citrate solution (1 wt%) and boiling for 15 min. This yielded a solution containing approximately 1000 nanoparticles/ml. DSPC, PEG(40)Stearate, and the gold nanoparticle suspension were suspended in deionised water (10 ml). This solution was then sonicated (setting 4) for 1 minute. The probe tip was then moved to the gas water interface followed by sonication under air at the same power for 20 seconds to produce gold microbubbles.

3.2.1.4 Magnetic microbubble formulation 1 (MMB)

DSPC (15 mg) was added to a vial along with PBS (15 ml). This solution was sonicated for 15 s (setting 4) with the probe fully immersed in the solution and for a further 15 s at the air liquid interface (setting 4). 15 µl of magnetite suspension was then added to the solution and swirled for 10 seconds. This solution was again sonicated (15 s with the probe immersed, 15 s at the air liquid interface). The solution was then manually shaken for 30 seconds [3]. SF6 was not used in this protocol.

3.2.1.5 Magnetic microbubble formulation 2 (CAMMB)

DSPC and PEG 40 Stearate at a molar ratio of 9:1 were dissolved in chloroform. The chloroform was allowed to evaporate off over 12 hours. Distilled water was added to the lipid film followed by heating to approximately 70 °C under constant stirring for one hour. The stirbar was removed and FluidMAG-CT (15 µl) was added to the solution. This was sonicated for one minute (setting 4) followed by sonication at the gas water interface under a positive pressure of SF_6 for 20s (setting 19) was and then cooled in ice water for 10 minutes.

3.2.1.6 Magnetic droplets and microbubbles (MDMBs)

DSPC/PEG-40-stearate microbubbles were produced as described above with SF_6 filling gas. Magnetic droplets were produced via the same method as magnetic microbubble formulation 1 but without either sonication at the air water interface or manual shaking. The magnetic droplets and microbubbles were mixed by drawing 0.5 ml of phospholipid/emulsifier microbubble solution into a syringe followed by 0.5 ml of magnetic droplets. The syringe was then inverted 3 times to ensure adequate mixing.

3.2.1.7 Biotin microbubbles formulation (BMBs)

DSPC, DSPE-PEG(2000), DSPE-PEG(2000)-biotin dissolved in chloroform were added to a glass vial in a ratio of 70:10:10 molar percent, This was allowed to dry overnight to produce a lipid film. PBS (5 ml) was then added and the temperature was raised above the lipid transition temperature (55 °C) under constant stirring for approximately 1 hour. This solution was then probe sonicated (setting 4, 1 minute)

followed by sonication at the gas-liquid interface under a positive pressure of SF_6 (setting 19, 20 seconds) producing a white solution. This was then centrifuged (300 RCF, 10 minutes) to concentrate the microbubbles [4].

3.2.1.8 Magnetic microbubble formulation 3 (LMMB)

DSPC and PEG(40)Stearate dissolved in chloroform were mixed in a glass vial at a molar ratio of 9:1 using 1.5 mg and 0.44 mg and this was heated to 50 °C and left for 12 hours. The lipid film was suspended in Deionised water (1.5 ml) for over 1 hour at 75 °C under constant stirring as above. The stirbar was removed and the suspension of (FluidMAG-Lipid) lipid coated magnetic nanoparticles in water (15 µl, 25 mg/ml) added. The solution was then sonicated (setting 4) for 90 s, followed by sonication at the gas water interface under positive pressure of SF_6 for 20 s at sonication power 19. The microbubble solution was then placed in an ice bath for cooling for approximately 10 minutes.

3.2.1.9 Charged magnetic microbubble solution 3 (CLMMB)

The production method was identical to that outlined above for LMMBs however the starting mixture was DSPC, DSEPC and PEG-40-Stearate at a molar ratio of 100:44:4.5. This microbubble formulation was used in order to bind siRNA for drug delivery. SF6 was used as the filling gas.

Table 3.1, Summary of microbubble compositions

Microbubble type	Abbreviation
Phospholipid Microbubbles (9:1 DSPC:PEG-40-Stearate)	PMBs
Microbubbles coated with Gold Nanoparticles	GMBs
Magnetic microbubble formulation 1 (DSPC with ferrofluid)	MMBs
Magnetic microbubble formulation 2 (Microbubbles coated with citric acid coated nanoparticles)	CAMMBs
Magnetic droplets mixed with non-magnetic microbubbles	MDMBs
Biotin expressing Microbubbles	BMBs
Magnetic microbubble formulation 3 (Microbubbles coated with lipid coated nanoparticles)	LMMBs
Charged magnetic microbubble formulation 3 (charged microbubbles coated with lipid coated nanoparticles)	CLMMBs

3.2.1.10 siRNA attachment

20 µl of siRNA oligo was added to the clear lipid solution. The solution was sonicated for 10s followed by sonication at the air water interface under SF_6 as described previously. The solution was then centrifuged (300 RCF, 10 min) in order to remove any excess siRNA. This was then analysed via fluorescence microscopy in order to determine if siRNA had successfully attached to the microbubble surface.

3.2.2 Optical analysis of microbubbles

Various methods for obtaining the size distribution and concentration of the microbubble suspensions were investigated. The buoyant and relatively fragile nature

of microbubbles makes them unsuitable for the majority of commercial particle sizing systems. The most reliable method for obtaining an accurate concentration and size distribution, as shown by Sennoga *et al,* was direct observation under an optical microscope combined with image processing relative to coulter counter/multisizer methods, photon correlation spectroscopy and laser diffraction [5]. Microbubble solution (10 µl) was added to a haemocytometer. This was then analysed via a Leica DM500 optical microscope (Larch House, Milton Keynes, MK14 6FG) using a 40 x objective lens.

3.2.2.1 Sizing software for bubble analysis

In order to obtain a representative size distribution for one batch of bubbles, at least 3 separate bubble samples must have 30 images taken via optical microscopy [5]. The bubble size distribution and concentration were then obtained using purpose written image analysis software in Matlab (2013b, The Mathworks, Natick, MA, USA) The software converts each micrograph to a binary images and single spheroid shapes are then located, measured and counted for each of the images analysed. A size distribution and count are then produced for the microbubbles. Since the dimensions of the haemocytometer and the microscope field of view are known, the volume concentration of microbubbles can also be estimated.

3.2.3 Fluorescence microscopy

3.2.3.1 Introduction

Fluorescence microscopy was used in order to investigate microbubble surface composition to determine: (i) the presence of biotin (ii) adsorption of droplets (iii) attachment of siRNA and also (iv) to detect whether fluorescent siRNA had been taken up by cells. A brief outline of the technique is given below and specific details will be provided in each chapter in which fluorescence microscopy is used (chapters 7 and 8).

3.2.3.2 Fluorescence microscopy

Fluorescence microscopy allows for observation of specific areas of interest in a specimen. Regions can be stained with fluorescent dyes or have fluorochromes inserted to visualise a specific feature or understand a function.

The sample is excited by a light source, normally a laser producing light of known wavelength and intensity. Part of the light is absorbed and re-emitted as fluorescence, i.e. at a longer wavelength than that of the incident light. An optical filter is used to block all light except that of the wavelength of interest. Any fluorescent material is thus seen as bright against a dark background. Comparison between fluorescence and phase contrast images indicates where the fluorophore is located in the sample [6]. For this study, qualitative fluorescence microscopy was used with images taken with a Leica DMI6000B fluorescence microscope (Larch House, Milton Keynes, MK14 6FG) using FITC settings (excitation wavelength of 490 nm and absorption of 525

nm) and a Nikon Ti fluorescence microscope (Kingston Upon Thames, Surrey, KT2 5PR) using the equivalent settings.

3.2.4 Transmission electron microscopy (TEM)

TEM was used to investigate the surface structure of individual microbubbles, for example to confirm incorporation of nanoparticles. 5ul of each microbubble solution was applied to a freshly glow-discharged carbon-coated copper grid and the grid was inverted for approximately 1 minute in order to allow a high concentration of microbubbles to remain in contact with the grid. The sample was then negatively stained with 2% w/v uranyl acetate. Samples were visualised at 80kV with an FEI Tecnai T12 electron microscope Low-dose images were acquired at ~0.8µm underfocus with 15e^-/Å on a high-sensitivity FEI Eagle 4096 x 4096 pixel CCD camera at a nominal magnification of x46000 which corresponded to a sampling size of 0.265 nm/pixel. On average 10 microbubbles were analysed for each sample. Microbubbles were only excluded if they appeared agglomerated such that one microbubble could not be differentiated from another. No other objects of the same size were observed in the solutions . This technique will be discussed in greater detail in chapter 4.

3.2.5 Zeta Potential

3.2.5.1 Introduction

Zeta potential measures the magnitude of the electrostatic repulsion or attraction between particles. This technique was used to assess the binding of siRNA to charged microbubbles in Chapter 8. An overview of the technique and the method is given below.

3.2.5.2 Overview

In order to measure particle charge an electric field is applied to the buffer/particle solution. The charged particle (e.g. microbubble or vesicle) will be surrounded by counter-ions in the solution and as such the electric charge will pull the charged particles in one direction but will also pull the counter-ions in the opposite direction. Some of the counter-ions will be strongly bound to the particle and as such will move with the particle, not towards the opposite charge. The "surface of shear" is where bound counter-ions separate from diffuse counter-ions and is some distance from the actual surface of the particle. The zeta potential is the electrostatic potential on the surface of shear. The measured charge will be a net charge taking the effect of counter-ions in the solution into account [7].

3.2.5.3 Technique

Measurements of lipid vesicles and microbubbles (separately) were performed via dynamic light scattering using a Zetasizer Nano-ZS, Malvern Instruments Ltd. (Worcestershire, UK) in a disposable capillary cell (DTS1070) from Malvern

Instruments Ltd (Worcestershire, UK). Each sample of the liposome or microbubble solution (60 µl) was added to 960 µl of 10% HEPES buffer and measured using the Jawalski protocol for up to 100 runs in order to produce an accurate zeta potential measurement.

3.2.6 Magnetic relaxivity

The different magnetic microbubble formulations were compared in terms of their magnetic relaxivity as this provides an indication of their responsiveness to a magnetic field. Measurements were performed using a Magnex 4.7T or 7.0T superconductive magnet driven by Varian DirectDrive™ spectrometer (Magnex Scientific and Varian Inc.; subsidiaries of Agilent Technologies, Santa Clara, CA, USA). A spin-echo sequence was used to acquire T_2 and T_1 maps. Single slice images were acquired with a matrix size of 128 x 128 pixels in all cases, corresponding to voxel dimensions of 0.4 x 0.4 x 5.0mm. T_2 maps were generated from a series of spin echo images (repetition time (TR) = 3.0s) in which the echo time (TE) was logarithmically distributed in 10 steps from 9.7ms to 100ms. The total experimental time was ~ 1 hour. T_1 maps were generated from a series of inversion recovery spin echo images (TR = 10.0s; TE = 9.7ms) in which the inversion recovery time was logarithmically distributed in 10 steps from 10ms to 6.0s. The total experimental time was ~ 3.5 hours. The relaxation maps were calculated using a standard mono-exponential fit employing a least squares procedure.

3.2.7 Magnetic targeting study

3.2.7.1 Introduction

Flow phantoms were designed and constructed in order to test the targeting ability of microbubbles in response to a magnetic field under different flow conditions.

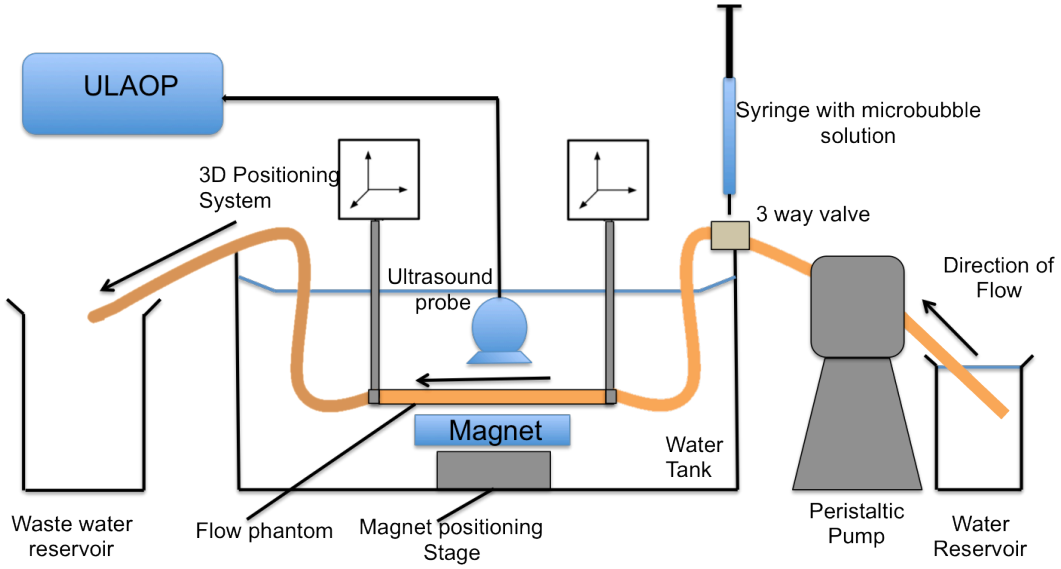


Figure 3-1, schematic of the flow phantom with the magnetic Halbach array inserted below

3.2.7.2 Overview

The equipment was set up as shown in Figure 3-1. The suspending liquid was pumped through a tube via a MINIPULS 3 peristaltic pump (Gilson, Middleton, WI, USA) from a reservoir. A three-way valve was inserted into the tube to allow microbubbles to be injected. The tube was submerged in a water tank and connected to the flow phantom. An outlet tube led from the phantom to a waste reservoir. The phantoms consisted of either latex tubes or cellulose capillary tubes according to whether ultrasound or optical imaging was used respectively. The flow phantom was

positioned above a magnetic array on a moveable stage. An ultrasound probe (9.4 MHz centre frequency LA523 microelectron. Syst. Design Lab., Univ. degli Studi di Firenze, Firenze, Italy) attached to an ultrasound engine (ULA-OP, microelectron. Syst. Design Lab., Univ. degli Studi di Firenze, Firenze, Italy) was positioned above the flow phantom in order to visualise the microbubbles flowing through. 9.4 MHz was chosen as the centre line frequency owing to the penetration depth of the magnetic field available (max 5 cm) limiting targeting to superficial targets in the clinic. As such a frequency used for target sites such as the breast and the carotid (5 – 10 MHz) was chosen [8]. Within 5 – 10 MHZ, 9.4 MHz centre line frequency also allowed best visualisation of microbubbles within the flow phantoms. For smaller tube diameters (200 μm) microbubble targeting was analysed using an optical microscope with a water immersion objective (LUMPLFLN 40XW Olympus Key Med Southend, Essex UK); giving 40x magnification when mounted on a World Precision Instruments microscope, H602-240, Sarasota, Fl, USA with a 10x eye piece). Videos were recorded of each experiment using a USB camera (DCU224M, Thorlabs). The magnetic field strength, vessel size and flow rate could be independently varied and experiments were performed for different combinations summarised below. Targeting was assessed through image analysis as described below.

3.2.7.3 Magnetic field strength

The magnetic field strength was varied by changing the distance from the surface of the magnet to the nearest wall of the flow phantom. The magnet used was a Halbach array consisting of 5 N52 grade NdFeB permanent magnets (10 mm x 10 mm x 25 mm, supplied by NeoTexx, Berlin, Germany) with transversal magnetisations (0.75

T) at angles of 90° from one to the next in the aluminium frame. The magnetic field gradient was 0.43 pN/mm (~55 T/m). An acoustic absorber was attached to the surface of the magnet of 5 mm thickness. Placing the magnet directly in contact with the flow phantom produced a magnetic field strength of 0.2 Tesla along the bottom of the vessel wall. Moving the magnet 1 cm away produced a magnetic field strength of 0.05 Tesla on the bottom wall and moving the magnet 2 cm below the phantom produced a field strength of 0.03 Tesla on the tube wall.

Three magnetic field strengths, corresponding to 0.2, 0.05 and 0.03 Tesla along the bottom of the flow phantom, were used for targeting in the 3 mm and 6 mm phantoms. 0.2 Tesla alone was used with the 1.6 mm flow phantom as no targeting could be observed at the lower magnetic field strengths. For the 200 μm capillary tube only one magnetic field strength could be applied as the tube would move towards the magnet and as such a maximum field strength of 0.2 T was applied.

3.2.7.4 Vessel sizes

For the experiments under ultrasound imaging 3 vessel sizes were used: A 6 mm (ID) vessel was used to mimic flow rates up to 400 ml/min corresponding those found in small arteries; a 3 mm (ID) vessel was used to mimic flow and shear rates found in veins and a 1.6 mm (ID) vessel was used to mimic shear rates found in venules/capillaries. 1.6 mm was determined to be the smallest inner diameter for which viewing was still possible with an ultrasound probe. To examine shear rates up to 1000/s, 200 μm cellulose capillary tubing was used. The vessel sizes used to not accurately represent vessel sizes found in the human body and are only used to mimic flow conditions.

In order to determine if the flow was laminar or turbulent the Reynolds' number was calculated using the following equation:

$$Re = \frac{QD_H}{\nu A} \quad 3.1$$

Where Q is the volumetric flow rate, and r is the radius of the flow phantom and D_H is the hydraulic diameter of the pipe, A is the cross sectional area of the flow phantom, ν is the kinematic viscosity (dynamic viscosity/density of the fluid). If the flow was found to be laminar the following equation was used in order to calculate the wall shear rate:

$$\gamma = \frac{4Q}{\pi r^3} \quad 3.2$$

The material used for the larger flow phantoms was latex, which has a reasonably similar acoustic impedance to water thereby allowing observation of the microbubbles flowing in the tube with minimal reflections from the walls [9]. Cellulose offered similar optical transparency for the microscope experiments

3.2.7.5 Flow conditions

The flow rate was caused by the number of rotations per minute of the peristaltic pump until a gravity feed was used. Starting conditions and the increase in flow rate are shown below.

In the 1.6 mm flow phantom experiments started at 0.1 ml/s and increased by 0.05 until magnetic targeting was no longer observed.

In the 3 mm phantom, experiments started at 0.09 ml/s and increased by 0.08 ml/s until magnetic targeting was no longer observed.

In the 6 mm diameter flow phantom, experiments started at 0.48 ml/s and increased by 0.05 ml/s until the gravity feed was used at 0.71 ml/s. The limiting flow rate of the gravity feed was 3.33ml/s.

In the 200 μm capillary tube flow conditions of 1.7 μl/s and 8.4 μl/s were analysed.

3.2.7.6 Ultrasound Image analysis

A purpose written Matlab script was used to estimate the concentration of bubbles retained in in each flow phantom[1]. Videos were recorded from each experiment using the ULAOP system. Each frame was then loaded into Matlab and processed to allow for the thresholding of microbubbles that have stuck. The image processing is as follows: An area of interest was selected along the bottom of the tube and along the top as a reference. The change in intensity was measured in both areas of interest and is plotted for each selected frame for the video. At the end of the video a plot of the change in intensity along the sides of the tube nearest and furthest from the magnet was produced. Criteria can then be assigned to check if targeting has successfully occurred. The intensity of the wall nearest the magnet must be a minimum of 5%

[1] This software was written by Paul Rademeyer who is gratefully acknowledged.

higher than the intensity of the wall opposite to the magnet for over 1000 frames in order for targeting to be considered successful.

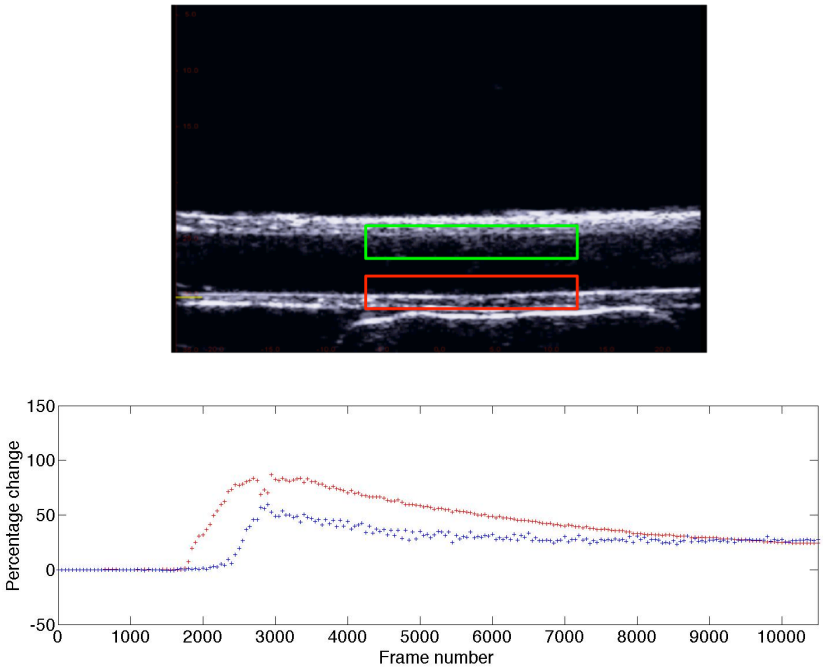


Figure 3-2, Ultrasound image of latex tube (6 mm ID) with a magnetic Halbach array positioned beneath. 2 areas of interest have been highlighted in red and blue. The change in intensity over time is then plotted on a graph shown below.

3.2.8 Acoustic response and targeting

For magnetic microbubble formations the acoustic response and targeting ability was measured using the set up outlined above. The flow phantom was set up as shown in Figure 3-1. With water flowing through the phantom at a set flow rate of 0.25 ml/s a video was recorded as a baseline. Magnetic microbubbles were then injected, the flow was started and a video was recorded over approximately 2 min. This process was repeated three times. The Halbach array was then inserted underneath the phantom and the same methods as outlined above were used to analyse the videos to determine if targeting had been successful.

3.2.9 Targeting against blood flow

In order to examine the effect of blood on the targeting efficiency of magnetic microbubbles the water in the reservoir was replaced with whole heparinised porcine blood. A full targeting analysis was only performed in the 1.6 mm flow phantom via the method outlined above. However as the impact of flowing blood had never been analysed on microbubble targeting a comparison between magnetic and biochemical targeting was performed. The methods for quantification of microbubble targeting in this study are outlined below.

3.2.9.1 Experimental set up

The flow phantom was set up as outlined for the 200 μm capillary tube highlighted above. The end of the capillary tube was inserted into a reservoir (500 μl) filled with either blood or PBS (450 μl) and bubble solution made up in PBS (50 μl) at a concentration of 10^8 microbubbles/ml. The syringe was set on withdraw and the blood or PBS was taken up at 10 μl/min. In a 200 μm capillary tube the shear rate is 212/s calculated using the equation above.

For Biotin coated microbubbles an avidin and a non-avidin coated tube were used and bubbles being held out of the flow observed over a period of approximately 4 minutes. The tube was coated in avidin by passing PBS with avidin (10 mg/ml) through the capillary tube, incubating for 30 min, followed by washing three times with PBS. The avidin has been previously shown to adsorb onto cellulose non-covelently [10]. Attachment of avidin to cellulose was confirmed using avidin bound

to FITC and examination by a Leica DMI6000B fluorescence microscope (Larch House, Milton Keynes, MK14 6FG) using FITC settings (excitation wavelength of 490 nm and absorption of 525 nm). Magnetic microbubbles were drawn through the capillary tube with and without a magnetic field (field strength of 0.2 T and gradient 0.43 pN/mm at the capillary wall) applied. Each experiment was performed 3 times and the results analysed in order to count the number of microbubbles retained against flow.

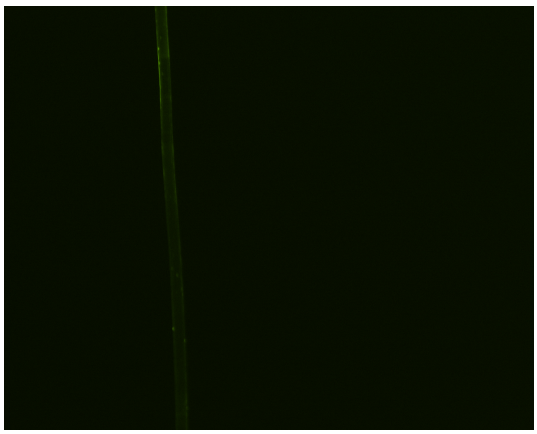


Figure 3-3, image of capillary tube (200 µm ID) after being exposed to FITC avidin for 30 minutes fluorescing against the background (600 ms, Gain 1).

3.2.9.2 Magnetic microbubbles quantification

The number of magnetic microbubbles retained was measured from the images by dividing the area of the magnetic bolus by the average cross-sectional area of a magnetic microbubble to estimate the number of microbubbles successfully targeted. It is recognised that the method of quantification will produce an underestimate of the number of targeted microbubbles as the image analysis was only performed in the focal plane. Since all measurements were relative however and the focal plane was

maintained between experiments this would not have affected the reduction owing to the effect of blood.

3.2.9.3 Biotin bubbles targeting quantification

A purpose written Matlab script estimates the amount of retention in a capillary tube as seen under a microscope[2]. Videos were recorded of each experiment using a USB camera (DCU224M, Thorlabs). Each frame was then loaded into Matlab and processed to allow for the thresholding of microbubbles that are adherent in the focal plane. The image processing was carried out as follows: 1) Image contrast is enhanced using contrast-limited adaptive histogram equalization (CLAHE), 2) the dynamic range is adjusted to an empirically set high level, 3) finally objects are classified using a binary threshold and Matlab's object analysis toolbox, too small objects are discarded and any holes are filled. An example of this is shown in Figure 3-4.

[2] This software was written by Paul Rademeyer.

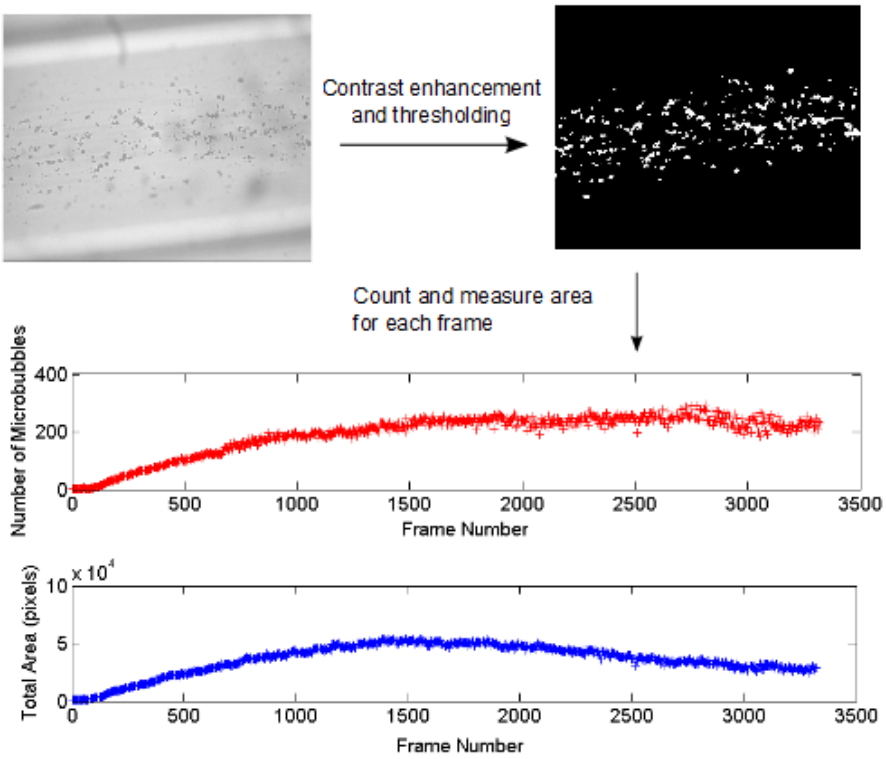


Figure 3-4, example of the image processing showing the contrast enhancement and thresholding and final data output

3.2.9.4 Non linear response

This experiment was designed to test if new magnetic microbubble formulations could be observed via contrast mode on a clinical ultrasound imaging platform. The equipment was set up in a similar manner to Figure 3-1 except no magnetic field was applied, and a Siemens Acuson S3000 imaging platform with a 9L4 Linear transducer at an MI of 0.07 using Cadence software CPS at a frequency of 4 MHz at 25 fps was used to observe the microbubbles. B-mode and Contrast were observed side by side. Flow was produced by a gravity feed rather than a peristaltic pump. Microbubbles were injected into the 3 mm flow phantom via the 3 way junction, flow was started and a video recorded.

3.2.10 Liver perfusion study

3.2.10.1 Perfusion set up

An extracorporeal normothermic liver perfusion device, that was developed for organ preservation prior to transplantation and which can maintain a liver in a functional state for in excess of 72 hours *ex vivo*, was used to provide a haemodynamically, physiologically-relevant model [11, 12]. A porcine experimental liver model was used due to its similarities with the human liver and because it is widely accepted as the most appropriate preclinical liver model [13]. 70 % of all microbubbles will be cleared by the liver and so the aim of these experiments was not targeted delivery to the liver [14]. The liver was meant to provide an *in vivo* environment to target magnetic microbubbles against a vessel wall. The blood vessels in the liver have a more clinically relevant structure than latex tubes and cellulose capillary tubes for observation of targeting on a human scale.

The liver was removed from the pig as described in the literature [15]. Heparin (20, 000 Units; CP Pharmaceuticals, UK) was administered to the pig intravenously. The pig liver was cold perfused with hyperosmolar citrate solution (Soltran; Baxter, UK). The liver was removed and placed in a bowl of saline ice slush. The portal vein and the hepatic artery were cannulated with 20 Fr and 10 Fr cannulae respectively (Sorin, Italy), and the common bile duct was cannulated with a Heidelberger extension set (B Braun, UK), placed in an intestinal bag and cool box for transportation to the laboratory. Normothermic perfusion was performed using a perfusion system. Using a perfusion circuit (Figure 3-5) that incorporated a hollow-fibre membrane

oxygenator (EOS ECMO PHISIO M; Sorin, Italy), a centrifugal pump (BPX80; Medtronic, USA) and a soft-shell reservoir (Capiox 1500; Terumo, USA). Two heat exchangers maintained the blood at 38 °C. The circuit was primed with approximately 1500 mL of autologous whole blood, heparin anticoagulation (10,000 Units; CP Pharmaceuticals, UK), calcium gluconate (10 mL of 10%; Braun, UK) and cefuroxime (750 mg; Glaxo-SmithKline, UK) which was circulated through before the liver was attached in order to reach the correct temperature. The liver, suspended in a silicone sling over a stainless steel bowl, was connected to the perfusion circuit (Figure 3-5) and perfusion was initiated with a progressively increasing pump speed over a few minutes until an IVC pressure of 0−5 mmHg was achieved. Ascites produced by the liver were collected in the stainless steel bowl and recirculated automatically via a peristaltic pump (Watson Marlow, Falmouth, UK) [15].

Following 30 minutes of normothermic machine perfusion, the ascites recirculation was stopped, the stainless steel bowl was removed from under the liver and the liver was placed in an acoustically transparent 50 x 50 cm sterile intestinal bag (3M, USA) filled with isotonic colloid solution 9 (Gelofusine, Braun, UK), which had been degassed and pre-heated to 37 °C. The bag was suspended in a silicone sling over a water bath containing an acoustic absorber in the base, which was continuously degassed and heated to 37 °C. A vessel was located using an ultrasound probe (model L10-5; Zonare Medical Systems, Mountain View, CA, USA) and a Zonare z-one (Zonare Medical Systems, Mountain View, CA, USA) ultrasound engine and a magnetic Halbach array was inserted underneath. The ultrasound probe was held in position with a clamp. A needle was then inserted directly into the vessel. The magnetic microbubbles were then injected directly into the vessel and observed using

ultrasound. Videos were recorded for 30 second bursts using the Zonare. Approximately 3 livers were examined and magnetic microbubbles were injected directly into a vessel or into the perfusion system supplying the liver with blood. For the second and third liver, blood flow was stopped and magnetic microbubbles were injected directly into a selected vessel.

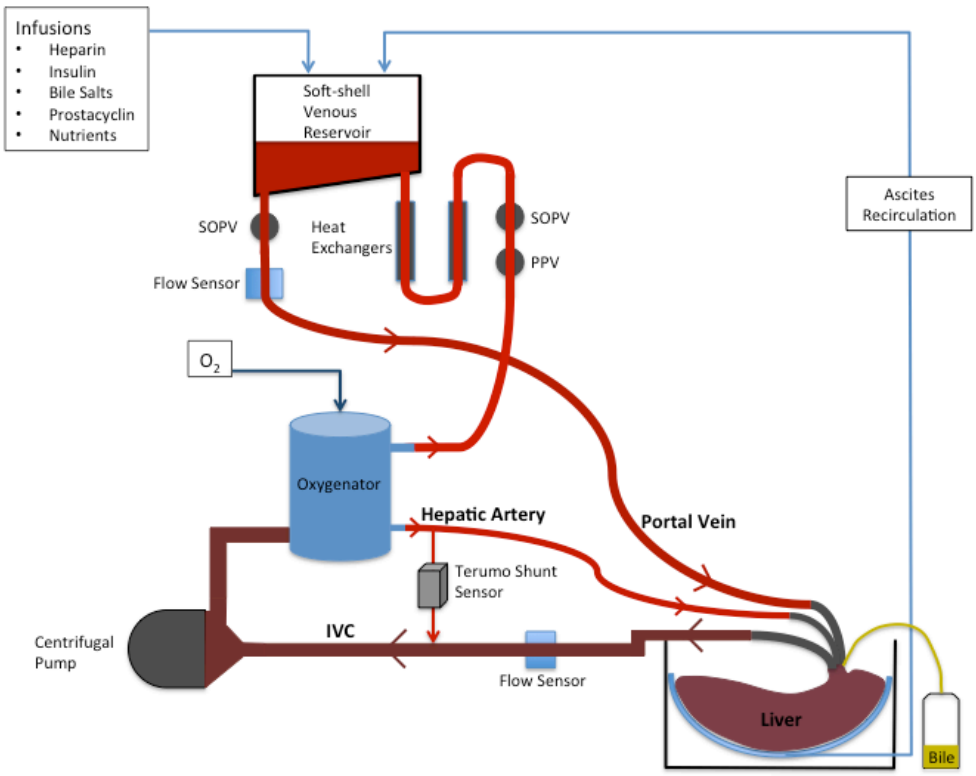


Figure 3-5, Schematic of the liver perfusion machine to maintain oxygenated blood flow. This image was taken from unpublished material kindly provided by David Holroyd [15].

One limitation of this study is that the liver contains Kupffer cells which have previously been shown to be responsible for the hepatic clearance of the microbubble Sonazoid [16]. The liver, along with the kidney and the lungs are responsible for microbubble removal in the body within 10 -15 minutes and as such the liver is not a viable organ for targeted therapy [14]. However, this is true for clearance of microbubbles systemically delivered and in these experiments microbubbles are injected directly into a vessel. Only microbubbles in the vessel observed via

ultrasound were examined for targeting potential and magnetic microbubbles were compared with non-magnetic microbubbles so any difference in targeting potential can be attributed to the magnetic field and not kupffer cells.

3.2.11 siRNA delivery

3.2.11.1 Cell culture

SY5Y Cells were used initially as a model cell line on account of their rapid replication rate and ability to be transfected using viral methods. The cells were cultured in flasks using Phenol free DMEM media with FCS and antibiotics. When the cells were at confluence they were trypsinised, centrifuged and distributed between Opticells (Thermo Fisher Scientific, Bishop Meadow Road, Loughborough, UK) in phenol free DMEM media. This gave a concentration of 1.5 $x10^7$ cells per Opticell. These were allowed to reach confluence overnight in an incubator at 37 ^oC. These cells were then taken for experiments as outlined in Chapter 8.

3.2.11.2 Ultrasound set up

The ultrasound equipment was set up as shown in Figure 3-6. An Opticell was inserted into the positioning system and the ultrasound probe was used to align a HIFU transducer with the centre of the Opticell on the bottom plate. The cells were grown on the bottom plate of the Opticell in order to be in close proximity to the magnetic field. From this six positions for insonation equispaced on the surface of the Opticell were located. The magnetic Halbach array was then inserted approximately 1 mm below the Opticell. This platform could be detached and replaced with a non magnetic metal block used to maintain an equivalent sound field.

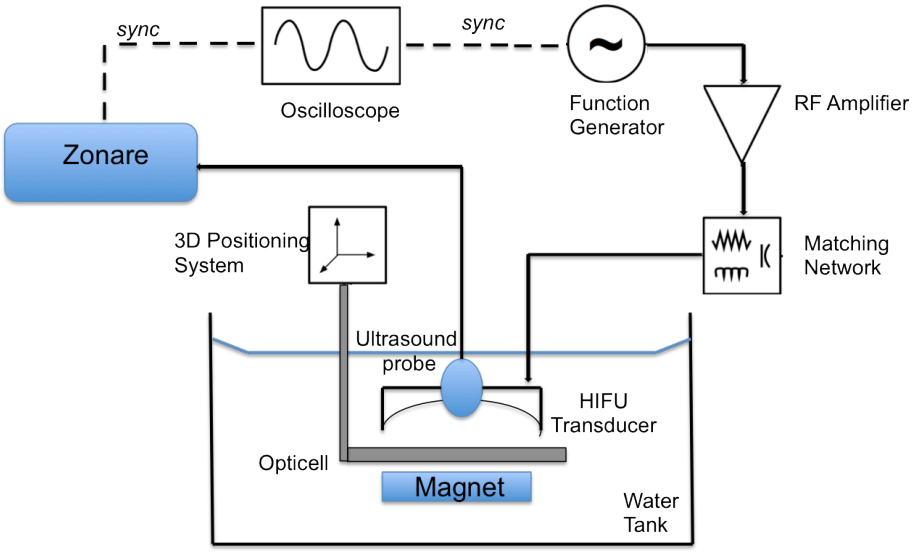


Figure 3-6, Equipment set up for magnetic and ultrasound exposure of the Opticell plates.

3.2.11.3 Opticell set up

After preparation of the siRNA loaded bubble suspension, 1 ml was added to an Opticell cell culture device with a confluent layer of cells on one membrane. This was kept dispersed and the Opticell was placed in a water tank at 37 C. Six spots were selected on the Opticell as shown in Figure 3-7. The first plate was left in the water bath for 10 minutes with the magnet removed. The second plate had each spot experience a magnetic field strength of (0.5 T). The third plate had each spot experience a magnetic field strength of (0.5 T) followed by 1 MPa (peak to peak) ultrasound at 0.5 MHz, 1 kHz pulse repetition frequency at 40s duty cycle for 10 seconds. These conditions were chosen based upon the results of Rahim et al and Stride et al and adapted in order to incorporate an ultrasound probe [3, 17]. These ultrasound conditions were repeated on six spots for plate 4 in the absence of a magnetic field but with a non magnetic metal block below the Opticell in order to keep the sound field the same. No acoustic absorber was used. All plates were then

left in the incubator for approximately 1 hour. The media with bubbles was then removed. The Opticell was washed with media (10 ml) followed by addition of media (15 ml) into the Opticells. These were then analysed via fluorescence microscopy and an automatic plate reader (described below) on the same day.

3.2.11.4 Ultrasound field calibration

The free-field focal pressure and beam profile of the HIFU transducer were calibrated in water using a 400μm diameter needle hydrophone (model Onda 1056; Onda Corporation, Sunnyvale, CA, USA). Pressure values referred to subsequently are peak negative focal pressures (PNFP)[3].

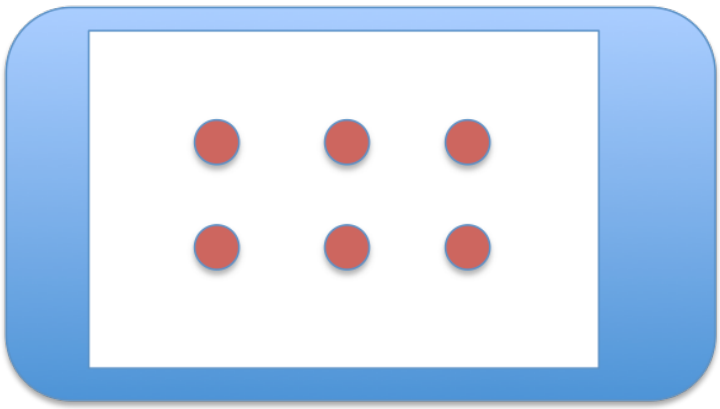


Figure 3-7, diagram of Opticell showing the insonation positions.

3.2.11.1 Fluorescence measurements

Fluorescence images were obtained on a Nikon Ti Fluorescence microscope using the FITC settings. Bubbles placed in an Opticell were analysed in order to determine the

[3] This calibration and assistance with operating the ultrasound system was provided by Calum Crake and is gratefully acknowledged.

conditions under which the fluorescent siRNA could be observed. Cells were examined at the same conditions in order to ensure a difference in fluorescence intensity existed. The final conditions used were 2s exposure, gain of 1. Brightfield images were also taken at exposure of 363 ms and gain of 1.

3.2.11.2 Large image analysis

In each area exposed to ultrasound brightfield (10 x) and FITC images were captured at the same location. A large stitched image of 5 mm by 5 mm was obtained at each spot in the Opticell. The maximum fluorescence intensity was then determined for each insonation spot.

Each fluorescence image was analysed in ImageJ in order to obtain an intensity histogram. The maximum intensity in the image was then recorded. For each plate an average and a standard deviation of the maximum intensities was obtained.

3.2.11.3 Plate reader experiments

The Opticells were placed in the BMG Labtech FLUOstar Omega and read using the FITC Opticell setting. Each run took 14 minutes and 22 seconds. The fluorescence intensity of the whole plate was then analysed.

3.3 References

1. Mei, H., Z.Y. Lin, and Q.S. Tong, *The roles of microRNAs in neuroblastoma.* World Journal of Pediatrics, 2014. **10**(1): p. 10-16.
2. Studart, A.R., et al., *Metallic foams from nanoparticle-stabilized wet foams and emulsions.* Journal of Materials Chemistry, 2012. **22**(3): p. 820-823.

3. Stride, E., et al., *Enhancement of Microbubble Mediated Gene Delivery by Simultaneous Exposure to Ultrasonic and Magnetic Fields.* Ultrasound in Medicine & Biology, 2009. **35**(5): p. 861-868.
4. Feshitan, J.A., et al., *Microbubble size isolation by differential centrifugation.* Journal of Colloid and Interface Science, 2009. **329**(2): p. 316-324.
5. Sennoga, C.A., et al., *On sizing and counting of microbubbles using optical microscopy.* Ultrasound in Medicine and Biology, 2010. **36**(12): p. 2093-2096.
6. Dost, F.W.D., *Fluorescence microscopy*. Vol. 1. 1992-1995: Cambridge University Press 1992-1995.
7. Malvern, *Zetasizer nano series user manual*. 2009: Malvern.
8. Farr R., F. and J. Allisy-Roberts P., *Physics for Medical Imaging*. 2005: Saunders.
9. Whitmore, R.L., *The flow behaviour of blood in the circulation.* Nature, 1967. **215**(5097): p. 123-126.
10. Orelma, H., et al., *Generic method for attaching biomolecules via avidin-biotin complexes immobilized on films of regenerated and nanofibrillar cellulose.* Biomacromolecules, 2012. **13**(9): p. 2802-2810.
11. Butler, A.J., et al., *Successful extracorporeal porcine liver perfusion for 72 hr1.* Transplantation, 2002. **73**(8): p. 1212-1218.
12. Brockmann, J., et al., *Normothermic Perfusion: A New Paradigm for Organ Preservation.* Annals of Surgery, 2009. **250**(1): p. 1-6 10.1097/SLA.0b013e3181a63c10.
13. Court, F.G., et al., *Segmental nature of the porcine liver and its potential as a model for experimental partial hepatectomy.* British Journal of Surgery, 2003. **90**(4): p. 440-444.
14. Quaia, E., *Microbubble ultrasound contrast agents: An update.* European Radiology, 2007. **17**(8): p. 1995-2008.
15. Holroyd DJ, et al. *Effects of Perfusion on Thermal and Cavitational Characteristics of HIFU Therapy Using a Novel Normothermic, Extracorporeal Liver Perfusion Model,* . in *International Society for Therapeutic Ultrasound*. 2012. Heidelberg.
16. Kindberg, G.M., et al., *Hepatic clearance of Sonazoid perfluorobutane microbubbles by Kupffer cells does not reduce the ability of liver to phagocytose or degrade albumin microspheres.* Cell and Tissue Research, 2003. **312**(1): p. 49-54.
17. Rahim, A., et al., *Physical parameters affecting ultrasound/microbubble-mediated gene delivery efficiency in vitro.* Ultrasound in Medicine and Biology, 2006. **32**(8): p. 1269-1279.

4 Transmission electron microscopy

4.1 Summary

The characterization techniques outlined in Chapter 2 do not provide sufficient information about microbubbles on the nanoscale. Thus the structure of the bubble coating, the location and concentration of nanoparticles still remain largely unknown. Understanding of these, however, is extremely important for predicting the stability and both the acoustic and magnetic response of microbubbles. Nano scale information also has the potential to improve techniques to encapsulate or attach therapeutic material to the microbubble surface. This chapter outlines a new technique developed by the candidate using electron microscopy to view the surface of the microbubble on the nanoscale.

4.2 Introduction

Conventional light microscopes are limited by diffraction to studying structures larger than ~1μm, which corresponds to a maximum useful magnification up to ~2000x. The small de Broglie wavelength of an electron beam, as compared to the visible light used in optical microscopes, allows for much higher spatial resolution and hence magnification (up to 10, 000, 000x) for visualizing objects on the nanoscale. The transmission electron microscope (TEM) uses electrostatic and electromagnetic lenses to control the electron beam and focus it to form an image. These are analogous to the glass lenses of an optical microscope. In transmission electron microscopy the electrons pass through an ultrathin specimen interacting with the sample to form an image. This image is then magnified and focused onto a fluorescent plate or camera. The scanning electron microscope (SEM) differs from TEM as it examines a

rectangular area with a focused electron beam. The interactions of the electrons with the specimen causes energy loss since energy is converted into other forms such as heat and light or X-ray emission all of which can be analysed to gain information about the properties of a specimen surface. At the simplest level TEM examines the internal structure of thin specimens and SEM is used to study the surface of bulk specimens [1]. Unfortunately, however, examination using an electron beam will often damage the sample. Even if the accelerating voltage is sufficiently low to avoid direct damage, samples must be coated with e.g. a thin layer of carbon or gold and placed in a vacuum in order for the electrons to interact with it. This is particularly problematic for studying microbubbles, which having a gaseous core, cannot retain structural integrity under vacuum. A number of different methods were therefore explored in this study to overcome this limitation.

4.3 Preliminary experiments

To investigate the internal structure of magnetic microbubbles on the nano scale, a preliminary freeze fracture Scanning Electron Microscope (SEM) study was conducted. The sample was fixed and dehydrated, then frozen and fractured and the resulting sections taken and analysed via SEM [2], the images from which are shown in Figure 4.1. An object similar to a multilamellar vesicle on the micro scale with nanoparticles within can be seen in panel A. The multilamellar surface and the nanoparticles can be seen in B more clearly. The size of the object is of a similar size to a microbubble and it could be a compressed/deformed microbubble or vesicle. In all the images, tiny white dots can be seen which could be replicas of iron oxide nanoparticles, in different stages of agglomeration stabilised and coated by phospholipid [3]. In images C and D vesicle structures with a roughly hexagonal

pattern on the surface can be seen. Similar patterns have been reported by Borden *et al.* and are thought to be due to lipids forming domains [4] which would be expected given the range of chain lengths in L-α-phosphatidylcholine. Please see Chapter 2 (section 2.6.2) for more information on domains.

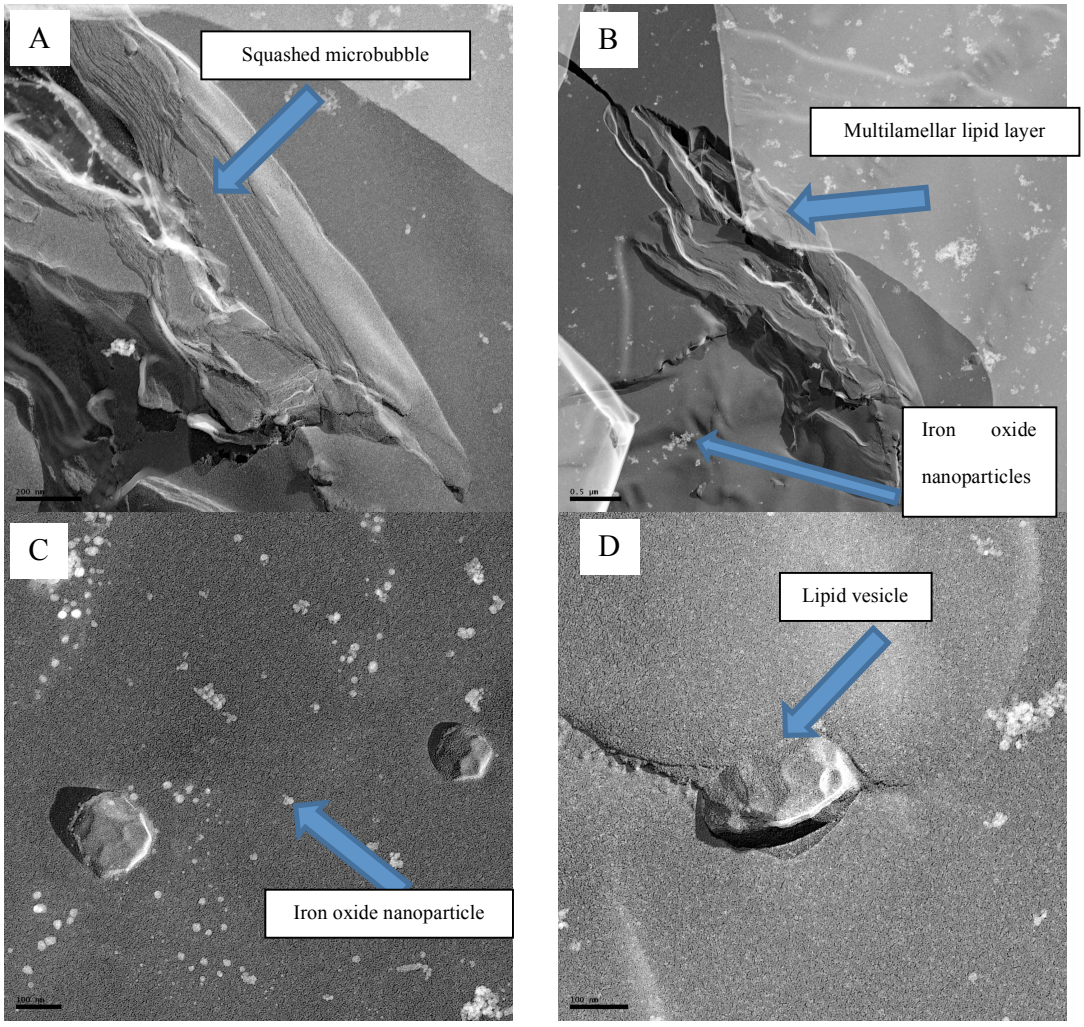


Figure 4.1, freeze fracture SEM images of magnetic microbubbles. The images are impressions so the white patches are most likely to be iron oxide nanoparticles. A) shows what could be a collapsed magnetic microbubble or vesicle with a multilamellar coating (scale bar 200 nm), as seen clearly in B), and nanoparticles within (scale bar 500 nm). C and D show what appear to be micelles with interesting structural formulations on the surface (Scale bars 100 nm).

Whilst these initial SEM images provided some information regarding microbubble structure, the microbubbles could not be observed clearly and/or appeared to have lost structural integrity. Thus any information obtained was rather inconclusive. A more robust alternative method was required.

4.4 Low temperature transmission electron microscopy (LTTEM)

LTTEM refers to the electron microscopy examination of specimens maintained at sub-zero temperatures (<130K) as thin suspensions or sections in order to reduce beam damage and reduce the need for fixatives. It is possible to vitrify thin layers of water spread on electron microscope grids by rapid immersion into liquefied ethane. This technique, called plunge freezing is one of the most popular used to study biological samples [5]. LTTEM allows for unfixed, unstained, hydrated samples and permits high resolution substructural and low resolution suprastructural investigations to be carried out. For magnetic microbubbles, incapable of surviving in the vacuum found in electron microscopes, it was hoped that being frozen in water and sectioned would allow the microbubble to remain intact.

Suspensions of microbubbles were pipetted on to a copper grid, then plunged into liquidified ethane for approximately 5 minutes. They were removed from the nitrogen and examined in the electron microscope using a specially cooled stage to maintain the sample at 130 K.

4.4.1 Preliminary Results

Results from the LTTEM indicated that the microbubbles were present but had been extruded from the ice. This is shown below in Figure 4.2 where circular holes can be observed but no remains of microbubbles or bubble material. The grid holes can be observed inside the larger holes produced by the microbubbles. The microbubble suspension appeared to have been successfully frozen. However, when entering the vacuum inside the microscope the microbubble structure collapsed and nothing remained to be analysed. A third microscopy technique was therefore investigated with the hope that it would enable microbubbles to survive the vacuum conditions intact.

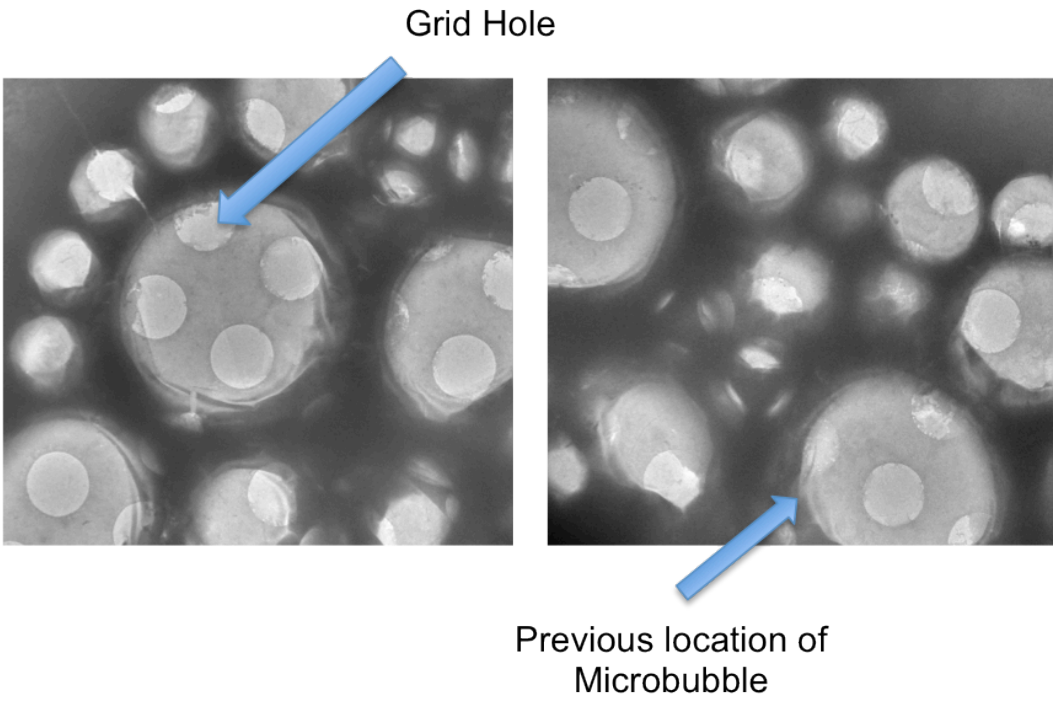


Figure 4.2, low temperature electron microscopy images of phospholipid microbubbles prepared via plunge freezing. The central microbubble is approximately 8 µm in diameter. The microbubbles appear to have been destroyed and only holes where they existed remain.

4.5 Uranyl Acetate Coating for Electron Microscopy

Staining with heavy metal ions has been widely used for imaging tissue in electron microscopy. The contrast between different features is directly related to the difference between the surface density (mass per unit area) of the object of interest and the surrounding embedded material. Hence heavy metals provide a means of increasing variations in surface density [6]. In this study however, the heavy metal stain was used to impart additional stability to the microbubble coating to allow the structure to remain intact under vacuum.

Uranyl acetate is widely used to examine liposomal structures and was therefore selected for this work [7]. For microbubbles however, the staining technique had to be adapted. The buoyancy of the microbubbles was exploited in order to confine and concentrate them against the microscope grid. The coating of uranyl acetate was then applied to the inverted grid. To the best of the candidate's knowledge this is the first time microbubbles have been successfully visualized intact under TEM[1].

4.5.1 Microbubble preparations

Several different types of microbubble were prepared for examination. Phospholipid microbubbles based on those commonly used as ultrasound contrast agents were analysed first. After successful examination of the structure of phospholipid microbubbles, contrast agents with nanoparticles attached to the surface were studied by a variety of methods in order to observe the difference. Bubbles analysed were phospholipid microbubbles (PMBs), Gold coated microbubbles (GMBs), Magnetic microbubble formulation 1 (MMBs), Magnetic Microbubble formulation 3 (LMMBs)

[1] The assistance of Alistair Siebert in operating the electron microscope and acquiring the images is gratefully acknowledged.

and magnetic droplets and microbubbles (MDMBs). Please see Chapter 3 for details of preparation methods.

4.6 Initial characterisation

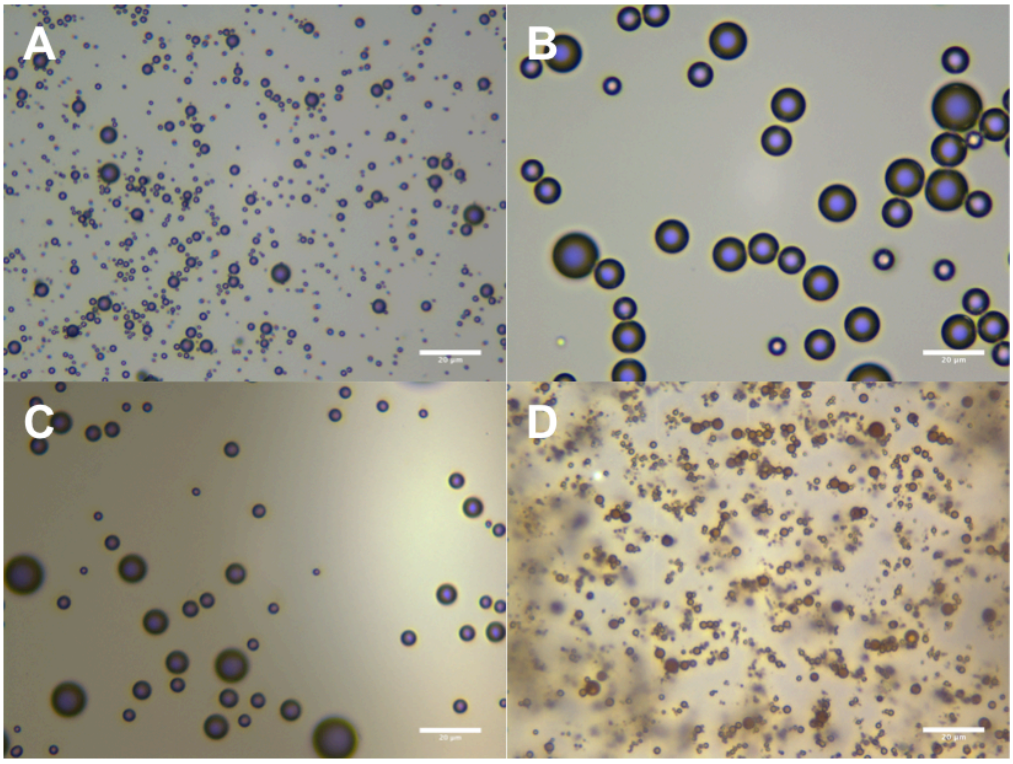


Figure 4.3, optical microscopy (bright field) images of microbubbles at 400 x magnification. A) Phospholipid microbubbles (PMBs), B) Gold microbubbles (GMBs), C) Magnetic microbubble formulation 3 (LMMB) and D) magnetic microbubble formulation 1 (MMB). Scale bar represents 10 µm.

All microbubble formulations were observed via optical microscopy (Figure 4.3) in order to ensure microbubbles had been successfully created. Concentrations and size distributions were obtained in order to confirm similar sized microbubbles were observed under TEM. Microbubbles (PMB) and magnetic microbubbles with

ferrofluid (MMB) both had modal average sizes below 2 μm, Magnetic microbubbles with nanoparticles (LMMB) had a modal size of 4 μm and gold coated microbubbles showed the largest modal size of 8 μm. The size distributions vary as addition of nanoparticles to the microbubble shell appear to increase the average size of the microbubbles produced. The reasons for this are unclear but ferrofluid does not appear to cause this phenomenon.

Table 4.1, Concentration of different microbubble formulations prepared for analysis by electron microscopy

Microbubble	Concentration (bubbles/ml)
Phospholipid (PMB)	1.13×10^9
Gold coated (GMB)	2.35×10^7
Magnetic formulation (MMB)	1.66×10^9
Magnetic formulation 3 (LMMB)	4.83×10^7

The trend in size was reversed with respect to concentration, with microbubble suspensions having a larger mean size having a corresponding lower concentration. This can clearly be observed in Table 4.1 in which gold coated microbubbles and magnetic microbubble formulation 3 had approximately 10^6 microbubbles per ml, whereas phospholipid microbubbles and magnetic microbubble formulation 1 has over 10^8 microbubbles per ml. This may be due simply to the fact that there is only a finite quantity of phospholipid and gas in the precursor solution and hence a limit on the number of microbubbles that can be produced. If more larger microbubbles (>10 μm) are produced the concentration will be lower relative to a sample with more

smaller microbubbles (<10 μm). In all cases, microbubbles were produced in sufficient concentration to be analysed via both optical and electron microscopy.

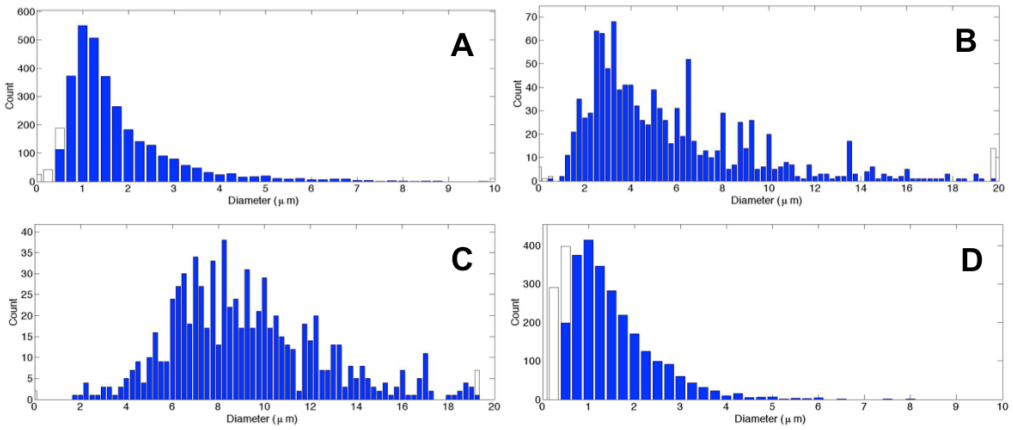


Figure 4.4, size distributions of microbubbles from optical microscope images showing distributions for A) Phospholipid microbubbles B) Magnetic microbubble formulation 2, C) Gold microbubbles and D) Magnetic microbubble formulation 1.

4.6.1 Phospholipid microbubbles

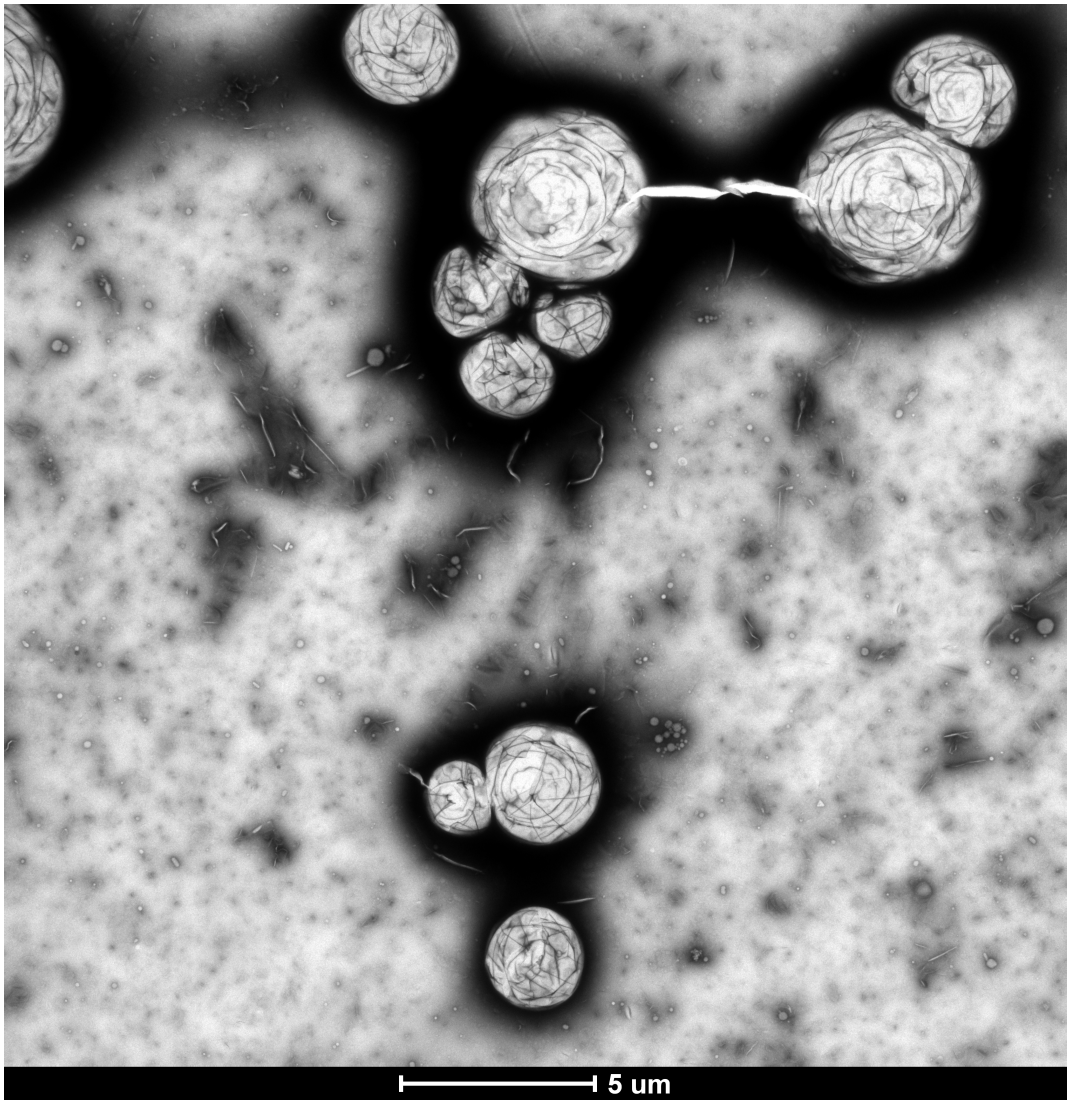


Figure 4.5, Electron microscopy images of phospholipid microbubbles after coating with uranyl acetate showing the intact structure of the microbubble.

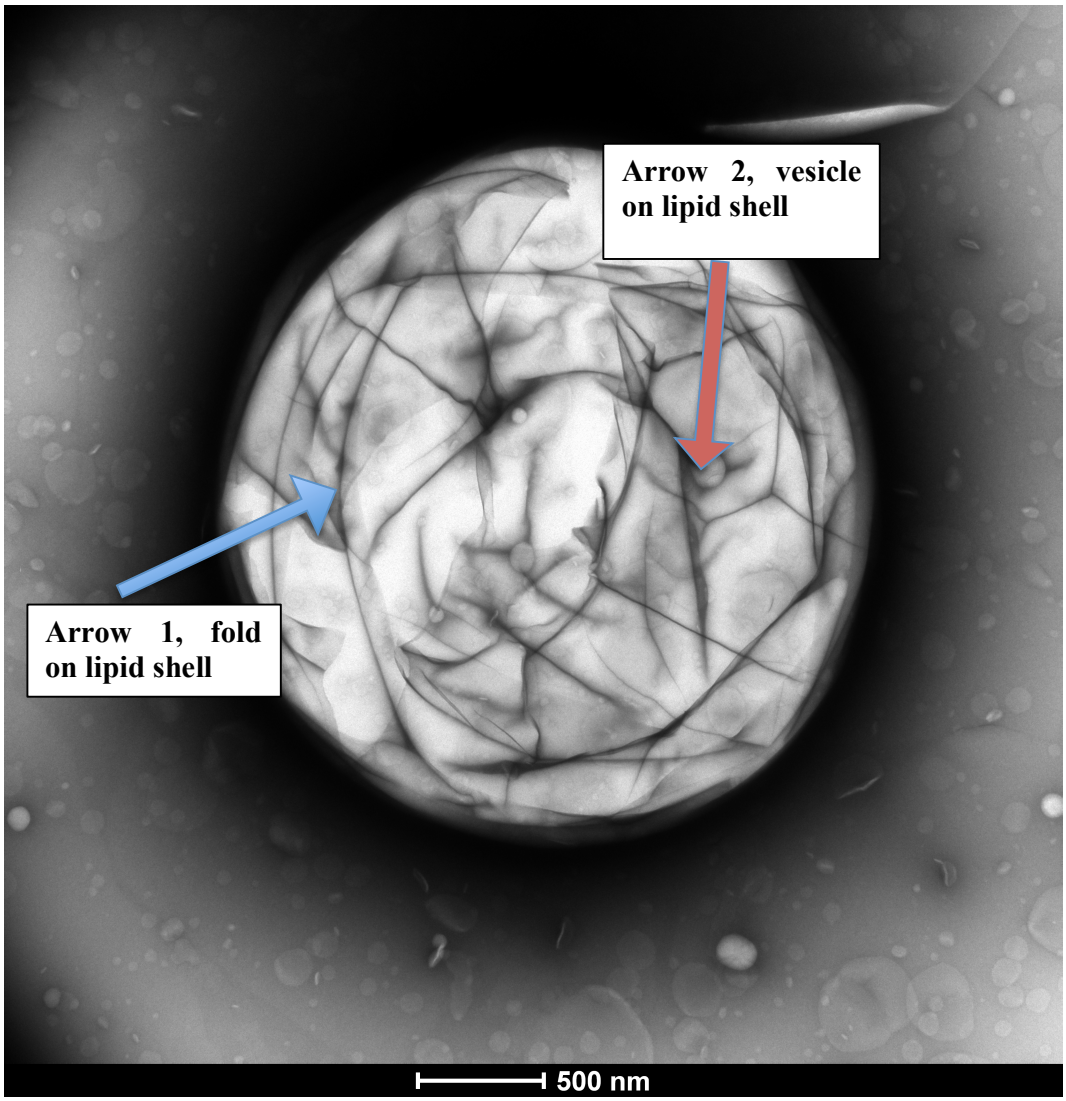


Figure 4.6, higher magnification image of a phospholipid microbubble showing vesicles on the surface.

Under electron microscopy, spherical crumpled objects approximately 1 – 4 μm diameter were observed. This was the expected size range for phospholipid microbubbles and optical microscopy revealed no other objects in the solution of that size. This indicates that microbubbles in the clinically relevant size range (<8 μm) were able to survive uranyl acetate processing and undergo direct observation in the electron beam. Examples of 9:1 DSPC:PEG 40 Stearate microbubbles are shown in Figure 4.5.

In Figure 4.6 the lipid coating can clearly be observed and vesicle like objects appear to be attached to the surface. This could be a reversible phenomenon or the vesicles could be bound to the surface as has been shown in previous research [8]. The microbubble appears to be crumpled with large lines or folds across the surface where stain has been excluded, but the shell remains intact (Figure 4.6 Arrow 1). Lipid vesicles on the microbubble surface appear to be at the same position as the lines/folds as indicated by Figure 4.6 Arrow 2. Faint spherical objects can also be observed on the surface in a variety of sizes. These are likely to be lipid vesicles incorporated into the shell during the sonication process. Domains, as seen by Kim *et al*. [9] and Borden *et al*. [4] on large bubbles were not observed on any microbubble surface for this phospholipid/emulsifier formulation, indicating that these do not necessarily form on small microbubbles (<2 μm). The formulation used for phospholipid microbubbles was identical to that used by Borden *et al.* and similar to that of Kim *et al.* with the exception of the fluorophore.

In addition, this image provides a useful example of a microbubble structure which can be compared with microbubble formulations incorporating nanoparticles to determine how they distribute and/or change the surface structure of microbubbles.

4.6.2 Gold Coated microbubbles

Figure 4.7 shows microbubbles prepared from the suspension of gold nanoparticles and phospholipid with diameters between 5 and 20 μm. Again vesicles can be observed having adhered to the surface of the gold microbubbles in the same manner

as for the phospholipid microbubbles. Folds can be observed on the surface where stain has been excluded but the microbubble has not crumpled to the same extent. This could be caused by the larger size of the gold microbubbles (5 – 20 μm), relative to the phospholipid microbubbles (1 – 4 μm) and as such the folds are not as pronounced in the images and appear smaller, or the increased stiffness of the microbubble owing to the gold nanoparticles incorporated in the shell. Unlike phospholipid microbubbles, gold coated microbubbles appear to have structures similar to lipid domains and grain boundaries on partial sections of the surface.

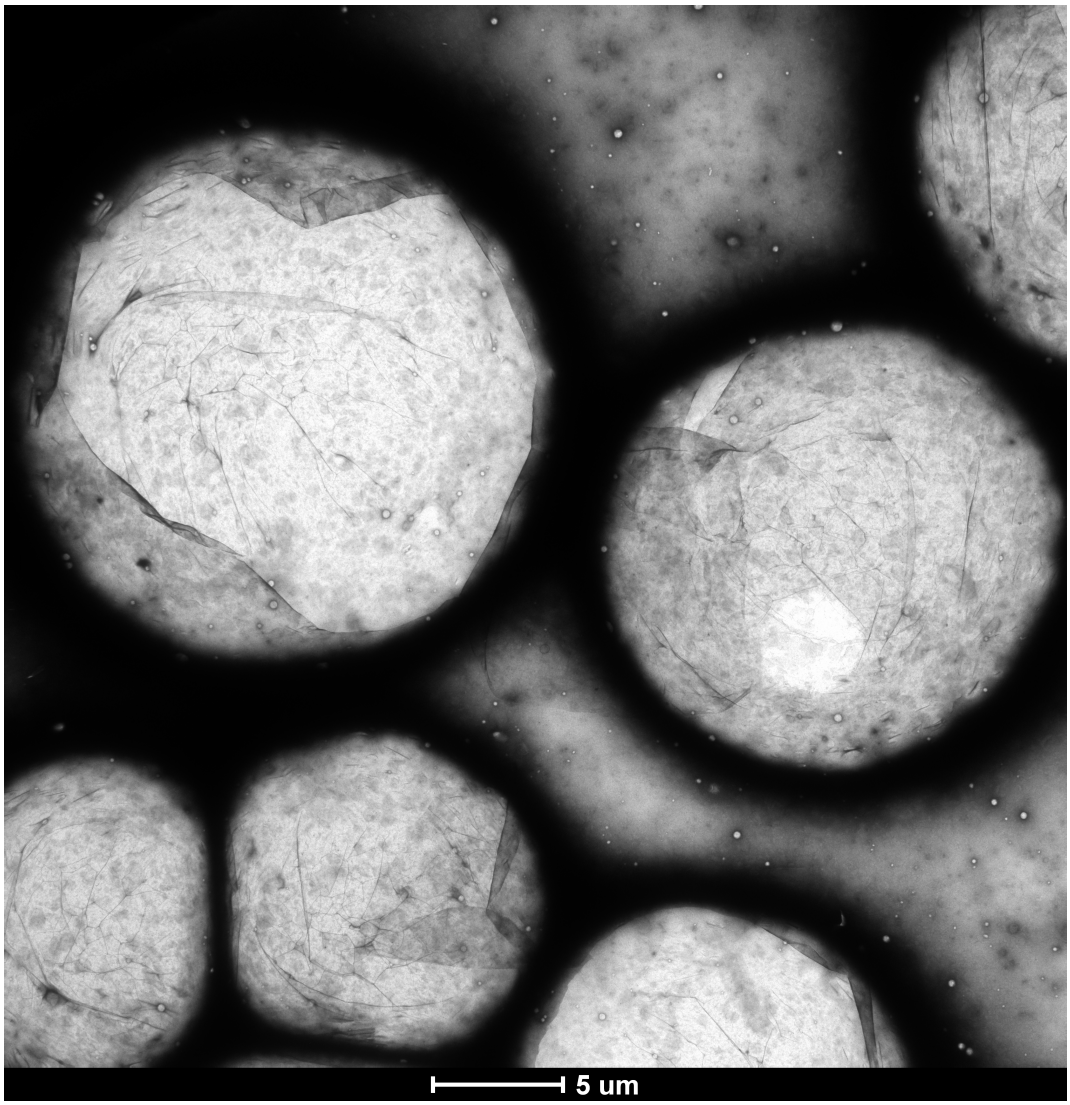


Figure 4.7, electron microscopy image of microbubbles created with gold nanoparticles on the surface.

The gold microbubbles were then examined at higher magnification (Figure 4.8), which enabled the domain boundaries or grain boundaries to be observed (Arrow 2) to be more clearly observed, and the presence of the gold nanoparticles on the surface to be confirmed (Arrow 1). The lipid domain boundaries are clearly defined and similar to those observed by Borden *et al.* appearing to showing condensed and expanded phases (Figure 4.8 Arrow 3). Borden *et al.* observed domains on microbubbles larger than 20 μm depending on the rate of cooling where the emulsifier would be excluded from the condensed phospholipid layer. Domain like structures can be faintly observed on the surface of gold microbubbles below 20 μm in size. However, a discernable pattern or repeating feature of the domains on the surface of the microbubbles could not be distinguished. No gold microbubbles below 5 μm in size were observed via electron microscopy and domain formation could be a function of size rather than the effect of gold. Domain formation will be discussed in greater depth in section 4.7.2.

As expected, given their much higher density, the gold nanoparticles appear dark in the image and their size and shape is consistent with previous observations of the particles under TEM (15nm diameter spheres) [10]. A large number of lighter coloured circular shapes can also be observed in the image in Figure 4.9 Arrow 3. As these objects were not observed with any other microbubble, it seems likely that these are gold nanoparticles incorporated into the bubble coating below the surface. If this is the case then it supports the hypothesis made in previous studies of nanoparticle coated bubbles that "jamming" of the particles on the surface occurs, giving rise to excellent bubble stability and an enhanced nonlinear response to ultrasound [10].

However, it is also possible that these small circular structures, Figure 4.9 Arrow 3, could be nanoscale domains of the lipid of an expanded phase and more research is required to investigate this.

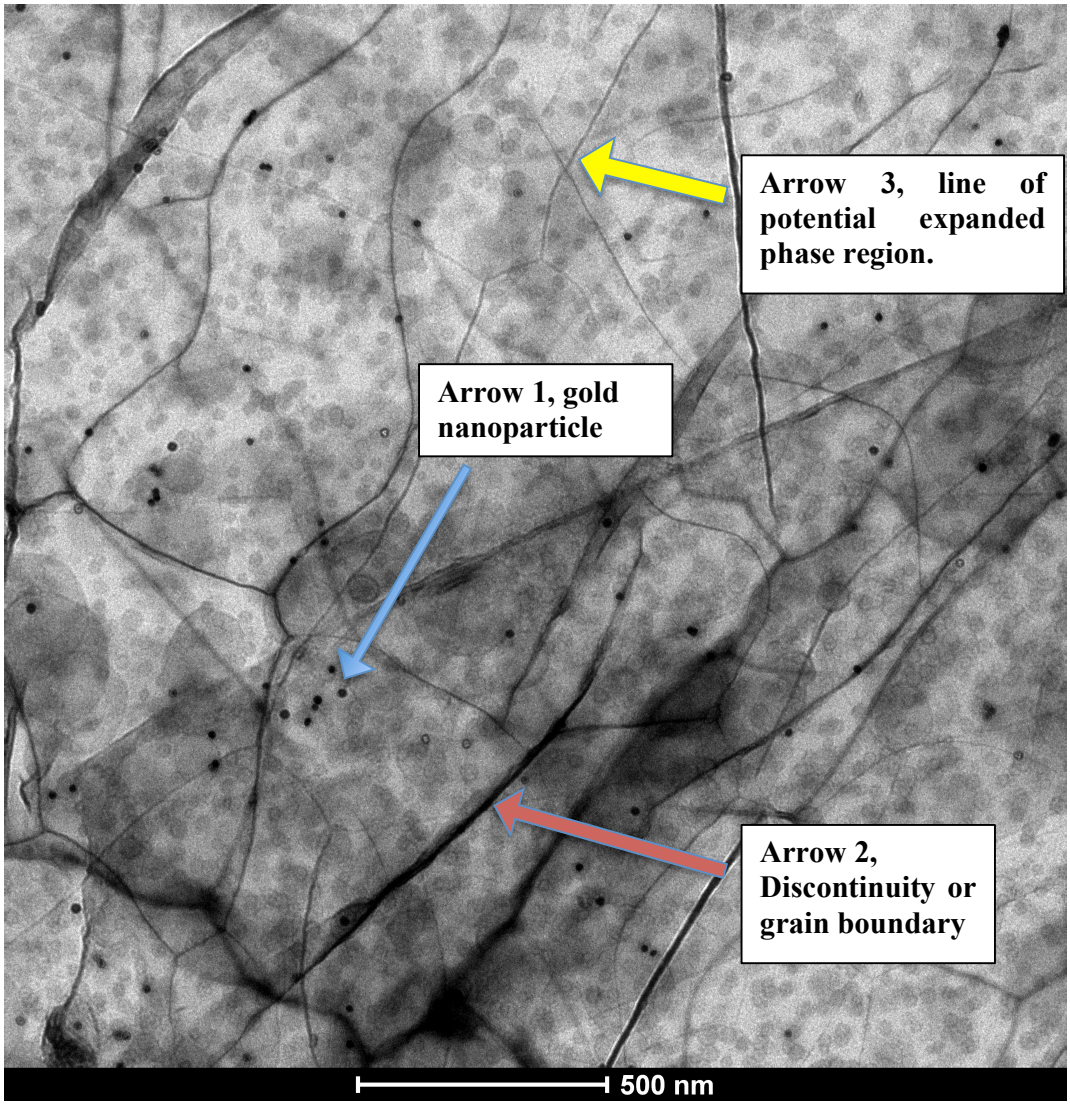


Figure 4.8, electron microscopy image of gold microbubble surface, Gold nanoparticles and grain boundaries can be observed.

This observation also suggests that the microbubble coating consists of multiple layers of phospholipid. The DSPC molecule is approximately 2 nm in length compared to a gold sphere of 15 nm, not including the coating. For the nanoparticle to be stabilised below the surface of a microbubble the shell must be multilamellar as the nanoparticle cannot physically be embedded in a 2 nm monolayer or held inside the gas core. A minimum of 8 layers (16 nm) would be required to have the correct thickness to stabilise the gold nanoparticle. This is in contrast to the assumption made in the majority studies and, in particular, theoretical descriptions of microbubbles, that the surface of the microbubble is coated by a single lipid monolayer. However, the other component of the microbubbles is the PEG-40-stearate (240 nm in length) which could be distributed over the microbubble surface in the brush configuration. Depending on the orientation of the PEG-40-stearate this could stabilise a 15 nm gold nanoparticle, however the distribution of PEG-40 stearate over a microbubble surface is still an ongoing area of research [4].

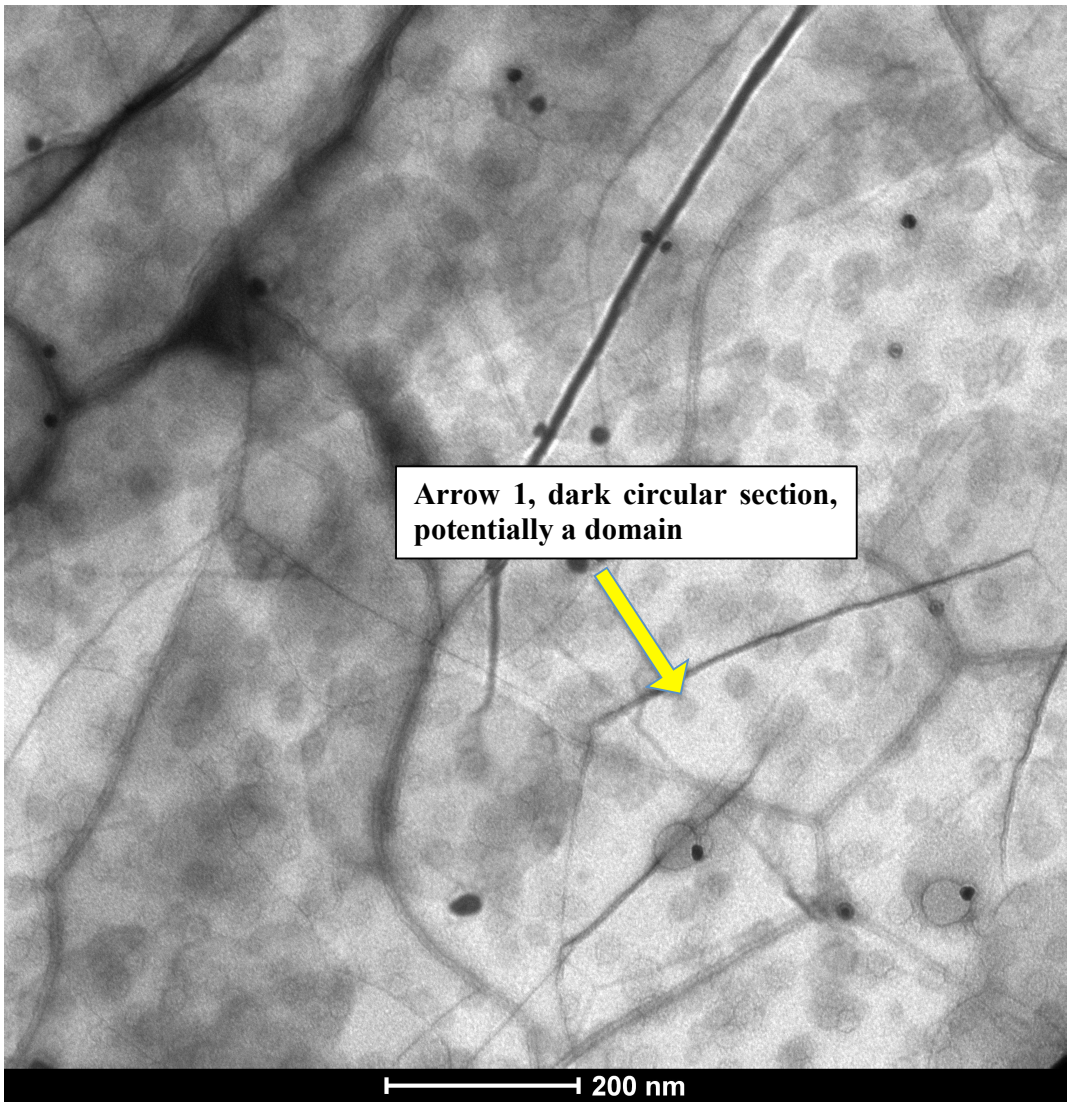


Figure 4.9, Electron microscopy image of the surface of a gold microbubble showing gold nanoparticles and darker vesicle objects which could be gold nanoparticles out of focus or vesicles containing gold.

4.6.3 Magnetic microbubble formulation 1

It has been hypothesised in previous studies that the structure of a magnetic microbubble consists of a gas core, surrounded by a layer of oil filled with iron oxide nanoparticles, that is stabilized by an outer layer of phospholipid [11, 12]. The outer surface would therefore be expected to have a structure similar to that of phospholipid microbubbles as shown in Figure 4.6. Figure 4.10, however, shows a microbubble

approximately 8 μm in diameter on whose surface nanoparticles and lipid domains are visible. The domains can be more clearly observed at higher magnification in Figure 4.11 and are arranged in irregular hexagons similar to the observations reported by Borden *et al.* [4] and Kim *et al*. [9]. This is interesting since the formulation does not contain PEG-40-stearate suggesting an alternative mechanism of domain formation. The ferrofluid contains long carbon chains and the nanoparticles are coated with detachable oleic acid, both of which could potentially act as an emulsifier causing the formation of expanded domains. The magnetic microbubble (8 μm) is also less crumpled relative to the phospholipid microbubble (2 μm) in Figure 4.6 making it more likely that nanoparticles embedded in the surface or cause the shell to be stiffer and more resistant to crumpling under electron microscopy.

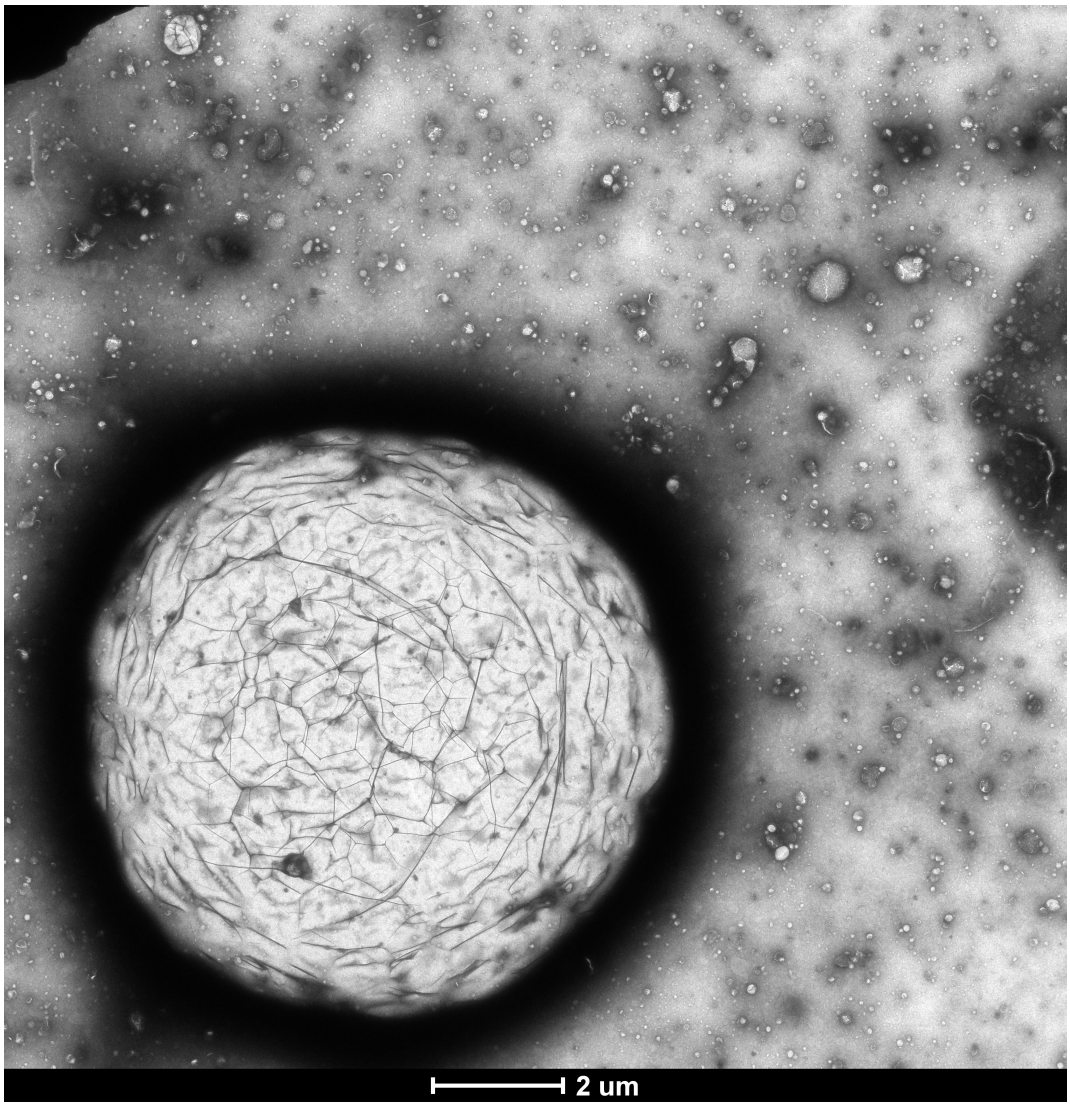


Figure 4.10, electron microscopy image of a magnetic microbubble showing an intact structure and other material/vesicles and nanoparticles contained within the neat solution.

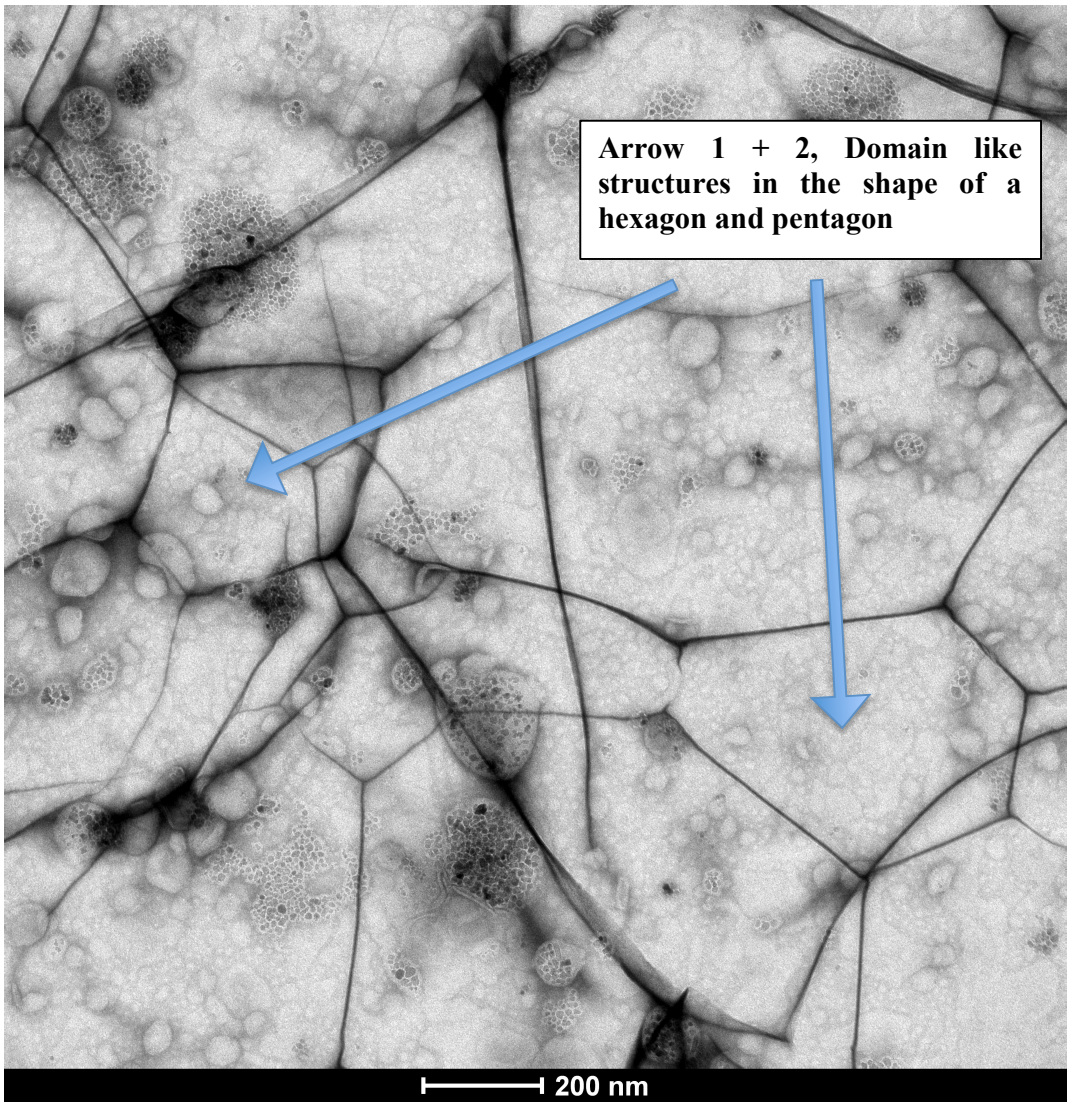


Figure 4.11, electron microscope image of the surface of a magnetic microbubble showing nanoparticles embedded in the surface and grain boundaries.

Vesicles can be observed on the microbubble surface including some containing magnetic nanoparticles Figure 4.12 Arrow 1. Evidence that the vesicles have adhered directly to the microbubble surface is given in Figure 4.12 where the boundary of a lipid domain can be seen cutting across a nanoparticle filled vesicle (Arrow 2). Nanoparticles can also be seen directly embedded in the surface of the microbubble. This was unexpected and suggests there may be additional mechanisms

by which iron oxide nanoparticles become attached to the microbubbles during preparation. This is discussed further in section 4.7.3. The magnetic microbubbles were slightly larger than optical results indicated but this could be due to the small number of bubbles observed relative to optical microscopy.

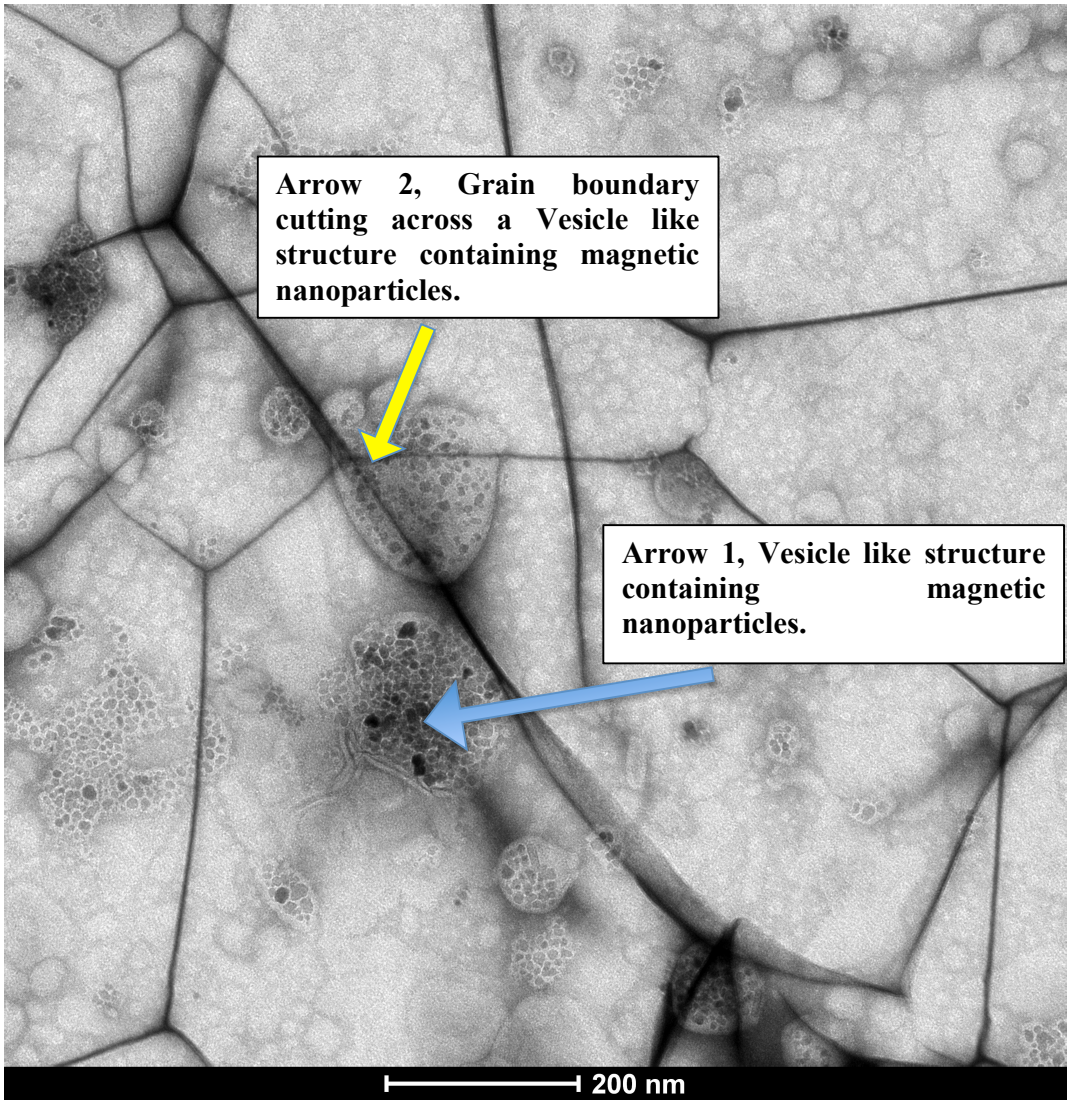


Figure 4.12, electron microscopy image of the surface of a magnetic microbubble showing nanoparticles embedded in vesicles embedded in the surface of the microbubble and domain boundaries.

4.6.4 Magnetic microbubble formulation 3

A second formulation of magnetic microbubbles was produced using lipid coated nanoparticles mixed directly into the lipid film before sonication (i.e. rather than being suspended in oil). An example of this type of bubble can be seen in Figure 4.13 and the size of microbubbles observed correlates with optical microscopy results. Hexagonal lipid domains (Arrow 1 + 2) on the surface of the microbubble (8 μm) can clearly be observed as well as dark patches on the microbubble surface. At higher magnification the dark patches were seen to contain magnetic nanoparticles (Figure 4.14 Arrow 1). The microbubbles (3 – 7 μm) show minimal signs of crumpling relative to phospholipid microbubbles (2 μm) providing more evidence for nanoparticles imparting stiffness to the shell.

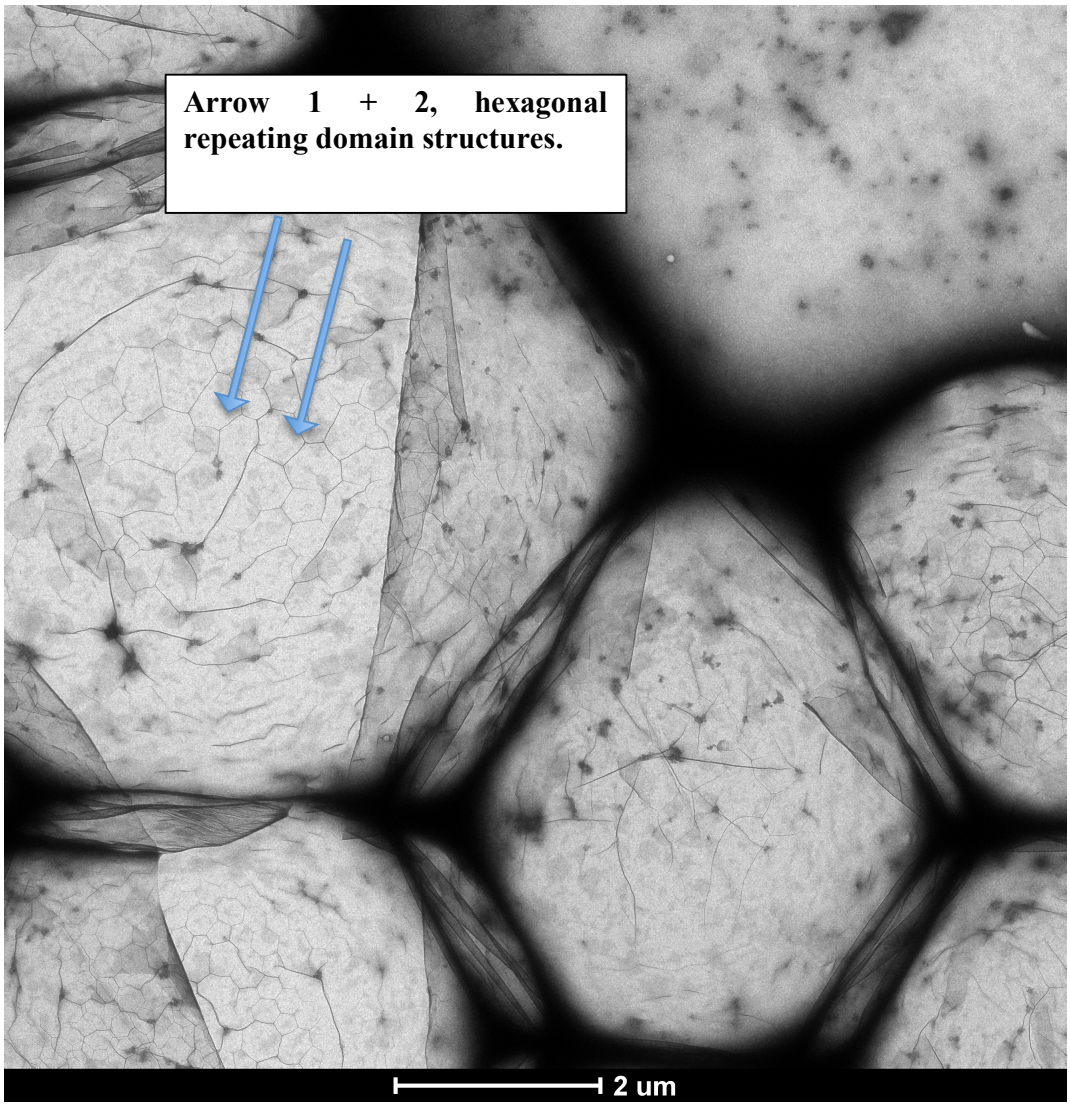


Figure 4.13, electron microscopy image of iron dome magnetic microbubbles and other material contained within the solution.

This formulation, but for the nanoparticles, is exactly the same as that of the phospholipid microbubble shown in Figure 4.5. Nanoparticles can be observed having been embedded in the microbubble shell. A regular pattern of domains can be observed on segments of the larger microbubbles (>6 μm) and is less pronounced on smaller microbubbles (< 2 μm) although a definite trend cannot be determined. The domain boundaries are also the location of the nanoparticles (Figure 4.14 Arrow 1)

indicating the potential influence of the nanoparticles on the microbubble structure and location of domains or vice versa. The increased average size of magnetic microbubble formulation 3 could indicate that only larger microbubbles with domains can stabilise nanoparticle attachment. However, a small proportion of nanoparticles are also embedded in areas without domains. More research is required to investigate the effect of nanoparticles and domains on microbubble formation.

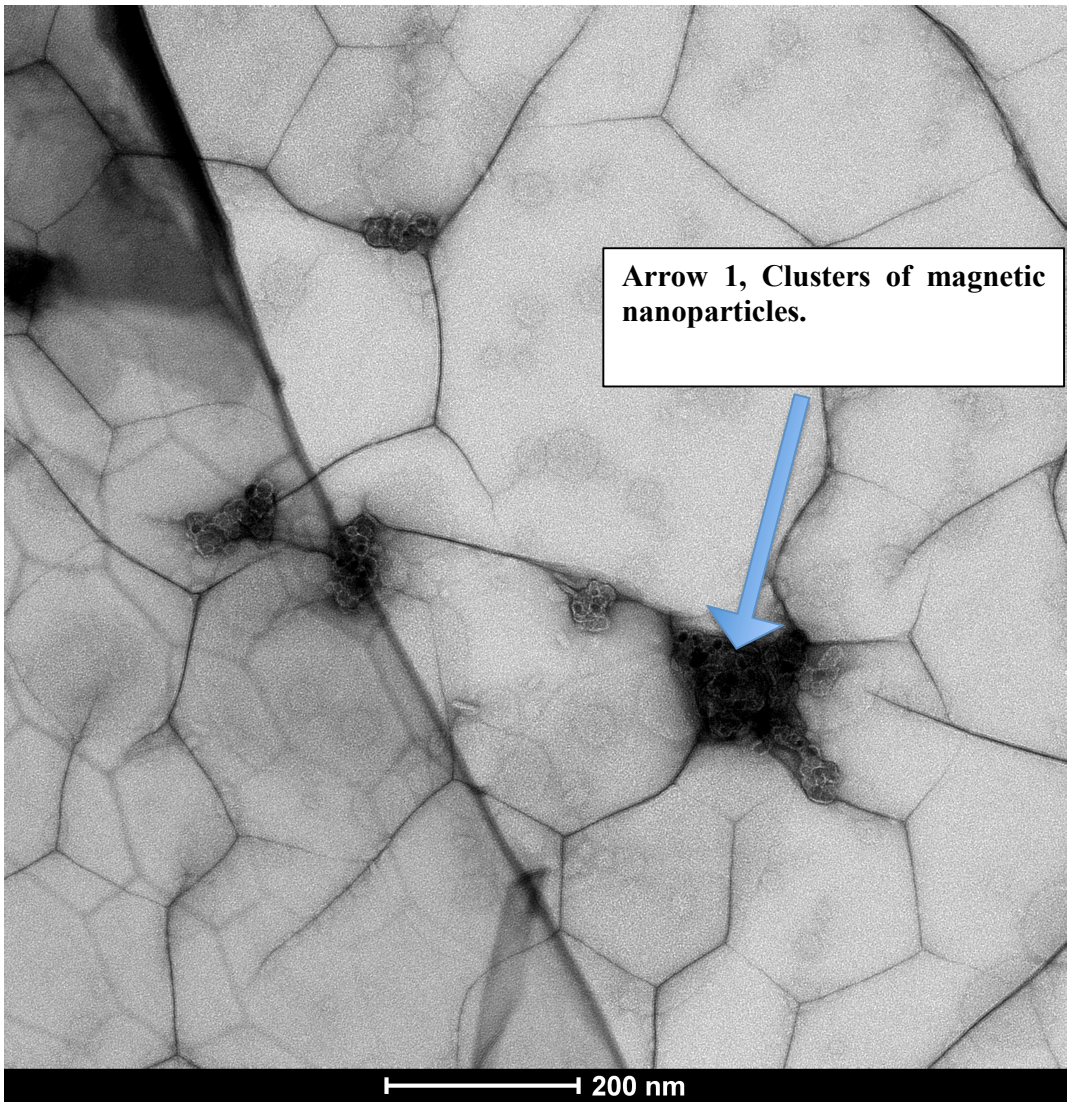


Figure 4.14, electron microscopy image of the surface of an iron dome magnetic microbubble showing nanoparticles embedded in the microbubble surface, grain boundaries and a repeating pattern of hexagonal shapes.

4.6.5 Magnetic droplets and microbubbles

A third type of magnetic microbubble formulation was also investigated consisting of a mixture of lipid-coated droplets of the magnetic nanoparticle suspension (ferrofluid) and phospholipid microbubbles. This formulation has been previously shown to promote equivalent levels of transfection to magnetic microbubbles under the influence of ultrasound and a magnetic field [11]. Initial theories proposed a binding between the magnetic droplets and microbubbles creating a magnetically responsive construct [8]. The TEM images obtained appear to support this finding. Figure 4.15 shows the bubble surface with dark regions corresponding to adherent magnetic droplets and this is confirmed at higher magnification in Figure 4.16 (Arrow 1)where the magnetic nanoparticles in one such region are clearly visible. The size range is similar to that observed via optical microscopy of phospholipid microbubbles. The shell structures do not appear as crumpled as phospholipid microbubbles alone, despite being of similar size. This could be caused by the adhesion of the magnetic droplets/nanoparticles but could also be due to the high concentration of microbubbles under observation in this particular image.

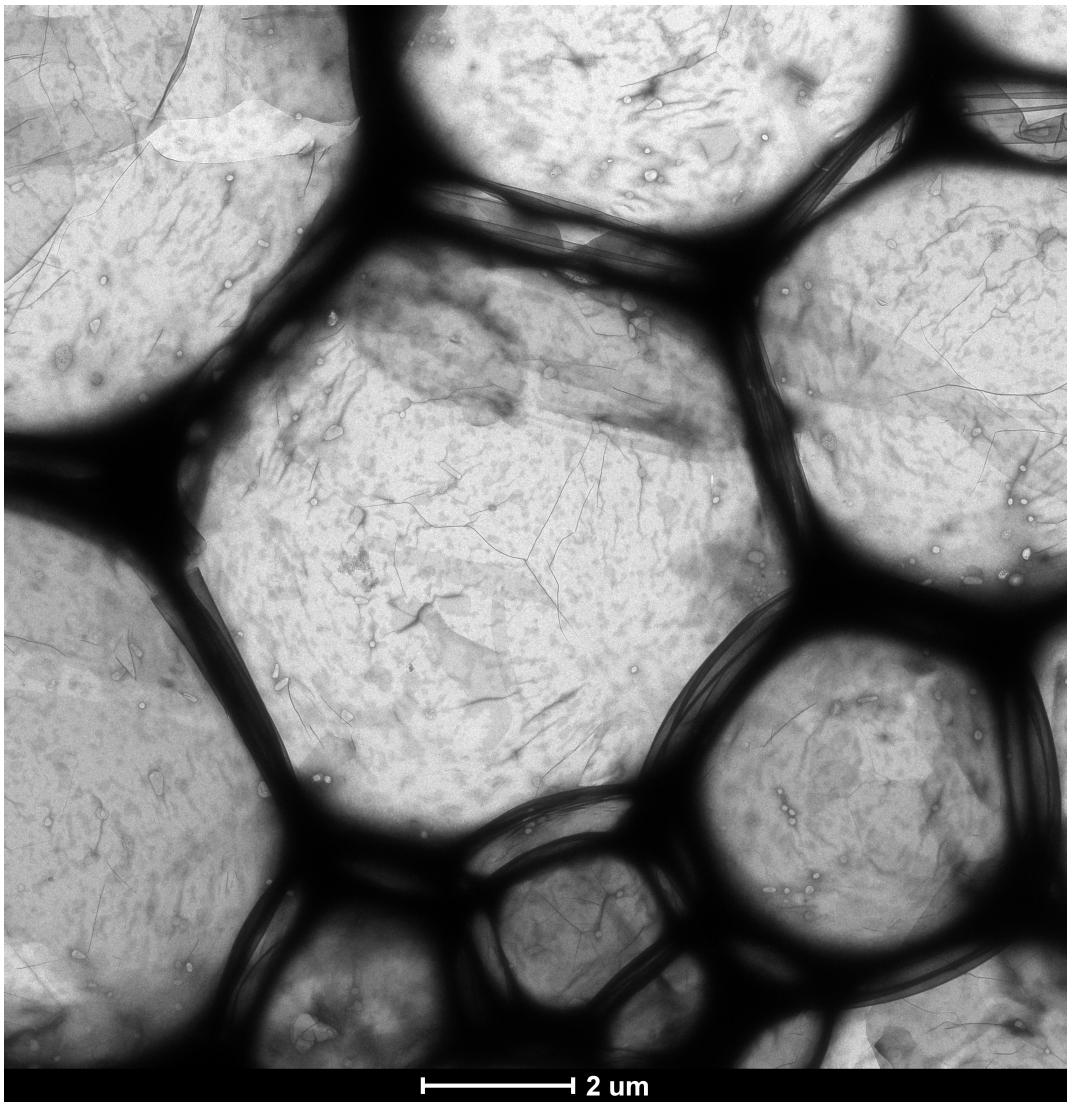


Figure 4.15, electron microscopy image of phospholipid microbubbles mixed with magnetic droplets.

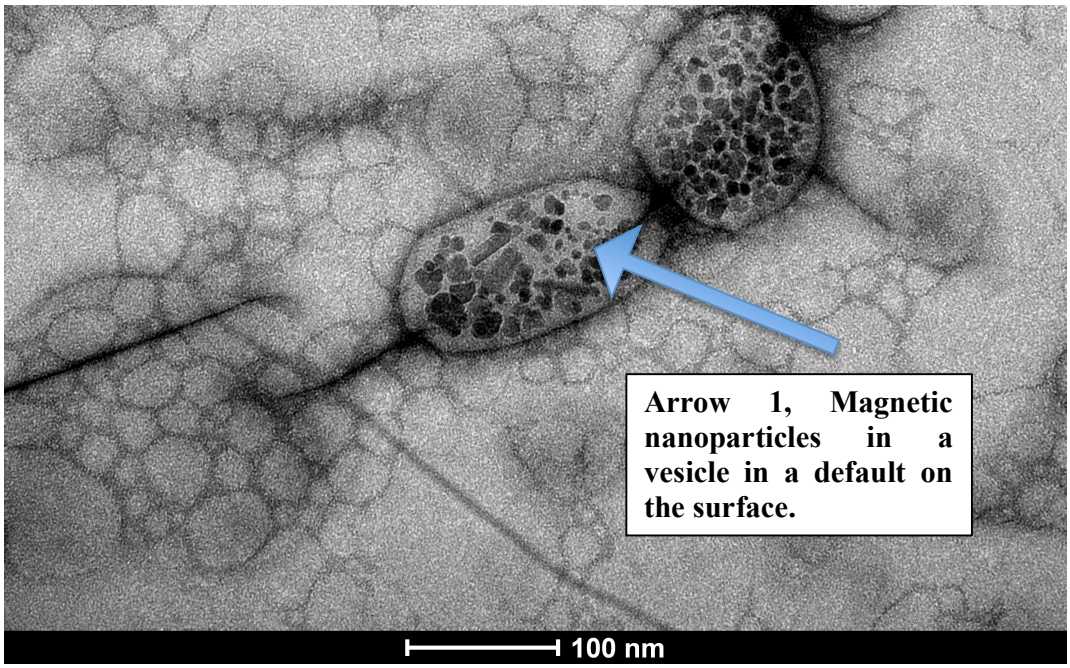


Figure 4.16, electron microscopy image of the surface of phospholipid microbubbles mixed with magnetic droplets. Vesicles filled with magnetic nanoparticles can be observed on the surface.

4.7 Discussion

4.7.1 Technique

Both scanning and transmission electron microscopy have been very widely used to visualize objects at the nanoscale. However, these techniques have proved difficult to apply to the study of microbubbles owing to the need to evacuate the sample chamber inside the electron microscope, which normally results in bubble destruction. In this study it was found that by concentrating the microbubbles on the microscope grid and coating them in uranyl acetate the structure of the coating could be successfully preserved allowing nanoscale imaging. Previous studies using fluorescence and low temperature electron microscopy have focused on larger microbubbles [9], whilst scanning electron microscopy has previously been used to study bubbles that had been either dried or frozen and sectioned [13].

4.7.2 Domains

Domains are regions of phase separation in the lipid layer between expanded and condensed phase lipids. It can occur because of many reasons such as temperature or due to compounds present in the lipid layer, in this case PEG-40-Stearate. Borden *et al.* [4] showed that domains indicated where PEG-40-stearate with expanded phase phopholipids and condensed phase phospholipids divided meaning the microbubble would have a heterogeneous covering of PEG exposing it to the immune system in the body. Reducing domain formation may be essential for microbubble persistence in the vasculature [4]. However, in this instance the lipid on the microbubble surface could be in the same phase and discontinuities. folds or grain boundaries present at random on the surface. This would not be a domain under the definition given above and further research is required to examine whether the discontinuities and grain boundaries contain expanded phase lipid. However, the structures observed are very similar to those reported by Kim *et al*. [9] which are labeled domains.

Examination of different types of microbubble revealed a number of interesting features. First, it has been hypothesized that microbubble shells composed of condensed phase monolayers of lipids which are fully compressed would have a surface tension of zero and could survive indefinitely [4]. Electron microscopy has shown a microbubble of approximately 2 μm in size without the domain structure observed on larger microbubbles (>20 μm) as shown in previous research. However, gold coated microbubbles and magnetic microbubble formulations 1 (MMB) and 3 (LMMB) both showed domains on sections of the surface. These microbubbles were approximately 8 μm in size, so domain formation could be linked to size rather than

the presence of nanoparticles on the surface. Those microbubbles <8 μm in size with nanoparticles showed minimal sign of domain formation.

The images of microbubbles formed with lipid-coated nanoparticles suggest that the majority of the nanoparticles agglomerate on the microbubble surface at the domain boundaries. Tailoring the manufacturing technique could allow for investigation of this in order to maximize the number of nanoparticles on the microbubble surface without compromising microbubble integrity.

4.7.3 Confirming hypothesised structures

The TEM images also enabled a number of hypotheses from previous studies to be tested. Solid nanoparticles adsorbed onto the surface of microbubbles have been known to influence both their stability and acoustic properties [10, 14]. It has been proposed that this is due to a high surface concentration of particles "jamming" to prevent the bubble from compressing but no direct evidence has previously been obtained. Figure 4.9 confirms that gold nanoparticles are indeed located on the surface of the microbubble and suggests that their concentration is relatively high although they are not located in single layer but rather in several layers surrounding the bubble. This structure would still enable particle "jamming" but does suggest that the very widely held hypothesis that microbubbles are stabilised by a phospholipid monolayer may not be correct. This hypothesis of multilamellar microbubble coatings is also supported by viscosity measurements of microbubbles using fluorescence lifetime imaging conducted by Hosny *et al.* [15].

Observation of magnetic microbubbles also suggested that their structure was different or at least more complicated than previously assumed. Rather than a gas core surrounded by an oil layer containing magnetic nanoparticles and stabilised by an outer phospholipid monolayer, the TEM images indicated that the surface was also coated with nanoparticles. This may have been due to droplets of magnetic fluid produced during sonication adhering to the bubble surface. This phenomenon was observed when non-magnetic microbubbles were mixed with magnetic droplets further confirming the results of a previous fluorescence microscopy study [8]. This is very important since the concentration of nanoparticles will influence both the acoustic and magnetic response of the microbubbles and potentially their circulation time *in vivo*. A technique for directly observing the concentration of nanoparticles on the surface is now available via electron microscopy.

4.7.4 Limitations

This technique provides a 2 dimensional projection of a 3 dimensional structure which inevitably limits what can be observed and deduced. It is known that the microbubble survives the processing technique, what effect this has upon the microbubble structure, however, is unknown. Signs of crumpling were observed in some bubbles but this is seen under optical microscopy also over time; no other obvious changes were seen. Objects in the solution that are reversibly bound to the microbubble surface cannot be differentiated from objects that are irreversibly bound, such as vesicles or nanoparticles. Another difficulty was the analysis of a large number of microbubbles to check for consistency and repetition of features across a population.

4.8 References

1. Goodhew P., J., Humphreys J., and Beanland R., *Electron Microscopy and Analysis*. Third ed. 2001: Taylor and Francis.
2. Haggis, G.H. and B. Phipps-Todd, *Freeze-fracture for scanning electron microscopy.* Journal of Microscopy, 1977. **111**(2): p. 193-201.
3. Amstad, E., et al., *Triggered release from liposomes through magnetic actuation of iron oxide nanoparticle containing membranes.* Nano Letters, 2011. **11**(4): p. 1664-1670.
4. Borden, M.A., et al., *Surface phase behavior and microstructure of lipid/PEG-emulsifier monolayer-coated microbubbles.* Colloids and Surfaces B: Biointerfaces, 2004. **35**(3-4): p. 209-223.
5. Echlin, P., *Low-Temperature microscopy and analysis*. 1st ed. 1992, New York ; London: New York ; London : Plenum. 539.
6. Watson, M.L., *Staining of tissue sections for electron microscopy with heavy metals. II. Application of solutions containing lead and barium.* The Journal of biophysical and biochemical cytology, 1958. **4**(6): p. 727-730.
7. Vlaskou, D., et al., *Magnetic and Acoustically Active Lipospheres for Magnetically Targeted Nucleic Acid Delivery.* Advanced Functional Materials, 2010. **20**(22): p. 3881-3894.
8. Owen, J., et al., *Understanding the structure and mechanism of formation of a new magnetic microbubble formulation.* Theranostics, 2012. **2**(12): p. 1127-1139.
9. Kim, D.H., et al., *Mechanical properties and microstructure of polycrystalline phospholipid monolayer shells: Novel solid microparticles.* Langmuir, 2003. **19**(20): p. 8455-8466.
10. Mohamedi, G., et al., *Effects of gold nanoparticles on the stability of microbubbles.* Langmuir, 2012. **28**(39): p. 13808-13815.
11. Stride, E., et al., *Enhancement of Microbubble Mediated Gene Delivery by Simultaneous Exposure to Ultrasonic and Magnetic Fields.* Ultrasound in Medicine & Biology, 2009. **35**(5): p. 861-868.
12. Mulvana, H., et al., *Theoretical and Experimental Characterisation of Magnetic Microbubbles.* Ultrasound in Medicine and Biology, 2012. **38**(5): p. 864-875.
13. Martin, M.J., et al., *Enhanced detection of thromboemboli with the use of targeted microbubbles.* Stroke, 2007. **38**(10): p. 2726-2732.
14. Stride, E., *The influence of surface adsorption on microbubble dynamics.* Philosophical Transactions of the Royal Society A: Mathematical, Physical and Engineering Sciences, 2008. **366**(1873): p. 2103-2115.
15. Hosny, N.A., et al., *Mapping microbubble viscosity using fluorescence lifetime imaging of molecular rotors.* Proceedings of the National Academy of Sciences of the United States of America, 2013. **110**(23): p. 9225-9230.

5 Characterisation of magnetic microbubbles

5.1 Introduction

Before magnetic microbubbles can be used effectively their characteristics must first be studied in detail. Specifically, their acoustic and magnetic response and efficacy as drug delivery vehicles need to be determined before *in vivo* experiments should be conducted and in order determine their potential ultimately for clinical use. Their acoustic properties and efficacy for gene delivery have already been explored in previous studies [1, 2]. Their magnetic response, however has received less attention. Since magnetic microbubbles are a relatively new type of drug delivery system compared with e.g. biochemically targeted microbubbles, liposomes or nanoparticles, new methods of analysis had to be devised in order to fully characterise targeting. For imaging and/or therapeutic delivery, magnetic microbubbles must be capable of targeting against flowing blood at clinically relevant tissue depths, via application of a magnetic field whose size and gradient are safe for human use. *In vitro* experiments using phantoms to mimic different flow conditions within the human body were therefore designed to ascertain if magnetic microbubbles can target *in vivo* against physiologically relevant shear rates and flow rates.

5.1.1 Magnetic targeting

In order to determine the magnetic field characteristics required to target magnetic bubbles the forces acting on a bubble need to be considered. First, a magnetic field gradient is required to exert a force on a magnetically responsive particle as a uniform field gives rise to torque, but no translational motion [3]. For a stationary particle in a vacuum only the magnetic field strength, the gradient, the size of the particle and the

material would be important. However for targeting magnetic microbubbles against flow the situation becomes more complicated.

The different forces and non-force quantities acting on a microbubble are indicated in Figure 5.1 below: v is the velocity of the microbubble, x is the distance from the centre of the bubble to the wall, Fd is viscous drag, Fb represents buoyancy, Fm represents the magnetic attractive force between the microbubble and the magnet, Frad1 and Frad2 represent acoustic radiation force.

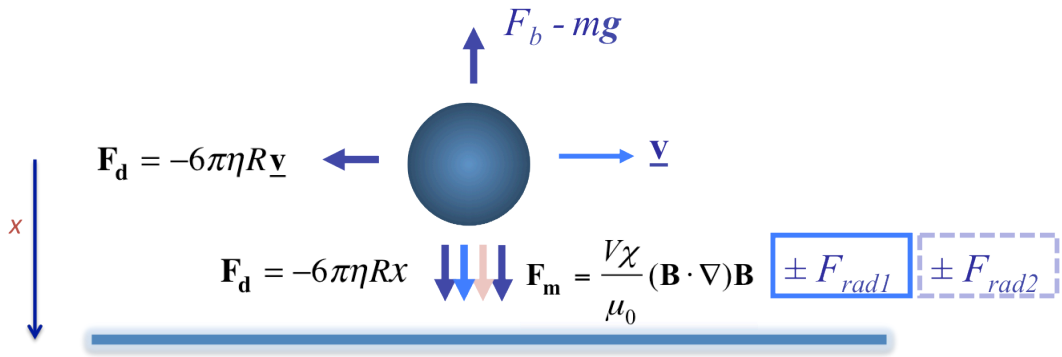


Figure 5.1, image of a magnetic microbubble in flowing water indicating all the forces and non-force quantities acting on the microbubble during magnetic targeting.

In order for a magnetic microbubble to be successfully targeted, its buoyancy and any drag forces acting on it must be overcome. In flowing liquid the particle also must remain in the magnetic field for sufficient time to travel the target site (e.g. the wall of a blood vessel). The conditions under which magnetic microbubble targeting should be theoretically possible were determined in a separate study through numerical simulations[1]. The results showed that it should be possible to target magnetic microbubbles against a significant proportion of the flow conditions found within the

[1] This research was performed by a master's student Qian Chen whose contribution is acknowledged. The equations used are included in the appendix.

human body using magnetic field strengths and gradients within the range already used in magnetic resonance imaging. The aim of the work described in this chapter was to test these findings experimentally.

As described in Chapter 2, magnetic targeting has been shown to be effective *in vivo* in small animal models for both microbubbles and other particles. However, the magnetic force on a particle decreases with the cube of the distance from the magnet. Therefore magnetic targeting in a human at depths of many centimetres may be significantly more challenging. Animal experiments, whilst useful for obtaining proof of principal and assessing toxicity give little information regarding the feasibility of magnetic targeting as a clinical technique. In this sense, *in vitro* phantom studies that allow length scales and flow conditions relevant to human physiology to be simulated are more valuable.

Previous studies have examined the targeting ability of magnetically and acoustically active agents. Vlaskou *et al.* magnetically retained acoustically active lipospheres in a 1 mm ID tube using an electromagnet with a field strength of >0.7 Tesla on the bottom of the tube and a gradient of 0.1 T/m. Flow rates were varied from 0.2 – 10 ml/min and found that magnetic targeting at 40 % efficiency occurred. However, this study did not vary vessel size or magnetic field strength or gradient. Also in the arteries the flow rate can be as high as 400 ml/min so this study only examined relatively mild flow conditions. The impact of shear rate was also ignored. In addition, whether the lipospheres were still acoustically active, which is necessary for drug delivery, after successful targeting was not explored [4].

Another study to examine magnetic targeting was performed by Wu *et al*. These microbubbles were also targeted to VCAM-1 and the magnetic field was used to augment targeting. The experiment was performed in a parallel plate flow chamber and shear rate was varied. Magnetic microbubbles showed increased targeting to VCAM-1 at higher wall shear stresses in the presence of a magnetic field than non-magnetic microbubbles [5]. Again, however no variations in vessel size and flow conditions were examined.

Successful targeting of magnetic microbubbles requires them both to be pulled out of flow and retained against the shear stresses at the wall. Flow conditions vary significantly within the human body depending on the location. In the smallest capillaries (~8 μm internal diameter), flow rates are extremely small but the shear rate can be as high as 800/s. The largest arteries can be greater than 10 mm in diameter with flow rates as high as 400 ml/min but with shear rates ~100/s. Veins vary in size from 0.5 mm to 0.5 cm [6] with the lowest shear rate in the body being found in the vena cavae at 60/s [7].

5.2 Flow regimes to be investigated

In order to establish the range of flow parameters that should be used for the experiments it was assumed a blood vessel could be approximated as cylindrical tube.

In order to determine if the flow was laminar or turbulent the Reynolds' number was calculated using the following equation.

	$Re = \frac{QD_H}{\nu A}$	5.1

Where D_H is the hydraulic diameter of the pipe, A is the cross sectional area of the flow phantom, ν is the kinematic viscosity (dynamic viscosity/density of the fluid). A low Reynolds number indicates laminar flow whereas a high Reynolds number indicates turbulent flow.

For Re <2500 it was assumed the flow would have a parabolic flow profile and hence the wall shear rate could be estimated as:

	$\gamma = \frac{4Q}{\pi r^3}$	5.2

Where Q is the volumetric flow rate, and r is the radius of the flow phantom tube.

The range of flow conditions examined in the experiments are shown in the Table 5.1 below. The flow rates and shear rates are given for each flow condition and tube size. Further description of how these were selected can be found in chapter 3. For each combination tests were performed with the magnetic array positioned at one of 3 distances away from the lower wall of the flow phantom corresponding to three different magnetic field strengths.

Table 5.1, table summarising the flow conditions which were used to examine magnetic targeting of microbubbles.

tube diameter (cm)	radius (cm)	cross sectional area (cm^2)	flow rate (cm^3/s)	shear rate (/s)	Reynolds number	mag field strength (T)		
						0.25	0.05	0.03
0.16	0.08	0.02	0.10	248.68	79.26	Y	N	N
0.16	0.08	0.02	0.15	373.02	118.89	Y	N	N
0.16	0.08	0.02	0.20	497.36	158.52	Y	N	N
0.16	0.08	0.02	0.25	621.70	198.15	Y	N	N
0.30	0.15	0.07	0.09	33.95	38.05	Y	Y	Y
0.30	0.15	0.07	0.17	64.13	71.86	Y	Y	Y
0.30	0.15	0.07	0.25	94.31	105.68	Y	Y	Y
0.30	0.15	0.07	0.33	124.49	139.50	Y	Y	Y
0.30	0.15	0.07	0.41	154.68	173.32	Y	Y	N
0.30	0.15	0.07	0.50	188.63	211.36	Y	Y	N
0.30	0.15	0.07	0.58	218.81	245.18	Y	Y	N
0.30	0.15	0.07	0.65	245.22	274.77	Y	N	N
0.30	0.15	0.07	0.74	279.17	312.81	Y	N	N
0.60	0.3	0.28	0.48	22.46	100.65	Y	Y	Y
0.60	0.3	0.28	0.56	26.20	117.42	Y	Y	Y
0.60	0.3	0.28	0.71	33.68	150.97	Y	Y	Y
0.60	0.3	0.28	1.00	47.16	211.36	Y	Y	Y
0.60	0.3	0.28	2.00	94.31	422.72	Y	Y	N
0.60	0.3	0.28	3.33	157.19	704.54	Y	Y	N

5.2.1 Acoustic observation of magnetic targeting

When used *in vivo*, microbubbles are observed via ultrasound. Therefore the first set of experiments used an ultrasound imaging system to detect magnetic targeting. The videos obtained were analysed to determine if magnetic targeting of microbubbles had been successful in terms of by the criteria described below.

5.2.2 Targeting analysis

A purpose written Matlab script was used to estimate the quantity of microbubbles retained at the location of the magnet for each set of flow conditions. This is described in detail in Chapter 3 (section 3.2.7.6). Two areas of interest were selected:

along the bottom of the tube at the location of the magnet and along the top of the tube at the same axial position. The change in intensity over the course of the experiment was measured in both areas of interest and plotted for each set of flow conditions.

The minimum criterion for successful targeting was that the percentage change in intensity with respect to the start of the experiment along the bottom of the tube is higher than the percentage change along the top. The reverse would be true in the absence of a magnetic field due to microbubble buoyancy. It was decided that the criteria for successful targeting were that this difference in intensity change should be sustained for >1000 frames and be greater than >5 % increase in intensity. All flow conditions were examined via this method to confirm if magnetic targeting had taken place. Measurements were repeated 3 times for each set of conditions and if targeting was observed on 2 out of 3 occasions it was deemed to be possible under these flow conditions.

5.2.3 Targeting time and intensity analysis.

For successful drug delivery to occur, magnetic microbubbles must be retained in sufficient concentration and for a length of time for therapeutic compounds to be delivered. From the ultrasound videos obtained it was possible to extract the amount of time for which microbubbles were retained. From the intensity increase it was also possible to discern trends about the quantity retained.

In the results presented below, targeting intensity refers to the maximum intensity increase along the phantom wall nearest the magnet after subtracting the maximum

intensity increase from the wall furthest from the magnet. The results are given in percent (%) with 0 being initial wall intensity.

Targeting time refers to the time when the intensity along the phantom nearest the magnet is higher than the intensity along the vessel wall furthest from the magnet. The results are given in seconds.

The imaging signal will vary with bubble size, size distribution, concentration and variations in thickness of the vessel wall. However, the consistency of the first three of these between samples was verified by microscopy (see Chapter 3 section 3.2.2.1) and the impact of vessel wall thickness was not expected to significant compared with the change in intensity due to targeting. Intensity analysis has been used to detect whether or not biochemical targeting of microbubbles *in vivo [8]*; but assessing the quantity and time of targeting from acoustic intensity has, to the candidate's knowledge never been attempted before.

5.2.4 Optical observation of targeting

Acoustic observation of magnetic targeting of microbubbles was not possible in a vessel of a smaller size than approximately 1.6 mm ID. Below this size, differentiating between the bottom and the top of the flow phantom was difficult at the frequencies relevant for diagnostic imaging and so measuring relative increases in intensity was impossible. In order to investigate conditions in the capillaries where high shear rates (>800/s) occur with very low flow rates it was decided to use optical imaging. This would flow phantoms with much smaller inner diameters than 1 mm to

be used for more accurate simulation of in vivo flow conditions in the capillaries. 200 μm capillary tubes have previously been used for targeting of microbubbles via acoustic radiation force [9]. The apparatus for this is described in chapter 3 (section 3.2.7.2).

5.2.5 Effect of targeting on microbubbles

Before targeting, individual magnetic microbubbles (MMB) can be clearly identified as separate entities with an average size of approximately 2 μm as shown in Chapter 4. Magnetic targeting results in the formation of a bolus of microbubbles in which individual bubbles cannot be easily distinguished. After the removal of the magnetic field bubble agglomerates could potentially block vessels in vivo and as such confirmation that the microbubbles did not remain agglomerated was required. This was investigated by examining magnetic microbubbles before and after targeting had occurred via optical microscopy.

5.3 Results

5.3.1 Retention of magnetic microbubbles against flow

The images in Figure 5.2 show magnetic microbubbles in flow phantoms of all 3 vessel sizes. The large increase in image intensity above the magnetic Halbach array in images B and D shows that magnetic microbubbles are successfully targeted against flow in each case. Targeting has successfully occurred in F but is not as easy to discern.

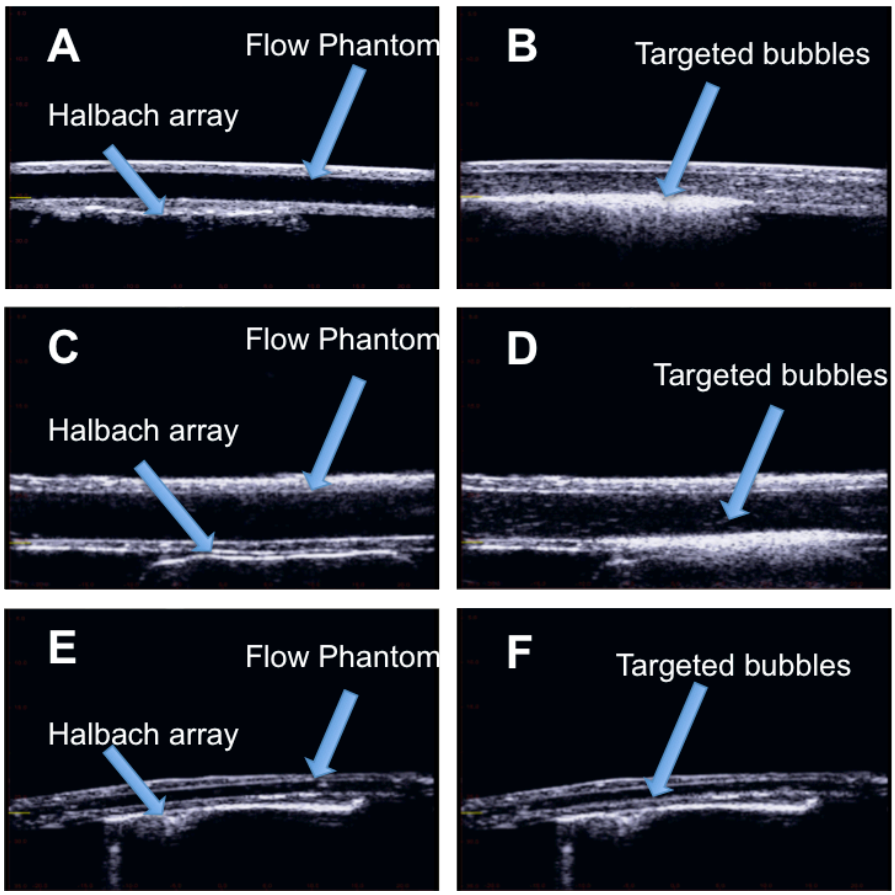


Figure 5.2, images of magnetic targeting before and after magnetic microbubbles have passed over the magnetic Halbach array in all tube sizes. A) before and B) after magnetic microbubbles have flowed through in a 3 mm ID flow phantom. C) before and D) after magnetic microbubbles have flown through in a 6 mm (ID) flow phantom. E) before and F) after magnetic microbubbles have flown through in a 1.6 mm ID flow phantom.

All the results from magnetic targeting were successfully analysed and the limits of magnetic targeting for the range of conditions investigated were determined. The results are summarised in Table 5.2 below.

Table 5.2, Table of the maximum flow conditions at which magnetic targeting has found to successfully occur at the highest magnetic field strength of 0.2 T.

Tube Diameter (mm)	Fluid	max flow rate (ml/s)	shear rate (/s)	magnetic field strength (T)
6.0	water	3.34	157	0.20
6.0	water	2.00	94	0.05
6.0	water	0.71	33	0.03
3.0	water	0.74	272	0.20
3.0	water	0.50	189	0.05
3.0	water	0.25	94	0.03
1.6	water	0.20	497	0.20

In the human body the maximum shear rate in the capillaries is ~800/s. In the large veins the maximum shear rate is ~200/s and in the venae cavae it is ~60/s. In the ascending aorta the shear rate can be as high as 190/s. Flow rates in the body vary greatly and in the capillaries are as low as 3.21×10^{7} ml/s, the veins up to 0.15 ml/s the arteries can be as high as 6.7 ml/s or 400 ml/min [7].

Comparing the data in the table to the *in vivo* flow data listed above it is apparent that, with the magnetic field strength and gradient used in these experiments, magnetic microbubbles cannot be retained at all conditions within the body. However, targeting can still occur at flow rates up to approximately 200 ml/min (3.34 ml/s) and at shear rates up to 500/s. This means that the magnetic targeting of microbubbles can occur easily in veins, the venae cavae and the ascending aorta. Targeting in the capillaries is discussed below.

5.3.2 Targeting time

For drug delivery, microbubbles must be in contact with the target cells long enough for ultrasound to be applied in order to deliver therapeutic compounds. Consequently the time for which bubbles were retained was analysed for all flow conditions.

Graphs showing the variation in targeting time with flow velocity are shown in Figure 5.3 for the highest magnetic field strength along the bottom of the tube (0.2 T). For a 1.6 mm (ID) flow phantom as the flow velocity increases the targeting time decreases until at 0.25 ml/s the targeting time is 10 seconds (A). After this flow rate, targeting time is reduced to zero. For a 1.6 mm flow phantom the decrease in targeting time appears to be linear and to correlate directly with shear rate. For a 3 mm (ID) flow phantom a linear decrease is also observed reducing targeting time from 1 minute at 0.3 ml/s to approximately 5 seconds at 0.75 ml/min (272/s). As the vessel is larger the field cannot penetrate as far and as such targeting time decreases to zero at a lower shear rate than in the 1.6 mm flow phantom. For a 6 mm (ID) flow phantom a similar trend is observed. At the maximum flow rate of 3.34 ml/s magnetic microbubbles target for approximately 40 seconds. But this flow rate only corresponds to a shear rate of 157/s, where targeting successfully occurred in the 3 mm and 1.6 mm flow phantom. A higher flow rate could not be obtained with the current set up. The results indicate that shear rate was the limiting factor in targeting time.

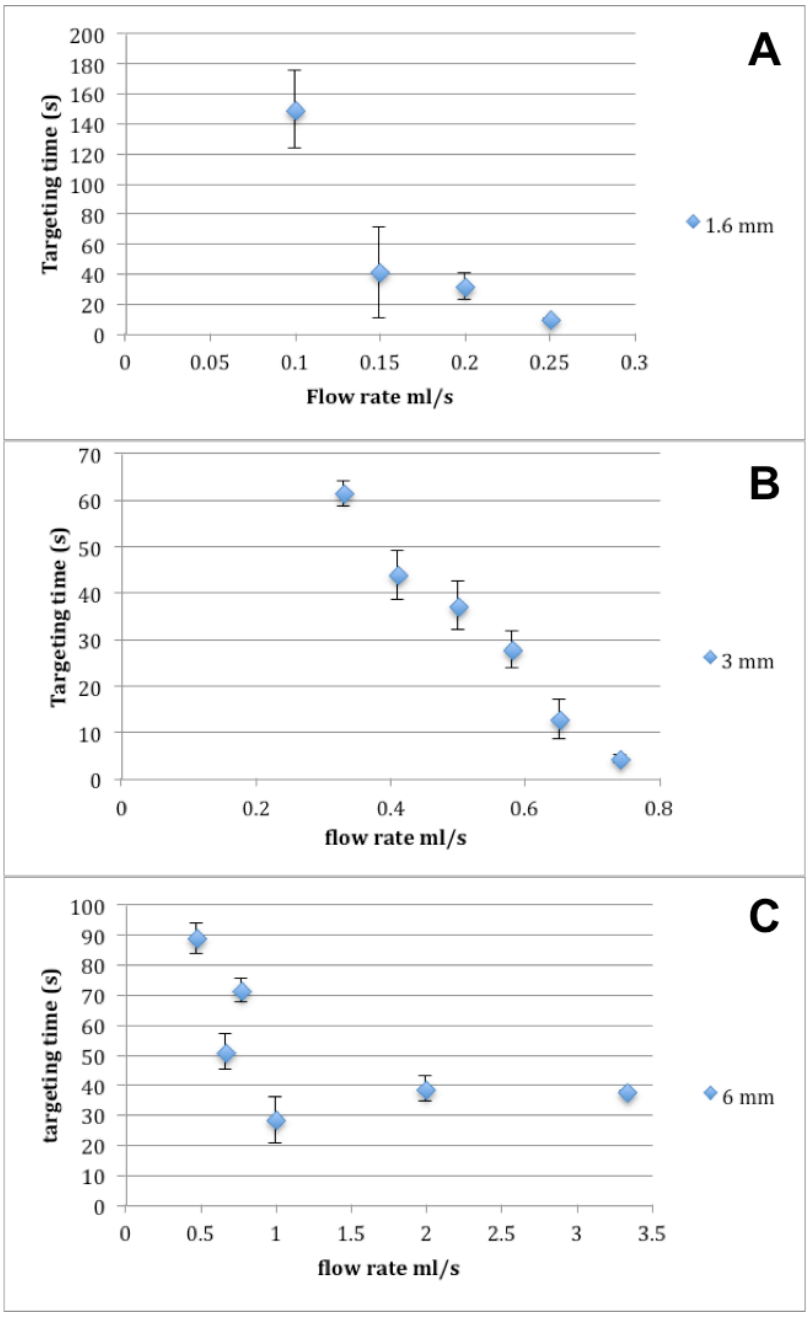


Figure 5.3, time microbubbles are successfully targeted against the volume flow rate of water. Shown at high magnetic field strength for A) 1.6, B) 3.0 and C) 6.0 mm ID flow phantoms respectively. (n = 3)

5.3.3 Quantification of targeting

The results above for targeting time are also reinforced by trends in the acoustic intensity of targeted microbubbles. The intensity of the bolus gives an indication of

the number of microbubbles that have successfully targeted and how this decreases with increasing flow rate in all vessel sizes.

The highest increase in image intensity was plotted against flow velocity, as shown in Figure 5.4. Even with variability in concentration, distribution and bubble size the acoustic intensity of the targeted microbubbles again decreases linearly with flow velocity in a 1.6 mm flow phantom from an approximately 45 % at 0.1 ml/s to 10 % at 0.34 ml/s. The trend in the 3 mm (ID) phantom is not linear as an increase in targeting intensity occurs from 0.33 ml/s (133 %) up to 0.5 ml/s (200 %) with greater variation in the amount of targeting. This then decreases to 50% at 0.74 ml/s. After this targeting can no longer be detected. Variation in results can again be observed in a 6 mm flow phantom but a linear decrease can be observed. From a 50 % maximum at 0.48 ml/s to 10 % at 0.34 ml/s with minimal variability.

These results do show large variability between phantoms and variability in results at the same flow velocities in vessels. Accurate concentrations of microbubbles cannot be determined from the results. However, a definite trend can be observed whereby with increasing flow rate the acoustic intensity of the targeted microbubbles decreases. As outlined above for targeting time this appears to be mainly shear rate dependent.

The results for targeting time and acoustic intensity for lower magnetic field strengths are in the appendix. These results showed more variability and trends were much harder to discern.

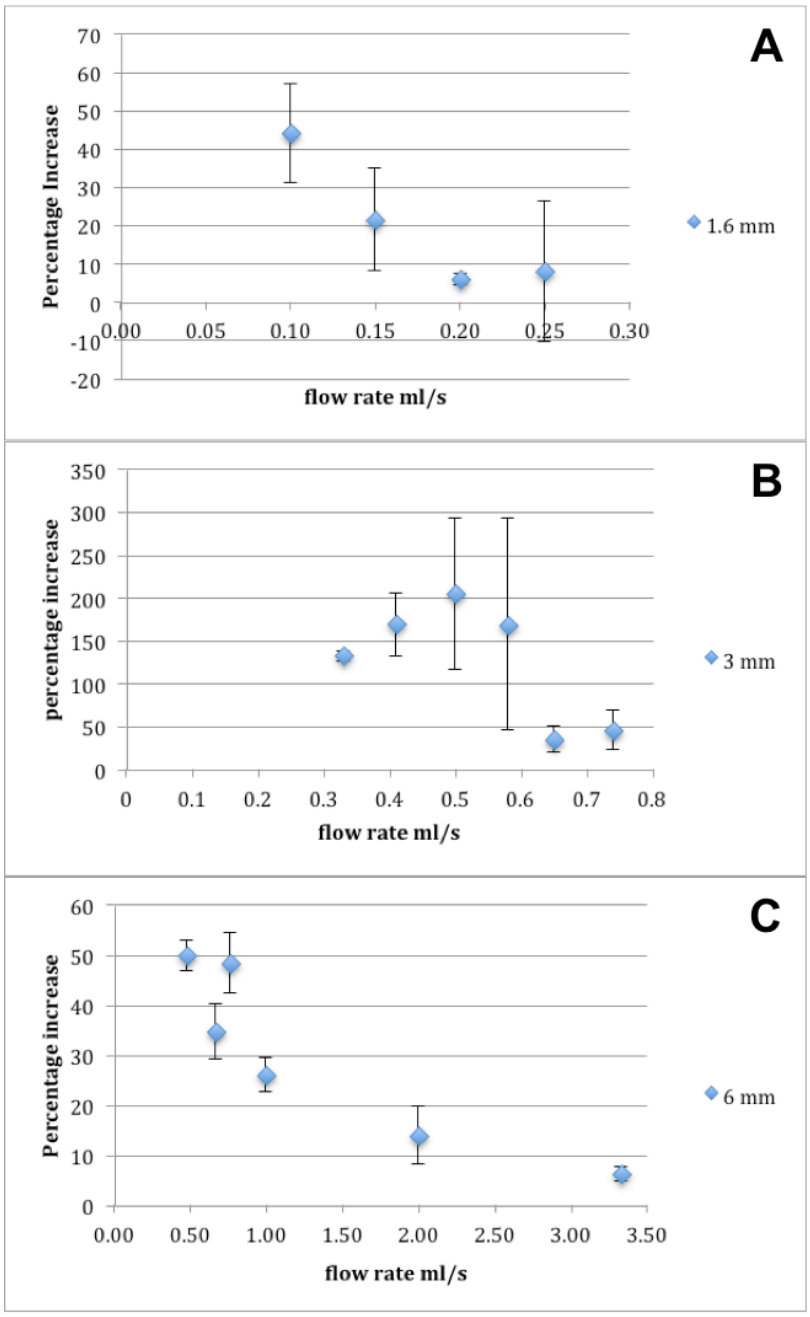


Figure 5.4, percentage increase in signal intensity along the bottom of the tube against volume flow rate of water at a high magnetic field strength in a 2.6, 3.0 and 6.0 mm ID flow phantom.

5.3.4 Optical observation of magnetic targeting

The capillary flow phantom and imaging protocol are described in Chapter 3, section 3.2.7.2. The flow rate in the capillary tube was varied and videos recorded from the microscope. Unfortunately only one capillary size was available (200µm inner diameter). Magnetic microbubbles could easily be observed successfully targeting against the flow (Figure 5.5).

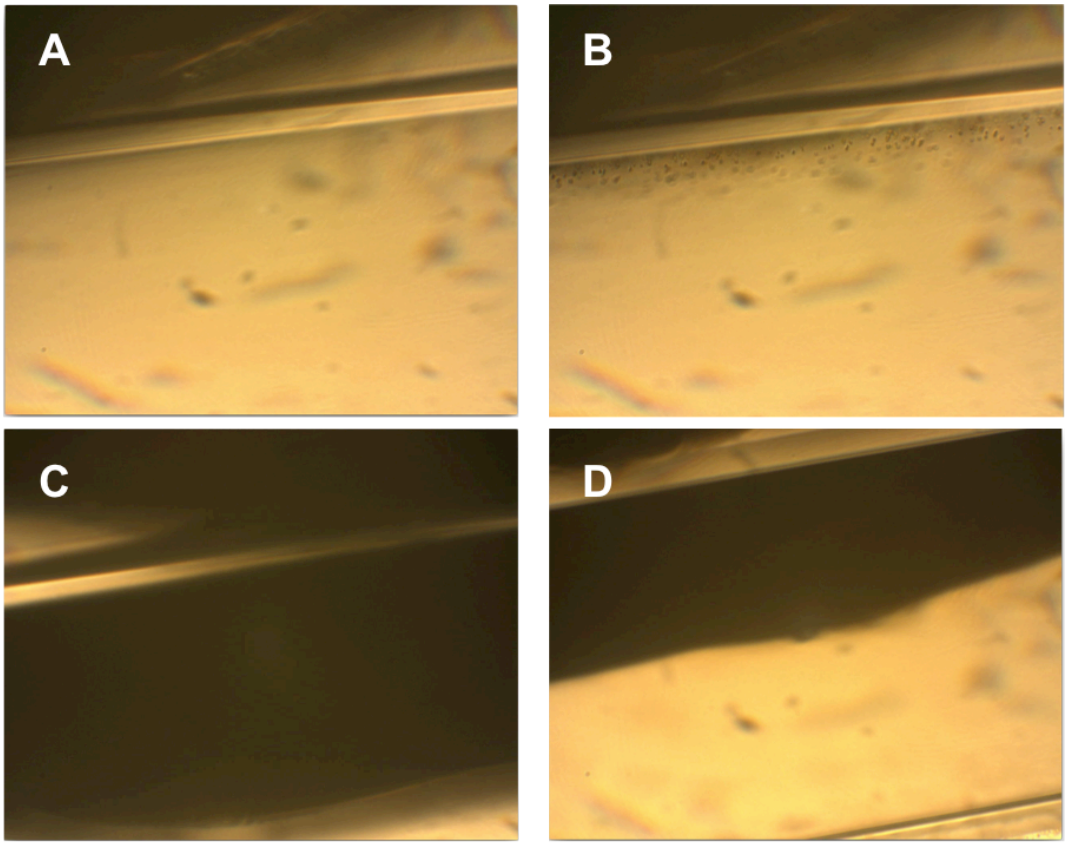


Figure 5.5, optical microscope images of targeting. A) image of 200 µm (ID) capillary tube with a magnet placed alongside and water flowing through. B) Microbubbles being pulled out of flow and targeting at a shear rate of 216/s. C) the bolus of microbubbles formed after 3 minutes at a shear rate of 216/s D) the bolus of microbubbles successfully targeted at a shear rate >1000/s.

Over approximately 3 minutes such a large number of microbubbles successfully targeted that a bolus of magnetic microbubbles was formed which extended out 150 μm into the capillary tube (C) i.e. three quarters of the width. When the experiment was repeated with a shear rate >1000/s, as observed in certain parts of the capillary system in the human body, magnetic targeting was still observed to take place although the bolus of microbubbles formed was smaller only covering one third of the width of the capillary tube (65 μm). The magnet could not be moved further away from the capillary tube as the targeting microbubbles pushed the capillary tube towards the magnet reducing reproducibility. However, these results indicate that magnetic microbubbles are capable of being successfully targeted at shear rates of over 1000/s with a wall magnetic field strength of 0.2 T and gradient of 55 T/m. The microbubbles also targeted for the length of the video (4 min).

5.3.5 The effect of targeting on microbubbles

Magnetic microbubbles before targeting are shown in high concentration in panel A in Figure 5.6. They were indistinguishable from previous magnetic microbubble batches in size distribution, concentration and appearance.

After targeting had been observed under ultrasound and the magnetic field removed the flow was continued in order to disperse the bolus of microbubbles. The resulting suspension, light brown in colour, was examined optically as shown in panel B in Figure 5.6. The concentration is greatly reduced but individual magnetic microbubbles can still be observed owing to the dark circular shapes observed. No large agglomerated objects were discovered in over 30 optical microscope images taken from the sample. Size distributions were analysed but the microbubbles were so

diluted after being flown through that a meaningful comparison could not be obtained. However, no large variations could be observed.

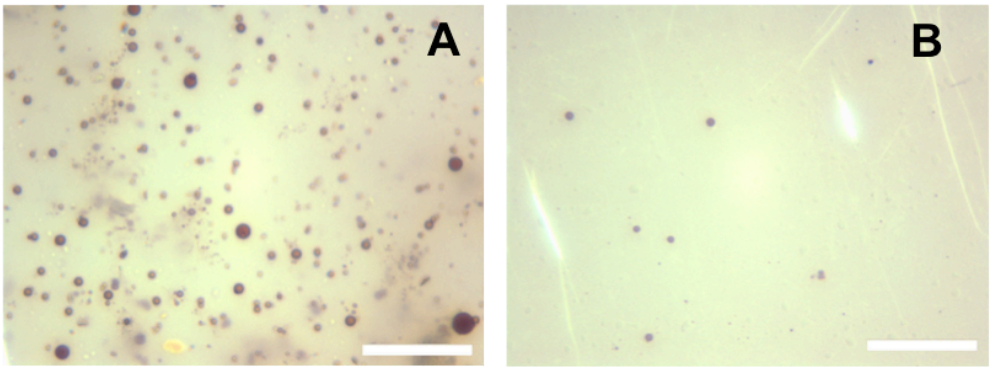


Figure 5.6, optical microscope images of magnetic microbubbles at 400x magnification A) before being injected into the flow phantom and B) after being injected into the flow phantom. Scale bar is 40 µm.

5.4 Discussion

Magnetic microbubbles were successfully targeted against flowing water with a variety of flow conditions, vessel sizes and magnetic field strengths. Acoustic detection of microbubble targeting showed that a bolus of microbubbles could be observed in flow conditions mimicking minor arteries (200 ml/min), all veins and capillaries up to a shear rate of approximately 500/s [7]. However, optical observation of targeting in a 200 µm capillary tube indicated that magnetic microbubbles are capable of targeting at shear rates even higher than those found in the capillaries (>1000/s, 0.0084 ml/s) in high concentration [7].

A major application for targeted therapeutic delivery is cancer chemotherapy. The blood supply to tumours is most commonly via the capillaries and veins. Consequently, targeting is more likely to occur at flow conditions found in the

capillaries, venules and veins and not at the high flow rates found in the arteries (400 ml/min) [10]. Red blood cell velocity can also be an order of magnitude lower in tumour vessels compared to normal vessels and consequently, the results outlined above provide a proof of concept for the feasibility of magnetic targeting for cancer therapy even with the relatively small magnetic field strengths used in the experiments [11]. The magnetic field strengths can be increased using guidelines established for MRI, where magnetic fields within patients can be as high as 2.5 T [12], with much more relevance for cancer therapy at greater depths *in vivo*. Alternatively, for a thrombus the flow rate in the artery will be reduced and consequently magnetic targeting may be feasible under these conditions [13].

To the best of the author's knowledge only one other publication has examined the targeting of magnetic microbubbles *in vitro* (Vlaskou *et al*). As described above, the study used magnetic acoustically active liposomes (MAALs) in a 1 mm ID tube with a flow rates between 0-9.9 ml/min. A 0.9T electromagnet with a field gradient of 100 T/m was placed directly below. Magnetic targeting was detected by examining fractions that had passed through; direct observation did not take place. The study concluded that MAALs could target against a flow rate of 9.0 ml/min. This is equivalent to a shear rate of approximately 191/s. The magnetic microbubble formulation published by Stride et al can magnetically target at a shear rate >1000/s and a flow rate in a 6 mm ID vessel of 200 ml/min at a lower magnetic field strength (0.2 T) and gradient (55 T/m). These are much more clinically relevant flow conditions. Vlaskou *et al.* also did not examine different vascular sizes to determine the effects of flow rate, shear rate and magnetic field penetration. Targeting was only quantified as the number of MAALs that did not flow through the vessel were

assumed to have been magnetically targeted [4]. The present study showed direct observation of microbubbles targeting optically and acoustically and trends in the quantity and targeting time of microbubbles were obtained.

The results in Figure 5.6 indicate that magnetic microbubbles do not undergo any major structural changes after targeting. A more rigorous approach may be required to prove no harmful side effects are possible via *in vivo* studies but these preliminary results indicate targeting is safe with respect to the risk of embolism from agglomerated bubbles. As low flow rates were used in this study and large quantities of bubbles were targeted and no large agglomerated objects could be discerned targeting of magnetic microbubbles will not produce large objects that could potentially cause harm *in vivo*. This also provides evidence that magnetic nanoparticles incorporated into microbubbles remain superparamagnetic and do not change to become ferromagnetic as agglomeration does not occur.

5.5 Limitations

The large standard deviations observed in Figure 5.3 and Figure 5.4 show the variability in targeting from batch to batch and within each batch over time. This occurred even with magnetic microbubbles produced via exactly the same protocol. The reason for this is due to sonication being used as the manufacturing process which produces a large quantity of microbubbles in a relatively short space of time [14]. For non-magnetic microbubbles this can vary the shell thickness, microbubble size and acoustic response of the microbubbles. Incorporating a layer of ferrofluid now varies the magnetic response of all microbubbles as the oil layer thickness changes in each microbubble. As such there is a large variability in some results depending on the distribution of magnetic microbubbles used. This is more pronounced in data obtained at low magnetic field strengths (Appendix).

The linear decrease in targeting with increasing flow/shear rate and the standard deviations (n = 3) indicate that this technique has been successful in elucidating targeting profiles for magnetic microbubbles but further comparisons with optical targeting or drug delivery under flow could further be used to confirm this new technique.

The experiments are constrained by the magnetic Halbach array which has a magnetic field strength of 0.75 Tesla at the surface and a field gradient that decreases by half every 5 mm. As such the maximum field strength available at the tube wall is very low (0.5 T) compared to that used in MRI machines (>9 T). A higher field strength at the same gradient will have deeper penetration and is more likely to attract more

microbubbles further from the magnet than a lower magnetic field strength. MR imaging also uses much higher magnetic field strengths within the human body so much higher magnetic field strengths can be used to target in the human body. Being able to target against the maximum possible flow rate and shear rate would provide the best evidence that magnetic microbubbles can target in the human body for drug delivery.

One of the major limitations with the software for analysing targeting is that the user has to assign the area of interest, which can vary. The criteria used to judge whether magnetic targeting has taken place may also be too harsh as magnetic microbubbles could be targeting in such small quantities as to not be detected by ultrasound. The best way to determine whether this has taken place would be to combine magnetic targeting with therapeutic delivery to cells in vitro to ensure microbubbles had successfully targeted for a long enough time and in sufficient concentration to successfully deliver drugs.

5.6 References

1. Stride, E., et al., *Enhancement of Microbubble Mediated Gene Delivery by Simultaneous Exposure to Ultrasonic and Magnetic Fields.* Ultrasound in Medicine & Biology, 2009. **35**(5): p. 861-868.
2. Mulvana, H., et al., *Theoretical and Experimental Characterisation of Magnetic Microbubbles.* Ultrasound in Medicine and Biology, 2012. **38**(5): p. 864-875.
3. Pankhurst, Q.A., et al., *Applications of magnetic nanoparticles in biomedicine.* Journal of Physics D: Applied Physics, 2003. **36**(13): p. R167-R181.
4. Vlaskou, D., et al., *Magnetic and Acoustically Active Lipospheres for Magnetically Targeted Nucleic Acid Delivery.* Advanced Functional Materials, 2010. **20**(22): p. 3881-3894.

5. Wu, J., et al., *Efficacy of contrast-enhanced US and magnetic microbubbles targeted to vascular cell adhesion molecule-1 for molecular imaging of atherosclerosis.* Radiology, 2011. **260**(2): p. 463-471.
6. Guyton, A.C. and J.E. Hall, *Textbook of Medical Physiology*. 11th ed. 2006: Philadelphia : Elsevier Saunders. 1116.
7. Whitmore, R.L., *The flow behaviour of blood in the circulation.* Nature, 1967. **215**(5097): p. 123-126.
8. Weller, G.E.R., et al., *Ultrasonic imaging of tumor angiogenesis using contrast microbubbles targeted via the tumor-binding peptide arginine-arginine-leucine.* Cancer Research, 2005. **65**(2): p. 533-539.
9. Zhao, S., et al., *Radiation-force assisted targeting facilitates ultrasonic molecular imaging.* Molecular Imaging, 2004. **3**(3): p. 135-148.
10. Jain, R.K., *Normalizing Tumor Microenvironment to Treat Cancer: Bench to Bedside to Biomarkers.* Journal of Clinical Oncology, 2013. **31**(17): p. 2205-2218.
11. Ribatti D., *Morphological Aspects of Tumour Microcirculation*. 2012: Springer.
12. Farr R., F. and J. Allisy-Roberts P., *Physics for Medical Imaging*. 2005: Saunders.
13. Yamashita, A., et al., *Increased Vascular Wall Thrombogenicity Combined With Reduced Blood Flow Promotes Occlusive Thrombus Formation in Rabbit Femoral Artery.* Arteriosclerosis, Thrombosis, and Vascular Biology, 2004. **24**(12): p. 2420-2424.
14. Feshitan, J.A., et al., *Microbubble size isolation by differential centrifugation.* Journal of Colloid and Interface Science, 2009. **329**(2): p. 316-324.

6 *In vivo* factors

6.1 Summary

Magnetic microbubble formulation 1 (MMB) was examined against conditions found *in vivo.* A liver perfusion system was used to examine magnetic targeting in a clinically relevant model. The impact of blood on magnetic microbubbles in a both a static and dynamic environment was then examined. Blood was found to decrease magnetic microbubble targeting efficiency but a more pronounced effect was noticed on biochemical microbubble targeting. Evidence indicates, in both cases, that the decrease in targeting is due to collisions with red blood cells.

6.2 Liver study

Targeted drug delivery of magnetic microbubbles has already been successfully demonstrated in a mouse model [1]. However, as described in the previous chapter, for magnetic targeting a mouse does not accurately represent the in vivo conditions of a human being. A more clinically relevant model for *in vivo* experiments was however kindly made available by Dr. Daniel Chung and Dr. David Holroyd as described in Chapter 3 section 3.2.10.1 and developed by Prof. Constantin Coussios. Using a perfusion system, blood flow can be simulated and magnetic microbubbles could be injected into the flow or injected into a vessel in the liver. The organ can be imaged with ultrasound and a magnetic field can be brought into close proximity making it an ideal candidate for examining magnetic targeting *in vivo*. This formed the basis for a preliminary examination of *in vivo* factors such as blood flow, the presence of microvasculature, vessel wall elasticity and interaction of microbubbles

with *in vivo* components which could not be analysed in the experiments described in Chapter 5 but which are likely to be very important clinically.

6.2.1 Materials and methods

Magnetic microbubble formulation 1 (MMB) was prepared and the liver perfusion experiments conducted as described in Chapter 3.

In the *in vitro* studies the maximum flow rate at which significant magnetic targeting was observed was 200 ml/min in water at 0.5 T and 55 T/m. Given the comparatively large size of the liver, the maximum magnetic field strength and gradient that could be achieved with the available magnetic array in a suitable vessel were 0.025 T and 55 T/m. The flow rate in the vessel was ~400 ml/min as observed by Doppler imaging mode using an ultrasound probe (model L10-5; Zonare Medical Systems, Mountain View, CA, USA) and a Zonare z-one (Zonare Medical Systems, Mountain View, CA, USA). Preliminary experiments confirmed that observable targeting of microbubbles could not be achieved. The subsequent experiments were therefore performed at a reduced flow rate (< 1 ml/min).

6.2.2 Results

Two livers were utilised in the experiments. Non-magnetic microbubbles were first injected into the target vessel as shown in Figure 6.1A to confirm they could be visualized under ultrasound. As expected the bubbles were washed through the vessel and not retained.

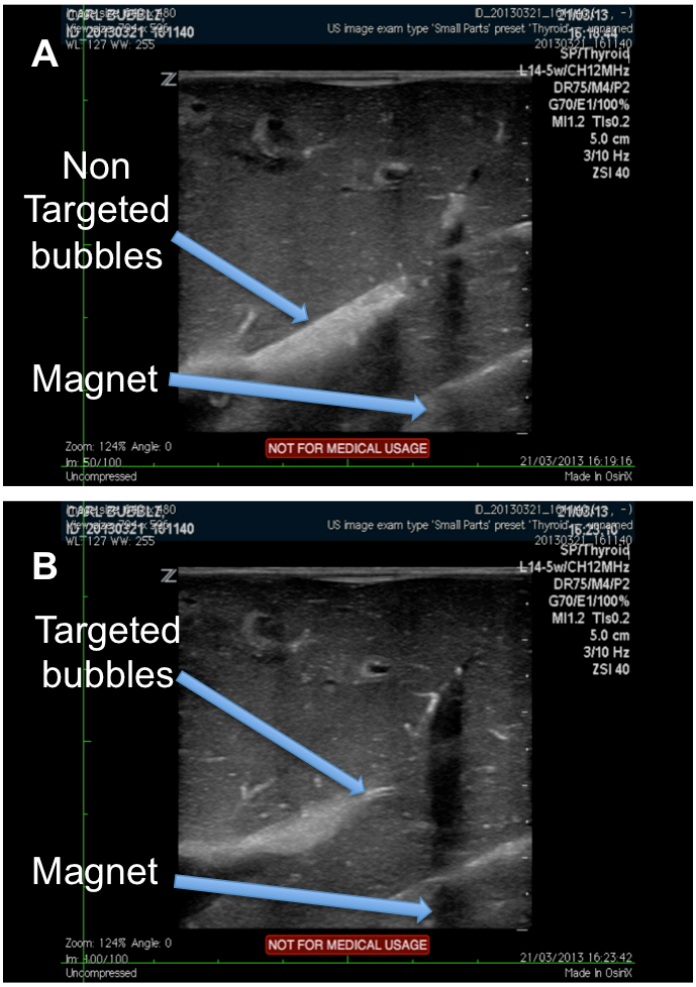


Figure 6.1, Microbubbles being injected into a liver with no flow in the vessel A) image of vessel after non-targeted microbubbles have been injected. B) An image of the vessel after washing with flowing blood, stopping the flow and injecting targeted microbubbles.

Magnetic microbubbles were then injected into the vessel. As indicated by the arrow in Figure 6.1B an increase in brightness was observed at the wall of the vessel at the point nearest the Halbach array.

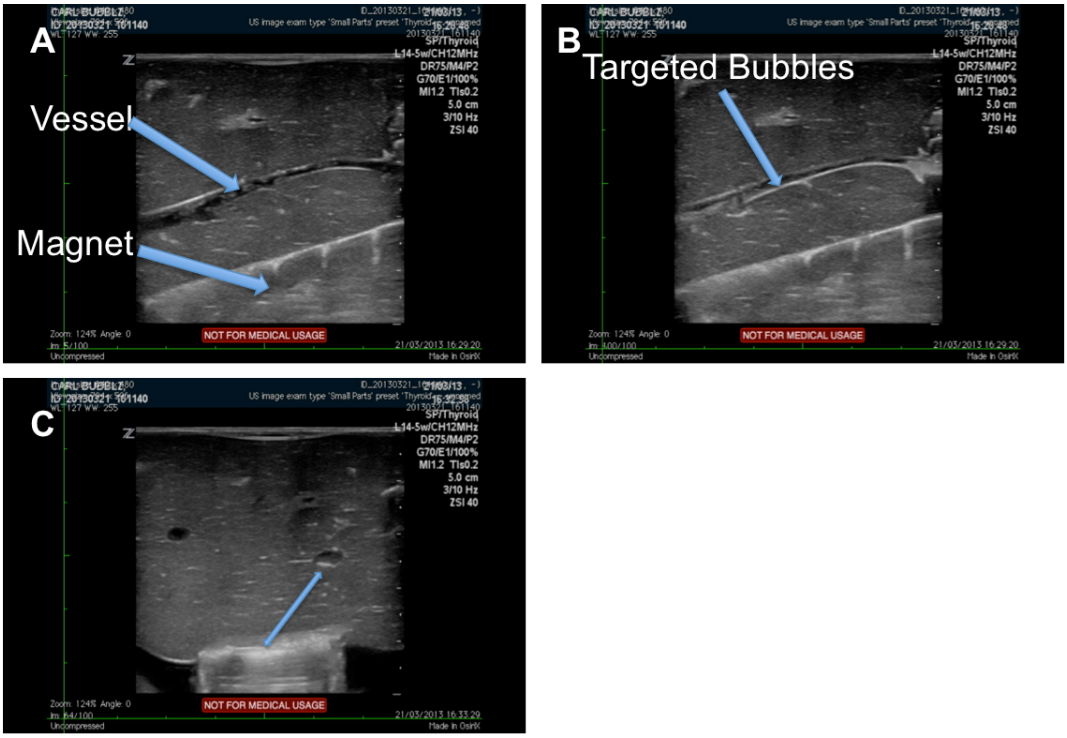


Figure 6.2 Targeting of magnetic microbubbles in a perfused liver. A) image of vessel in liver with a magnetic Halbach array positioned 1 cm (0.05 T) below. B) The flow was stopped and magnetic microbubbles were injected and were pulled onto the bottom of the vessel by the magnetic field. C) Side on view showing the vessel was not above the centre of the magnetic halbach array.

The experiment was repeated in a second liver. In this case it was possible to position the Halbach array closer to the vessel of interest giving a field strength of approximately 0.05 T along the bottom of the vessel as shown in Figure 6.2A. A needle was inserted directly into the vessel and magnetic microbubbles were injected. The microbubbles settled along the bottom of the target vessel as shown in Figure 6.2B. As far as could be seen from the images, the microbubbles remained in the vessel and did not enter the microvasculature and or extravasate through the vessel wall.

6.2.3 Limitations

The Halbach array could not be removed during experiments as the vessel would be lost and the ultrasound view would be different. This forced the use of non-magnetic microbubbles as control rather than magnetic microbubbles without a magnetic field. However, as magnetic microbubbles have been shown through numerous *in vitro* studies not to target or overcome buoyancy without application of a magnetic field the candidate believes that the study is still valid for examining the feasibility of magnetic microbubbles as targeted drug delivery vehicles *in vivo*.

6.3 The impact of blood upon the targeting of microbubbles

The magnetic targeting experiments in the perfused liver model further demonstrated the importance of achieving a sufficient magnetic field strength and gradient at the target location to retain microbubbles at high volume flow rates. Another feature of the *in vivo* environment that these experiments indicated affected targeting was the different rheological behaviour of whole blood as opposed to saline.

6.3.1 The impact of blood upon targeting

To the best of the candidate's knowledge, no previous studies on the targeting of microbubbles has attempted to look at the effects that the characteristics of blood might have on retention *in vitro* before undertaking *in vivo* experiments. Two studies of targeted microbubbles suggested that blood should be examined but the candidate has not been able to find any evidence that this study took place [2, 3].

Blood is very different to saline in terms of its rheological properties. It contains approximately 40 % concentration by volume (haematocrit) of particles, mainly consisting of deformable red blood cells (RBC) or erythrocytes, which make the macroscale properties of blood non-Newtonian. As such the shear viscosity changes with the shear rate. At low shear (< 1/s) erythrocytes start agglomerating into rouleaux and under high shear (>200/s) they move towards the centre line of the vessel leaving a plasma rich region next to the vessel wall with a lower viscosity (vessel size 20 -300 μm) [4-6].

Munn *et al.* showed that this phenomenon is important in terms of immune reactions. As the disc shaped red blood cells move to the centre line of the blood flow, the more spherical leukocytes and platelets are forced to the RBC free layer. Subsequent collisions of leukocytes with the cell layer promotes molecular interactions [7, 8]. Some studies have been made of the interaction between blood components and other types of particle. Gentile *et al.* found that the combination of shear rate and particle shape determined whether or not particles became marginalized to the plasma rich layer [9].

Charoenphol *et al.* used a parallel plate flow chamber with one section coated in endothelial cells to examine the targeting of differently sized particles (0.2 to 5 μm) against blood flow. Laminar and pulsatile flow with a wall shear rate of 500 and 1000/s was used. Increasing the haematocrit increased binding of smaller particles (2 μm) and decreased the binding efficiency of larger ones (5 μm). Hematocrit had minimal effect on targeting of nano scale particles which was consistently below the efficiency of microspheres. The authors found optimum sizes for targeting particles

which were 3-4 μm in laminar and pulsatile flow, and 5-6 μm in recirculating whole blood flow which is due to the size of the red blood cell free layer [10]. This is the relevant order of magnitude for microbubbles.

Namdee *et al.* examined the effect of red blood cells on the margination of coated spheres of various sizes to inflamed tissue in vitro using rectangular flow channels on the order of human arterioles and venules (20 – 200 μm). 200, 500 nm and 2 and 5 μm polystyrene spheres coated with a ligand targeted to E-selectin expressed by inflamed endothelial cells were examined in a home made microfluidic chamber with a monolayer of cells on the top and wall shear rates of 100, 200 and 500/s. Increasing particle diameter increased particle adhesion density and increasing ligand density on the particle surface increased adhesion [6].

Increasing the concentration of red blood cells (hematocrit) has been shown to increase the quantity of bound particles, but this is more pronounced with microparticles than with nanoparticles. The size of the RBC free layer has a large impact on targeting efficiency but microspheres consistently outperformed nanospheres under all flow conditions [6].

Research has been performed into how the acoustic response of microbubbles can be affected by being insonated in blood by Stride *et al.* In this case no effect was observed on the attenuation or speed of sound through the microbubble suspension [11]. However, red blood cells have been found to have an impact upon therapeutic delivery. For example erythrocytes were found to bind and inactivate type 5 adenovirus [12]. The impact of blood and the constituents of blood on the targeting

of microbubbles in general have not been examined. As the majority of targetable microbubbles utilize biochemical targeting it was decided to use this opportunity in order to compare magnetic and biochemical targeting and the relative impact of blood upon both.

6.3.2 The effect of blood on the microbubbles

Magnetic microbubbles were synthesised as described in Chapter 3 and a size distribution obtained as shown in Figure 6.3A. 500 µl of the bubble solution was mixed with 500 µl of either PBS or blood and both samples were analysed via optical microscopy after approximately 5 minutes. The aim of the first study was to examine if microbubbles behave differently in blood and saline under static conditions.

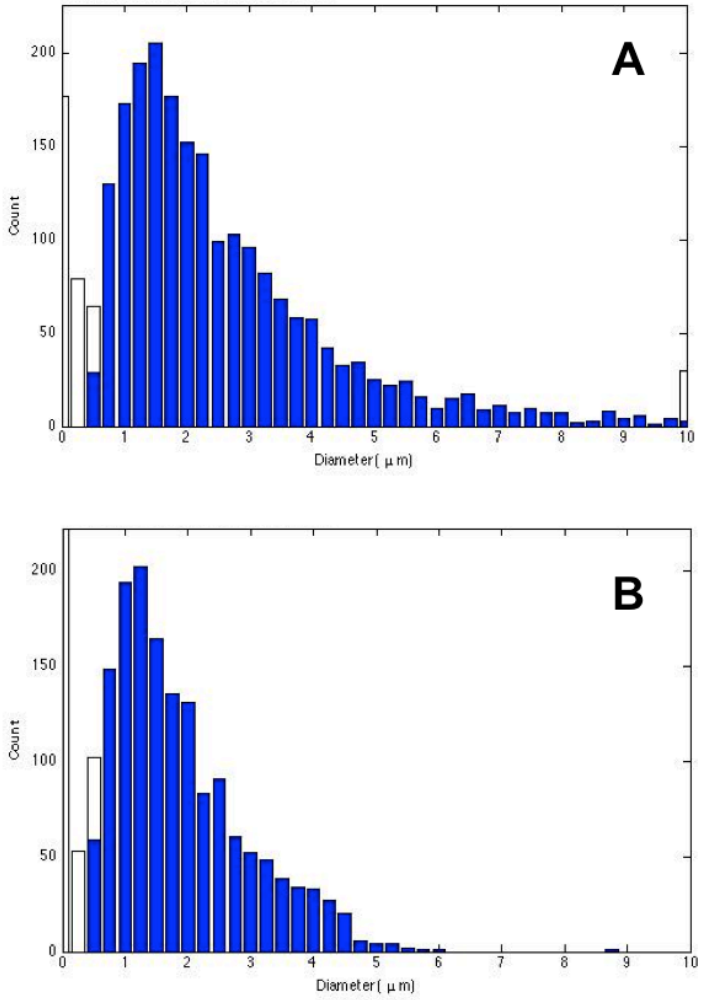


Figure 6.3, size distribution of magnetic microbubbles. A) size distribution of magnetic microbubbles in water, B) size distribution upon diluting 500 µl of magnetic microbubble solution in blood (500 µl).

Diluting the microbubbles in water had minimal impact upon microbubble concentration and size distribution within the margins of error. Diluting the magnetic microbubbles in blood seemed to have a similar effect to diluting the microbubbles in water (Figure 6.3). The average size decreased to 1.90 µm from 2.59 µm but this is within the standard deviation and error due to the measurement technique based on analysis of optical images.

No great differences can be seen in the size difference of the magnetic microbubbles. Overall concentrations also seemed to be very similar indicating that magnetic microbubble destruction is not taking place.

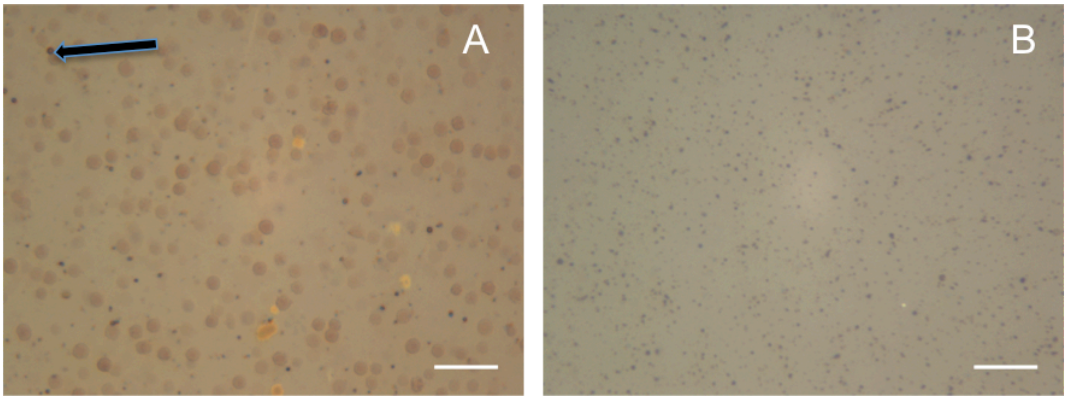


Figure 6.4, A) image of magnetic microbubbles with red blood cells, the arrow points to a magnetic microbubble. B) image of magnetic microbubbles along the bottom of the slide where red blood cells would be found. Scale bare is 50 µm.

Optical observation of magnetic microbubbles again show that the red blood cells are not having a detrimental effect. This is clearly shown in Figure 6.4A, where objects of similar shape to magnetic microbubbles can be seen alongside red blood cells. No agglomeration or change in microbubble shape can be discerned. From optical observation and size analysis it can be concluded that within the timeframe of the experiments blood does not have a detrimental effect on magnetic microbubbles.

6.3.3 Limitations

Microbubble stability was only examined for 5 minutes whereas microbubble survival time in vivo is approximately 10 – 15 minutes [13]. For magnetic microbubble targeting experiments the total experiment time from injection is <5 minutes. For the purposes of the magnetic experiments taking place in this research the lack of change of microbubble structure or microbubble agglomeration in blood helps confirm any

results obtained. However, to have a complete profile of microbubble stability in blood for use in clinical trials longer stability studies in blood must be performed for as long as magnetic microbubbles can survive. The blood used in these experiments has been heparinized which is not representative of blood *in vivo*. However, in order to use blood *in vitro* it must be heparinized. Whether and if so how this will affect targeting is unclear.

6.4 Examination of the impact of blood on magnetic targeting in a medium size vessel

6.4.1 Introduction

In order to determine the effect of flowing blood on magnetic microbubbles the flow experiments were repeated in a 1.6 mm (ID) flow phantom at all flow rates examined in chapter 5. It was also decided to further examine the impact of blood by attempting magnetic targeting in a 3 mm ID flow phantom under the same conditions in water and in blood for which a large bolus had previously formed.

6.4.2 Materials and methods

The same method as presented in chapter 3 section 3.2.7.2 above was used in a 1.6 mm (ID) flow phantom with blood as the suspending fluid at all flow rates used in chapter 5. The same experimental set up was used with a 3 mm (ID) flow phantom to examine the impact of blood on the magnetic microbubbles bolus. However, the flow was kept constant at 0.25 ml/s and each experiment was repeated 3 times. After obtaining results for 1) flowing PBS, 2) magnetic microbubbles in flowing PBS and

3) magnetic microbubbles in flowing PBS with an applied magnetic field the experiments were then repeated with flowing blood.

6.4.3 Results

The impact of blood on the maximum flow conditions for magnetic targeting in a 1.6 mm ID flow phantom is shown in Table 6.1. A reduction in the maximum flow conditions against which magnetic targeting of microbubbles was observed. Magnetic microbubbles can target against a maximum shear rate of 373/s in blood down from 497/s in water in a 1.6 mm ID flow phantom. Blood reduced the maximum shear rate against which magnetic microbubbles could target. The viscosity of blood at a shear rate of 300/s is 5 mPa.s which is higher than water at 500/s which has a value of 1 mPa.s [14]. However, viscosity is a bulk phenomenon of the fluid and the individual microbubble will be surrounded by aqueous solution with the same viscosity as water when flowing in blood. As such the impact of viscosity should be minimal.

Table 6.1, Table of the maximum flow conditions at which magnetic targeting has found to successfully occur

Tube Diameter (mm)	Fluid	max flow rate (ml/s)	shear rate (/s)	viscosity (mPa.s)	magnetic field strength (T)
1.6	water	0.20	497	10	0.20
1.6	blood	0.15	373	50	0.20

In the 3 mm phantom the results for magnetic microbubbles in PBS were as expected; no increase in intensity was observed for PBS alone, no targeting was observed for magnetic microbubbles alone and strong targeting was observed when a magnetic

field was applied as shown in Figure 6.5. This was successful on each occasion and is backed up by the results obtained in Chapter 5.

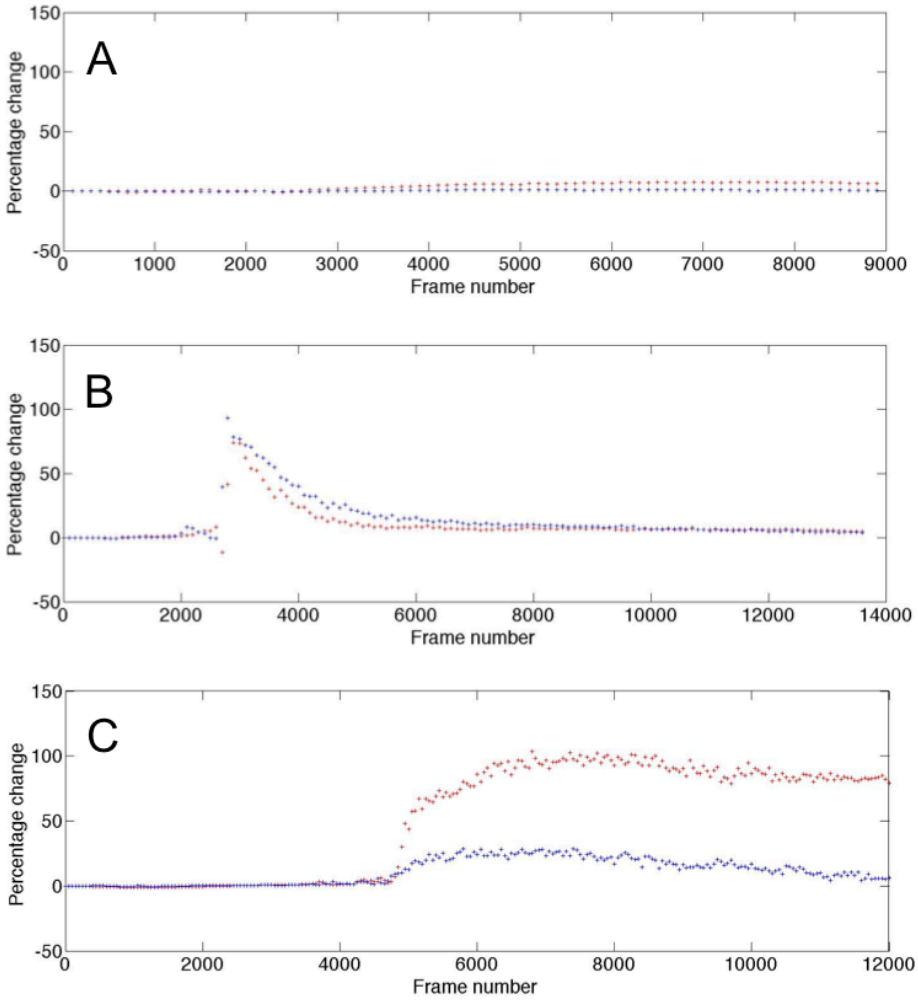


Figure 6.5, percentage change in intensity plotted against frame number for the side nearest the magnet (red) and the side furthest from the magnet (blue). A) the intensity profile for PBS alone flowing, B) The intensity profile for magnetic microbubbles flowing through and C) the intensity profile for magnetic microbubbles flowing through in the presence of a magnetic field. The red line passing above the blue in percentage change indicates that targeting has occurred.

Blood alone caused no change in intensity along the vessel walls which was expected (Figure 6.6A). Magnetic microbubbles in blood showed no signs of targeting in the

absence of the magnetic array (B). Upon application of a magnetic field, targeting of microbubbles was observed. However, the intensity of the image in the target region was significantly reduced as shown in C. This was repeated three times and the result shown in Figure 6.6 represents the largest increase in intensity observed.

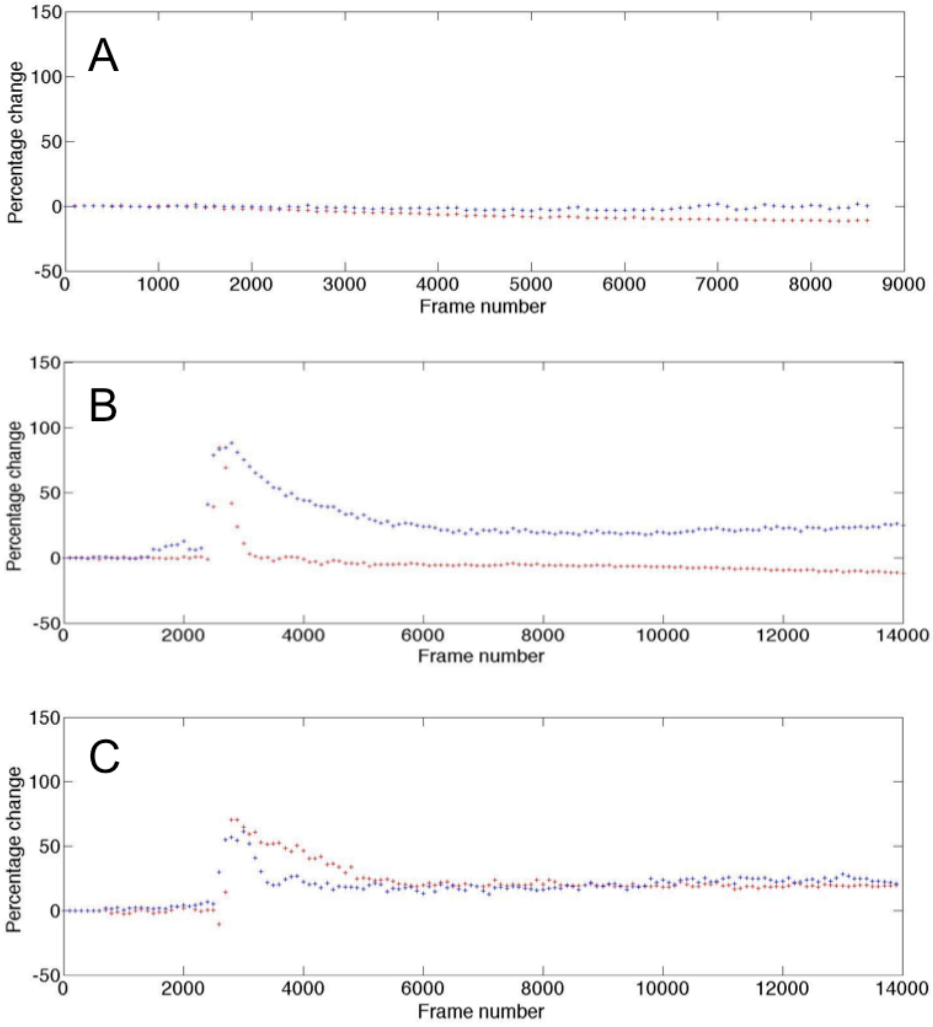


Figure 6.6, Percentage change in intensity plotted against frame number for the side nearest the magnet (red) and the side furthest from the magnet (blue). A) the intensity profile for blood alone flowing, B) The intensity profile for magnetic microbubbles flowing through in blood and C) the intensity profile for magnetic microbubbles flowing through blood in the presence of a magnetic field. The red line passing above the blue in percentage change indicates that targeting has occurred.

Because such a pronounced decrease in targeting efficiency was observed via ultrasound it was decided to observe the effects optically in a capillary tube, to visualise what occurs.

6.5 Optical analysis of the impact of blood

The apparatus used for examining microbubbles in a capillary under optical microscopy could be readily adapted to observe magnetic targeting in the presence of blood.

As indicated above, it was decided to investigate the impact of blood upon biochemical targeting in the same experiment. This would also provide a useful comparison between biochemical and magnetic targeting. Avidin Biotin was chosen as the biochemical targeting strategy owing to its low cost, its versatility, its reliability and because it has shown to work in previous publications. For example, Zhao *et al.* have shown previously that biotin coated microbubbles can be targeted to the walls of cellulose capillary tubes coated with avidin [15]. Biochemical targeting could not be observed in the latex tube flow phantoms used to quantify magnetic targeting as the concentration of successfully targeted microbubbles was too low.

6.6 The effect of blood on magnetic targeting

The set up is as described in Chapter 3 section 3.2.9

Magnetic microbubbles were successfully targeted in a capillary tube at a flow rate of 10 μl/min. This was repeated three times. Upon repeating the experiments in flowing

blood a reduction in the number of targeted magnetic microbubbles was observed (Figure 6.7).

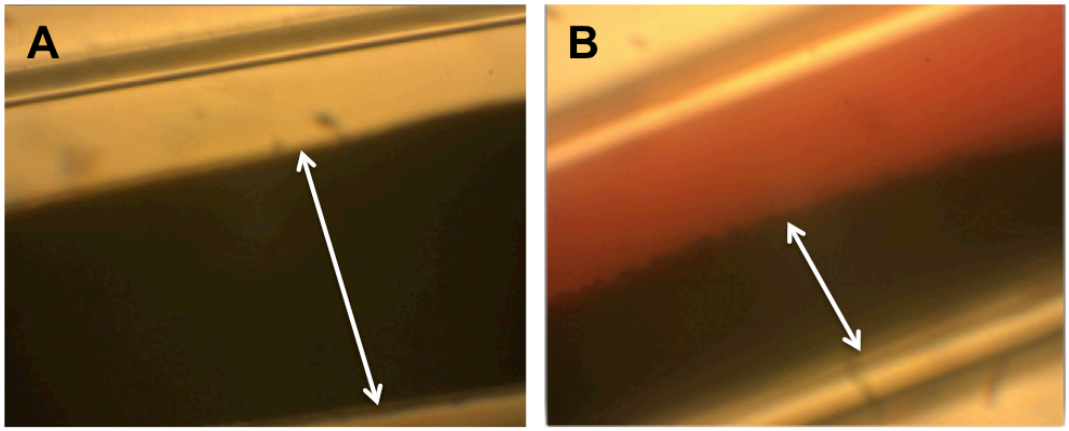


Figure 6.7, images of magnetic targeting of microbubbles in a capillary tube (200 um ID) in a) PBS and b) blood at a flow rate of 10 ul/min and a shear rate of 212/s.

In order to provide a quantitative comparison the microbubble bolus was measured from the images using ImageJ software. This was then divided by the average projected area of a magnetic microbubble as obtained from the size distribution (2 μm) to provide an approximate indication of the number of bubbles retained. Analysing all the data that were obtained in this way produced a bar chart as shown in Figure 6.8. As shown below in PBS, in the field of view, on average 1600 microbubbles were retained. However in blood, this was reduced to approximately 600 microbubbles, a reduction of approximately 60 %. For control experiments when no magnetic field was applied no targeting was observed in blood or water.

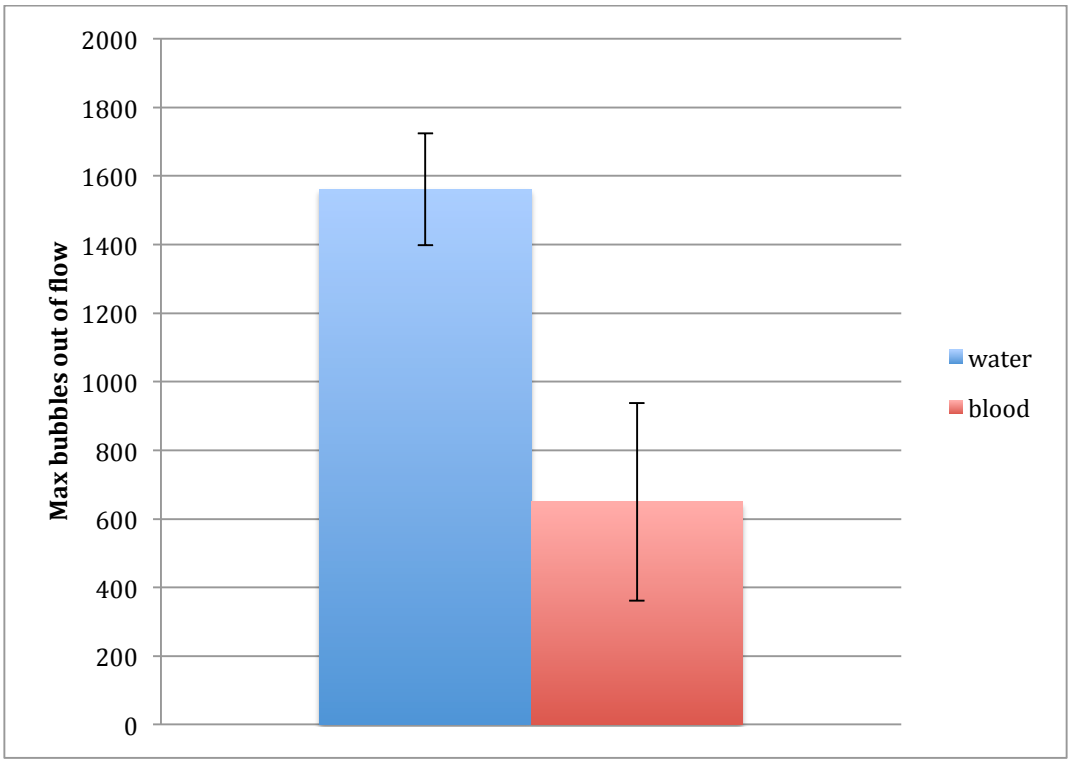


Figure 6.8, Quantification of the amount of magnetic targeting that has occurred in flowing water and in flowing blood.

6.6.1 The effect of blood on biochemical targeting

As blood was determined to have a detrimental effect on magnetic targeting it was decided to examine the impact of blood on biochemical targeting as a comparison. Biotin coated microbubbles were prepared as described in Chapter 3 section 3.2.1.7. Capillary tubes were coated with avidin and the top of the tube is viewed via optical microscopy as owing to buoyancy the majority of microbubbles will reside near the top. Each experiment was repeated three times.

6.6.2 Results

Biotin coated microbubbles were flown through the avidin coated capillary tube at 10 µl/min in PBS and in blood. In PBS microbubbles were observed coming out of flow and attaching to the surface of the capillary tube. After approximately 1.5 minutes no additional microbubbles had come out of flow (Figure 6.9A). Similar results were observed in each of the experiments. When blood was substituted for PBS a reduction in targeting efficiency was instantly noticed (Figure 6.9B). Similar results were observed on each repeat. All videos were analysed via the method outlined in Chapter 3 section 3.2.9.3.

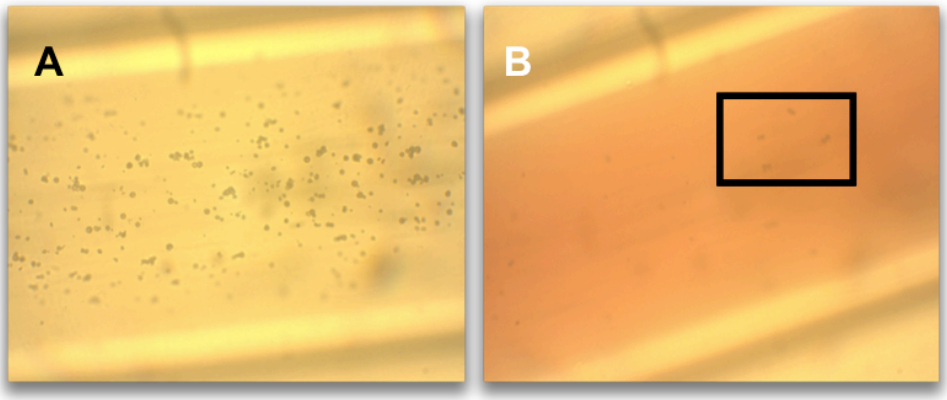


Figure 6.9, optical microscope images (x 40 magnification) of biotin microbubbles after having flown through an avidin coated capillary tube (ID 200 µm) in A) PBS and B) blood after three and a half minutes. Black box indicates the location of the targeted microbubbles in blood.

As the number of bubbles targeted was much lower it was possible to count them directly from the images. The results are shown in Figure 6.10. In PBS the maximum number of bound biotin microbubbles within the field of view varied between 100 and 200; on average 140. In blood the average decreased by 90 % to a maximum of 9 successfully targeted microbubbles. This is reinforced by the control results from

targeting biotin microbubbles to an uncoated capillary tube. In water on average a maximum of about 20 – 30 microbubbles attached to the tube surface, when blood is substituted this was reduced to zero.

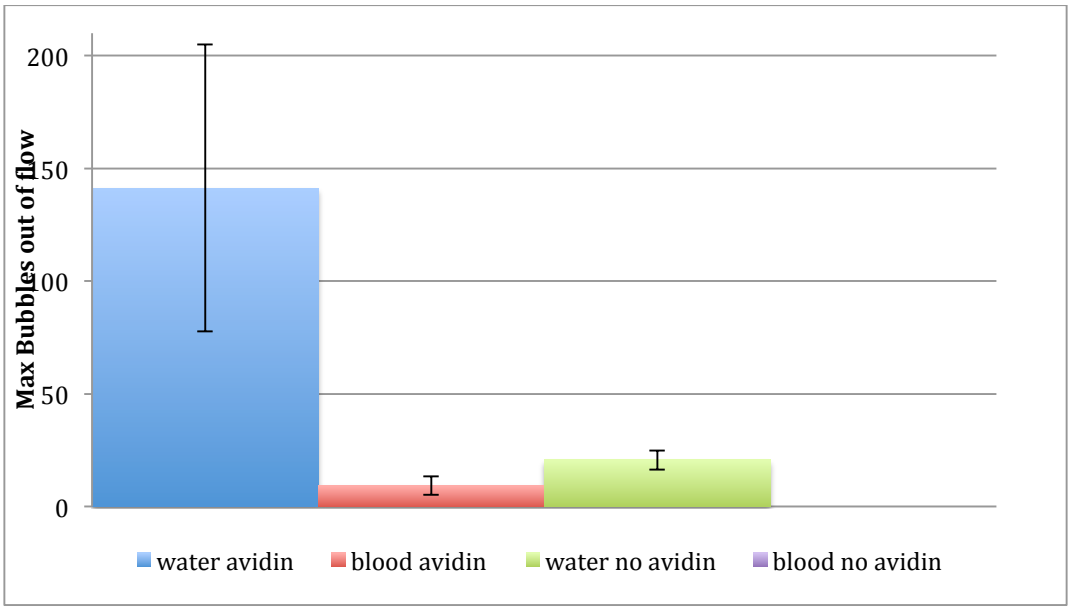


Figure 6.10, quantification of biochemical targeting showing the maximum number of biotin microbubbles in the field of view in water and blood in a capillary tube coated with avidin and with no avidin present.

6.7 Discussion

The results presented above indicate that blood has a significantly detrimental effect on the targeting of microbubbles. Magnetic microbubbles show a 60 – 70 % reduction in the number of targeted bubbles whereas biochemical targeting of microbubbles underwent a 90 % reduction. Both are very high but biochemical microbubbles are affected to a higher degree. This will have a significant impact on any *in vivo* targeting results and could explain the large discrepancy between excellent *in vitro* targeting data and reduced efficiency moving *in vivo* reported in numerous studies [16-19].

The quantity of microbubbles targeted was found to be very different for magnetic and biochemical targeting. Approximately three times as many magnetic microbubbles were successfully targeted in blood compared to biotin microbubbles in PBS. This indicates magnetic targeting may have advantages for drug delivery applications.

6.7.1 Reason for reduction in targeting efficiency

There are numerous reasons why blood could cause a reduction in targeting efficiency. The first is that blood is much more viscous than water alone which would increase the shear stress at the vessel wall. Targeting of microbubbles is reduced with increasing shear rate. However, viscosity is a bulk property of the blood. On the micrometre scale the microbubble is surrounded by plasma which has a similar viscosity to water, as such it is not clear that the shear stress the microbubble experiences would be significantly different in PBS and blood.

Another possible reason could be interactions between the microbubbles and blood components causing agglomeration or destruction of the microbubbles. However the time taken for the experiments is only 5 minutes and the stability studies shown above in section 6.3.2 were performed examining the impact of blood on the microbubbles did not indicate any such effect. The biotin microbubbles also were unaffected in blood on the timescales relevant to the experiments.

A third possibility is collisions between microbubbles and red blood cells and/or other components. As above red blood cells, make up approximately 40 % by volume of blood, they are~8 μm in size and so could easily collide with microbubbles and/or

prevent them moving to a target site. In order to investigate if it was red blood cells which caused a decrease in targeting intensity magnetic microbubbles were targeted against blood with 20 % haematocrit and slowly the haematocrit was increased. This was performed in a 3 mm latex tube and observed with the ULAOP imaging probe as mentioned in section Chapter 5. As the quantity of red blood cells increased, the targeting (as indicated by the image intensity at the vessel wall closest to the magnet) decreased. This is shown in Table 6.2. This provides evidence for a collision based mechanism reducing targeting efficiency both magnetically and biochemically although the very high standard deviations in the measurement indicate that corroboration by another method would be highly desirable.

Varying the hematocrit also varies the bulk viscosity of the solution but as discussed before the viscosity experienced by the microbubble will be that of phosphate buffered saline (PBS). In the experiments for increasing hematocrit PBS and not plasma was used removing any possibility of a viscosity increase between the plasma (1.0-1.3 mPa.s) and the PBS (1.0 mPa.s) having an impact on targeting [20]. Another factor which could impact on results for increasing hematocrit is scattering of ultrasound from red blood cells which could affect the results [21]. However, red blood cells are considered weak scatterers, relative to microbubbles, as the impedence contrast between red blood cells and plasma is around 13% and as such this effect was not considered [22]. For future experiments, taking into account the impact of red blood cell scattering would produce more reliable results from the acoustic intensity of targeted microbubbles.

Table 6.2, Differences between magnetic microbubble retention in blood at different haematocrits as measured by the increase in ultrasound image intensity in the target region[1].

Tube Diameter (mm)	Flow medium	Average intensity increase (%)	Standard deviation (%)	Flow rate (ml/s)
3.0	Blood (20% haematocrit)	53	43	0.21
3.0	Blood (40% haematocrit)	38	11	0.21
3.0	Blood (60% haematocrit)	4	2	0.21

6.7.2 Limitations to the technique

The investigation of the effect of blood on the targeting of magnetic microbubbles used heparinised blood in order to prevent clotting. Heparin is naturally occurring in the body but in much lower quantities than used in the above experiments. If heparin had not been used, the blood would have coagulated and clotted and could not have been used in flow. Heparin should not affect how the red blood cells flow in the capillary tube and other papers report use of anti clotting agents in order to allow the blood to be used [23]. However, heparin in the quantities used in the experiments would not be found *in vivo.* Another limitation is to assume that the reason for magnetic targeting reduction is also true for biochemical targeting. Finally, the experiments only used one flow condition, there may be some flow regimes where collisions with red blood cells can improve targeting efficiency. As indicated in the introduction this has been seen for micrometre scale particles but its impact on microbubbles has never been investigated [6].

The bolus that is observed in the optical images of magnetic targeting (Figure 6.7) is three dimensional. The estimates of bubble quantity are measured from two

[1] This study was performed with Philip Grove whose contribution is greatly acknowledged.

dimensional images meaning that the number of microbubbles successfully targeted will actually be far higher in both blood and water than what is shown above in Figure 6.8. However, the percentage reduction in targeting between PBS and blood should not differ between two and three dimensions as the microbubbles target in a similar manner. The estimate of microbubble quantity is also useful until the bolus can accurately be measured in three dimensions.

6.8 References

1. Mulvana, H., et al. *Enhanced gene transfection in vivo using magnetic localisation ofultrasound contrast agents: Preliminary results*. 2010. San Diego, CA.
2. Weller, G.E.R., et al., *Ultrasonic imaging of tumor angiogenesis using contrast microbubbles targeted via the tumor-binding peptide arginine-arginine-leucine.* Cancer Research, 2005. **65**(2): p. 533-539.
3. Villanueva, F.S., et al., *Albumin microbubble adherence to human coronary endothelium: Implications for assessment of endothelial function using myocardial contrast echocardiography.* Journal of the American College of Cardiology, 1997. **30**(3): p. 689-693.
4. Caro, C.G.P., T. J.; Schroter, R. C.; Seed, W. A., *The mechanics of circulation*. 1st ed. 1978: Oxford University Press.
5. Zhang, J., P.C. Johnson, and A.S. Popel, *Effects of erythrocyte deformability and aggregation on the cell free layer and apparent viscosity of microscopic blood flows.* Microvascular Research, 2009. **77**(3): p. 265-272.
6. Namdee, K., et al., *Margination propensity of vascular-targeted spheres from blood flow in a microfluidic model of human microvessels.* Langmuir, 2013. **29**(8): p. 2530-2535.
7. Munn, L.L., R.J. Melder, and R.K. Jain, *Role of erythrocytes in leukocyte-endothelial interactions: Mathematical model and experimental validation.* Biophysical Journal, 1996. **71**(1): p. 466-478.
8. Walcheck, B., et al., *Neutrophil-neutrophil interactions under hydrodynamic shear stress involve L-selectin and PSGL-1: A mechanism that amplifies initial leukocyte accumulation on P-selectin in vitro.* Journal of Clinical Investigation, 1996. **98**(5): p. 1081-1087.
9. Gentile, F., et al., *The effect of shape on the margination dynamics of non-neutrally buoyant particles in two-dimensional shear flows.* Journal of Biomechanics, 2008. **41**(10): p. 2312-2318.
10. Charoenphol, P., et al., *Particle-cell dynamics in human blood flow: Implications for vascular-targeted drug delivery.* Journal of Biomechanics, 2012. **45**(16): p. 2822-2828.

11. Stride, E. and N. Saffari, *Theoretical and experimental investigation of the behaviour of ultrasound contrast agent particles in whole blood.* Ultrasound in Medicine and Biology, 2004. **30**(11): p. 1495-1509.
12. Carlisle, R.C., et al., *Human erythrocytes bind and inactivate type 5 adenovirus by presenting Coxsackie virus-adenovirus receptor and complement receptor 1.* Blood, 2009. **113**(9): p. 1909-1918.
13. Quaia, E., *Microbubble ultrasound contrast agents: An update.* European Radiology, 2007. **17**(8): p. 1995-2008.
14. Baskurt, O.K., Hardeman, M. R., Rampling, M.W., Meiselman, H. J.,, ed. *Handbook of Hemorheology and Hemodynamics*. Biomedical and Health Research. Vol. 69. 2007, IOS Press. 468.
15. Zhao, S., et al., *Radiation-force assisted targeting facilitates ultrasonic molecular imaging.* Molecular Imaging, 2004. **3**(3): p. 135-148.
16. Ellegala, D.B., et al., *Imaging tumor angiogenesis with contrast ultrasound and microbubbles targeted to αvβ3.* Circulation, 2003. **108**(3): p. 336-341.
17. Lindner, J.R., et al., *Ultrasound assessment of inflammation and renal tissue injury with microbubbles targeted to P-selectin.* Circulation, 2001. **104**(17): p. 2107-2112.
18. Rychak, J.J., et al., *Deformable gas-filled microbubbles targeted to P-selectin.* Journal of Controlled Release, 2006. **114**(3): p. 288-299.
19. Villanueva, F.S., et al., *Microbubbles targeted to intercellular adhesion molecule-1 bind to activated coronary artery endothelial cells.* Circulation, 1998. **98**(1): p. 1-5.
20. Késmárky, G., et al., *Plasma viscosity: A forgotten variable.* Clinical Hemorheology and Microcirculation, 2008. **39**(1-4): p. 243-246.
21. Coussios, C.C., *The significance of shape and orientation in single-particle weak-scatterer models.* Journal of the Acoustical Society of America, 2002. **112**(3 I): p. 906-915.
22. Franceschini, E., B. Lombard, and J. Piraux, *Ultrasound characterization of red blood cells distribution: A wave scattering simulation study.* Journal of Physics: Conference Series, 2011. **269**(1).
23. Thompson, A.J., E.M. Mastria, and O. Eniola-Adefeso, *The margination propensity of ellipsoidal micro/nanoparticles to the endothelium in human blood flow.* Biomaterials, 2013. **34**(23): p. 5863-5871.

7 New magnetic microbubble formulations

7.1 Summary

By analysis of magnetic droplets and microbubbles a new mechanism of formation was discovered for magnetic microbubbles. This was used in order to design and produce a new magnetic microbubble formulation for imaging and therapeutic delivery. The aim was to produce a microbubble without an oil layer, which has been shown to reduce the non-linear scattering to attenuation ratio [1]. As such magnetic microbubbles without an oil layer were produced in high concentration repeatedly and examined for targeting potential.

7.2 Introduction

Previous experiments analysing the therapeutic efficacy of magnetic microbubbles showed the highest transfection rates, under ultrasound and a magnetic field, were achieved with both magnetic microbubbles and, unexpectedly, by a mixture of non-magnetic microbubbles and magnetic droplets [2].

Two possible explanations were proposed for this: The magnetic droplets, under the application of a magnetic field, sensitised the cells in close proximity, allowing the oscillations of the microbubbles to transfect the cells from a distance. Or the magnetic droplets interacted with the microbubbles forming a type of magnetic microbubble.

In order to explore the magnetic droplet/microbubble mixture as a potential therapeutic delivery vehicle a series of experiments were performed in order to understand the phenomenon.

7.3 Results of droplets and bubbles.

In order to determine the nature of the interaction between the magnetic droplets and the microbubbles fluorescence microscopy experiments were designed and conducted. The fluorophore BODIPY C_{10} (Boron dipyrromethane) with a hydrocarbon chain attached, which shows fluorescent activity in a number of environments including water, was used as a means of tagging different species in the suspension.

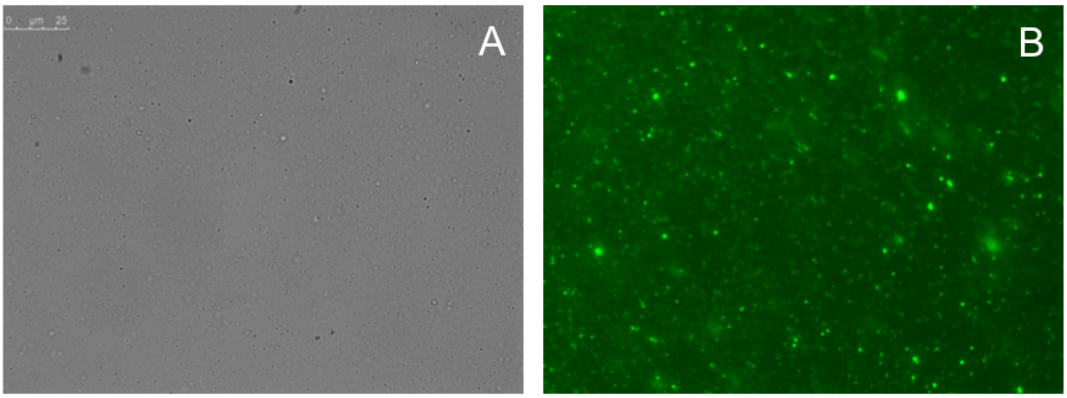


Figure 7.1, magnetic micelles synthesised with the fluorophore BoDIPY showing the phase image and fluorescence.

Microbubbles were synthesised that showed no fluorescence and magnetic micelles were synthesised incorporating the fluorophore BODIPY. The larger vesicles could be seen optically and fluorescently, as shown in Figure 7.1. It is most likely that there are many nanoscale objects such as fluorescent micelles that could only be seen by electron microscopy (see Chapter 4).

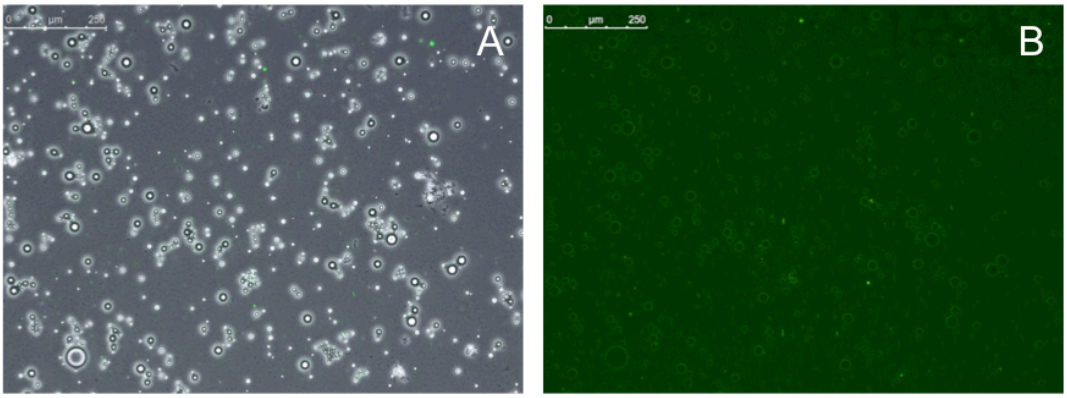


Figure 7.2, microbubbles mixed with fluorescent magnetic micelles. The bubble structure remains intact but the bubbles are now fluorescing.

The magnetic droplets were mixed with microbubbles by using a 1 ml syringe and half filling with magnetic droplets, then filling the rest with microbubbles. The microbubbles then floated through the mixture as they did in the original transfection experiment. The syringe was inverted three times and 10 µl of the mixed solution was placed upon the microscope slide. The microbubbles were now seen to fluoresce as shown in Figure 7.2.

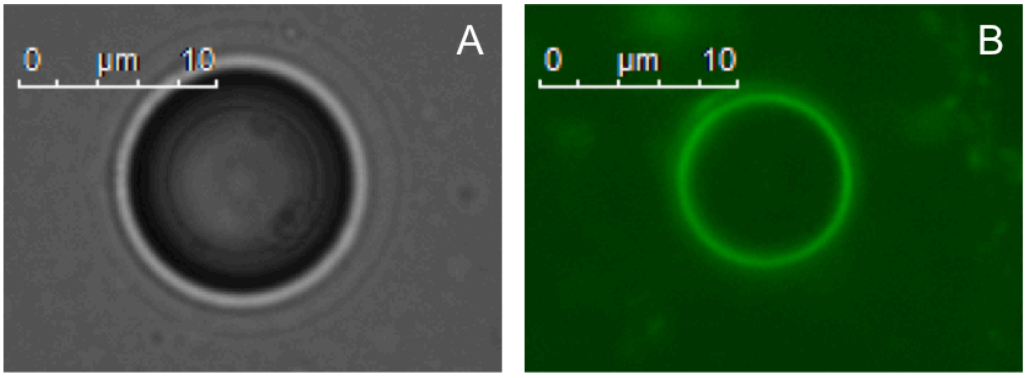


Figure 7.3, A) phase contrast image of a magnetic microbubble and fluorescent magnetic micelles. B) The magnetic microbubble can be seen to fluoresce.

From Figure 7.3 it can be concluded that the microbubble surface has incorporated fluorescent magnetic droplets. The permanence of the interaction was tested by repeating the analysis after centrifugation of the sample (10,000 rpm 3 times).

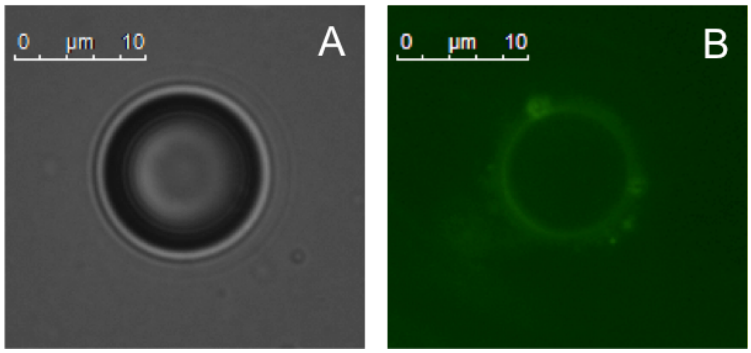


Figure 7.4, a microbubble surrounded by fluorescent magnetic micelles after centrifugation can be seen in a phase contrast image in A and fluorescing in B.

The microbubbles were still fluorescent although the intensity was less than before. This is shown in Figure 7.4. In this image objects can be discerned upon the outside of the microbubble visualised fluorescently (B) but not optically (A). The fluorescent magnetic droplets form a strong interaction with the microbubbles as they coat its surface. This was also observed with non-magnetic droplets indicating the magnetic nanoparticles are not responsible for the interaction.

7.3.1 Targeting Under Flow

In order to visualise what occurs when magnetic droplets/microbubbles respond to a magnetic field the optically visualised flow experiment used in chapter 5 (chapter 3

section 3.2.7.2) was repeated with a maximum flow rate flow rate of 0.1cm/s. The magnetic droplet/microbubble mixture was injected into the 200µm diameter capillary and the flow was stopped when particles were observed (Figure 7.5A). A single 1.5T permanent magnet was applied and the microbubbles were seen to form chains and move towards the magnetic field just as pre-formed magnetic microbubbles were seen to do (Figure 7.5) [1]. At a maximum flow rate of 0.1cm/s the microbubbles continued to form chains and were successfully retained against the capillary tube wall as shown in Figure 7.5C. This provides more evidence that the magnetic droplet/microbubble aggregate could be an effective targeting agent for *in vivo* conditions.

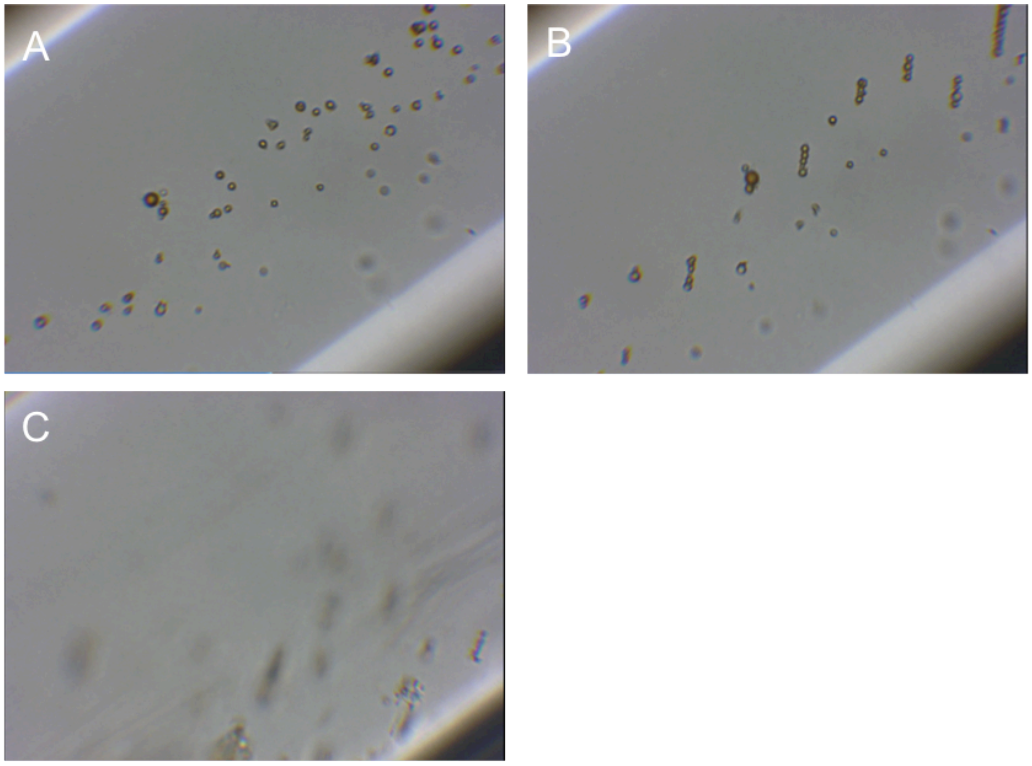


Figure 7.5, 200 µm capillary tube with a flow rate of 1 mm/s and the droplet/microbubble aggregates were retained by a 1.5 T FeNdB magnet

[1] Chain formation from magnetic microbubbles can be observed in results published by Stride et al 2. Stride, E., et al., *Enhancement of Microbubble Mediated Gene Delivery by Simultaneous Exposure to Ultrasonic and Magnetic Fields.* Ultrasound in Medicine & Biology, 2009. **35**(5): p. 861-868..

The above experiments assumed that the micrometre scale particles were microbubbles. It is important to note, however, that optical images of large magnetic droplets can appear very similar to magnetic microbubbles. Droplets and microbubbles can be more effectively differentiated by their acoustic response. The droplet/microbubble mixture was also therefore observed acoustically in the flow system used above for magnetic microbubble trapping in chapter 5 to confirm magnetic actuation of acoustically active objects. A 3mm (ID) vessel was used in this case and a constant shear rate of 60/s was used. In Figure 7.6A below non-magnetic microbubbles are flowing through the system and, as expected, there is no retention upon application of a magnetic field, in B magnetic droplets cannot be seen acoustically at all. In Figure 7.6C the magnetic droplet/microbubble mixture shows microbubbles being retained against a flow of 1.88 cm/s upon application of a magnetic field. This confirms that the structures formed through aggregation are indeed acoustically responsive microbubbles.

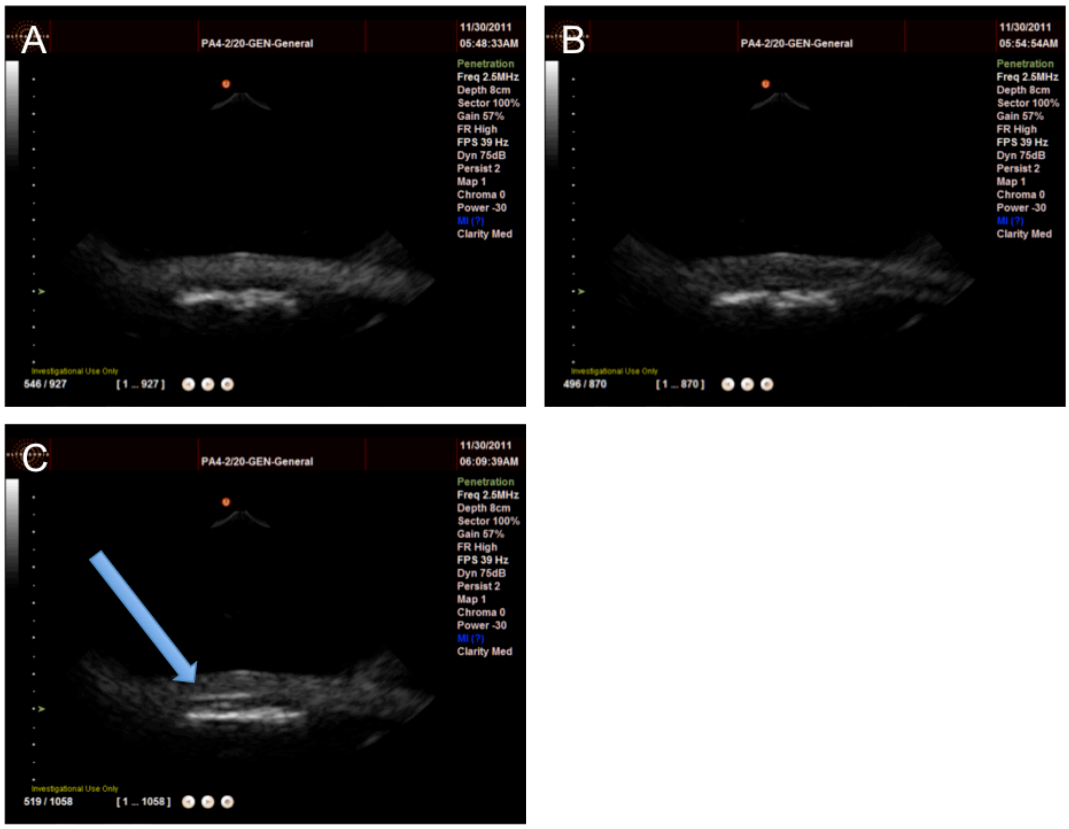


Figure 7.6, magnetic droplets and microbubbles being retained against flow in vitro. A) DSPC microbubbles showing no retention upon application of a magnetic field, B) magnetic droplets showing no ultrasound signal when flowing through a latex tube as the tube appears empty, C) a mixture of magnetic droplets and microbubbles being retained by a magnetic field against drag forces.

This evidence shows that the magnetic droplets coat the microbubbles via a strong interaction and the resulting magnetic droplet/microbubble aggregate forms a magnetic microbubble. This was also confirmed via electron microscopy as shown in Chapter 4.

7.4 Discussion of Magnetic Droplets/Microbubbles

7.4.1 Proposed Mechanism

Droplets appear to coat the microbubbles via an irreversible process. This interaction is strong enough to withstand centrifugation and resist hydrodynamic forces. The microbubbles and the magnetic droplets are both coated in phospholipids with polar head groups pointing into the water and as such should be stable with no need for interaction. One possible mechanism is Ostwald Ripening whereby large objects in solution grow at the expense of smaller ones.

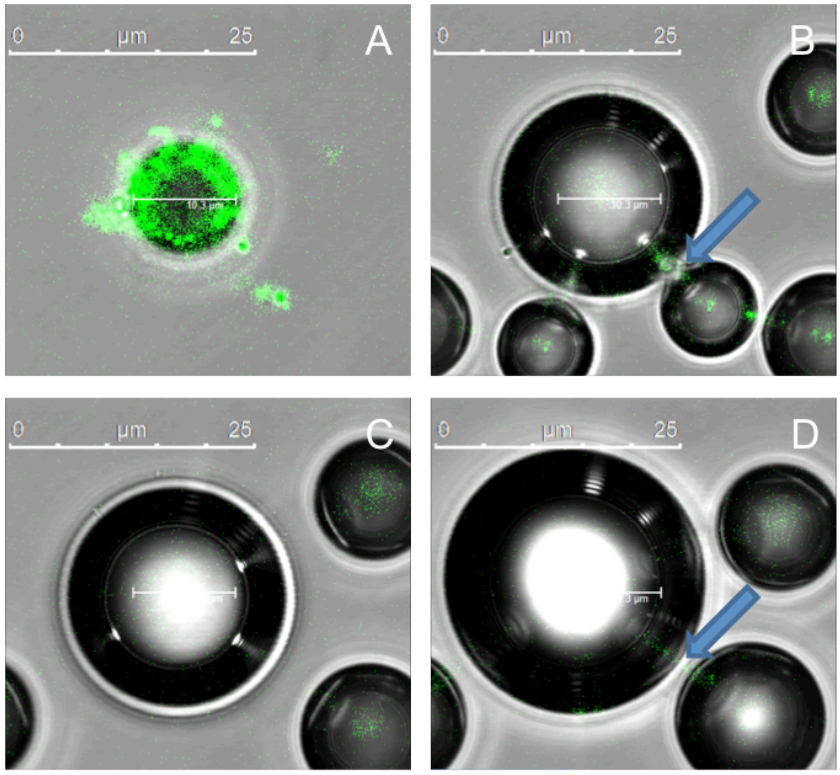


Figure 7.7, a fluorescent magnetic microbubble in glycerol (A) and after a high powered laser has been focused upon it (B). Fluorophores can be seen to be passing from the smaller to larger microbubble as indicated by the arrow. Eventually the smaller microbubble is absorbed into the larger (C) which continues to grow and in D) the same process begins again with lipids appearing to pass from the smaller structure to the larger.

Evidence for rapid Ostwald ripening [3] in magnetic microbubbles can be observed in Figure 7.7 where a magnetic microbubble is exposed to the laser beam in a fluorescence microscope at high power. As the microbubble expands fluorophores were observed, and as such presumably lipids, passing from the smaller bubble into the larger one until the smaller microbubble was eventually absorbed (B and C). This simply shows how lipids can pass from a smaller droplet/microbubble to a larger one.

It was evident from its colour, even under optical microscopy, that the magnetic droplet suspension contained objects on the nano- as well as the micro- scale which cannot be resolved optically [4]. These nano-scale magnetic droplets most likely interact with the phospholipid microbubbles. Evidence for this is that when the microbubbles fluoresce, microscale droplets are still fluorescing nearby and optical microscope images appear to show no interaction between the microscale droplets and the microbubbles. As the microbubbles now fluoresce it is reasonable to assume that interaction must come from nanoscale droplets.

To the authors' knowledge, no studies or models have been reported which examine the interaction between bubbles and droplets. Studies have been performed however on lecithin vesicles where large droplets grow at the expense of smaller ones due to size disproportionation or Ostwald ripening [5] and one possibility is that it is a similar mechanism by which droplets and microbubbles form magnetic microbubbles. Such a process is determined by energetic stability, small droplets are kinetically stable whereas large droplets are thermodynamically stable; due to the surface to volume ratio [3].

In order to obtain an approximate comparison of the relative surface energies of the microbubble and the magnetic droplet, the Laplace pressure must be calculated using:

$$P_\sigma = \frac{2\sigma}{R} \quad 7.1$$

where σ is the interfacial tension and R is the radius of the bubble or droplet. The surface energy can then be found as:

$$F = \sigma \int dA - P_\sigma \int dV \quad 7.2$$

Where A is the surface area and V is the volume. The interfacial tension for an air and water interface is 72.75 mN/m at room temperature, and for water and isoparaffin is 48 mN/m [6]. The microbubbles had a modal diameter of 2.5 μm. The droplets coating the microbubbles must be on the nanoscale and a variable size between 20 and 200 nm was assumed. With these figures a surface energy of -2.38×10^{-12} Nm is obtained for a 2.5 μm air microbubble in water which is lower than -1.01×10^{-16} Nm for a 20 nm oil droplet. A 200 nm droplet has a surface energy of -1.01×10^{-14} Nm which is still lower than for a microbubble. A 2 μm droplet has a surface energy of -1.01×10^{-12} Nm which is of the same order of magnitude as the microbubble. This indicates that a nanoscale droplet would be likely to interact with the microbubble whereas a micrometre scale droplet would not.

The magnetic droplet solution is formed by sonicating lipids in water with ferrofluid. The solution is filled with droplets of many different sizes from the nano to the micro scale. When the microbubbles are added, nanoscale droplets must instantaneously grow into the microbubbles to such an extent that they fluoresce and respond to a magnetic field. The ferrofluid within the droplets must also be deposited within the

microbubble. This was again confirmed by the electron microscopy images in Chapter 4.

These calculations do not take into account the lipid coating of the droplet or the microbubble. The presence of a lipid monolayer would lower the interfacial tension in both cases. However, the system would still be expected to adopt a more energetically favourable state and lipids are known to mediate fusion between droplets and membranes [7]. The influence of additional membrane components such as polyethylene glycol (PEG), which are present in commercially available microbubbles to aid biocompatibility, might inhibit interaction between microbubbles and droplets but the aim of this study was to investigate the microbubble compositions used in [19] which did not contain PEG.

7.5 Design of New Magnetic Microbubbles

The magnetic microbubble formulation (MMB) currently used in all experiments is made via a different procedure to non-magnetic microbubbles. More importantly the oil layer of the magnetic microbubble, whilst having potential toxic effects, also reduces the non-linear character of the acoustic response which is undesirable for imaging and/or therapeutic monitoring [1]. Consequently, based on experiments described above and previous studies of the existing magnetic microbubble formulation new types of magnetic microbubble were designed.

Firstly, the mechanism of formation outlined above for droplets mixed with microbubbles produced a new magnetic microbubble formulation. The magnetic droplets could, theoretically, be added to any microbubble formulation rendering it

magnetic. However, the oil will still be present with potential toxic effects and acoustic damping.

Magnetic nanoparticles could be attached to the microbubble surface via the method used by Lentacker *et al.* to produce liposome bound microbubbles [8] or the process used to produce targeted microbubbles by Ellagalla *et al.* [9]. Another possible mechanism could be use of a charged interaction between the nanoparticles and the microbubbles [10, 11]. Finally, magnetoliposomes could be created and bound to the surface using Maleimide-thiol linkages [8]. However, all of the above would increase the number of production steps and/or require the use of potentially immunogenic factors.

The technique identified above involving magnetic droplets and microbubbles could also be adapted to bind magnetic nanoparticles directly to microbubbles. The energetically favourable binding of the oil droplets to the microbubble surface might be possible with commercially available nanoparticles to produce magnetic microbubbles. To the candidate's knowledge this has never before been tested.

Another potential mechanism is to incorporate nanoparticles into the lipid film during the production process so the nanoparticles become embedded in the microbubble coating. According to Feshitan *et al.* when a lipid film is hydrated, heated and sonicated it forms a large number of lipid droplets of various sizes [12]. Some groups actually use extrusion devices to control the size of the lipid droplets/liposomes before microbubble formation [13]. These droplets are then broken apart via shaking or sonication at the air water interface and the remains of their structures form the

shell of the microbubble [12]. This provides the opportunity for nanoparticles to be directly incorporated into the microbubble coating during the sonication step. This would be a one step formation mechanism and to the candidate's knowledge has never previously been attempted.

From the examples above two techniques were examined to produce magnetic microbubbles via: i) the droplet/microbubble technique was imitated with magnetic nanoparticles and ii) the magnetic nanoparticles were sonicated with phospholipid vesicles (microbubble precursors) followed by sonication at the air water interface to embed nanoparticles in the shell. Both techniques have very simple production mechanisms and no immunogenic factors, such as charge or avidin-biotin, are used.

Initial experiments were attempted using the phospholipid microbubble (PMB) formulation with oleic acid coated nanoparticles without isoparaffin as a stabilising solution. Experiments produced microbubbles, none of which responded to a magnetic field. The reasons for this are unclear. The nanoparticles are coated in oleic acid which can detach from the microbubble surface. In water the nanoparticles appeared to agglomerate as they could be visualised at the bottom of the solution. Sonication could not suspend the particles for long enough in the water in order to stabilise them in the microbubble structure. Oleic acid coated nanoparticles will dissolve in non-polar solvents such as isoparaffin as the carbon chains of the nanoparticle point out into the solution. Adding the nanoparticles to water is not energetically favourable and the nanoparticles agglomerate into larger particles or crash out of solution before bubble production can occur. As such magnetic nanoparticles with different coatings were tested.

7.6 Magnetic microbubbles with lipid coated nanoparticles (LMMB)

If the nanoparticles were already coated in phospholipid such that the polar heads of the lipids pointed out into the water the nanoparticles could act like magnetic droplets or vesicles and the oil would not be present. These nanoparticles could be incorporated into the shell during the sonication process or fuse with the cell in a similar manner to magnetic droplets.

Using lipid coated nanoparticles could give rise to microbubbles via two possible mechanisms. Firstly via sonication; if the microbubble coating is multilamellar then the lipid coated nanoparticle could be incorporated within the layers during microbubble formation, as indicated in Figure 7.8 where it would be stabilised by the number of lipid layers. The lipids could allow for an inclusion in the layers in a similar way to proteins sitting in cell membranes [7]. This structure would form during sonication at the air water interface as the remains of the lipid structures coat gas microbubbles. The lipid coated nanoparticles should be incorporated into and stabilised in the microbubble microbubble during the sonication process. Evidence from viscosity studies indicates that sonicated microbubbles could in fact have multilamellar coatings [14].

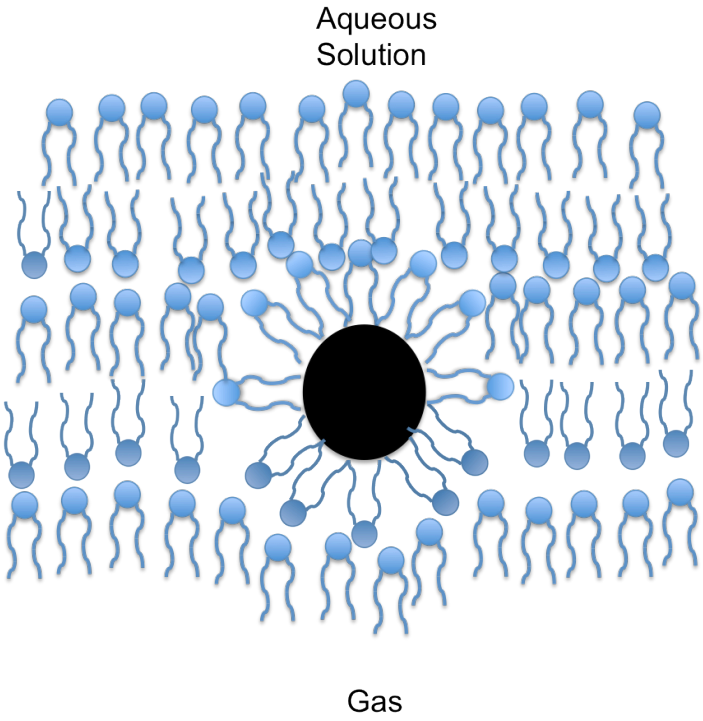


Figure 7.8, image of lipid coated nanoparticles embedded in a multilamellar lipid coating of a microbubble indicating how the nanoparticle would be stabilized in the layer

The second mechanism of formation would be related to size and stability. As has been shown with lipid coated magnetic droplets, it is energetically favourable for nanoscale droplets to incorporate into the microbubble coating. As the lipid coated nanoparticles are approximately 50 nm in size this means it could be energetically favourable for them to be associated with the microbubble surface in such a way as to form a magnetically responsive microbubble. The nanoparticle would be adsorbed onto the microbubble surface as shown in Figure 7.9 in a hydrophobic pocket. However, no evidence exists for this structure and it is purely theoretical.

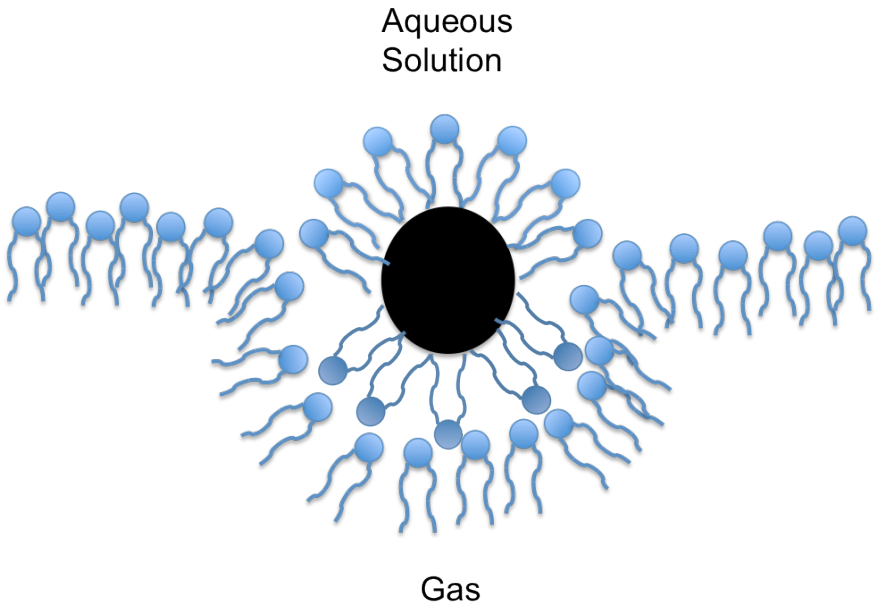


Figure 7.9, image of lipid coated nanoparticle associated with a unilamellar coating of a lipid stabilized microbubble proposing how the nanoparticle would be stabilized on the surface of a monolayer in a hydrophobic pocket.

7.6.1 Preliminary Studies

Preliminary studies of lipid coated magnetic nanoparticles mixed with phospholipid microbubbles via the same technique as magnetic droplet/microbubble formation were unsuccessful. The technique appears to require the layer of oil. Sonication of lipid coated nanoparticles with phospholipids in a manner similar to magnetic microbubble formulation 1 Chapter 3 showed microbubbles had formed and responded to a magnetic field. However the concentration was low and a large amount of debris was found in the solution.

7.6.2 Improvements to the formulation

It was decided to use the formulation for phospholipid microbubbles in Chapter 3 section 3.2.1.2, DSPC:PEG-40-Stearate, (9:1 molar ratio) as a basis for the

microbubble. Heavy gas would be used in order to prolong the lifetime and produce more microbubbles. It was also decided to increase the amount of magnetic nanoparticles in the solution by an order of magnitude in order to improve the magnetic response of the microbubbles. The aim was to produce a targetable formulation which can be used for drug delivery.

7.7 Results

After sonicating at the air water interface the solution turned light brown and microbubbles appeared to have formed. These were then examined under the microscope (40 x objective magnification) on a haemocytometer (see Chapter 3). Microbubbles could clearly be observed floating at the top of the haemocytometer and no objects could be observed on the bottom of the slide (Figure 7.10). Objects appeared to be microbubbles and similar in appearance to lipid only coated microbubbles (i.e. unlike formulation 1 magnetic microbubbles).

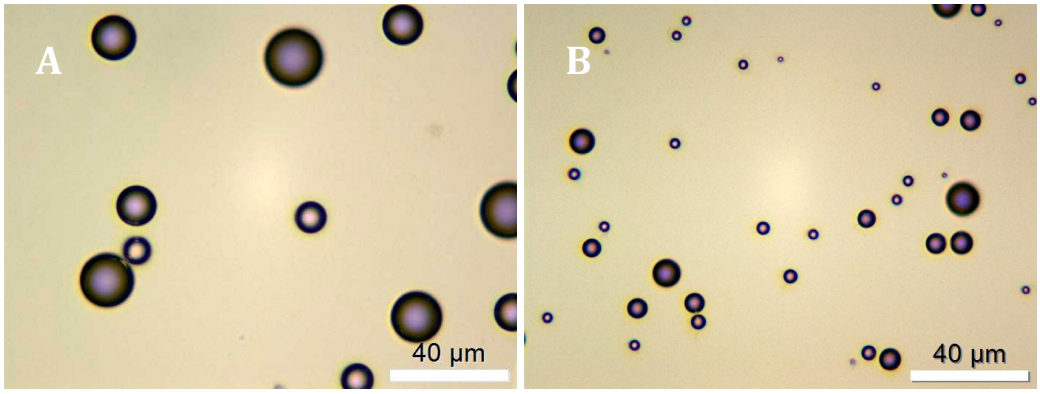


Figure 7.10, optical microscope images (400x magnification) of microbubbles made with lipid coated nanoparticles. A) shows the larger microbubbles observed and B) the variation in size.

7.7.1 Magnetic Response

In order to quickly test the magnetic response of the microbubbles, a 0.75 T single bar magnet was brought close to the haemocytometer. Microbubbles pressed against the top of the slide began to move towards the magnet. This can be clearly observed in Figure 7.11 below where the microbubbles have moved towards the bottom of the image in B. The smaller microbubbles (<10 µm) move towards the magnetic field whilst the larger microbubbles (>10 µm) remain stationary or show minimal movement. This is due to ratio of surface area to volume. The small microbubbles (<10 µm) have a high surface area to volume ratio whereas the reverse is true for larger microbubbles (>10 µm). As the nanoparticles are located on the microbubble surface a higher surface area to volume will allow the microbubble to overcome friction with the glass slide when a magnetic field is applied and the nanoparticles attempt to move the bubble down the field gradient.

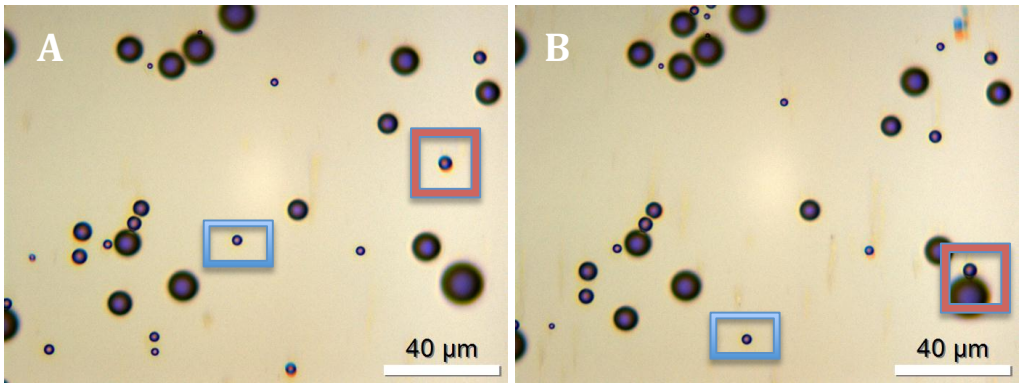


Figure 7.11, microbubbles A) before and B) 20 seconds after the application of a magnetic field, showing movement of microbubbles towards the magnet (below the picture). Boxes indicate examples of microbubbles that have been displaced.

This was also observed in the bulk suspension alone. Bringing a magnet close to the vial caused the microbubbles to move down the magnetic field gradient and closer to the strongest point of the magnetic field. This is shown below in Figure 7.12.

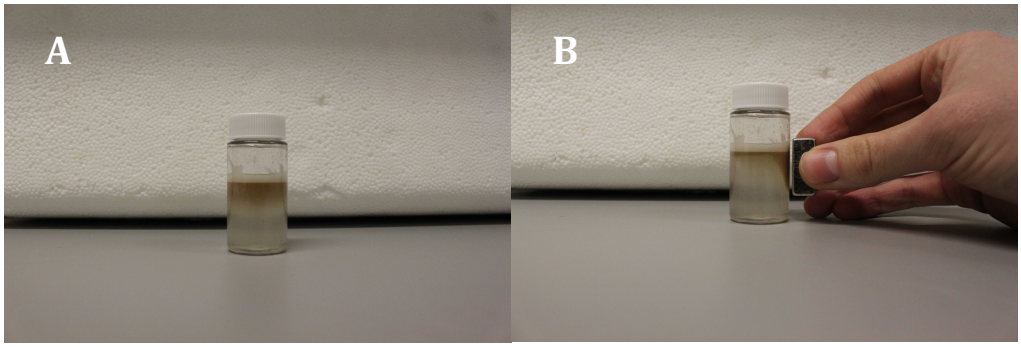


Figure 7.12, an image of magnetic microbubbles in a vial below a layer of foam A) before and B) after application of a magnetic field.

Actuation of magnetic microbubbles pressed against the glass slide of a haemocytometer was never successfully observed for magnetic microbubble formulation 1 (MMB).

7.7.2 Size and Concentration

Images of microbubbles from 3 batches were analysed to obtain their size distribution and concentration. For each microbubble sample, 30 images were taken at 400 x magnification. An example of the data obtained is shown in Figure 7.13. The average microbubble concentration was found to be 6.7 x 10^7 bubbles/ml and the average size of the microbubbles was 4.53 ± 5.01 µm. Many microbubbles were above 8 µm in size and few microbubbles were below 1 µm. The concentration is lower than that of SonoVue or non-magnetic phospholipid microbubbles which usually contain 1 x10^9 bubbles/ml. The original magnetic microbubble formulation also has a higher concentration and lower size distribution.

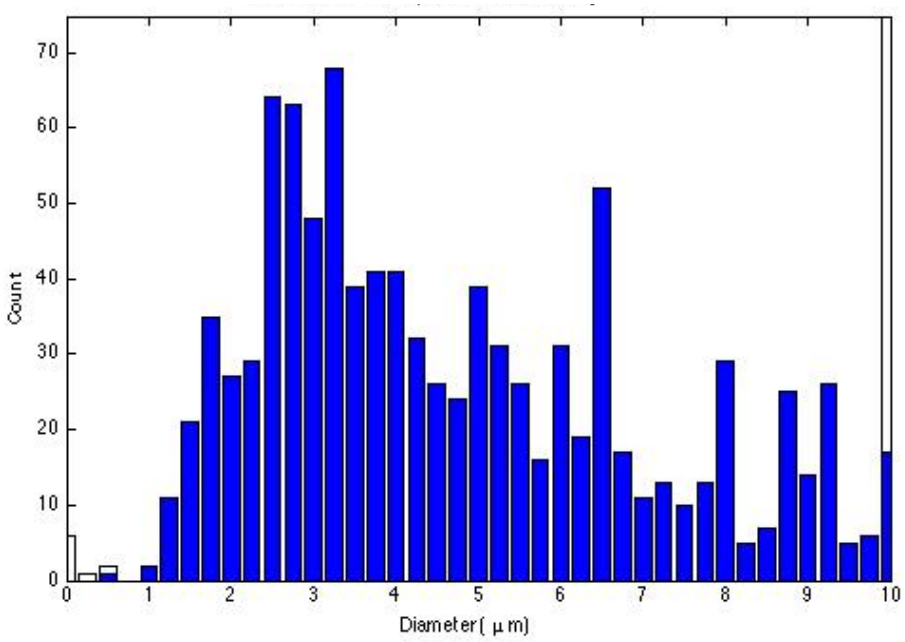


Figure 7.13, example of size distribution of microbubbles also indicating the average concentration of microbubbles.

7.7.3 Acoustic response

In order to confirm that microbubbles (as opposed to liquid droplets) have been synthesized and are acoustically active the microbubbles were observed under ultrasound imaging in the flow system described in Chapter 3. Upon injection of 0.5 ml of the microbubble solution into the flow system (latex tube 3 mm ID) a strong signal could be observed. This was repeated three times and an example is shown in Figure 7.14 below.

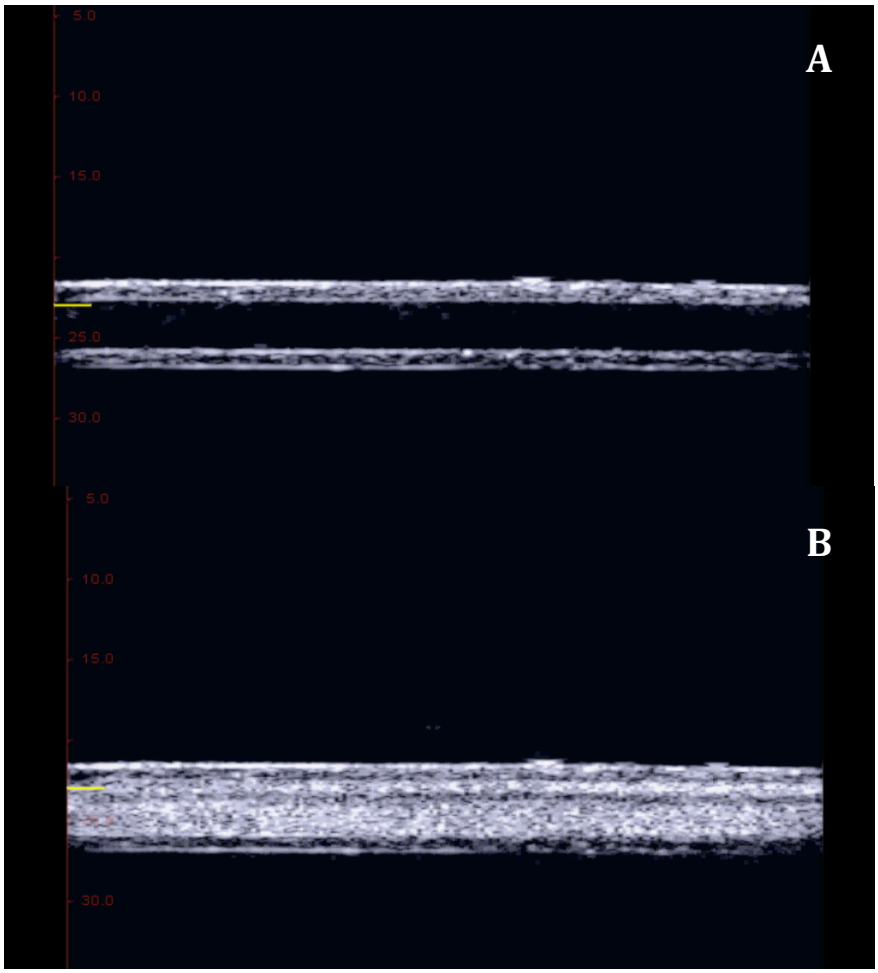


Figure 7.14, ultrasound image of latex tube (3 mm ID) with A) water alone flowing through, the tube perfused with the magnetic microbubble solution is shown in B.

7.7.4 Retention Analysis

The microbubbles were shown, optically, to move upon application of a magnetic field. The microbubbles were now observed under flow to ensure that acoustically active objects were magnetic and could be retained against flow. As in previous experiments, a Halbach array was inserted beneath the latex tube giving a magnetic field strength of approximately 0.2 T at the bottom of the tube. The magnetic microbubbles were pulled out of the flow towards magnet as shown in Figure 7.15B where at the wall nearest the magnet the intensity was much higher (B) than the

control (A). This experiment was repeated with three different samples of magnetic microbubble indicating it is reproducible.

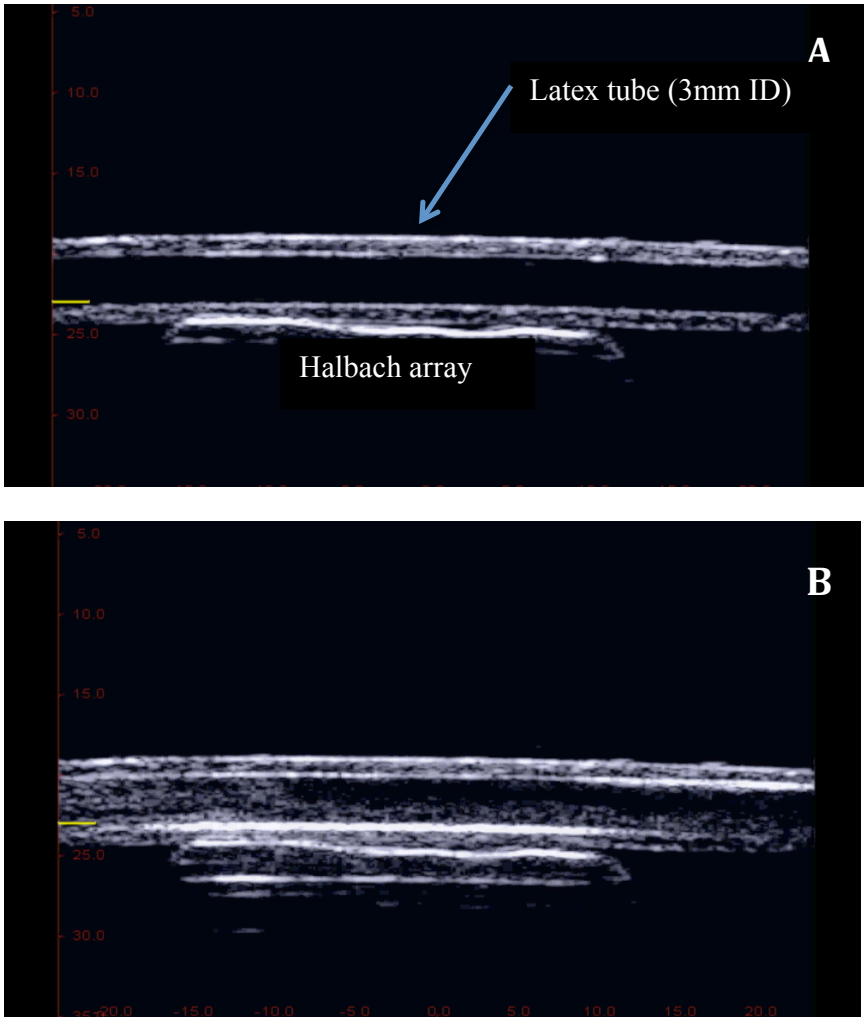


Figure 7.15, A) image of latex tube with magnetic Halbach array positioned below before perfusion of microbubbles and B) after perfusion with magnetic microbubbles showing retention of magnetic microbubbles along the bottom of the tube.

The videos above were analysed using the Matlab software described in Chapter 3 section 3.2.7.6. An example of the plots obtained is shown in Figure 7.16. When no magnetic field is applied the majority of the microbubbles flow along the top wall of the latex tube owing to buoyancy (A). When the magnetic field is applied the

majority of microbubbles move to the wall nearest the magnet overcoming buoyancy (B). The initial bleep at the start of the signal is an air bubble, from the injection of the microbubble mixture, passing through the flow phantom which reflects ultrasound. This increases the intensity along the top and decreases the intensity along the bottom for approximately 100 frames.

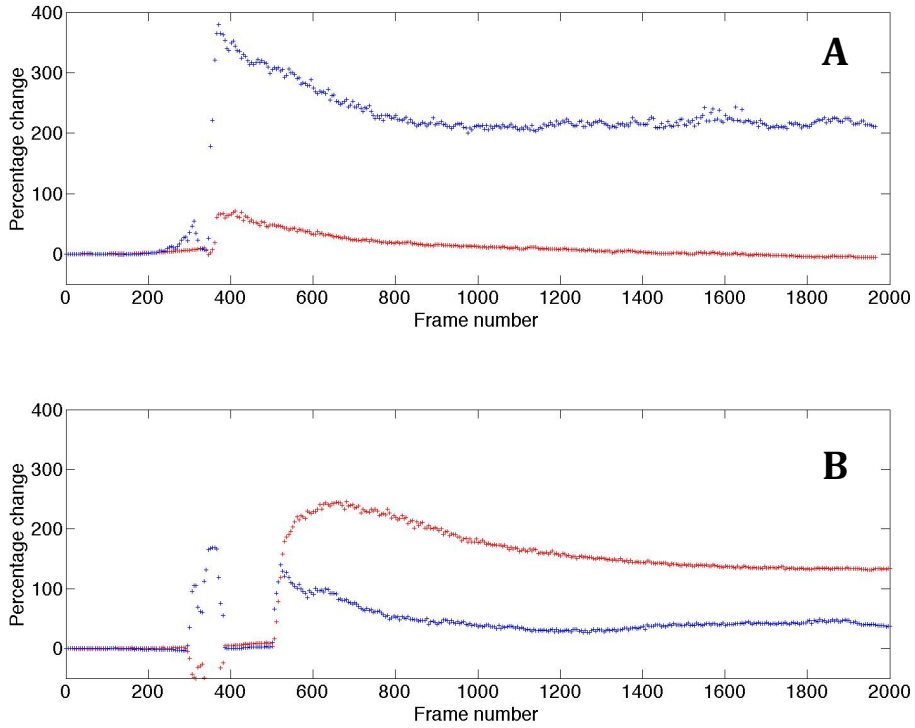


Figure 7.16, Percentage change in intensity along the side of the latex tube nearest the magnet (red line) and furthest away (blue line) against frame number. A) microbubbles flowing through in the absence of a magnetic field and B) with 0.5 T magnetic field strength along the bottom of the tube.

7.7.5 Contrast ultrasound imaging mode

The LMMB were also imaged using the contrast package on a clinical ultrasound scanner (Chapter 3 section 3.2.9.4) in order to test their non-linear response. A latex tube was submerged in a water bath and analysed by an imaging probe. Water was flown through via a gravity feed which could be stopped with a plug. The water flow

was stopped and microbubble formulation LMMB was injected into the tube. The video sequence was then started and the flow allowed to proceed. The image was recorded in B mode and contrast mode to observe what was taking place in both sequences.

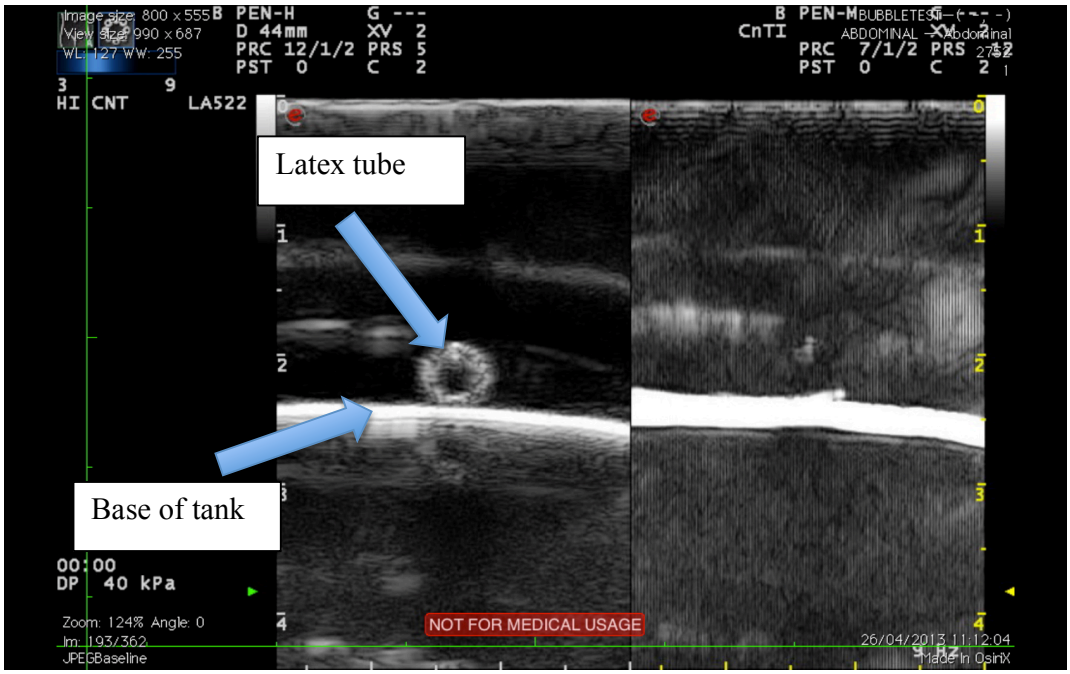


Figure 7.17, ultrasound image of a latex tube on the bottom of tank. The image on the left shows the latex tube with water being injected through, the image on the right shows the contrast image of the same latex tube.

The latex tube could be discerned clearly in B-mode and no image was observed in contrast imaging indicating that no non-linear scatterers were present (Figure 7.17.) Upon injection of the new magnetic microbubble formulation through the flow the centre of the tube could be observed in contrast imaging mode and B-mode as shown in Figure 7.18. This indicates that the addition of magnetic nanoparticles to the formulation does not have a detrimental effect on the acoustic response of the microbubbles and they can still be used for contrast imaging.

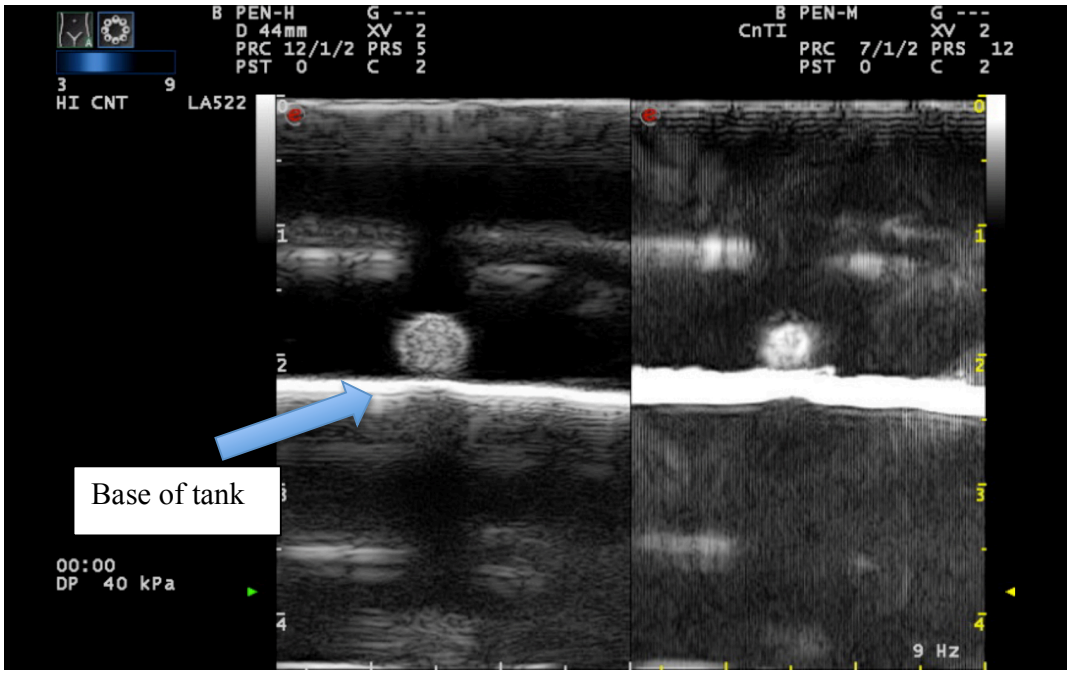


Figure 7.18, B mode (left) and contrast image (right) of magnetic microbubbles formulated with lipid coated nanoparticles (LMMB) flowing through the latex tube.

7.7.6 Magnetic relaxivity

The results in Figure 7.19 show the magnetic relaxivity of the new microbubble formulation (LMMB) as 0.9×10^{6} bubbles^{-1}sec^{-1} compared to a relaxivity of 1.0×10^{-6} bubbles^{-1}sec^{-1} for the original magnetic microbubble formulation (MMB). The new magnetic microbubble formulation (LMMB) was washed via centrifugation so the only magnetic objects in the solution were the microbubbles. This could not be performed for the original magnetic microbubble formulation (MMB) as after centrifugation only the non-magnetic microbubbles came out of solution and magnetic droplets and microbubbles remained present in solution. As such the original magnetic microbubble solution contained a large number of magnetic droplets which would affect the results. The original magnetic microbubble solution also had a higher concentration of microbubbles, these factors explain the above result

whereby $1/T_2$ is higher for the original magnetic microbubble formulation. However the gradient of each line is similar and as such both magnetic microbubble formulations have similar magnetic relaxivity for use as MRI contrast agents. This also gives an indication of their ability to be magnetically targeted as relaxivity is directly related to the parameters determining magnetic force. As the gradient of both lines is similar, the flow conditions against which the microbubbles (LMMB) can be retained should be similar to the original magnetic microbubble formulation (MMB).

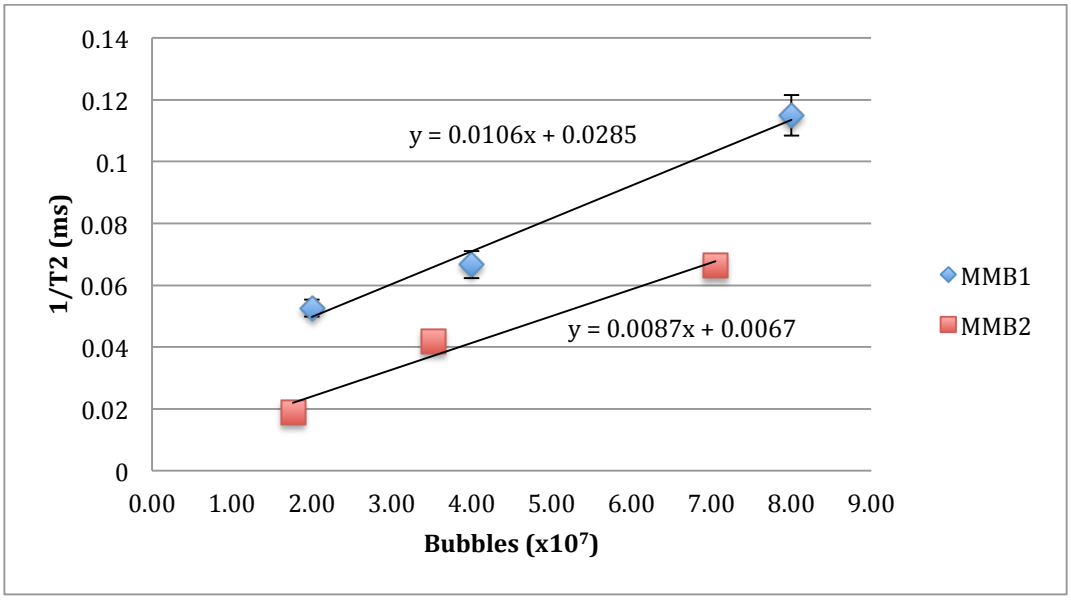


Figure 7.19, magnetic relaxivity of original magnetic microbubble formulation (MMB1) and of magnetic microbubble formulation 2 created with lipid coated magnetic nanoparticles (MMB2) for 3 concentrations of microbubbles.

7.7.7 Improvements to size and Concentration

The new magnetic microbubble formulation contains acoustically active objects with non-linear acoustic response and no magnetic droplets/vesicles are in the solution.

However, the lipid nanoparticle coated magnetic microbubble (LMMB) had a large size distribution and lower concentration relative to the original magnetic microbubble formulation (MMB). As such, it was decided to look into methods to increase the concentration and lower the size distribution of microbubbles in order to use the lipid nanoparticle coated microbubbles for therapeutic delivery.

Results from Unger *et al.* show that use of glycerol and propylene glycol can improve the yield and size distribution of microbubbles [15]. Propylene glycol is used as a foaming agent in many commercial products such as shaving foam. This technique was not successful applied to magnetic microbubble formulation 1 (MMB). However, as magnetic microbubble formulation 3 (LMMB) uses DSPC and PEG 40 Stearate in a 9:1 ratio and the production method is similar to phospholipid microbubbles these techniques can be applied in order improve the yield. The fabrication technique explained above was performed again except using a solution of saline, glycerol and propylene glycol, at a ratio of 8:1:1 instead of deionised water.

Optical analysis of microscope images (Figure 7.20) showed use of glycerol and propylene glycol with the LMMBs gave rise to a much higher concentration, 2.99 x10^9 bubbles/ml with an average diameter of 1.23 ±0.79 μm. A second sample showed 2.79 x10^9 bubbles/ml with a diameter of 1.46 ±1.05 μm, and a third 2.81 x10^9 bubbles/ml with a diameter of 1.36 ±0.87 μm showing the repeatability of the technique. An example of the size distribution is shown in Figure 7.21. No bubble exceeded 10 μm in size in all three attempts showing the potential for use *in vivo.*

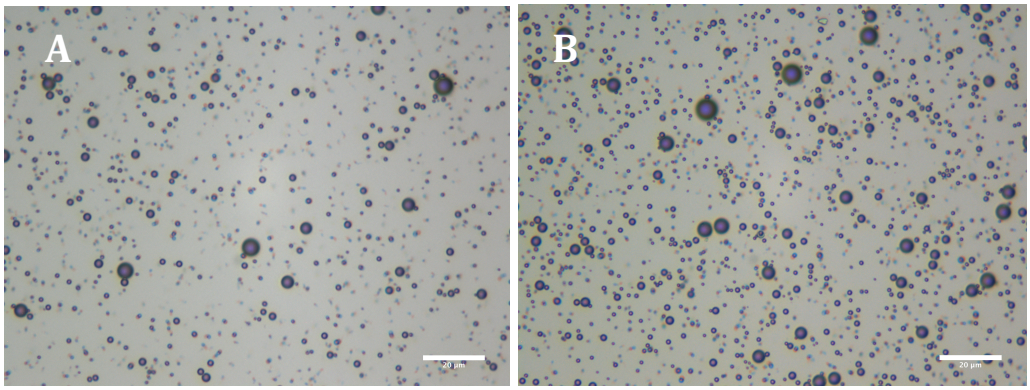


Figure 7.20, images of magnetic microbubbles made with a solution of saline, glycerol and propylene glycol, at a ratio of 8:1:1 A) before and B) after centrifugation indicating that the magnetic microbubbles could survive centrifugation. Scale bar is 20 µm.

The yield of the microbubbles (LMMB) has been increased the average size reduced meaning they can be used directly *in vivo* after a one step production mechanism. After centrifuging the microbubbles the colour became white as the bubbles were concentrated. For cosmetic purposes this is important for clinical usage[2]. The size distribution remained the same as in Figure 7.21 with a slight increase in concentration.

[2] This was suggested by Dr David Holroyd and Dr Daniel Chung.

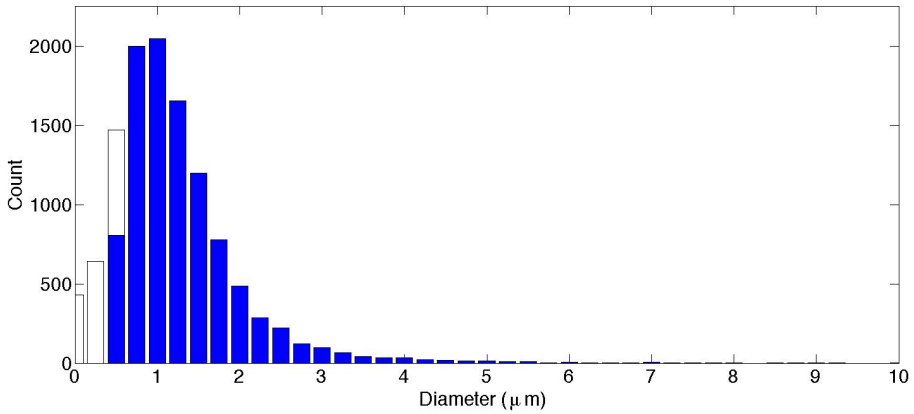


Figure 7.21, An example size distribution of magnetic microbubble formulation created with a solution of saline, glycerol and propylene glycol, at a ratio of 8:1:1.

7.8 Discussion

A new mechanism for the formation of magnetic microbubbles was identified after investigating the improved transfection of magnetic droplets and microbubbles observed in a previous study. The microbubbles and the droplets bound together into a magnetic microbubble owing to size and surface energy considerations. The microbubble coated in the droplets could be magnetically targeted against flow.

This same principal was adapted in order to prepare microbubbles whereby nanoparticles were incorporated into the microbubble shell during the sonication process. This removes the need for multistep production and use of biochemical interactions such as avidin-biotin.

As the original magnetic microbubble formulation suffers in terms of performance due to the presence of oil the new designs examined one step procedures for incorporating nanoparticles into microbubbles.

The microbubble design used a lipid coated iron oxide nanoparticle. This was sonicated with the lipid vesicles in order to incorporate into the microbubble shell. Lipid coated nanoparticles were successfully embedded into microbubbles producing ultrasound contrast agents. These responded to a magnetic field and the majority of microbubbles targeted against flow. The new magnetic microbubbles could also be visualised via contrast mode.

As the size distribution of the LMMBs was relatively broad and the concentration low relative to magnetic microbubble formulation 1 a solution of saline, glycerol and propylene glycol, at a ratio of 8:1:1 was used. This improved the yield and lowered the size distribution. However, concentration of magnetic nanoparticles on each bubble is unknown and it is likely there is a homogeneity of nanoparticles on the microbubble surface. As such each microbubble with have a different magnetic response.

To the candidate's knowledge this is the first time that lipid coated nanoparticles have been directly incorporated into a microbubble coating via a one step production mechanism. Electron microscopy images in Chapter 4 confirm this to have taken place. The next chapter examines the therapeutic potential of the new magnetic microbubble formulation (LMMBs).

7.9 References

1. Mulvana, H., et al., *Theoretical and Experimental Characterisation of Magnetic Microbubbles.* Ultrasound in Medicine and Biology, 2012. **38**(5): p. 864-875.

2. Stride, E., et al., *Enhancement of Microbubble Mediated Gene Delivery by Simultaneous Exposure to Ultrasonic and Magnetic Fields.* Ultrasound in Medicine & Biology, 2009. **35**(5): p. 861-868.
3. Taylor, P., *Ostwald ripening in emulsions.* Advances in Colloid and Interface Science, 1998. **75**(2): p. 107-163.
4. Amstad, E., et al., *Triggered release from liposomes through magnetic actuation of iron oxide nanoparticle containing membranes.* Nano Letters, 2011. **11**(4): p. 1664-1670.
5. Johnson, N.W. and E.W. Kaler, *Size disproportionation in vesicular dispersions.* Journal of Colloid and Interface Science, 1987. **116**(2): p. 444-457.
6. NPL. http://www.kayelaby.npl.co.uk/general_physics/2_2/2_2_5.html. 2011 [cited 2012 28 February].
7. Mouritsen, O., *Life - As a Matter of Fat*. 2001: Springer.
8. Lentacker, I., et al., *Lipoplex-loaded microbubbles for gene delivery: A trojan horse controlled by ultrasound.* Advanced Functional Materials, 2007. **17**(12): p. 1910-1916.
9. Ellegala, D.B., et al., *Imaging tumor angiogenesis with contrast ultrasound and microbubbles targeted to αvβ3.* Circulation, 2003. **108**(3): p. 336-341.
10. Soetanto, K. and H. Watarai. *Ferromagnetic Ultrasound Microbubbles Contrast Agent*. 2003. Cancun.
11. Vlaskou, D., et al. *Magnetic microbubbles: Magnetically targeted and ultrasound-triggered vectors for gene delivery in vitro*. 2010. Rostock.
12. Feshitan, J.A., et al., *Microbubble size isolation by differential centrifugation.* Journal of Colloid and Interface Science, 2009. **329**(2): p. 316-324.
13. Lentacker, I., et al., *Design and evaluation of doxorubicin-containing microbubbles for ultrasound-triggered doxorubicin delivery: Cytotoxicity and mechanisms involved.* Molecular Therapy, 2010. **18**(1): p. 101-108.
14. Hosny, N.A., et al., *Mapping microbubble viscosity using fluorescence lifetime imaging of molecular rotors.* Proceedings of the National Academy of Sciences of the United States of America, 2013. **110**(23): p. 9225-9230.
15. Unger, E.C., et al., *Acoustically active lipospheres containing paclitaxel - A new therapeutic ultrasound contrast agent.* Investigative Radiology, 1998. **33**(12): p. 886-892.

8 SiRNA delivery using magnetic microbubbles

8.1 Summary

Lipid coated magnetic nanoparticles incorporated into microbubbles (LMMB) were examined as therapeutic delivery vehicles. siRNA, which shows great potential for therapy but is difficult to deliver, was successfully bound to the new magnetic microbubble formulation (LMMB). The siRNA/microbubble conjugate was then used to deliver siRNA to a neuroblastoma cell line. Exposure to a magnetic field, ultrasound, or bubbles alone resulted in negligible uptake. Only combination of ultrasound and a magnetic field resulted in significant uptake of siRNA by the neuroblastoma cells. The results show the potential of the magnetic microbubble formulation as a targeted therapeutic delivery vehicle.

8.2 Introduction

In Chapter 7 a new magnetic microbubble formulation was developed using lipid coated iron oxide nanoparticles. This new magnetic microbubble formulation has shown promise for magnetic targeting, visualisation via contrast specific ultrasound imaging and as such potential for molecular imaging or treatment monitoring. However, its performance for therapeutic delivery has yet to be demonstrated. As discussed in Chapter 2, one promising candidate for delivery via ultrasound and magnetic fields is small interfering RNA (siRNA).

siRNA can be used to target a specific messenger RNA which leads to downregulation of an encoded protein. siRNA has significant potential benefits but

is extremely difficult to deliver. To realise the widespread use of RNA therapeutics for disease prevention and treatment requires the development of clinically viable, safe and effective drug delivery vehicles [1].

Naked siRNA needs to reach the target site in a sufficiently high concentration to elicit the desired activity. However, blood ribonucleases easily degrade them, the kidneys rapidly eliminate them and the hydrophobicity of siRNAs strongly impair their cellular internalization [2]. The negatively charged siRNA backbone having to cross a negatively charged cellular membrane also reduces uptake [1, 3]. As such, methods are actively being developed in order to protect siRNA, transport it to the target location and cause the desired cells to internalise it.

The viral approach is still the most efficient for delivery of siRNA, however immune response and difficulty of production on a large scale prevents repeated administration [4]. Hydrodynamic injection involves direct injection of siRNA in buffer into the liver. However, the technique is very invasive and although some tumours are candidates for direct local injection the majority are not [5]. Cholesterol has been conjugated to siRNA for uptake for cell entry but no targeting is possible [6]. Cationic delivery systems such as lipids and liposomes, cationic polymers, cationic dendrimers and cationic cell penetrating peptides have been investigated for the delivery of siRNA[4]. Liposomes with a fusogenic moiety, such as transferrin, on the end of PEG chains for internalisation are also being explored [2].

As outlined previously (Chapter 2), microbubbles can be used to deliver therapeutic compounds such as drugs and genes when ultrasound is applied via a process called sonoporation [3, 7] after being concentrated at the target location.

Magnetic microbubbles have been successfully used for gene transfection by Stride *et al.* [8]. The results showed that exposing the cells to a combination of ultrasound and a magnetic field resulted in the highest transfection rate [8]. However, the DNA, in this case, was simply in the surrounding medium and not bound to the microbubbles. Delivery of siRNA bound to magnetic microbubbles has not previously been attempted. The aim of the experiments described below was to conjugate siRNA to the new magnetic microbubble formulation (LMMB) and determine transfection efficiency *in vitro*. Firstly the formulation had to be charged in order to successfully bind siRNA. After producing a charged siRNA bound magnetic microbubble formulation delivery of siRNA to a neuroblastoma cell line was attempted.

8.3 Methods

8.3.1 Experimental procedure

The microbubble fabrication protocols and apparatus used for the experiments were as described in Chapter 3 (section 3.2.11). Opticells containing a confluent monolayer of neuroblastoma cells were filled with microbubbles binding fluorescent siRNA. Each Opticell was premarked with six equispaced spots that were exposed to ultrasound with or without an applied magnetic field. The ultrasound and the Opticells were set up as outlined in Chapter 3. Each plate has six exposure spots. The exposure conditions applied to each plate are summarised in Table 8.1.

Table 8.1, conditions for each Opticell plate after injection of magnetic microbubbles bound to siRNA.

Plate	Conditions
1	NA
2	Magnetic field
3	Ultrasound and a magnetic field
4	Ultrasound

8.4 Results

Charged microbubbles and charged magnetic microbubbles were successfully produced. Representative images of the latter are shown in Figure 8.1.

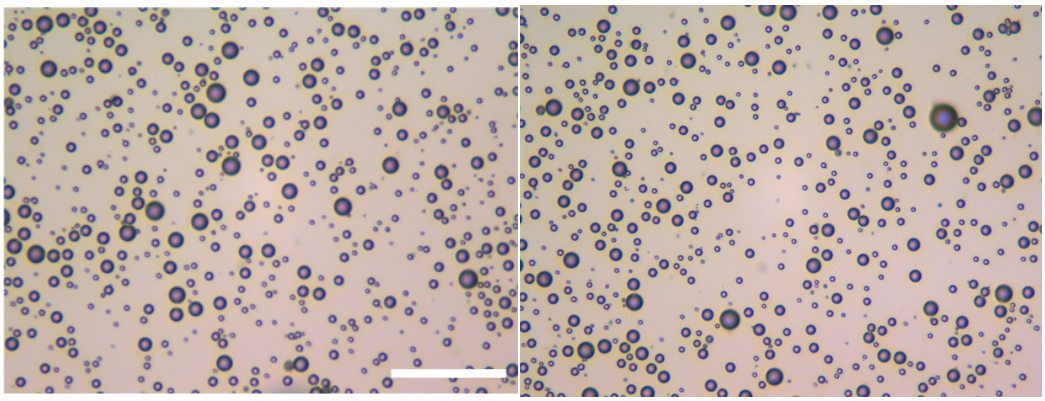


Figure 8.1, optical microscope images taken with a 40 x objective of Magnetic Microbubble 2 created with a charged lipid. Scale bar is 40 µm.

From the optical microscopy images the concentration and size distribution were measured. Adding a charged lipid to the formulation increased the number of magnetic microbubbles produced to an average of 7.05 x10^8 bubbles/ml and narrowed

the size range so the majority of microbubbles were below 8 μm (Figure 8.2). The mean diameter was 2.38 ±1.37 μm. As such the microbubbles could be produced in PBS alone without using the solution of glycerol and propylene glycol used in Chapter 7.

The improvement in microbubble concentration and size distribution was unexpected but useful for therapeutic delivery. It is likely to be caused by charge repulsion preventing the formation of larger microbubbles but this requires further investigation. Sonication alone could have an impact on the size distribution of microbubbles produced depending on the sonication time, temperature reached and cooling time of the bubble solution. However, the sonication times and temperatures chosen were based on literature research and experience to produce the best microbubble formulation in terms of concentration and size distribution [9, 10]. As sonication conditions between charged and uncharged microbubbles were kept the same it is likely that it is the charge which is causing the difference in size distribution and not sonication time.

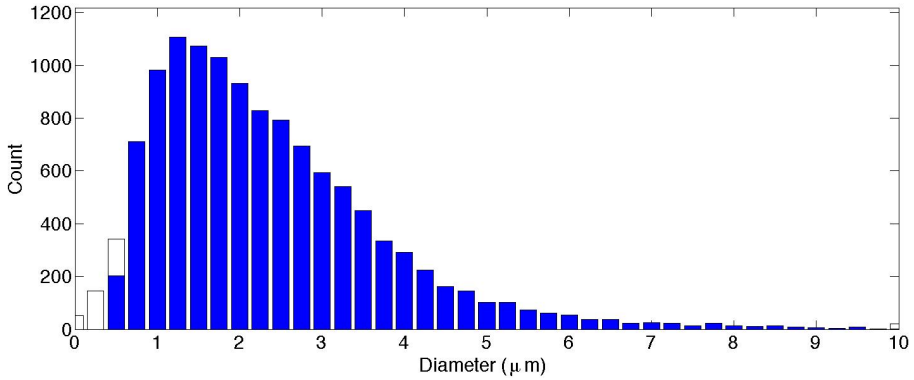


Figure 8.2, size distribution of charged magnetic microbubbles.

8.4.1 Zeta potential

The zeta potential of charged vesicles (microbubble precursors before sonication at the gas/water interface) and microbubbles were obtained and no difference could be observed between the two. This is shown in Figure 8.3. The same was found to be true for magnetic microbubbles and magnetic vesicles. As microbubbles are buoyant and will float during the zeta potential measurements this limits the amount of time the measurement can be performed and reduces the accuracy of the measurement. Lipid vesicles are neutrally buoyant and can be measured more accurately for longer periods of time. As microbubbles and vesicles were found to have the same zeta potential, examinations of siRNA attachment were performed on vesicles.

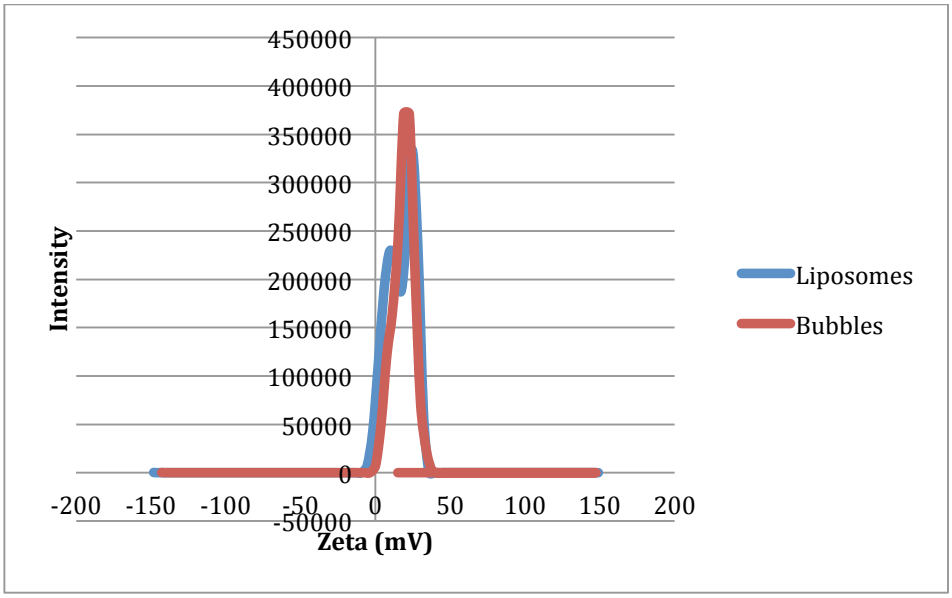


Figure 8.3, zeta potential measurement of charged microbubbles and vesicles before addition of siRNA. N>30.

It was found that magnetic microbubbles/vesicles had a lower zeta potential than non-magnetic microbubbles (Figure 8.4). As the nanoparticles are coated with neutral

phospholipid this was unexpected. However, the zeta potential was still positive and negatively charged siRNA should be able to bind to it. For ensuring maximum siRNA attachment in future experiments more positively charged lipids may need to be incorporated into the magnetic microbubbles.

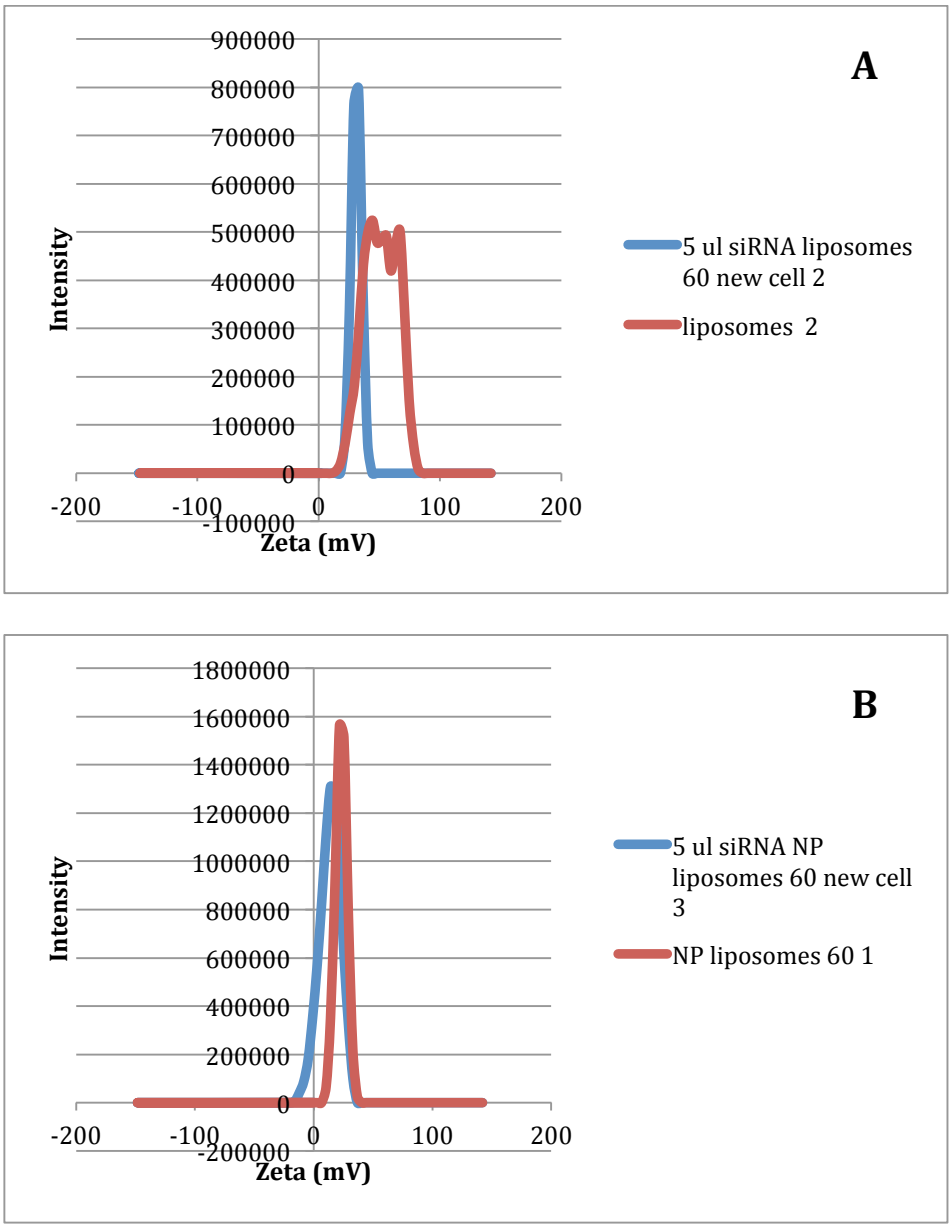


Figure 8.4, zeta potential measurements of A) charged liposomes before and after mixing with siRNA and B) charged magnetic liposomes before and after mixing with siRNA.

Upon addition of siRNA to the vesicle mixtures, followed by sonication, the zeta potential was found to have decreased. This occurred for magnetic and non-magnetic vesicles as shown in Figure 8.4. This reduction in zeta potential indicated that siRNA had successfully bound to the microbubble surface.

8.4.2 Fluorescence imaging

Charged magnetic microbubbles were analysed via fluorescence microscopy and no fluorescence could be observed at any conditions. This is shown in Figure 8.5 where microbubbles can be observed and no fluorescent objects can be observed when excited at a wavelength of 475 nm: the wavelength at which the selected siRNA fluoresced.

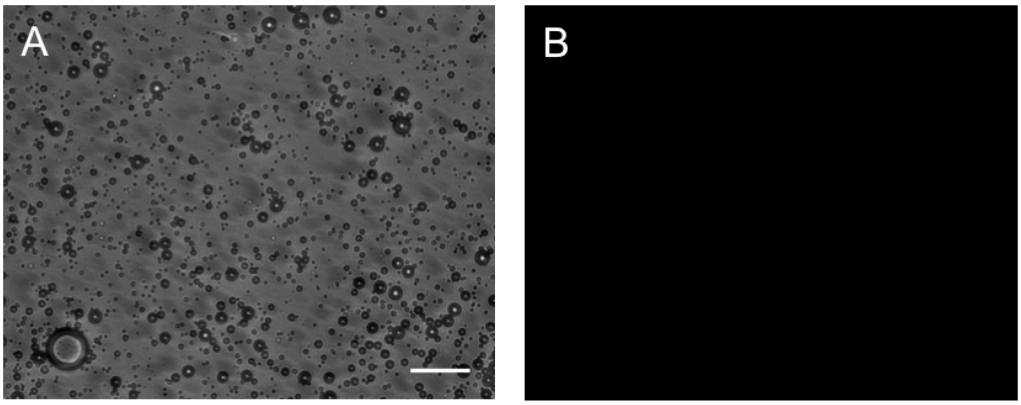


Figure 8.5, fluorescence microscopy images of magnetic microbubbles without siRNA in brightfield and fluorescence (10s G1) using a 20x objective. Scale bar is 50 µm.

Magnetic microbubbles sonicated with siRNA followed by centrifugation fluoresced against the background. The circular shape of the microbubbles could also be discerned in the images. This can be observed in Figure 8.6. Addition of siRNA to the charged magnetic microbubbles after microbubble formation did not produce the

same result. Only sonication of the siRNA with the lipid vesicles followed by sonication at the gas/liquid interface produced siRNA coated magnetic microbubbles.

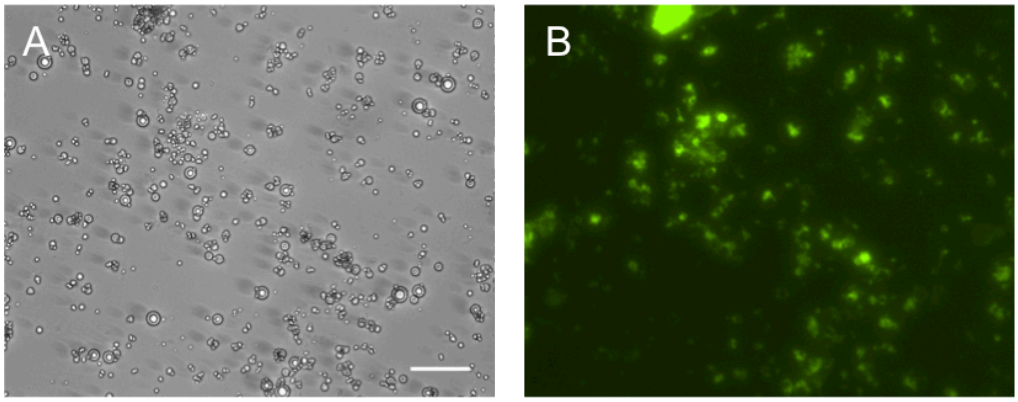


Figure 8.6, fluorescence microscopy images of magnetic microbubbles bound to siRNA after centrifugation in A) brightfield and B) fluorescence (10 s exposure, G1) using a 20x objective. Scale bar is 50 µm.

The zeta potential and the fluorescence data both indicate that the siRNA has successfully attached to the microbubbles and they were therefore ready to be used for the transfection experiments.

The amount of siRNA that attached is based on the work of Carson *et al*. [7] where it was determined that the maximum amount of siRNA which can be attached to 1 $x10^{9}$ microbubbles is 7 µg (approximately the number of microbubbles per ml). This was the quantity of siRNA added to the bubble mixture and is equivalent 7 $x10^{-9}$ µg of siRNA per microbubble.

8.4.3 Ultrasound field calibration

The spatial distribution of the ultrasound field from the transducer is shown in Figure 8.7. The highest point of the sound field was discerned and this was aligned with the exposure positions on the Opticell plate (7.3 cm)[1].

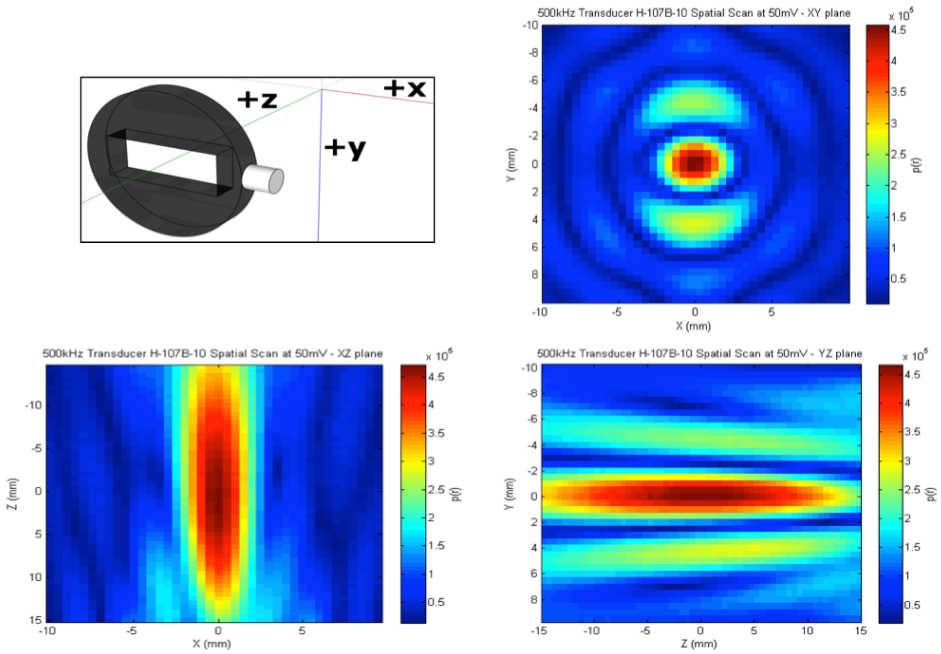


Figure 8.7, Spatial distribution of peak negative pressure of the ultrasound field transducer in the XY, XZ and YZ planes.

8.5 Transfection results

8.5.1 Plate reader results

Before and after ultrasound exposure the Opticells were examined for fluorescence on the plate reader. The plate before exposure was used as the negative control and

[1] The assistance of Calum Crake in performing this calibration is gratefully acknowledged.

siRNA bound microbubbles in an Opticell were used to ensure the siRNA could be successfully observed. The background fluorescence of the cells can be observed in Figure 8.8A and the fluorescence of microbubbles in an Opticell in Figure 8.8B. This was done simply to ensure the plate reader could detect fluorescence from the siRNA loaded bubbles in the range of wavelengths of interest.

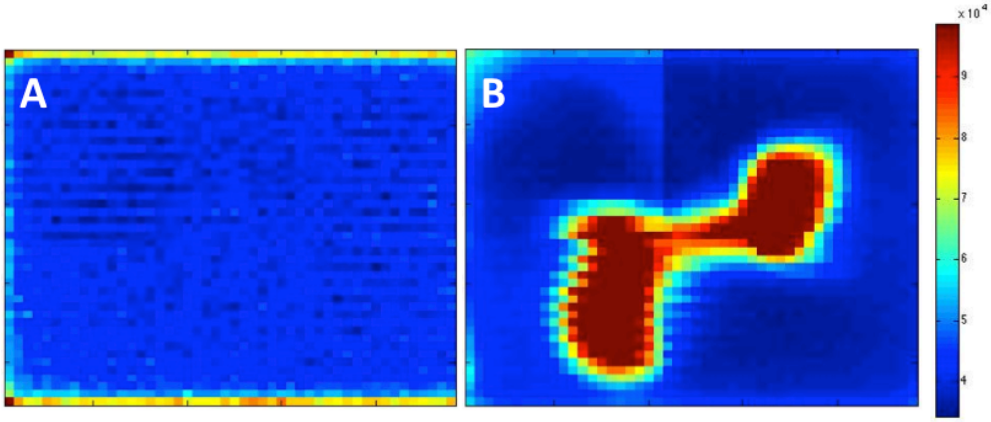


Figure 8.8, Control heat maps of whole Opticells. A) cells in media and B) magnetic microbubbles bound to fluorescent siRNA in an Opticell. The colour indicates fluorescence with dark red being the maximum pixel fluorescence. Scalebar represents fluorescence intensity units.

After the plates were exposed to the conditions outlined in Table 8.1 they were analysed in the plate reader. The cells exposed to microbubbles alone (Figure 8.9) in plate 1 showed minimal signs of fluorescence. Plate 2 and Plate 4 where only a magnetic field or ultrasound were applied respectively showed minimal fluorescence. In plate 3, where a magnetic field and ultrasound were applied in conjunction, cells were observed to fluoresce. This can be seen in Figure 8.9 (plate 3). However, only 3 out of 6 insonation zones showed signs of fluorescence. The most likely reason for this is that the magnetic microbubbles were not evenly distributed across the Opticell. The microbubbles were injected into the Opticell halfway through loading with PBS

to distribute evenly throughout the solution. However, as shown in Figure 8.8B the microbubbles are not evenly distributed over the Opticell. This is caused by microbubble buoyancy and the top surface not being perfectly flat resulting in microbubble clustering.

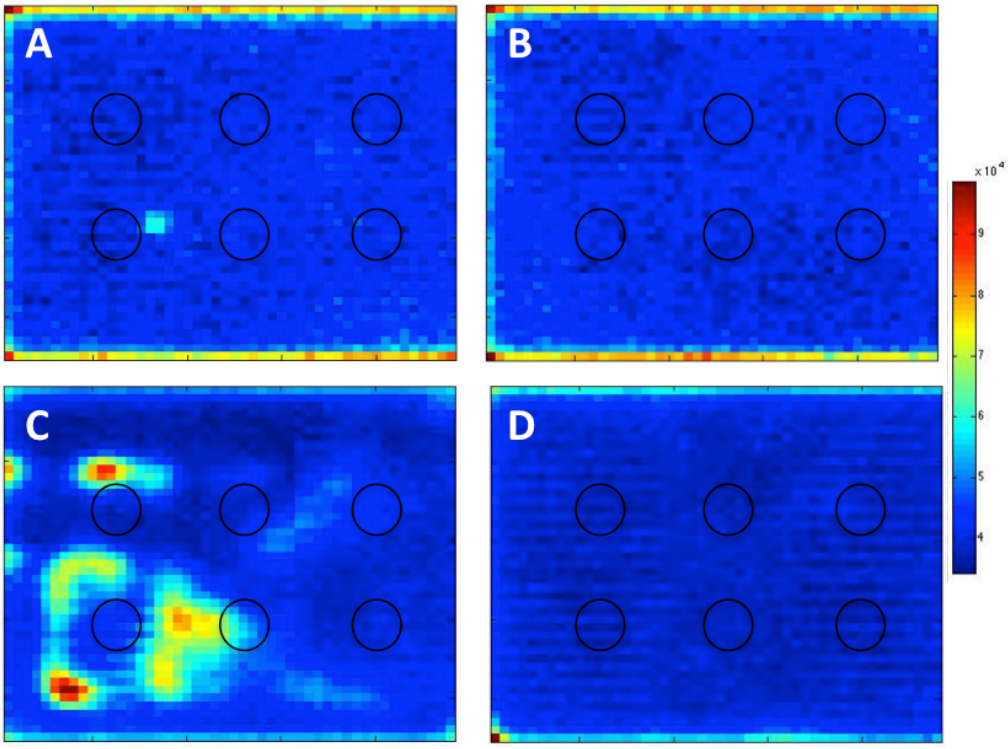


Figure 8.9, Heat maps of whole Opticells after exposure to ultrasound. Plate 1 (A) shows cells after exposure to microbubbles alone, Plate 2 (B) exposure to microbubbles in the presence of a magnetic field, Plate 3 (C) exposure to microbubbles, a magnetic field and ultrasound and Plate 4 (D) shows exposure to microbubbles and ultrasound. Scalebar represents fluorescence intensity units. The six black circles represent areas of ultrasound application.

8.5.2 Fluorescence microscopy

In order to determine whether or not siRNA was taken up by the cells fluorescence microscopy images were obtained. A control image was taken of the cells before bubbles were added to give an indication of the background fluorescence. Bubbles were added to an Opticell and images taken (without exposure to ultrasound or a

magnetic field) to obtain conditions whereby the fluorescent siRNA could be observed. Observation of bubbles was clearest at 2 s exposure with a gain of 1 as shown Figure 8.10. With these conditions all plates were analysed and the maximum intensity on each plate was recorded.

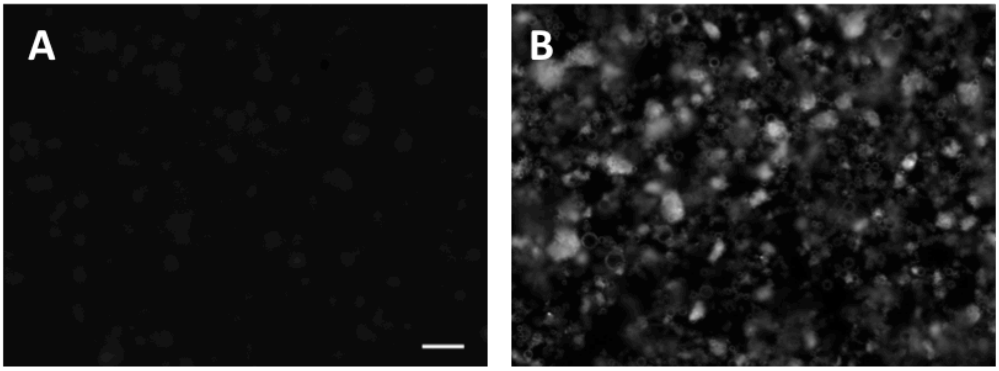


Figure 8.10, Fluoresence microscope images using a 10 x objective of A) cells in an Opticell before exposure to magnetic microbubbles and B) magnetic microbubbles bound to fluorescent siRNA in an Opticell using FITC settings at an exposure time of 2s and Gain of 1. Scale bar is 200 µm.

All spots on each Opticell were analysed. Fluorescence images agreed with the plate reader data that was obtained above. Only plate 3 where ultrasound and a magnetic field were applied in conjunction showed a large increase in fluorescence intensity at 3 insonation locations. Representative images from each plate are shown in Figure 8.11.

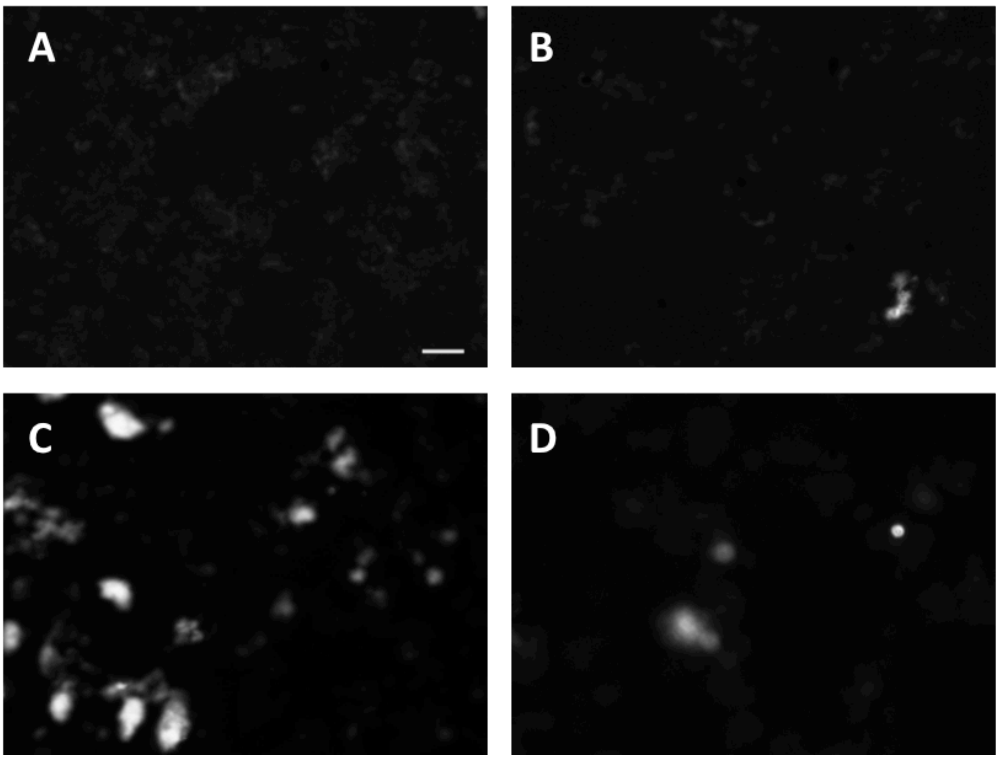


Figure 8.11, Fluorescence microscopy images of cells at 2s exposure under FITC filters at 10x magnification. A) Exposure to microbubbles alone, B) exposure to microbubbles and a magnetic field, C) exposure to microbubbles, ultrasound and a magnetic field, D) exposure to microbubbles and ultrasound. Scale bar is 200 µm.

All the images obtained from each plate were then analysed for fluorescence intensity by ImageJ in order to obtain the maximum fluorescence for each image. The pixel area over which the fluorescence was measured consisted of 1 stitched image 3 mm by 3 mm around one insonation zone. The increase in fluorescence for each pixel in this image was then measured and an average with standard deviation was then obtained for all the images for each plate. The average maximum fluorescence intensity across all the insonation spots was then plotted. The results are shown in Figure 8.12.

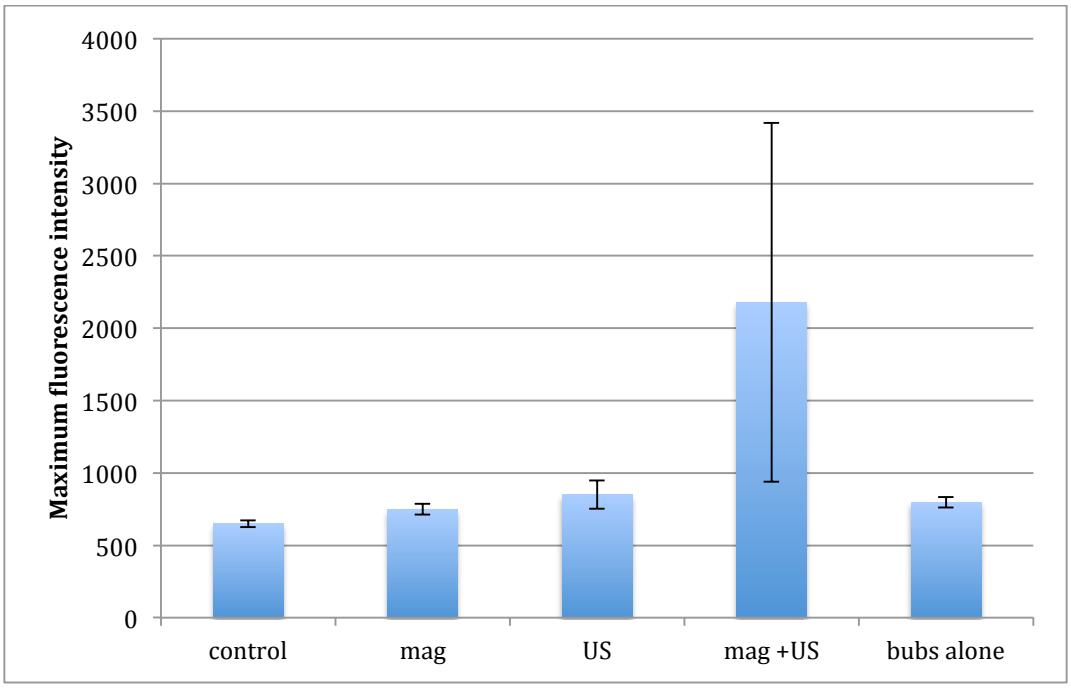


Figure 8.12, bar chart of average maximum fluorescence intensity from all images obtained of cells. Positive control is fluorescence intensity of siRNA on the bubbles. Control is cells without exposure to siRNA, all other results are after exposure to microbubbles with siRNA. Error bars indicate standard deviation (n = 6, except for mag where n = 3).

Cells, before exposure to magnetic microbubbles, had a background fluorescence intensity of over 500 fluorescence intensity units (FIU) and microbubbles with siRNA attached reached an intensity of 4000 FIU. Increases in average fluorescence are observed for cells exposed to bubbles alone (Plate 1) and a magnetic field and microbubbles (Plate 2). Ultrasound with microbubbles increased the average fluorescence to 800 FIU (Plate 4). However, microbubbles exposed to a magnetic field and ultrasound showed an average fluorescence of over 2000 FIU (Plate 3): Over four times the background fluorescence. Some results were as high as 3500 FIU. However, results for all six insonation zones are included in the bar chart which is why the standard deviation for Plate 3 (Mag +US) is so high. These results agree with the plate reader results shown above.

A two tailed Students T test was performed to compare 'US and mag' and 'US' in Fig 8.12. P=0.023 This is lower than p = 0.05 and was found to be statistically significant with one star between US alone and US and mag.

8.5.3 Cell morphology

Papers have reported that after sonoporation certain cell lines have shown reduced viability [11]. Due to this, bright field images were obtained from all plates of cells before and after exposure conditions. An example from Plate 3 is shown in Figure 8.13. Cell morphology did appear to have changed and the quantity of cells reduced. However, this was observed for all plates, including the controls to which no ultrasound, magnetic field or microbubbles were applied. The reason for the observed changes was believed to be related to the Opticell. When changing the media, air locks can easily occur and the internal pressure can rise such that cells can be sheared off the membrane. A large number of cells were removed from Plate 2 to the extent that only three spots could be successfully analysed.

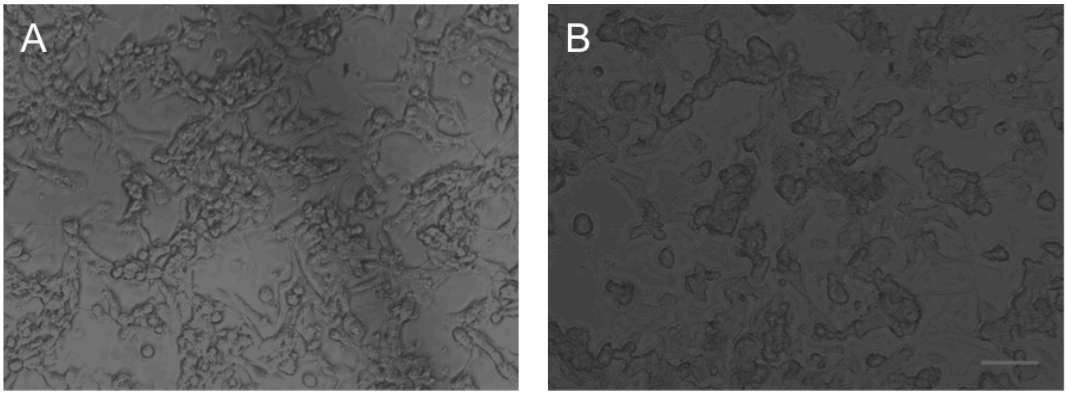


Figure 8.13, 20 x optical microscope images of cells A) before and B) after insonation from plate 3. Scale bar is 50 µm.

8.6 Discussion

Charged magnetic microbubbles were produced with siRNA attached via an electrostatic interaction. siRNA was successfully bound to the surface of the microbubbles as observed via fluorescence microscopy and the change in zeta potential. However, zeta potential measurements indicated that the charge on the microbubble was not reduced to zero indicating the potential to bind more siRNA. Zeta potential measurements vary depending on concentration and the dispersant used. The microbubbles were prepared in PBS for use with cells, however PBS has too a high salt content for use in the zeta sizer. As such 60 ul of the solution was dispersed in 940 ul of 10 mM HEPES buffer solution. This means that the charge could be different in PBS alone. However, zeta potential measurements are not as accurate as techniques such as electrophoresis to determine the maximum quantity of siRNA which can be attached to the microbubble. Optimisation of the loading of microbubbles needs to be performed but proof of principle of binding has been shown. Fluorescence microscopy also confirmed attachment of the siRNA to the microbubble surface.

An interesting observation was that siRNA added to charged microbubbles does not bind directly to the microbubbles, in fact bubbles cannot be seen fluorescing against the background. However, adding siRNA to vesicles before sonication to produce microbubbles did bind the siRNA to the bubbles as shown by fluorescence microscopy. The reasons for this are unclear but may be related to the size of microbubbles and vesicles. The vesicles, being on a much smaller scale, will have a higher concentration of charge thus attracting the siRNA to a greater degree than a microbubble where the charged lipids are distributed over a larger area. Once the

siRNA is bound to the vesicle, the vesicle is broken up to form microbubbles with siRNA still attached. Whether this process will damage the therapeutic efficacy of the siRNA needs to be determined. One possibility for the lack of binding efficiency to the microbubbles alone was quenching of siRNA molecules in close proximity to each other. However, the quantity of siRNA used was the maximum amount of siRNA Carson et al. attached to a microbubble surface (7 μg per 1x10^9 microbubbles) which should not achieve a high enough concentration on an individual microbubble for quenching to occur. Also, the nano scale vesicles will have a smaller surface area and as such quenching is more likely to occur; yet the vesicles coated in siRNA could be observed via fluorescence microscopy.

Magnetic microbubbles were then used to deliver siRNA to cells under a variety of conditions. Use of a magnetic field alone, ultrasound alone or simply exposure to the microbubbles did not increase the fluorescence intensity of cells to the same degree as exposure to a magnetic field and ultrasound simultaneously. This backs up and conforms to results previously published by Stride *et al.* [8]. The microbubbles must be in close proximity to target cells in order to successfully deliver the therapeutic agent of choice. However, Stride *et al.* did not have the DNA to be transfected attached to the microbubble surface and used a different magnetic microbubble formulation (MMB). The new magnetic microbubble formulation (LMMB) has never been used for therapeutic delivery and the loading of the therapeutic compound on the microbubble surface is much more feasible for clinical application. This allows for intravenous delivery whereby the microbubble and the therapeutic compound will reach the target location at the same time, relative to co-injection which will be

limited to the target site. The increase in fluorescence against the background was confirmed by two methods: fluorescence microscopy and via a plate reader.

As above, only three out of six exposure locations showed an increase in fluoresence intensity for plate 3 (US and mag). This is most likely due to the size of the Opticell resulting in a non-uniform distribution of microbubbles. The microbubbles are injected into the Opticell, mixed via agitation and then placed in a water bath for exposure to ultrasound or a magnetic field. A positioning system moves the Opticell such that the magnetic field and ultrasound are a maximum at one specific point. This experimental set up assumes the microbubbles are evenly distributed throughout the Opticell. The microbubbles are more likely to agglomerate at certain points throughout the Opticell and exposure to a magnetic field may move the bubbles such that the majority are destroyed in the first few exposures meaning little will happen at later exposure zones. This was observed via fluorescence microscopy and the plate reader where not all spots showed equal fluorescence intensity. On average the plate showed a higher fluorescence but the large standard deviation shown in Figure 8.12 for exposure to a magnetic field and ultrasound shows the variation observed. For future experiments a smaller plate with a single insonation zone would be more desirable.

8.7 Limitations.

The highest fluorescence on images was located where cells were present indicating siRNA has entered cells. The cells still seemed viable one day after exposure however a long cell viability study was not performed. Whether the siRNA is still able to function after siRNA uptake requires to be tested. A recent study by Liu *et al.*

has indicated that use of ultrasound to drive therapeutic agents into cells can lead to cell death [12]. Although the study used 1 MHz, 0.5 MPa and a 1 minute exposure time which is different to conditions used in this study.

8.7.1 Potential Limitations in vivo

For targeted therapy the microbubbles will have an *in vivo* lifetime between 10 -15 minutes limiting the time frame for application of a magnetic field and ultrasound before clearance [13]. The quantity of siRNA which can be delivered via the microbubbles is also important. For transdermal injection into a muscle site of a mouse 100 μg of siRNA was injected for an observable therapeutic effect [14]. However, Carson *et al.* injected 5 μg of siRNA tagged to microbubbles into a mouse intra-arterially for knockdown of EGF under ultrasound and a reduction in tumour volume [7]. The magnetic microbubbles would allow for a similar quantity (5 μg) via systemic injection which has been shown to be adequate for a therapeutic effect. One limitation for drug delivery is penetration of the magnetic field which can currently extend a few cm into the body at field strengths and gradients required for targeting. This limits targeting to the extremities of a human being, limiting potential locations for magnetically targeted siRNA delivery.

8.8 References

1. Whitehead, K.A., R. Langer, and D.G. Anderson, *Knocking down barriers: Advances in siRNA delivery.* Nature Reviews Drug Discovery, 2009. **8**(2): p. 129-138.
2. Gomes-Da-Silva, L.C., et al., *Lipid-based nanoparticles for siRNA delivery in cancer therapy: Paradigms and challenges.* Accounts of Chemical Research, 2012. **45**(7): p. 1163-1171.

3. Florinas, S., et al., *Ultrasound-assisted siRNA delivery via arginine-grafted bioreducible polymer and microbubbles targeting VEGF for ovarian cancer treatment.* Journal of Controlled Release, 2014. **183**(1): p. 1-8.
4. Gao, K. and L. Huang, *Nonviral methods for siRNA delivery.* Molecular Pharmaceutics, 2009. **6**(3): p. 651-658.
5. Lewis, D.L. and J.A. Wolff, *Systemic siRNA delivery via hydrodynamic intravascular injection.* Advanced Drug Delivery Reviews, 2007. **59**(2-3): p. 115-123.
6. Soutschek, J., et al., *Therapeutic silencing of an endogenous gene by systemic administration of modified siRNAs.* Nature, 2004. **432**(7014): p. 173-178.
7. Carson, A.R., et al., *Ultrasound-targeted microbubble destruction to deliver siRNA cancer therapy.* Cancer Research, 2012. **72**(23): p. 6191-6199.
8. Stride, E., et al., *Enhancement of Microbubble Mediated Gene Delivery by Simultaneous Exposure to Ultrasonic and Magnetic Fields.* Ultrasound in Medicine & Biology, 2009. **35**(5): p. 861-868.
9. Feshitan, J.A., et al., *Microbubble size isolation by differential centrifugation.* Journal of Colloid and Interface Science, 2009. **329**(2): p. 316-324.
10. Unger, E.C., et al., *Acoustically active lipospheres containing paclitaxel - A new therapeutic ultrasound contrast agent.* Investigative Radiology, 1998. **33**(12): p. 886-892.
11. Liu, Y., J. Yan, and M.R. Prausnitz, *Can Ultrasound Enable Efficient Intracellular Uptake of Molecules? A Retrospective Literature Review and Analysis.* Ultrasound in Medicine and Biology, 2012. **38**(5): p. 876-888.
12. Zhong, W., et al., *Sonoporation induces apoptosis and cell cycle arrest in human promyelocytic leukemia cells.* Ultrasound in Medicine and Biology, 2011. **37**(12): p. 2149-2159.
13. Quaia, E., *Microbubble ultrasound contrast agents: An update.* European Radiology, 2007. **17**(8): p. 1995-2008.
14. Wolff, J.A., et al., *Direct gene transfer into mouse muscle in vivo.* Science, 1990. **247**(4949): p. 1465-1468.

9 Conclusions and future work

9.1 Conclusions

9.1.1 Overview

The aims of this chapter are to summarise the contributions of the work and conclusions drawn and to make proposals for future research in those areas identified as a result of the work as requiring further investigation. This chapter will also examine the results obtained so far against criteria for an ideal magnetic microbubble: 1) Ability to magnetically target at the majority of blood flow conditions in the human body in high concentration, 2) Capable of targeting against flowing blood, 3) Magnetic targeting can be observed in vivo, 4) Is capable of attachment of a therapeutic compound. 5) Delivery of therapeutic compounds to cells under ultrasound and a magnetic field.

9.1.2 Electron Microscopy

A new method to analyse the structure of microbubbles on the nanoscale has been developed using electron microscopy. This is the first occasion that phospholipid microbubbles below 2 um in size have been directly observed through the use of a uranyl acetate stain.

Domains, previously observed via fluorescence microscopy, were observed on microbubbles <8 um in diameter. Phospholipid microbubbles <2 um in size were observed without any discernable domains on the microbubble surface as predicted by Borden et al [1]. Vesicles on the nanoscale could be observed embedded in microbubble surface indicating how the microbubble successfully formed. Samples of microbubbles with nanoparticles embedded in their surfaces were also successfully imaged. Three microbubble structures predicted theoretically in previous studies were confirmed via this technique.

The information gained from these studies could facilitate optimisation of both microbubble composition and production technique by demonstrating the nanoscale structural changes produced by a given protocol.

limitations

The TEM provides a 2D projection of a 3D object which limits conclusions which can be drawn from the images. The uranyl acetate coating may influence shell structure underneath relative to microbubbles in aqueous solution.

9.1.3 Magnetic Targeting

A flow phantom was developed to examine the magnetic targeting of microbubbles. Experiments determined the limits of magnetic targeting under flow conditions simulating those found *in vivo* in terms of volume flow rate and wall shear rate.

Using ultrasound imaging, results were obtained for three different vessel sizes at a variety of flow rates and shear rates in both saline and whole blood. Optical microscopy was used to examine targeting in a 200 μm capillary at the highest shear rates. The results indicate that magnetic targeting of magnetic microbubbles should be possible in the human body using magnetic field strengths and gradients that are safe for clinical use. Targeting was successful for all flow conditions relevant to capillaries, venules and veins; and for arteries with flow rates up to ~200 ml/min. For larger arteries, higher magnetic field gradients would be required which might be difficult to achieve at large tissue depths due to the large magnetic field gradients required. It is important to note, however that the upper limits in terms of safety on magnetic field gradients produced by permanent magnets have not been defined. This partly fulfils criteria 1 proving magnetic targeting is possible at blood flow conditions within the human body.

Limitations

A large standard deviation was obtained with some targeting results due to variations in the bubble formulation. The results are also constrained by the magnetic field strength applied (0.5 T) which is below medical limits for MRi (>9 T)

9.1.4 In vivo Liver Targeting

Magnetic field strength decreases with the third power of the distance from the magnet. Small animal experiments thus do not provide a relevant length scale for testing magnetic targeting for potential application in humans. An organ perfusion system was utilised to perform a preliminary experiment in porcine livers to determine whether there were features of the *in vivo* environment not captured in the flow phantom model that would significantly impact magnetic targeting. Magnetic targeting was successfully observed and no extravasation or reduction in acoustic response of the microbubbles was seen. The study also highlighted the importance of magnetic field orientation *in vivo* and ultimately the need for a three dimensional array in order to ensure the maximum field strength was located at the target area. Due to the configuration of the experimental apparatus, the orientation of the magnetic array in these experiments was not optimised and this limited the maximum flow rate at which targeting was observed. This fulfils criteria 3 indicating observation of magnetic targeting is feasible *in vivo*.

Limitations

The use of non-magnetic microbubbles as a control rather than magnetic microbubbles without a magnetic field limits what can be determined from the acoustic response. The use of the liver as the target organ is not desirable for *in vivo* targeting owing to the presence of Kupffer cells and experiments must be attempted in another perfused organ for confirmation of results.

9.1.5 Targeting against Blood

It was found using a combination of ultrasound imaging and optical microscopy that the number of magnetic bubbles that could be successfully retained was reduced by up to 60 % when blood was substituted for water under the same flow conditions.

An even greater effect was seen in the case of biochemical targeted microbubbles with a 90% reduction in the number of bubbles retained. The reason for the reduction in targeting efficiency was thought to be the presence of red blood cells. Microbubbles and red blood cells are approximately the same size and can collide with another. This would both detach targeted microbubbles and prevent access to

target sites for flowing microbubbles. This needs to be taken into account in any *in vivo* targeting study of microbubbles and has significant implications for the translation of targeted microbubbles into clinical use. However, mechanisms for improving magnetic targeting would be easier to implement: specifically improving the microbubble formulation to increase susceptibility and/or utilising three dimensional magnetic arrays providing stronger trapping forces and the ability to manipulate the trapping volume. This result also showed that magnetic targeting of microbubbles is also possible against flowing blood fulfilling criteria 2.

limitations

The blood used in these experiments was heparinised on a scale which does not occur in vivo.

9.1.6 Magnetic Droplets and Microbubbles

In a previous study a variety of microbubble formulations were tested as transfection agents. It was found unexpectedly that magnetic droplets mixed with phospholipid microbubbles gave high rates of transfection. The reasons for this were not fully understood. As described in chapter 7, fluorescence experiments showed that magnetic droplets coat the microbubbles with an interaction strong enough to resist centrifugation. Subsequent targeting experiment under ultrasound imaging indicated that microbubbles that responded upon application of a magnetic field had been produced. Surface energy calculations also indicated that the resulting microbubble is more energetically favourable as a structure than the magnetic droplet, meaning a process similar to Ostwald ripening, fusing the droplet to the microbubble, could occur. Electron microscopy further confirmed the nano-scale surface structure of the microbubble with nanoparticles embedded in the microbubble surface.

In addition to explaining the results of the previous study, these findings suggested a new method by which magnetic microbubbles could be prepared.

9.1.7 New Microbubble Formulation

A new composition and method for fabricating magnetic microbubbles that shows improved performance compared with the original formulation was developed. In this case phospholipid coated iron oxide nanoparticles were incorporated directly into phospholipid microbubbles. This removed the need for a suspending oil layer which had been shown previously to reduce the nonlinear character of the microbubbles and could have potentially raised concerns over microbubble toxicity.

The mechanism of formation embeds the nanoparticles into the microbubbles in a single manufacturing step without the need for inducing an electrostatic charge or using a biochemical linker. The new formulation showed strong targeting under flow and relaxivity measurements indicated the limits of magnetic targeting should be similar to the original magnetic microbubble formulation. It was also confirmed that the new microbubbles exhibited non-linear behaviour under contrast ultrasound imaging.

Limitations

Glycerol and propylene glycol had to be added to the solution to improve microbubble size distribution and concentration.

9.1.8 Transfection study of newly designed Magnetic microbubbles

The new magnetic microbubbles were formulated using a positively charged phospholipid which allowed fluorescent siRNA to be successfully bound to it. This was confirmed by zeta potential and fluorescence microscopy. The loaded microbubbles were then used to deliver the siRNA to neuroblastoma cells. Results obtained via fluorescence microscopy, indicated that only when ultrasound and a magnetic field were applied in combination did cells show a significant increase in fluorescence intensity. When a magnetic field or ultrasound was applied alone, only minimal increases in fluorescence intensity were observed relative to the control. The results indicate that the new magnetic microbubble formulation has potential as a new therapeutic delivery vehicle: Therapeutic material can be attached to the surface, it can be magnetically targeted against the majority of flow conditions found in the human body it can be observed under ultrasound without damping and under high

intensity focused ultrasound has shown the potential to deliver siRNA to cells. These results fulfil criteria 4 and partially fulfils criteria 5 as therapeutic knockdown was not attempted.

Limitations

Cell viability was not examined after the experiments nor the potential for the siRNA to knockdown a desired protein.

9.2 Future Work

9.2.1 Electron microscopy of microbubbles with liposomes bound to the surface

The ability to relate microbubble composition and/or fabrication technique directly to the coating structure has considerable potential for improving the effectiveness of microbubble agents for both imaging and therapeutic applications. For example, understanding the location and concentration of functional species such as nanoparticles or drug loaded liposomes within the bubble structure is very important for optimising their characteristics for a particular application. Similarly, the stability of microbubbles has been shown to be closely related to the coating structure and hence processing method. Moreover, whilst the focus of the work described in chapter 4 was phospholipid microbubbles, the technique could be applied to both polymer and protein microbubbles.

Electron microscopy has shown the ability to observe domains on a variety of microbubble formulations smaller than 20 μm. To the candidate's knowledge this has never been demonstrated before. But similar cooling experiments to those performed in previous research could be used to examine domain formation on the nanoscale directly on the surface of clinically relevant microbubbles. Comparison with other techniques, such as fluorescence lifetime imaging, would provide the best information regarding the properties of the microbubble for clinical use.

9.2.2 Agglomeration of microbubbles in blood

Longer term examination of biotin coated microbubbles under flow did indicate that agglomeration of microbubbles started to occur when the flow stopped. This phenomenon has not yet been explained as the microbubbles were coated with a lipid expressing PEG. However it was not simply unique to the biotin expressing bubbles as a similar agglomerating effect was observed with SonoVue®, which is commercially available as an ultrasound contrast agent. However, this clumping was only noticed when blood flow was stopped whilst for the experiment blood flow was constantly running and individual microbubbles can be observed successfully targeting eliminating the possibility of macrophage or platelet action.

9.2.3 Effect of single red blood cells in an 8 μm channel.

The effect of red blood cells in a 200 μm micron channel has been demonstrated successfully. In the capillaries (6 – 10 μm) red blood cells deform and travel through one at a time pressed up against the vessel wall. Flow studies have shown magnetic microbubbles can target against shear rates found in the capillaries but not whether there is a lower limit on capillary size. Attempting targeting in an microfluidic flow phantom would allow observation of whether the red blood cell can dislodge the microbubble, deform around the microbubble or if the microbubble can cause occlusion of the vessel. This will be an important study for whether or not magnetic and/or other targeting can occur in the microvasculature. However, the lack of known biomarkers in the capillaries makes them an ideal candidate for magnetic targeting.

9.2.4 Magnetic Droplets and Commercial Contrast Agents

A new mechanism for magnetic microbubble formation has been determined via nanoscale magnetic droplets fusing with non-magnetic microbubbles. This mechanism has been successfully adapted and improved to form new magnetic microbubbles. The magnetic droplets could also be mixed with commercial agents in order to determine if the mechanism can adapt an existing type of microbubble for magnetic targeting. Initial experiments have indicated that e.g. SonoVue can be made to respond to a magnetic field. This could potentially lead to much more rapid clinical translation.

9.2.5 Citric acid coated iron oxide nanoparticles

Microbubbles with gold attached to the surface have been successfully created by Stride *et al* [2]. The gold nanoparticles are coated in citric acid and adsorb onto the microbubble surface during microbubble production. The mechanism of formation could be adapted in order to produce magnetic microbubbles. Citric acid coated iron oxide nanoparticles could be used as a replacement to produce a new magnetically responsive microbubble formulation. Preliminary experiments have been performed and the new microbubble formulation does respond to a magnetic field as shown in Figure 9.1. However, the targeting is not as strong as for the previous magnetic microbubble formulations and further development of this technique is required.

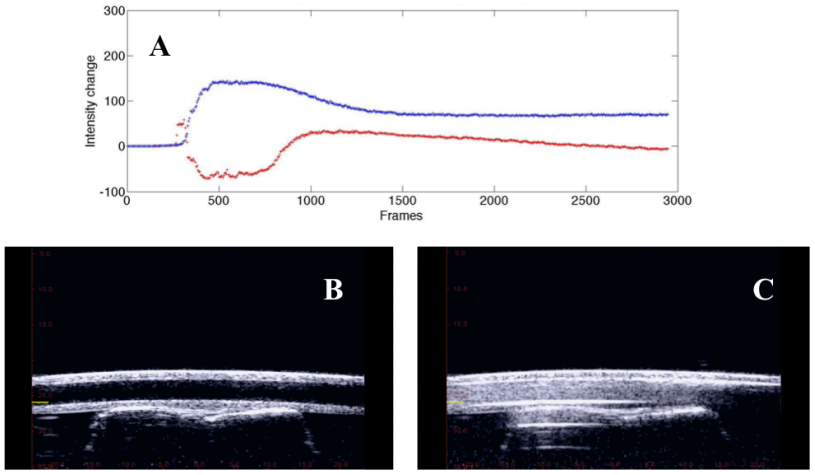


Figure 9.1, Magnetic microbubbles being perfused through a latex flow phantom in the presence of a magnetic field. A) intensity change along the wall furthest from the imitation magnet (blue) and wall closest to the imitation magnet (red). B) Image of latex flow phantom with imitation magnet positioned underneath before and C) after perfusion with magnetic microbubbles showing all microbubbles to be along the top of the latex vessel.

9.2.6 Janus Bubbles

Lipid coated iron oxide nanoparticles were successfully incorporated into microbubbles. These microbubbles could be manipulated with a magnetic field and successfully delivered siRNA to cells. This formulation could be adapted to produce a so called "Janus" microbubble with gold and iron oxide nanoparticles on the surface

attached through the same binding mechanism. A solution of phospholipids, lipid coated gold nanoparticles and lipid coated iron oxide nanoparticles could be sonicated to produce a microbubble with iron oxide and gold on the surface. This would be similar to Janus nanoparticles which have been proposed for dual contrast imaging [3]. The Janus microbubble would be a triple contrast agent for ultrasound, MRI and CT.

9.2.7 Biotoxicity, Biocompatability and Pharmacokinetics

Before attempting siRNA delivery in vivo the following experiments would have to be performed to assess microbubbles in vivo. Initially, Detection of an immune response to the microbubbles in an animal model by examination of the blood at set time points after injection. Secondly, stability and lifetime in blood of the magnetic microbubbles; An examination of the bloodstream persistence relative to Sonovue would have to be performed for clinical relevance [4]. The excretion pathway of the microbubbles will need to be determined to ensure the pharmacokinetics are similar to clinically available formulations [5]. All of the above will have to be examined with respect to dosage in order to determine the appropriate dose. The dose will initially based upon quantities (ml/kg) used clinically for imaging [6] and those previously used in animal experiments for therapeutic delivery [7].

9.2.8 Examination of knockdown with siRNA and in vivo experiments.

Future experiments with the new magnetic microbubble formulation will use a custom made siRNA for the knockdown of STATVI. Knockdown of this protein has shown potential for cancer therapy [8]. Preliminary experiments have been performed and fluorescence microscopy indicates that STATVI siRNA successfully binds to the microbubble as shown in Figure 9.2. There is likely to be heterogeneity of siRNA binding over the bubble shell, causing heterogeneity of fluorescence, owing to use of DSPC as the major component in the microbubble shell. Use of DPPC would lead to a more homogeneous distribution of siRNA over the bubble shell and this will be looked at in future microbubble structures [9]. Delivery efficiency and knockdown measurements will shortly be performed. Cell viability and survival will also be examined since previous literature has shown that sonoporation can kill large numbers of transfected cells [10].

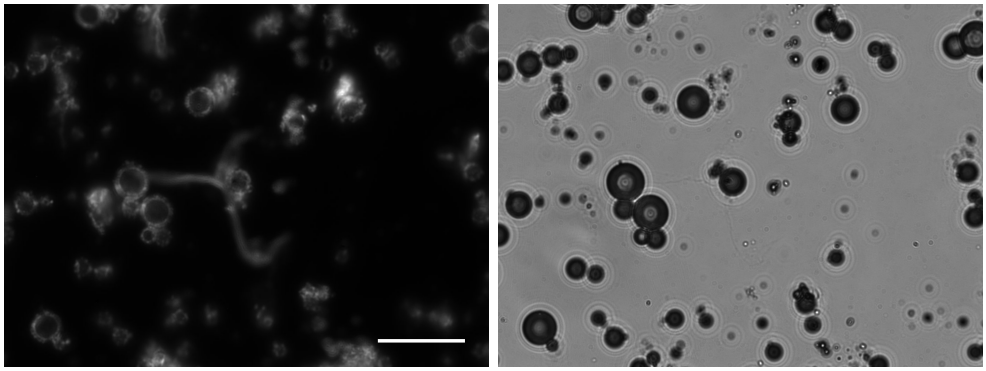


Figure 9.2, 40x microscope images of microbubbles bound to STATVI siRNA in A) far red and B) brightfield. Scale bar is 50 µm. Exposure time 5s and gain of 1.

Owing to problems with the Opticell device, a new system for delivering cells has been designed based upon a 38 mm well plate with an acoustically transparent lid designed and produced in house. Each well plate has a single insonation spot and limits the degree to which microbubbles can disperse, thereby providing more accurate results for comparison.

9.2.9 Three dimensional magnetic arrays for targeting

Chapter 6 highlighted the problems of magnetic field orientation for targeting *in vivo*. A more accurate targeting system is required to ensure the highest magnetic field strengths and gradients are located at the target sites. Magnetic navigation systems have been designed for movement of magnetically-enabled guidewires, in three dimensions, for percutaneous coronary intervention [11]. A similar system could be designed for the targeting of magnetic microbubbles *in vivo*.

9.3 References

1. Borden, M.A., et al., *Surface phase behavior and microstructure of lipid/PEG-emulsifier monolayer-coated microbubbles.* Colloids and Surfaces B: Biointerfaces, 2004. **35**(3-4): p. 209-223.
2. Stride, E., et al., *Increasing the nonlinear character of microbubble oscillations at low acoustic pressures.* Journal of the Royal Society Interface, 2008. **5**(24): p. 807-811.
3. Lattuada, M. and T.A. Hatton, *Synthesis, properties and applications of Janus nanoparticles.* Nano Today, 2011. **6**(3): p. 286-308.

4. Chen, C.C., et al., *Effect of Surface Architecture on InVivo Ultrasound Contrast Persistence of Targeted Size-Selected Microbubbles.* Ultrasound in Medicine and Biology, 2012. **38**(3): p. 492-503.
5. Quaia, E., *Microbubble ultrasound contrast agents: An update.* European Radiology, 2007. **17**(8): p. 1995-2008.
6. Morel, D.R., et al., *Human pharmacokinetics and safety evaluation of SonoVue(TM), a new contrast agent for ultrasound imaging.* Investigative Radiology, 2000. **35**(1): p. 80-85.
7. Carson, A.R., et al., *Ultrasound-targeted microbubble destruction to deliver siRNA cancer therapy.* Cancer Research, 2012. **72**(23): p. 6191-6199.
8. Youngren, S.R., et al., *STAT6 siRNA matrix-loaded gelatin nanocarriers: Formulation, characterization, and Ex vivo proof of concept using adenocarcinoma cells.* BioMed Research International, 2013. **2013**.
9. Kooiman, K., et al., *DSPC or DPPC as main shell component influences ligand distribution and binding area of lipid-coated targeted microbubbles.* European Journal of Lipid Science and Technology, 2014.
10. Zhong, W., et al., *Sonoporation induces apoptosis and cell cycle arrest in human promyelocytic leukemia cells.* Ultrasound in Medicine and Biology, 2011. **37**(12): p. 2149-2159.
11. Kiemeneij, F., et al., *Use of the Stereotaxis Niobe® magnetic navigation system for percutaneous coronary intervention: Results from 350 consecutive patients.* Catheterization and Cardiovascular Interventions, 2008. **71**(4): p. 510-516.

10 Appendix

Equation for magnetic field strength for Figure 5.1

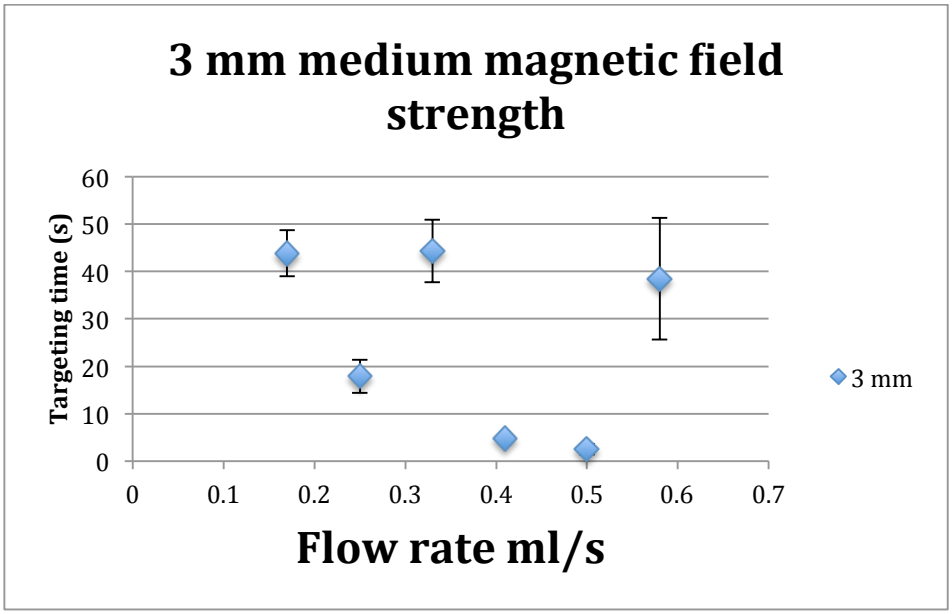
$$m\ddot{y}(t) + 6\mu_L \pi R_{02} \dot{y}(t) = F_B - mg - F_M - F_A(t)$$

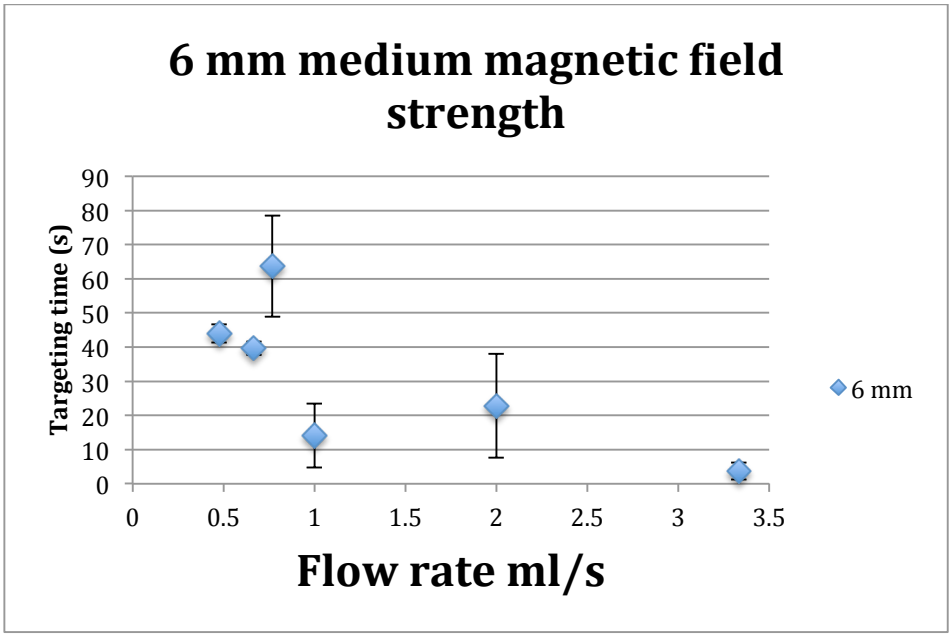
Let: $F_B - mg - F_M = G$, and: $-F_A(t) = amp * \sin(2\pi f t) * \exp\left(-4\left(\frac{t-\tau}{\tau}\right)^2\right)$

$$m\ddot{y}(t) + 6\mu_L \pi R_{02} \dot{y}(t) = G + amp * \sin(2\pi f t) * \exp\left(-4\left(\frac{t-\tau}{\tau}\right)^2\right)$$

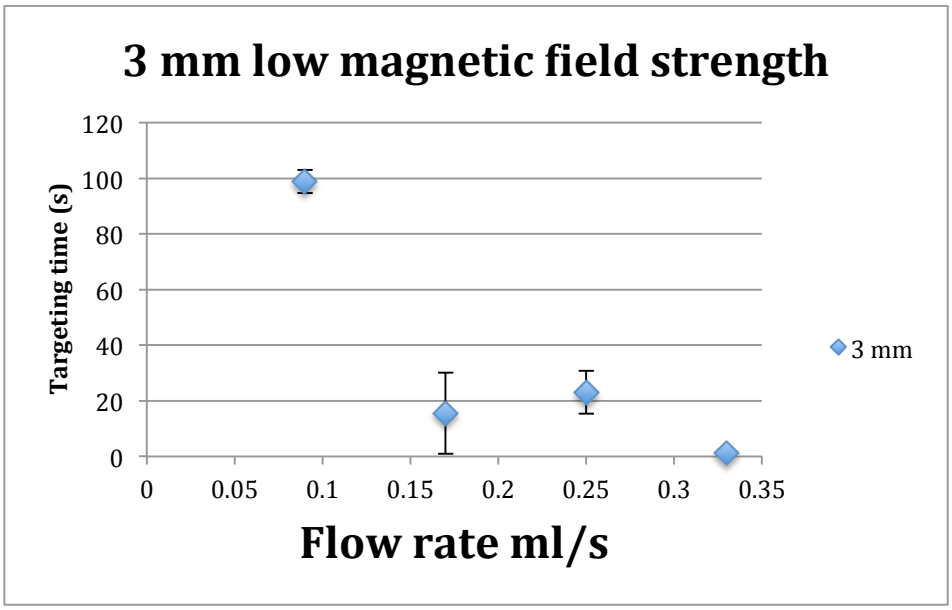
Targeting time

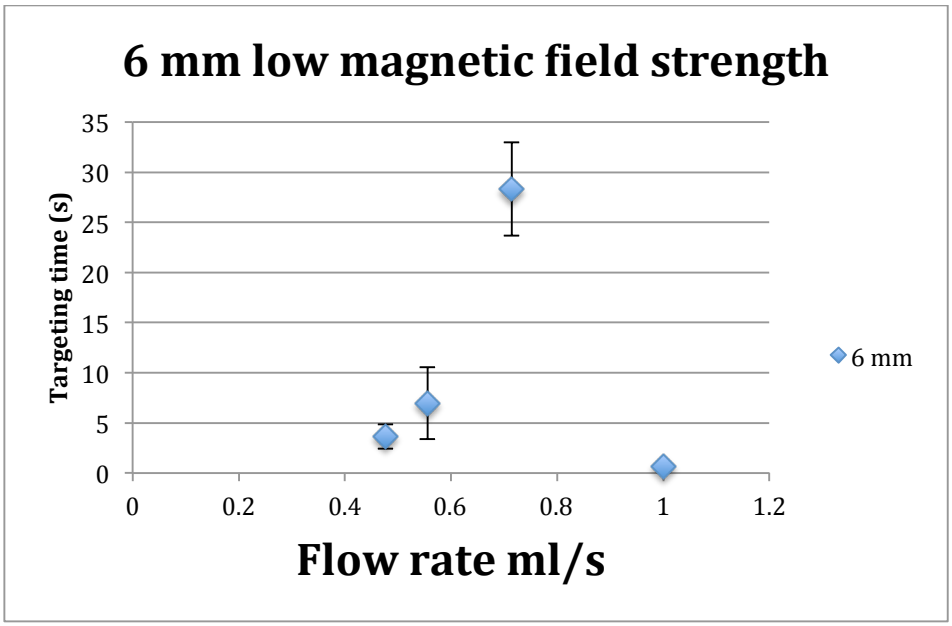
Magnetic field strength 0.05 T





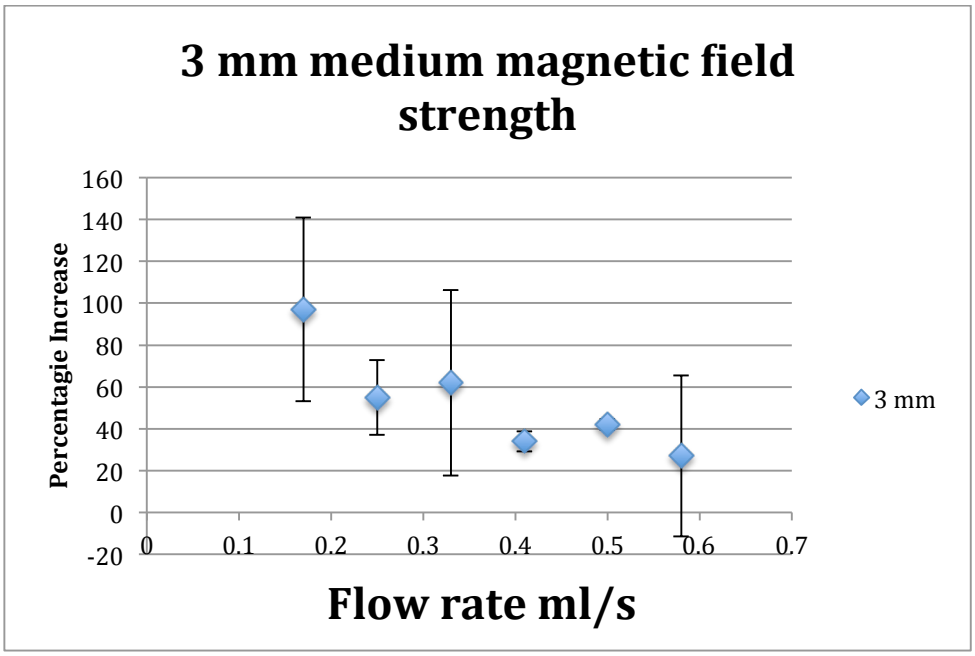
Magnetic field strength (0.03 T)

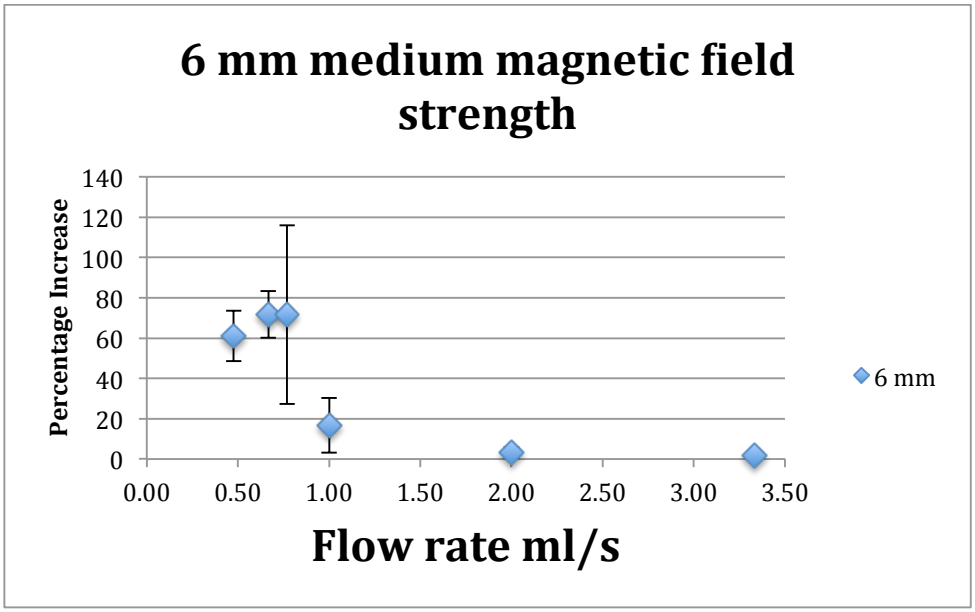




Targeting Intensity

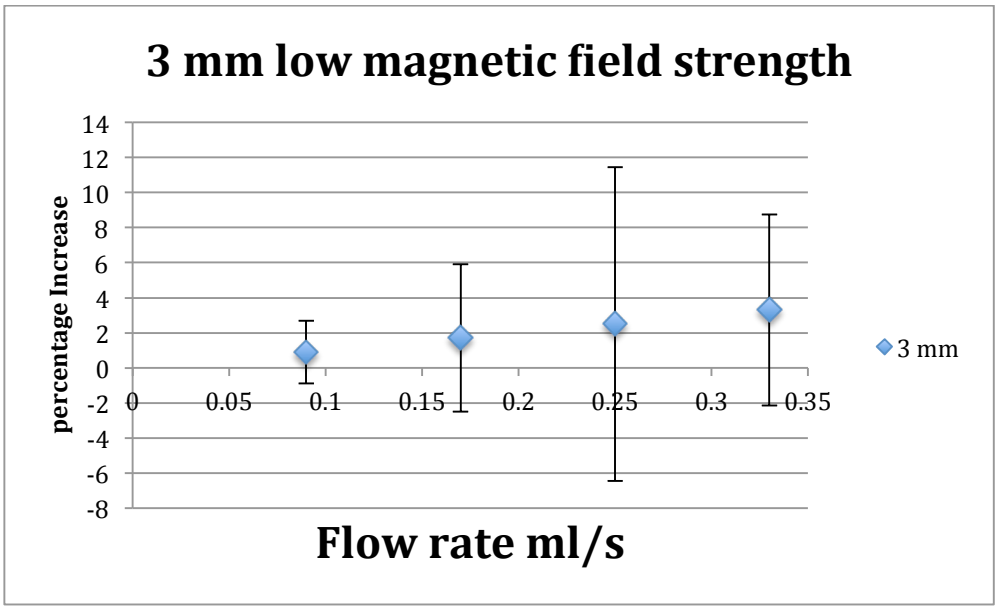
Magnetic field strength 0.05 T

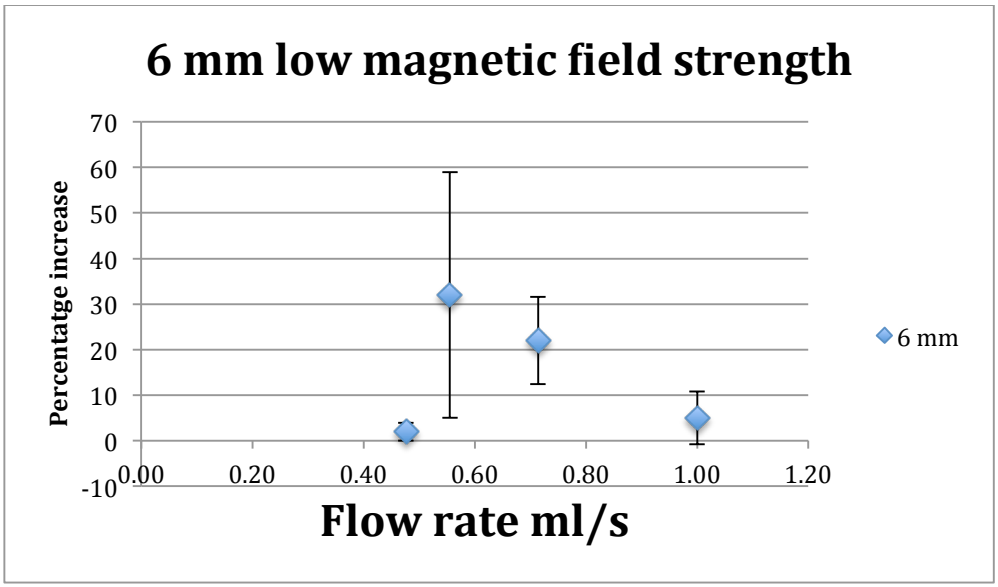




Targeting Intensity

Magnetic field strength (0.03 T)


3 mm low magnetic field strength
percentage Increase
14
12
10
8
6
4
2
0
-2
-4
-6
-8
0
0.05
0.1
0.15
0.2
0.25
0.3
0.35
Flow rate ml/s
3 mm


6 mm low magnetic field strength
Percentatge increase
70
60
50
40
30
20
10
0
-10
0.00
0.20
0.40
0.60
0.80
1.00
1.20
Flow rate ml/s
6 mm